SENSORLESS DRIVES FOR PERMANENT MAGNET SYNCHRONOUS MOTORS

BY

SOH CHENG SU, M. Eng.

A THESIS SUBMITTED

FOR THE DEGREE OF DOCTOR OF PHILOSOPHY

DEPARTMENT OF ELECTRICAL AND COMPUTER ENGINEERING

NATIONAL UNIVERSITY OF SINGAPORE

2010

Abstract

Initiated by the advent of high performance processors and energy concerns, Permanent Magnet Synchronous Motors (PMSM) are increasingly being adopted in numerous consumer products. PMSM with sensors have traditionally been driven sinusoidally. However, in many applications such as Hard Disk Drives (HDDs), sensorless Brushless DC (BLDC) drive is applied onto PMSM despite existing drawbacks. The research work in this thesis aims to address the concerns in these applications. In an attempt to introduce and integrate the work to the industry, the architectural design, algorithm codes and on-board testing were performed on Field Programmable Gate Array (FPGA).

Sensorless control schemes utilizing back-EMF zero crossing points (ZCPs) to estimate the rotor position have been widely used. Derived from this principle, a popular strategy, Terminal Voltage Sensing, however, suffers from inductive commutation spikes during ZCPs detection. As a result, terminal voltage waveforms are traditionally pre-filtered prior to usage for BLDC commutation. Such a strategy limits its performance, especially at high speed. In this thesis, a sensorless BLDC drive derived from ZCP centering is conceived with heuristic logic incorporated, for zero delay ZCP detection. The implemented design, as intended, operated with zero delay, yet is robust against spikes and makes the drive well-suited for wide speed range.

BLDC drive applied on PMSM whilst brought about the advantages of robustness and simplicity, unfortunately, suffers from severe torque pulsation and aggravated by commutation torque ripple. In this dissertation, the root cause for these deficiencies, in

particular, the inductance and back-EMF effects is derived and analyzed. A quasi-BLDC drive utilizing current advance as well as varying voltage to reduce current spikes is proposed. The simulations as well as experimental results show that the commutation current spike is largely improved. The torque ripple factor gave a significant improvement from 65% to 12.5%. It is also seen that the acoustics has also been greatly reduced by up to 15dB.

Self-starting is a key concern in sensorless drives and particularly so for surface mounted PMSM. To address this challenging class of motor, a novel initial rotor detection method has been conceptualized and successfully applied. The proposed method, simple yet accurate, is presented together with detailed analysis supported by numerical simulations. A digital variant of the method is implemented on hardware and has been successfully deployed for sensorless BLDC self-starting on various HDDs. This method shaves off 90% of the starting time, an enticing figure for the industry. Coupled with the ill-presence of existing solution applicable for surface mounted PMSM, the successful application of the proposed method on this challenging class of motor will draw both academic and industry interests.

In applications where motors with large inertia or low back-EMFs are used, knowledge of initial rotor position will be insufficient to launch a successful start-up. Existing methods of open loop start-up coupled with gate turn-off proves deficient. A novel gate signal masking six step open loop strategy is proposed and investigated. It has been shown by simulation and hardware that the strategy offers the advantages of (i) an earliest possible crossover while making no assumption on the crossover frequency, (ii) smooth crossover as the motor rotation is continued, and (iii) continuance of frequency

skewing during detection. Apart from improved operation and robustness, the hardware implementation indicates an improvement of 40% in starting time over the conventional method of gate turn-off.

PMSMs have permanent magnet rotors generating sinusoidal back-EMFs in rotation. From the perspective of torque performance, a PMSM should be driven with sinusoidal drive. In applications like Hard Disk Drives (HDDs), Brushless Direct Current (BLDC) Drive is adopted instead of Sinusoidal Drive due to ease of implementation. The adoption, however, comes at the expense of increased harmonics, losses, torque pulsations and acoustics. In this thesis, we propose a sensorless optimal sinusoidal BLDC drive. First and foremost, the derivation for an optimal sinusoidal drive is presented, and a power angle control scheme is proposed to achieve an optimal sinusoidal BLDC. The scheme maintains a linear relationship between the motor speed and drive voltage. In an attempt to execute the sensorless drive, an innovative power angle measurement scheme is devised. It takes advantage of the freewheeling diodes, and measures the power angle through the detection of diode voltage drops. The proposed scheme is straightforward, brings about the benefits of sensorless sinusoidal drive and negates the need for current sensors by utilizing the freewheeling diodes.

Acknowledgements

I am deeply grateful to Professor Chong Tow Chong for providing me the opportunity to pursue the PhD degree at Data Storage Institute, and for his trust and generous support that have made this dissertation possible.

I also like to thank my mentor, Assoc Professor Bi Chao, for his invaluable insights, guidance and advice. I am deeply appreciative for his immense patience and trust in my research. We shared many ideals, his passion and enthusiasm have spurred me to greater heights. I would also like to thank other fellow colleagues, Dr Chang Kuan Teck as well as the motor team for their support and friendship.

My three years of study at the Data Storage Institute has been one of the most challenging periods of my life, having to balance family, work and study. Special thanks to my wife, Rachel, mother of our two lovely kids, David and Jubilee, for enduring the task of child rearing with less assistance than she might have had, and for her support and encouragement that made this dissertation possible. I would like to extend my gratitude to my parents, for their selfless love and care they have provided me through these years.

Last, I thank God, my heavenly father, for his salvation, love and patience. He has been gracious to me throughout my life.

Table of Contents

List of Figures

List of Tables

CHAPTER 1. INTRODUCTION

1.0 Introduction

Market demands for various kinds of electric motors have been surging, initiated by the availability of semiconductor Integrated Circuits (IC), such as digital signal processors (DSPs) and field programmable gate arrays (FPGA), and the emergence of new applications. In these applications, manufacturers are increasingly replacing universal and single-phase induction motors with three phase Permanent Magnet Synchronous Motors (PMSMs) to increase efficiency, reliability and power density. Today, PMSMs is found in vast applications, such as automotive, home appliances, A/V equipment, industrial and military instruments [149].

Figure 1.1 PMSM used in various applications (clockwise) (a) HDD (b) DVD (c) Automotives and (d) Cooling fans.

1.1 Brushless Direct Current (BLDC) Drive

PMSMs have permanent magnet rotors generating sinusoidal back-EMFs in rotation. For constant torque production in PMSM, Sinusoidal Drive, where sinusoidal currents are continuously injected based on the rotor position is used. High-resolution optical encoders or resolvers are typically used for rotor position determination. However, in many applications such as Hard Disk Drives (HDDs), Brushless Direct Current (BLDC) drive is adopted instead of sinusoidal drive. BLDC drive is conventionally applied on BLDC motors, a class of permanent magnet motors with trapezoidal back-EMFs, for smooth torque production. In three phase BLDC drives, the motor is typically driven by a three-phase inverter circuit as shown in Figure 1.2. It consists of six power semiconductor transistors with a protection diode connected in parallel to each of these transistors.

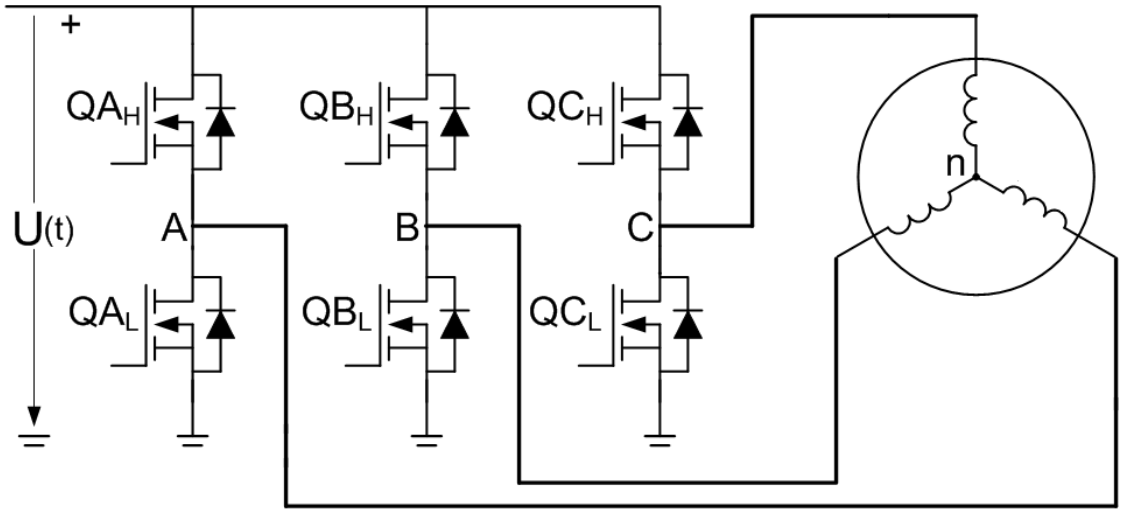

Figure 1.2 Bridge circuit for BLDC drive.

Each transistor is gated by a 120º-conduction drive, in which each gate turns on for 120 electrical degrees in each cycle. For maximum torque production, the gating with respect to the back-EMF is given in Figure 1.3.

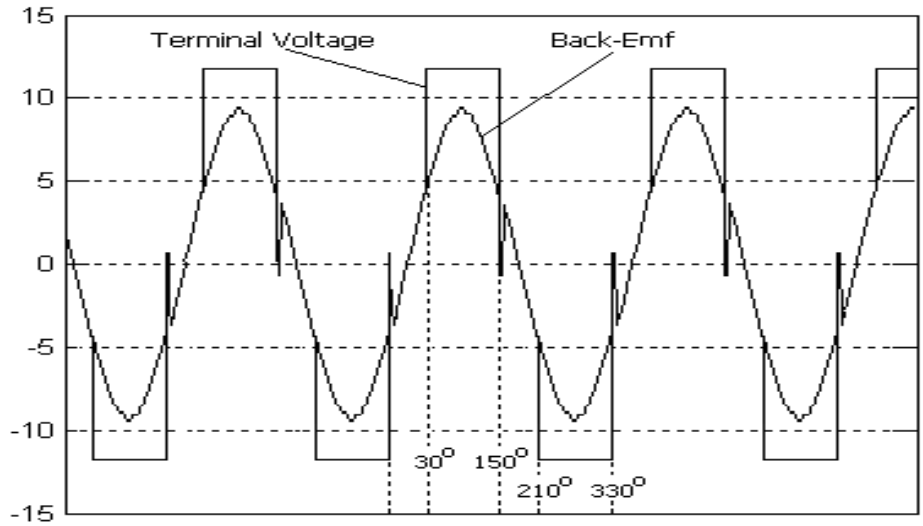

Figure 1.3 Back-EMF versus terminal voltage.

It can be observed that there will be two unexcited 60º periods, where the voltage terminals are floating, namely 330º - 30º and 150º - 210º intervals. During the unexcited phase, the phase voltage gives the phase back-EMF. By measuring the phase back-EMF during this window, commutation sequence can be established. This commutation sequence is, similarly, replicated for phases B and C respectively phased at 120º and 240º delays. Thus, commutation occurs at every 60 electrical degrees of rotation in the sequence "Q_{AH}, Q_{BL}", "Q_{AH}, Q_{CL}", "Q_{BH}, Q_{CL}", "Q_{BH}, Q_{AL}", "Q_{CH}, Q_{AL}" and "Q_{CH}, Q_{BL}". The commutation sequence is provided in Figure 1.4.

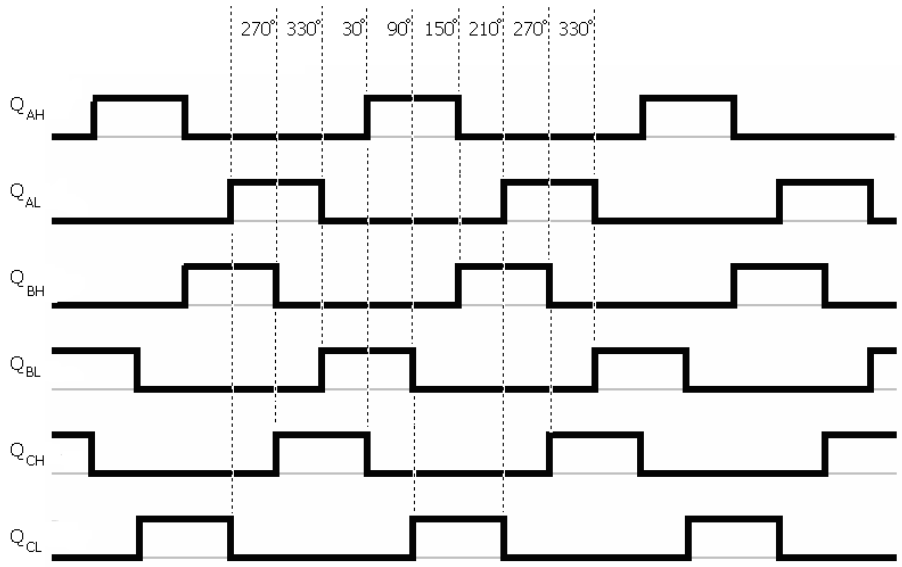

Figure 1.4 Commutation sequence for BLDC drive.

1.2 Sensorless Brushless Direct Current (BLDC) Drive

From the commutation sequence, it can be seen that BLDC drive requires only a six-step positional detection. For this reason, hall effect sensors are traditionally used for rotor position determination. However, these sensors are undesirable as they incur additional cost and space. With the advance and progress in semiconductor processes, the introduction of integrated circuits (ICs) and digital signal processors (DSPs) have made it possible to control a BLDC motor without sensors, commonly termed, Sensorless Control.

Sensorless control has been one of the major research focuses in drive technology over the past two decades. In the reported literature, sensorless control techniques can be broadly classified into the following categories

1. Back-EMF measurement based methods,
2. Flux calculation based methods,
3. Observer based methods and
4. Inductance variation methods.

1.2.1 Back-EMF Measurement Based Method

The measurement of back-EMF during the silent phase can be broadly classified as "back-EMF sensing" method. Under this category, several techniques can be found in research literature, namely,

i. Terminal voltage sensing,
ii. Third harmonic back-EMF sensing,
iii. Freewheeling diode conduction and
iv. Back-EMF integration.

1.2.1.1 Terminal Voltage Sensing

In this technique, the fundamental idea is to locate the zero crossing points (ZCPs) of the phase back-EMFs [1-18]. These ZCPs represent position information. Based on this, self-sensing operation using back-EMF ZCP detection is established. For all phases,

the commutation is such that these ZCPs should be positioned mid-way in the silent period. In other words, commutation occur 30º away from the ZCPs.

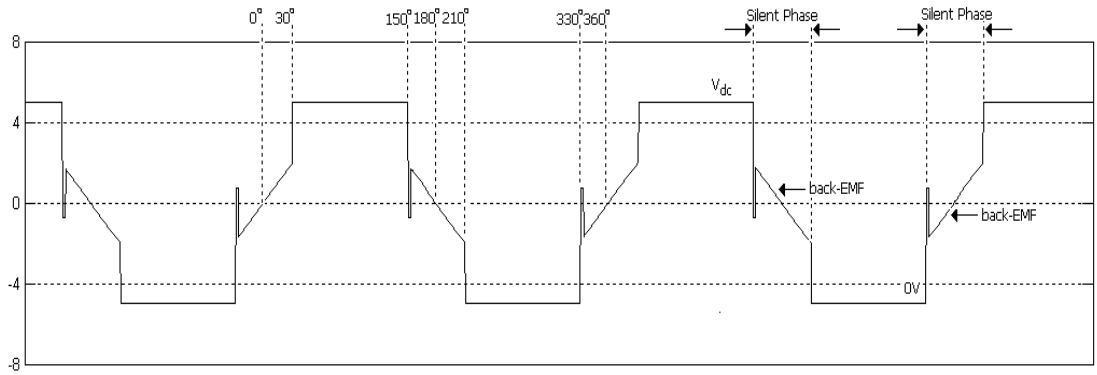

Figure 1.5 Phase A terminal voltage.

1.2.1.2 Third Harmonic Back-EMF Sensing

This method has been proposed for BLDC motors [19], motors with trapezoidal back-EMFs which have been extended to PMSM [22]. The back-EMFs for these motors contain a third harmonic component which can be utilized for the determination of the commutation points. The back-EMF of a permanent magnet motor can be generally described as

$$Emf_a = E_1 \sin\theta + E_3 \sin 3\theta + E_5 \sin 5\theta + E_7 \sin 7\theta + \ldots \quad (1\text{-}1)$$

The extraction of the third harmonic component can be elegantly performed by a summation of the three phase voltages. The summation would leave only the triplen components due to the fact that the summation of the non-triplen harmonics is zero. Neglecting the negligible harmonics at order higher than three,

$$\sum_{x=a,b,c} Emf_x = 3E_3 \sin 3\theta , \tag{1-2}$$

and by conducting an integration,

$$\psi_{3rd} = \int \left(\sum_{x=a,b,c} Emf_x \right) d\theta = -E_3 \cos 3\theta . \tag{1-3}$$

The rotor flux can be estimated and the commutation taken as the zero crossing points.

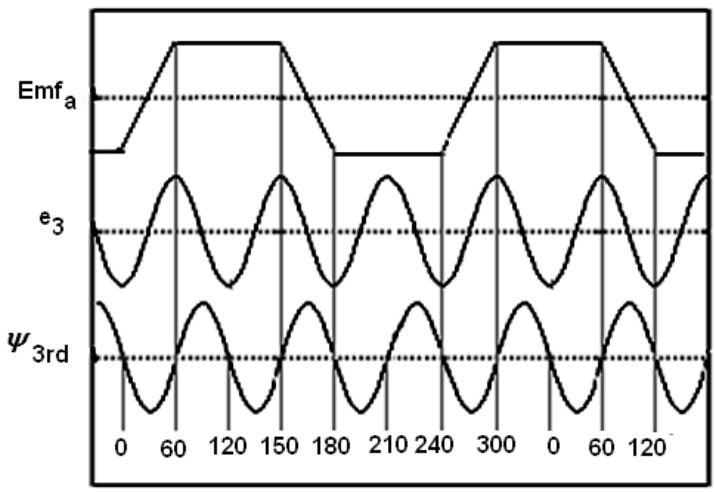

Figure 1.6 Rotor determination from 3rd harmonic.

In this method, there is a reduced requirement on filtering and it offers a wider speed range. However, it is not applicable in the following cases [24]

i. Unavailability of the neutral line,

ii. Absence of third harmonics, and

iii. Unbalance of three phases.

1.2.1.3 Freewheeling Diode Conduction Sensing

In reference [27], the authors proposed a sensorless drive based on the detection of the freewheeling diode conduction.

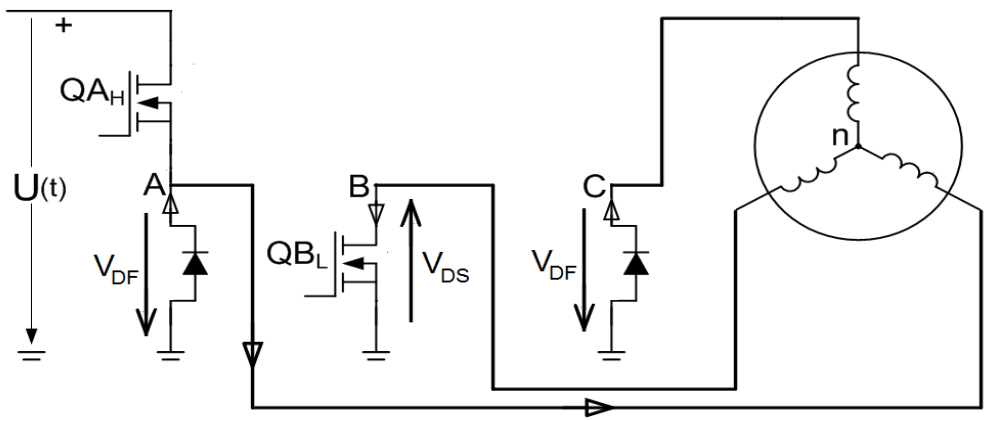

Figure 1.7 Current flow and active components during commutation.

In the suggested chopper control, take for instance during a A_HB_L drive, it has been shown that during an off state, the expression for phase C terminal voltage v_c is

$$v_c = e_c + \frac{V_{DS} - V_{DF}}{2} - \frac{e_a + e_b}{2}, \tag{1-4}$$

where e_x denotes the respective phase voltages,

V_{DS} denotes the voltage drop across the conducting MOSFET and

V_{DF} denotes the voltage drop across the freewheeling diode.

Assuming negligible transistor and diode voltage drop as well as a balanced trapezoidal back-EMF, current in the open phase starts flowing through the freewheeling diode when the back-EMF crosses zero. Hence, by detecting the instant when the freewheeling diode start conducting will provide the back-EMF zero crossing point (ZCP). This point,

however, leads the commutation by 30˚ and the corresponding commutation signals are phase-shifted with a phase shifter.

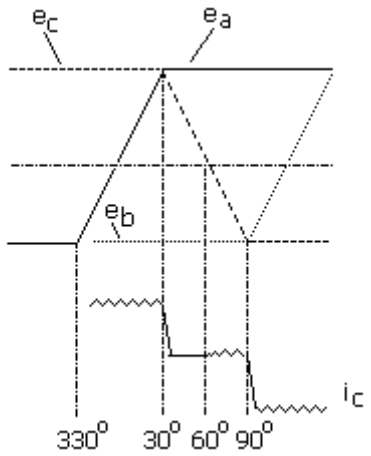

Figure 1.8 Current flow with respect to back-EMFs.

Practically, however, this method requires the use of six isolated power supplies for each of the comparator used for free-wheeling diode detection.

1.2.1.4 Back-EMF Integration

In order to address the problem of switching noise, the back-EMF of the silent phase is integrated [28-32]. Integration begins when the back-EMF crosses zero and commutation takes place when the integral reaches some pre-defined threshold value.

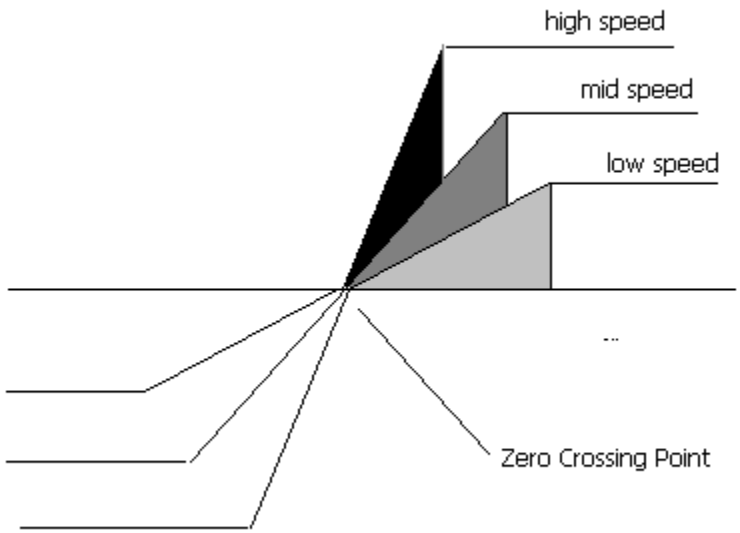

Figure 1.9 Back-EMFs at various speeds.

Assuming a linear relationship between the back-EMF and its speed, this threshold is constant for all speeds. However, this threshold depends on the motor as well as the alignment of the current against the back-EMF. In addition, this method also suffers from integration offsets.

1.2.2 Flux-Linkage Variation

A theoretical and fairly straightforward method is to sense the position using flux-linkage variation. From the phase voltage equation,

$$v = i \cdot R + \frac{d\psi}{dt} \ , \qquad (1\text{-}5)$$

where v denotes the phase voltage,

i denotes the phase current,

R denotes the phase resistance, and

ψ denotes the phase flux linkage.

Alternatively,

$$\psi = \int (v - i \cdot R) dt \,. \tag{1-6}$$

It looks somewhat simple; however, the operation involves integration and introduces the problems of initial value and dc drift which inevitably deteriorates the accuracy [33, 34]. Solutions to this problem include implementation of H^2 and H^∞, observer [36] and adaptive controller [38]. Another practical problem is the necessity of isolators for the measurement of phase voltages. Because of this, the phase voltage is estimated with the applied voltage and gating signals. Such estimation, nevertheless, suffers from the neglected dead time effect errors. Research has been conducted to resolve these differences [39, 40].

1.2.3 Observer Based Methods

For a system given by

$$\begin{aligned} \dot{x}(t) &= Ax(t) + Bu(t), \\ y(t) &= Cx(t), \end{aligned} \tag{1-7}$$

and considering an observer

$$\begin{aligned} \dot{\hat{x}}(t) &= A\hat{x}(t) + Bu(t) + L[y(t) - C\hat{x}(t)], \\ \hat{y}(t) &= C\hat{x}(t), \end{aligned} \tag{1-8}$$

where $\hat{x}(t)$ = estimated state.

Defining the estimation error as

$$\tilde{x}(t) = x(t) - \hat{x}(t) \ , \tag{1-9}$$

it can be shown that

$$\dot{\tilde{x}} = (A - LC)\tilde{x} \ , \tag{1-10}$$

or

$$\dot{\tilde{x}} = \overline{A}\tilde{x} \ . \tag{1-11}$$

Assuming $\tilde{x}(0) = x(0) - \hat{x}(0)$,

$$\tilde{x} = e^{\overline{A}t}\tilde{x}(0) \ . \tag{1-12}$$

Thus, if the eigenvalues of $\overline{A}$ (poles of the observer) is stable, $\tilde{x}(t) \to 0$ as $t \to \infty$. Hence, the observer design is reduced to the determination of L for the desired observer poles. A possible procedure for observer design is

1. Choose the observer poles 3-5 times faster than control poles;
2. Use a pole placement algorithm to get L; and
3. Implement the observer

Full state observer has been implemented in [46,49,59]. Other observers include reduced-order observers [56,57,61,64,66], non-linear observers [41,57-62], disturbance observers [53,55], and sliding mode observers [45,49,50,52,58,60,63,65,67,70,74]. Among these variants, the Sliding Mode Observer is the most promising and it is no surprise that it has drawn increasing research attention. The sliding mode observer is simple to implement yet robust against disturbance, parameter deviation and noise. The main distinction of a sliding mode observer over a state observer is that an additional term containing the sign of the estimation error is included,

$$\dot{\hat{x}}(t) = A\hat{x}(t) + Bu(t) + K \cdot \mathrm{sgn}(\tilde{x}) \ , \tag{1-13}$$

where

$$\mathrm{sgn}(\tilde{x}) = \begin{cases} 1 & \tilde{x} \geq 0 \\ -1 & \tilde{x} < 0 \end{cases} . \tag{1-14}$$

For sliding mode convergence,

$$\frac{1}{2}\frac{d}{dt}\tilde{x}^T\tilde{x} < 0 , \tag{1-15}$$

or equivalently

$$\dot{\tilde{x}}^T\tilde{x} < 0 . \tag{1-16}$$

Since

$$\dot{\tilde{x}}(t) = A\tilde{x}(t) - K \cdot \mathrm{sgn}(\tilde{x}) \tag{1-17}$$

K must be chosen to ensure convergence. While methodology based on observers has been in existence, several considerations have limited its applications, namely,

i. Parameters must be accurately known as well as the nonlinearities must be reasonably incorporated,

ii. Accurate measurement of terminal currents and voltages, and

iii. Knowledge of initial rotor position.

1.2.4 Inductance Variation Methods

Key to this approach is the utilization of the variance of inductance due to motor saliency and magnetic saturation. Figure 1.10 shows a plot variation of the coil's inductance as a function of rotational angle. It can be seen that through the measurement

of the inductance, it is possible to detect if the coil is aligned well with the rotor magnets. For proper control of a permanent magnet motor, it is also desirable to detect whether the coil is aligned with a north or south pole. This is possible by applying a DC current to the winding.

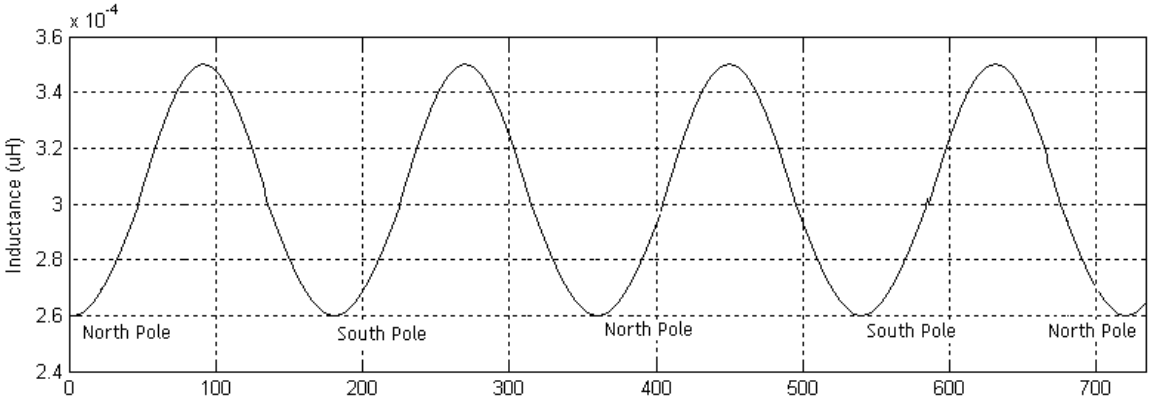

Figure 1.10 Positional (electrical cycle) inductance variation.

Figure 1.11 shows the coil inductance as a function of rotor position when the coil adds flux to the flux produced by the rotor magnets. When a north pole is aligned with the coil, the current in the coil increases the flux linked by the coil, increases stator saturation, and slightly decreases the inductance. When a south pole is aligned with the coil, the current in the coil decreases the flux linked by the coil, decreases stator saturation, and slightly increases the inductance that was present. In the machine theory, this phenomenon is known as armature reaction [140]. Since the inductance of the coil is different for north and south poles, one can distinguish the polarity of the rotor pole that is aligned with the coil.

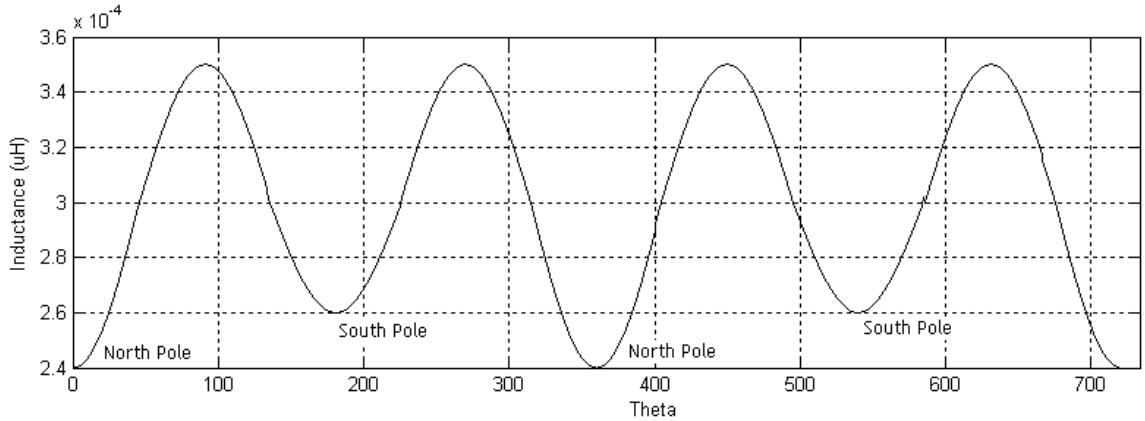

Figure 1.11 Positional (electrical cycle) inductance variation with saturation.

Hinging on positional inductance variation, this property can be utilized for position detection and can be deployed even at stationary where the back-EMF is zero. Since inductances influence the current change rate, an indirect method is to measure the current change rate under a pulse signal injection. The fundamental approach in the pulse signal injection is the application of voltage pulses to the stator windings at standstill [76-88]. The initial rotor position is thus estimated by the evaluation of the corresponding currents made distinctive by inductance variations due to motor saliencies and magnetic saturation. Another approach, also relying on the inductance variation, is the carrier signal injection method. In this approach, the rotor position is estimated via the injection of high-frequency excitation [89-107] which interacts with the machine saliencies producing specific measurable frequency components. These methods, although effective, are

i. Sensitive to parameter variation,

ii. Require accurate measurements, and

iii. Additional core losses are induced.

1.3 Sensorless Starting

To implement a sensorless drive, a crucial aspect is the starting of the motor from standstill. Published literature presented schemes can be categorized into three types,

1. Starting from open-loop,
2. Starting from aligned position, and
3. Starting from estimated position.

1.3.1 Starting from Open-Loop

In this scheme, specific gate patterns providing a rotating stator field are injected [108-113]. These signals are voltage skewed and/or frequency skewed, thereby providing a rotating gating signals increasing in magnitude and/or frequency. The operation is then similar to operating the motor as a permanent magnet synchronous machine. At low frequencies, the rotor field interacts with the stator field to provide a torque large enough to overcome friction and dynamic torque induced by inertia, and the rotor starts to rotate. Once the motor reaches a particular threshold speed/condition, open-loop operation is substituted by closed-loop sensorless operation.

Starting from an unknown position has resulted in several difficulties. As mentioned, the voltage and/or frequency are skewed. The voltage and/or frequency skew

profile have to be carefully established. Failure of profiling will result in unpredictable rotor movement, such as temporary reverse rotation, vibration or starting failure. In a successful startup, it might still result in lengthy starting time. This is not acceptable in most applications. Thus, this scheme is deployed only in certain applications, such as pump and fan drives. Nevertheless, the main culprit for the instability is due to the lack of knowledge in the rotor's initial position. The following two categories address this challenge.

1.3.2 Starting from Aligned Position

Two sub-classes arose from this concept, alignment of rotor during (i) starting and (ii) stopping [114-119]. In the alignment of the rotor during starting, a straightforward way is to excite a particular phase to cause the rotor to shift and lock into the intended position. This method, nevertheless, still suffers from the possibility of reverse rotation. As for alignment of the rotor during stopping, additional stopping circuit is required.

1.3.3 Starting from Estimated Position

Among the three schemes, this approach [76-88] has drawn the greatest interest and attention. The development in this approach is largely an extension of that discussed in 1.2.4 where positional inductance variation is utilized.

1.4 Torque Pulsation

It is optimum to inject rectangular stator phase currents to a BLDC (with ideal trapezoidal back-EMF) for maximum torque and minimum torque ripple production. However, for the HDD spindle motors with sinusoidal back-EMFs, even with rectangular currents, torque ripples are introduced.

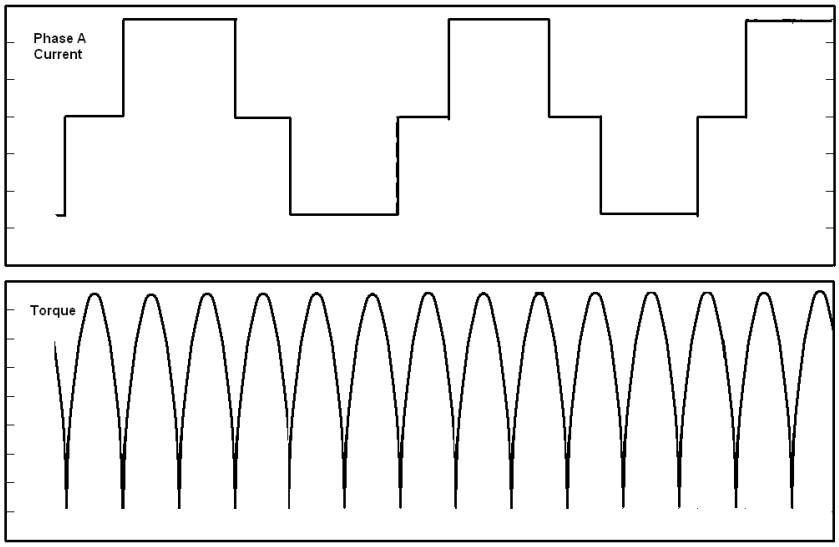

Figure 1.12 Torque profile with rectangular currents on sinusoidal back-EMF.

BLDC drives suffer from further additional torque ripple, commonly known as commutation torque ripple, which occurs during commutation. This ripple is brought about by the jerky current commutation from one phase to another due to the presence of inductance and back-EMF as well as difference in di/dt.

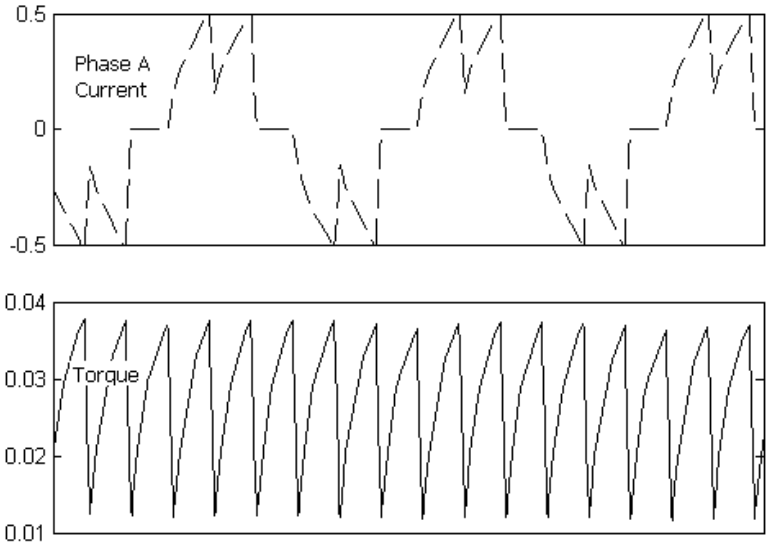

Figure 1.13 Current and torque response with inductive effects.

The details pertaining to this deficiency have been elaborated and discussed in the literature and several approaches have been proposed to address this issue. In [122-124], Fourier analysis was applied to get solutions centered about the suppression of current harmonics. In [124], Murai proposed the notion of "overlapping" technique where the on-going phases were given a head start in compensation for the slow current rise. Other researches such as Lee [132] and Nam [133], suggested the varying of applied input voltage with the goal of current ripple reduction.

1.5 Algorithm Implementation

Field programmable gate array (FPGA) is a semiconductor component containing programmable logic components and interconnects. It has traditionally been perceived as an essential platform for Application Specific Integrated Circuit (ASIC) prototyping.

However, in recent years, it has gained significant market share in end-product solutions. FPGA offers fast time to market, low design/manufacturing cost and risk, extremely high processing performance, and unrivaled flexibility. In the dynamic markets served by high-performance solutions, FPGAs allow for highly parallel architectures, thereby providing it with capability of handling high computational workloads. For instance, a 256 tap filter on a conventional DSP running 1GHz would operate at 4MSPS whereas a FPGA running at 500MHz would parallelized it and provide performance levels of 500MSPS. It is no accident to be reported in literature [135-141 that motor applications have also begun to be implemented on FPGA.

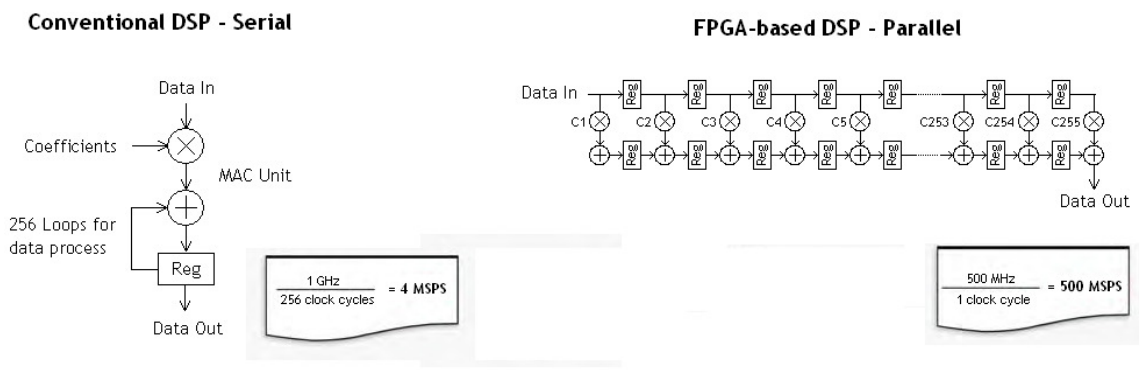

Figure 1.14 Illustration of the computational superiority of FPGA over DSP.

1.6 Main Contributions of Thesis

Revolving around the issues presented, the main contributions of this thesis are as follows:

1) The design and development of an integrative Sensorless Zero Delay ZCP Detection - BLDC drive on FPGA. A sensorless BLDC drive derived from ZCP centering is conceived and heuristic logic is incorporated for zero delay ZCP detection. The absence of delays makes the drive well-suited for wide speed range.

2) An analytical and simulation study as well as FPGA implementation of a proposed Quasi-BLDC method with the objective of commutation torque minimization. The proposed method offers significant improvement in torque ripple of well over 50% compared to the traditional BLDC drives.

3) An innovative and simple, yet accurate, initial rotor detection method has been conceptualized for fast sensorless starting. Several methodology variants from this proposed method are presented together with detailed analysis supported by simulations. A digital variant was implemented on the FPGA hardware and has been successfully deployed for sensorless BLDC self-starting on various HDDs. This method shaves off 90% of the starting time which is an enticing figure for the industry. Coupled with the ill-presence of existing solutions applicable for surface mounted PMSM, successful applications of this method on this challenging class of motor have drawn both academic and industry interests.

4) A novel gate signal masking six step open-loop strategy is proposed and investigated for starting time improvement. It has been shown by both simulation

and hardware that the strategy offers the advantages of (i) an earliest possible crossover while making no assumption on the crossover frequency, (ii) smooth crossover as the motor rotation is continued, and (iii) continuance of frequency skewing during the detection. This method is suited for motor with small back-EMF or large inertia where the knowledge of initial rotor position is insufficient. The experimental results from the FPGA implementation indicate an improvement of 40% in starting time.

5) A sensorless optimal sinusoidal BLDC drive for the reduction of acoustic noise and motor operation power loss has been conceived and implemented on FPGA. The novelty of the drive lies in the optimal derivation as well as its integration optimal sinusoidal drive into sensorless BLDC drive. A detailed analysis and simulation of the drive together with the hardware results are presented.

1.7 Structure of Thesis

Chapter 2 provides an effective mathematical model of BLDC. This model forms the background for the derivation and simulation in this thesis.

Chapter 3 presents the integrative Sensorless Zero Delay ZCP Detection - BLDC drive. It begins with the background and motivation to the work in it. The proposed drive is firstly presented requiring the assistance of filters. Heuristic control is

subsequently integrated to achieve zero delay ZCP detection. Simulation as well as hardware results are presented for validation and proof of concept.

Chapter 4 addresses the commutation torque ripple present in BLDC drives. The origination of this effect is derived and presented. A Quasi-BLDC drive based on windowing is proposed and presented. The investigation study shows significant improvement and this claim is well supported through simulation and hardware verification provided in the chapter.

Chapter 5 gives the analysis, simulation, implementation and application of an innovative proposed method for initial rotor position detection. This method hinges on positional inductance variation and is shown to provide distinct position information. The analysis, simulation and implementation unanimously point towards the same conclusion. The application and integration of the method into BDLC drives illustrate its relevance and effectiveness.

Chapter 6 gives the analysis, simulation and integration of a novel gate masking open-loop self-starting strategy. The method uses gate masking which opens additional window for Back-EMF detection. Both simulation and experimental results are provided and the method is validated.

Chapter 7 presents the analysis and implementation of a sensorless optimal sinusoidal BLDC drive. The drive controls its optimality by aligning the current and

back-EMF through power angle control. A novel power angle measurement method based on freewheeling current has been applied in order to achieve sensorless control. Both the simulation and hardware implementation are provided.

Chapter 8 gives a conclusion on the work performed in this thesis.

Chapter 9 provides a short discussion and scope for future research.

CHAPTER 2. MATHEMATICAL MODEL OF HDD SPINDLE MOTOR

2.0 Introduction

In the study of any dynamic system, the first step is to derive its mathematical model. The mathematical model of a dynamic system is defined as a set of equations that represent the dynamics of the system accurately or, at least, fairly well. However, a system may be represented in many different ways and therefore may have many mathematical models depending on one's perspective. Furthermore, the accuracy of the mathematical model can be improved by taking into consideration more factors. Thus to obtain a reasonable mathematical model, a compromise must be made between simplicity of the model and accuracy of the results of the analysis. In many applications, a simplified or reduced model is sufficient and preferred.

2.1 Motor Configuration

Figure 2.1 shows an underslung spindle motor, where the electromagnetic part of the motor is under the disks. One end of the shaft is fixed on the bottom of the motor shell which in turn is fixed to the HDD's base. The other end of the shaft is screwed onto

the HDD cover through a hole on the shaft. The permanent magnet ring is made from the bonded NdFeB material, protected by the rotor yoke in order to operate at high speed.

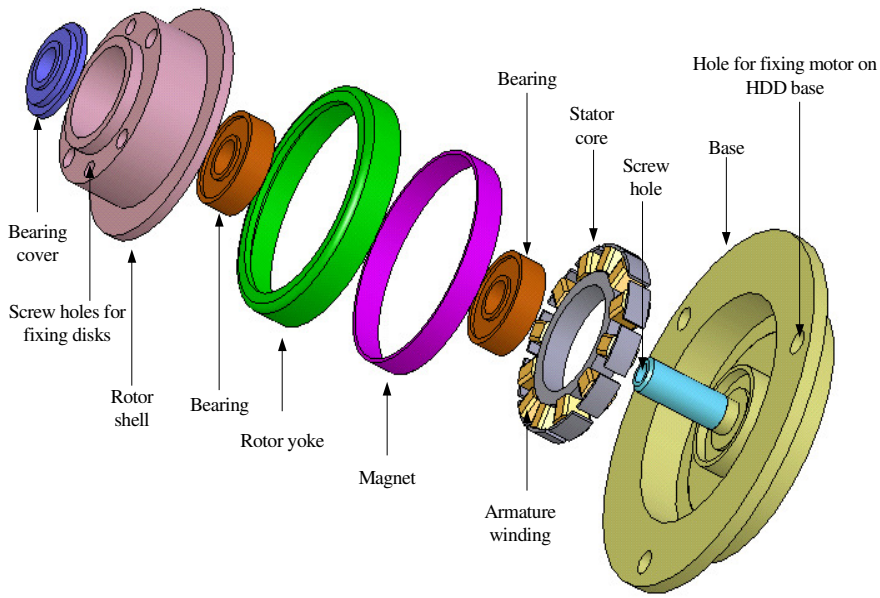

Figure 2.1 Key components in an underslung spindle motor assembly.

Compared to other PMSM structures, the surface mounted PMSM has several unique features. The rotor has got surface-mounted permanent magnet constructing a smooth and big air-gap machine. Therefore, electromagnetic (EM) torque contributed by reluctance torque can be neglected. In addition, the rotor utilizes fractional-slots which in turn make the cogging torque negligible. Other features, such as sinusoidal back-EMFs and a symmetrical three-phase structure, create a surface mounted PMSM.

2.2 PMSM Voltage Equation using ABC Model

The PMSM system can be conveniently modeled by using the ABC model. The model considers the PMSM system as an AC machine with 4 windings. They consist of a field winding f and three stator armature windings a, b and c. Each stator phase winding is represented as an inductance in series with a resistance. As a reduced model, rotor (permanent magnet) is also modeled fictitiously as a winding with a constant current i_f.

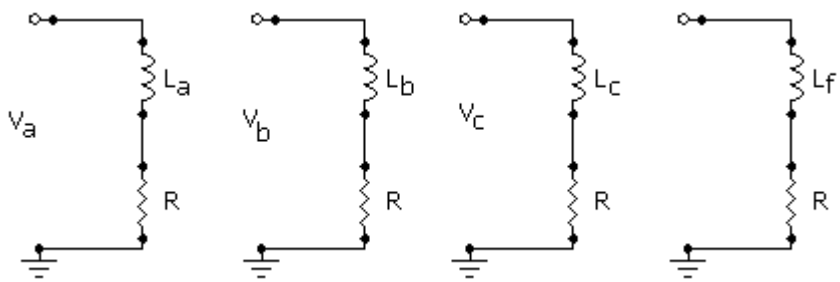

Figure 2.2 ABC model.

From the model, the corresponding voltage equations for each armature windings are as follow:

$$\begin{bmatrix} V_a \\ V_b \\ V_c \end{bmatrix} = R \begin{bmatrix} i_a \\ i_b \\ i_c \end{bmatrix} + \frac{d}{dt} \begin{bmatrix} \psi_a \\ \psi_b \\ \psi_c \end{bmatrix}, \tag{2-1}$$

where R represents phase resistance, i_a, i_b, i_c the phase currents and ψ_a, ψ_b, ψ_c the phase flux linkages. The phase flux linkages are in turn given as follows:

$$\begin{bmatrix} \psi_a \\ \psi_b \\ \psi_c \end{bmatrix} = \begin{bmatrix} L_a & M_{ab} & M_{ac} & M_{af} \\ M_{ba} & L_b & M_{bc} & M_{bf} \\ M_{ca} & M_{cb} & L_c & M_{cf} \end{bmatrix} \begin{bmatrix} i_a \\ i_b \\ i_c \\ i_f \end{bmatrix}, \tag{2-2}$$

where L_x represents the self inductance of winding x and M_{xy} the mutual inductance between coil x and y. Due to the construction of salient pole, all inductances are functions of electrical rotor position θ.

The self inductances of the stator winding are expressed as below:

$$L_a = L_o + L_2 \cos 2\theta + L_4 \cos 4\theta + L_6 \cos 6\theta + \dots \ , \tag{2-3}$$

$$L_b = L_o + L_2 \cos 2\left(\theta - \frac{2\pi}{3}\right) + L_4 \cos 4\left(\theta - \frac{2\pi}{3}\right) + L_6 \cos 6\left(\theta - \frac{2\pi}{3}\right) + \dots, \tag{2-4}$$

$$L_c = L_o + L_2 \cos 2\left(\theta - \frac{4\pi}{3}\right) + L_4 \cos 4\left(\theta - \frac{4\pi}{3}\right) + L_6 \cos 6\left(\theta - \frac{4\pi}{3}\right) + \dots, \tag{2-5}$$

$$L_f = L_{of} + L_{2f} \cos 2\theta + L_{4f} \cos 4\theta + L_{6f} \cos 6\theta + \dots \ . \tag{2-6}$$

The stator to stator winding mutual inductances are expressed as:

$$M_{ab} = M_{ba} = M_o + M_2 \cos 2\theta + M_4 \cos 4\theta + M_6 \cos 6\theta + \dots, \tag{2-7}$$

$$M_{bc} = M_{cb} = M_o + M_2 \cos 2\left(\theta - \frac{2\pi}{3}\right) + M_4 \cos 4\left(\theta - \frac{2\pi}{3}\right) + M_6 \cos 6\left(\theta - \frac{2\pi}{3}\right) + \dots, \tag{2-8}$$

$$M_{ca} = M_{ac} = M_o + M_2 \cos 2\left(\theta - \frac{4\pi}{3}\right) + M_4 \cos 4\left(\theta - \frac{4\pi}{3}\right) + M_6 \cos 6\left(\theta - \frac{4\pi}{3}\right) + \dots. \tag{2-9}$$

The stator to rotor inductances representing the non-sinusoidal rotor flux are expressed as follow:

$$M_{af} = M_{fa} = E_1 \cos\theta + E_3 \cos 3\theta + E_5 \cos 5\theta + E_7 \cos 7\theta + \ldots, \tag{2-10}$$

$$M_{bf} = M_{fb} = E_1 \cos\theta + E_3 \cos 3\left(\theta - \frac{2\pi}{3}\right) + E_5 \cos 5\left(\theta - \frac{2\pi}{3}\right) + E_7 \cos 7\left(\theta - \frac{2\pi}{3}\right) + \ldots, \tag{2-11}$$

$$M_{cf} = M_{fc} = E_1 \cos\theta + E_3 \cos 3\left(\theta - \frac{4\pi}{3}\right) + E_5 \cos 5\left(\theta - \frac{4\pi}{3}\right) + E_7 \cos 7\left(\theta - \frac{4\pi}{3}\right) + \ldots. \tag{2-12}$$

The machine is assumed to be symmetrical and the phase voltages are assumed to be balanced. Therefore, phases B and C have the same voltage equation delayed by 2π/3 and 4π/3, respectively. Thus by solving the voltage equation for phase A, the equation is derived as below:

$$V_a = i_a R + L_a \frac{di_a}{dt} + i_a \frac{dL_a}{dt} + M_{ab} \frac{di_b}{dt} + i_b \frac{dM_{ab}}{dt} + M_{ac} \frac{di_c}{dt} + i_c \frac{dM_{ac}}{dt} + i_f \frac{dM_{af}}{dt}. \tag{2-13}$$

And it can be rewritten as,

$$V_a = i_a R + i_a \omega \frac{dL_a}{d\theta} + i_b \omega \frac{dM_{ab}}{d\theta} + i_c \omega \frac{dM_{ac}}{d\theta} + L_a \frac{di_a}{dt} + M_{ab} \frac{di_b}{dt} + M_{ac} \frac{di_c}{dt} + i_f \omega \frac{dM_{af}}{d\theta}. \tag{2-14}$$

From the above equations, all the terms except the last term are armature current dependent. This last term is the back-EMF and its magnitude is proportional to the change rate of the flux linkage due to the permanent magnet. ω represents the electrical rotating speed.

2.3 Disk-drive Spindle Motor Voltage Equation

Due to the cylindrical rotor construction, the mutual inductances and the stator self inductances are no longer functions of the position θ. Hence,

$$\frac{dL_x}{d\theta} = 0, \tag{2-15}$$

$$\frac{dM_{xy}}{d\theta} = 0. \tag{2-16}$$

The voltage equation becomes:

$$V_a = i_a R + L_a \frac{di_a}{dt} + M_{ab} \frac{di_b}{dt} + M_{ac} \frac{di_c}{dt} + i_f \omega \frac{dM_{af}}{d\theta}. \tag{2-17}$$

In addition, the following assumptions were made:

$$L = L_a = L_b = L_c, \tag{2-18}$$

$$M = M_{ab} = M_{bc} = M_{ca}. \tag{2-19}$$

The voltage equation can be rewritten as:

$$V_a = i_a R + L_a \frac{di_a}{dt} + M \frac{d}{dt}(i_b + i_c) + i_f \omega \frac{dM_{af}}{d\theta}. \tag{2-20}$$

The absence of neutral line in the disk drive spindle motors eliminates all triplen components. Therefore, the following equation is always true.

$$i_a + i_b + i_c = 0. \tag{2-21}$$

The voltage equation can be further simplified to the following form:

$$V_a = i_a R + L_a \frac{di_a}{dt} + M \frac{d}{dt}(-i_a) + i_f \omega \frac{dM_{af}}{d\theta}, \tag{2-22}$$

$$V_a = i_a R + (L - M)\frac{di_a}{dt} + i_f \omega \frac{dM_{af}}{d\theta}. \tag{2-23}$$

Consequently, the corresponding voltage equations for phases B and C are as follows:

$$V_b = i_b R + (L - M)\frac{di_b}{dt} + i_f \omega \frac{dM_{bf}}{d\theta}, \tag{2-24}$$

$$V_c = i_c R + (L - M)\frac{di_c}{dt} + i_f \omega \frac{dM_{cf}}{d\theta}. \tag{2-25}$$

2.4 PMSM Torque Equation

The torque developed by the motor can be derived using the energy method which is based on the conservation of energy principle. The derived torque equation is:

$$T_m = \frac{\partial E_{em}}{\partial \theta_m} \tag{2-26}$$

where E_{em} is the electromagnetic energy of the motor EM system, and

$$E_{em} = \frac{1}{2}[I]^T[L][I]. \tag{2-27}$$

In the equation, [I] expresses the current and [L] express the inductance of the motor,

$$[I]^T = [i_a, i_b, i_c], \tag{2-28}$$

$$[L] = \begin{bmatrix} L_a & M_{ab} & M_{ac} & M_{af} \\ M_{ba} & L_b & M_{bc} & M_{bf} \\ M_{ca} & M_{cb} & L_c & M_{cf} \\ M_{fa} & M_{fb} & M_{fb} & L_f \end{bmatrix}. \tag{2-29}$$

In addition, denoting the pole number of the machine as p, the relationship between the electrical (θ) and mechanical angles (θ_m) is such that

$$\theta = p\theta_m / 2. \tag{2-30}$$

Consequently, the torque equation is expressed as follow:

$$T_m = \frac{p}{2}\begin{bmatrix} \frac{1}{2}\left(i_f^2 \frac{dL_f}{d\theta}\right) + \frac{1}{2}\left(i_a^2 \frac{dL_a}{d\theta} + i_b^2 \frac{dL_b}{d\theta} + i_c^2 \frac{dL_c}{d\theta}\right) + \\ i_a i_b \frac{dM_{ab}}{d\theta} + i_b i_c \frac{dM_{bc}}{d\theta} + i_c i_a \frac{dM_{ca}}{d\theta} + i_a i_f \frac{dM_{af}}{d\theta} + i_b i_f \frac{dM_{bf}}{d\theta} + i_c i_f \frac{dM_{cf}}{d\theta} \end{bmatrix}. \tag{2-31}$$

Moreover, it can be rewritten to express it in terms of its phase torque components. The rewritten equation is shown as follows:

$$T_m = \frac{p}{2}\left\{\begin{array}{l} \frac{1}{2}\left(i_f^2 \frac{dL_f}{d\theta}\right) + \left[\frac{1}{2}\left(i_a^2 \frac{dL_a}{d\theta} + i_a i_b \frac{dM_{ab}}{d\theta} + i_c i_a \frac{dM_{ca}}{d\theta}\right) + i_a i_f \frac{dM_{af}}{d\theta}\right] + \\ \left[\frac{1}{2}\left(i_b^2 \frac{dL_b}{d\theta} + i_a i_b \frac{dM_{ab}}{d\theta} + i_c i_a \frac{dM_{bc}}{d\theta}\right) + i_b i_f \frac{dM_{bf}}{d\theta}\right] + \\ \left[\frac{1}{2}\left(i_c^2 \frac{dL_c}{d\theta} + i_b i_c \frac{dM_{bc}}{d\theta} + i_c i_a \frac{dM_{ca}}{d\theta}\right) + i_c i_f \frac{dM_{cf}}{d\theta}\right] \end{array}\right\},$$

or

$$T_m = T_a + T_b + T_c + T_{cg} \ , \tag{2-32}$$

where

$$\left\{\begin{array}{l} T_a = \frac{p}{2}\left\{\left[\frac{1}{2}\left(i_a^2 \frac{dL_a}{d\theta} + i_a i_b \frac{dM_{ab}}{d\theta} + i_c i_a \frac{dM_{ca}}{d\theta}\right) + i_a i_f \frac{dM_{af}}{d\theta}\right]\right\} \\ T_b = \frac{p}{2}\left\{\left[\frac{1}{2}\left(i_b^2 \frac{dL_b}{d\theta} + i_a i_b \frac{dM_{ab}}{d\theta} + i_b i_c \frac{dM_{bc}}{d\theta}\right) + i_b i_f \frac{dM_{bf}}{d\theta}\right]\right\} \\ T_c = \frac{p}{2}\left\{\left[\frac{1}{2}\left(i_c^2 \frac{dL_c}{d\theta} + i_b i_c \frac{dM_{bc}}{d\theta} + i_c i_a \frac{dM_{ca}}{d\theta}\right) + i_c i_f \frac{dM_{cf}}{d\theta}\right]\right\} \\ T_{cg} = \frac{p}{2}\left\{\frac{1}{2}\left(i_f^2 \frac{dL_f}{d\theta}\right)\right\} \end{array}\right. . \tag{2-33}$$

A physical interpretation can be given for the above equations. In general, the torque produced by a PMSM consists of two components: excitation and reluctance torques. Excitation torque is the result of the interaction between the magnetic fields of the rotor and the stator excitation; it is the tendency of the rotor field to align with the stator field, and can only exist in a doubly excited machine. On the other hand, reluctance torque arises from reluctance (inductance) variations due to motor saliencies; it is the tendency of the rotor to take up a position of minimum reluctance (maximum inductance) when one winding (the stator or rotor) is excited and it exists only in a salient machine. In addition, there also exists a subclass of reluctance torque, known as cogging torque,

which is caused by the variation of the self-reluctance of field coil. This variation of self - reluctance of the field coil is caused by the geometric structure of the stator. The presence of slots on the stator causes the self reluctance of the field coil to vary with rotor position. As a result, cogging torque is generated which tends to make the rotor attain a position of minimum reluctance.

From the torque equation, the first three torque components in the A-phase torque give the reluctance torque components. The last term, dependent on the field current, gives the excitation torque. Similar arguments also hold for B and C phase torques. T_{cg} is termed as Cogging torque.

2.5 Disk-drive Spindle Motor Torque Equation

Assuming

$$L = L_a = L_b = L_c \text{, and} \tag{2-34}$$

$$M = M_{ab} = M_{bc} = M_{ca}, \tag{2-35}$$

the torque equation can be reduced to the following form:

$$T_m = T_a(\theta, i_a) + T_b(\theta, i_b) + T_c(\theta, i_c), \tag{2-36}$$

where

$$\begin{cases} T_a = \dfrac{p}{2}\left[i_a i_f \dfrac{dM_{af}}{d\theta} \right] \\ T_b = \dfrac{p}{2}\left[i_b i_f \dfrac{dM_{bf}}{d\theta} \right] \\ T_c = \dfrac{p}{2}\left[i_c i_f \dfrac{dM_{cf}}{d\theta} \right] \end{cases} . \tag{2-37}$$

It can be observed that the reluctance torque components of all three phase torques diminish to zero. As for cogging torque, the rotor utilizes fractional slot and causes the cogging torque to diminish to zero. It is therefore dropped off to simplify the analysis.

2.6 Motor Dynamic Equation in Time Domain

The motor dynamic equation relates the developed output torque of the motor to the mechanical output torque, inertia of the motor and power losses.

$$T_m = J\alpha + K_f \omega + T_L , \tag{2-38}$$

where T_m is the electromagnetic torque developed by the motor, J the total inertia of the motor and load, α the angular acceleration experienced by the rotor, K_f the damping coefficient of the rotor, ω the angular velocity of the rotor and T_L the load torque.

2.7 Motor Parameters

Table 2.1 contains the measured parameters of an enterprise motor used in the hardware testing as well as the simulation.

Table 2.1 Parameters of Enterprise Motor

Number of Pole Pair	4
Rated Speed (RPM)	10,000
Resistance (Ω)	2.15
Inductance max (mH)	0.350
Inductance min (mH)	0.250
Back-EMF Constant (V/kRPM)	0.795

CHAPTER 3. SENSORLESS BLDC DRIVE

3.0 Introduction

The cost, reliability and advantages of eliminating mechanical sensors and cabling for the measurement of position, velocity and flux have led to the development of methods commonly termed "sensorless" or "self-sensing" control of ac machines [1]. The goal of such methods is to estimate the rotor position using the power leads of the machine. This information is then used for torque and motion control.

Various methods of sensorless operation for BLDC motors have been reported and reviewed [1-107]. In particular, spindle motors in hard disk drives (HDDs) are operated by techniques categorized under back-EMF based sensorless methods, which are further sub-categorized as "Terminal Voltage Sensing" [2-7]. Owing to its adoption in HDDs, only this classification of sensorless technique is elaborated and investigated in this thesis.

3.1 Brushless DC (BLDC) Operation

In a BLDC drive, the motor is typically driven by a three-phase inverter circuit as shown in Figure 3.1. It consists of six power semiconductor transistors with a protection diode connected in parallel to each of these transistors.

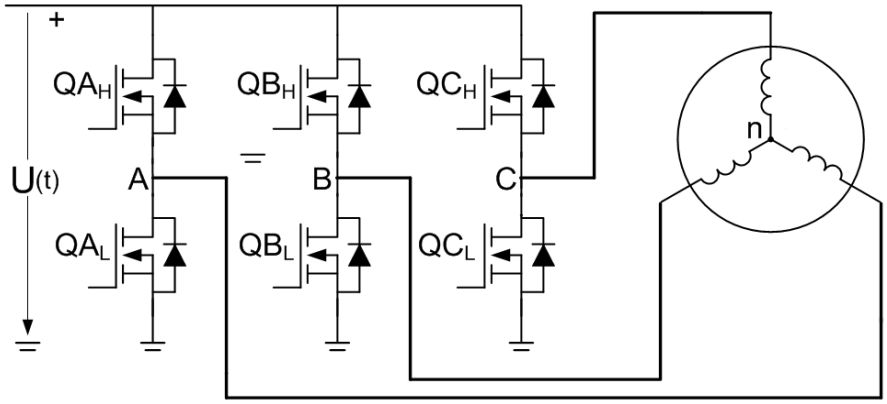

Figure 3.1 Bridge circuit for a BLDC drive.

Each transistor is gated by a 120º-conduction drive, in which each gate turns on for 120 electrical degrees in each cycle. For maximum torque production, the gating with respect to the back-EMF is given in Figure 3.2.

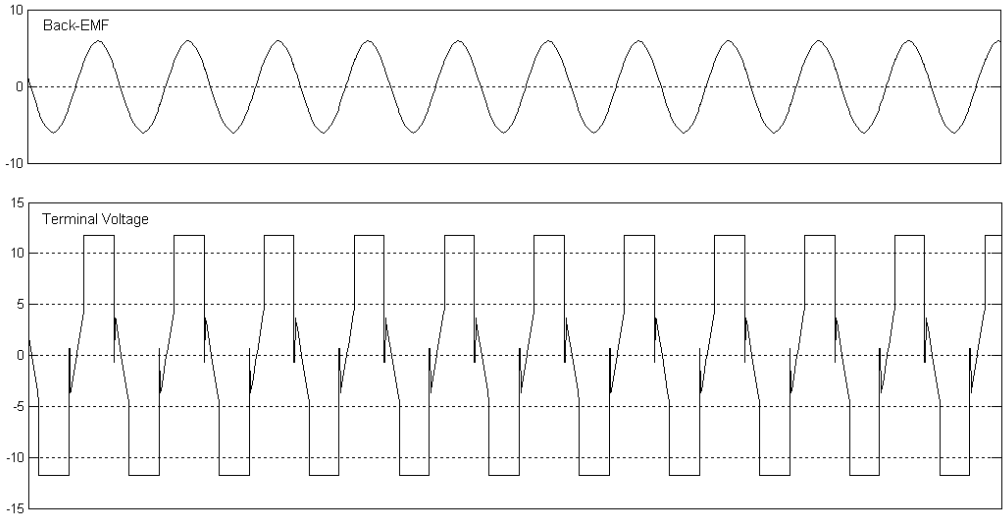

Figure 3.2 Back-EMF versus the terminal voltage.

It can be observed that for phase A, there are two unexcited 60º periods, namely 330º - 30º and 150º - 210º intervals. During the unexcited phase, the phase voltage gives the phase back-EMF. By measuring the phase back-EMF during this window, commutation sequence can be established. This commutation sequence is replicated for phases B and C but phased at 120º and 240º delays, respectively. Thus, commutation occurs at every 60 electrical degrees of rotation in the sequence "Q_{AH}, Q_{BL}", "Q_{AH}, Q_{CL}", "Q_{BH}, Q_{CL}", "Q_{BH}, Q_{AL}", "Q_{CH}, Q_{AL}" and "Q_{CH}, Q_{BL}". The commutation sequence is provided in Figure 3.3.

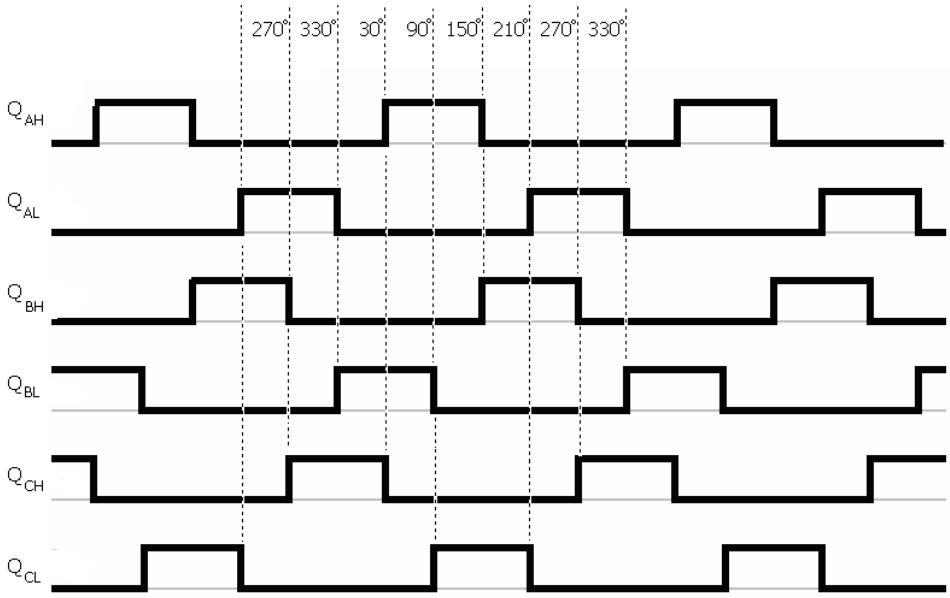

Figure 3.3 Commutation sequence for BLDC drive.

3.2 Terminal Voltage Sensing

Sensorless drive for spindle motors in HDD falls under the sub-category of "Terminal Voltage Sensing". The fundamental principle of this technique is to locate the zero crossing points (ZCPs) of the phase back-EMFs. These ZCPs represent position information. Based on this, sensorless operation using back-EMF ZCP detection is established. Accordingly, for all phases, the commutation is such that these ZCPs should be positioned mid-way in the silent periods. In other words, commutation occur 30º away from the ZCPs.

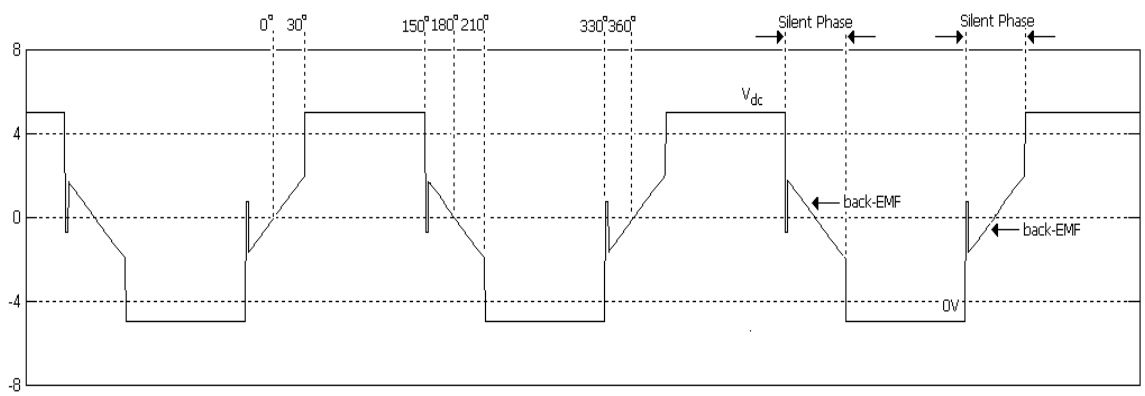

Figure 3.4 Phase A terminal voltage

In terminal voltage sensing, these ZCPs are determined by sensing the terminal voltages. For example, during the 330º - 30º silent phase interval, it is:

$$v_{an} = i_a R + L\frac{di_a}{dt} + e_a \ , \tag{3-1}$$

or

$$v_{an} = e_a \ , \tag{3-2}$$

since

$$i_a = 0 \, . \tag{3-3}$$

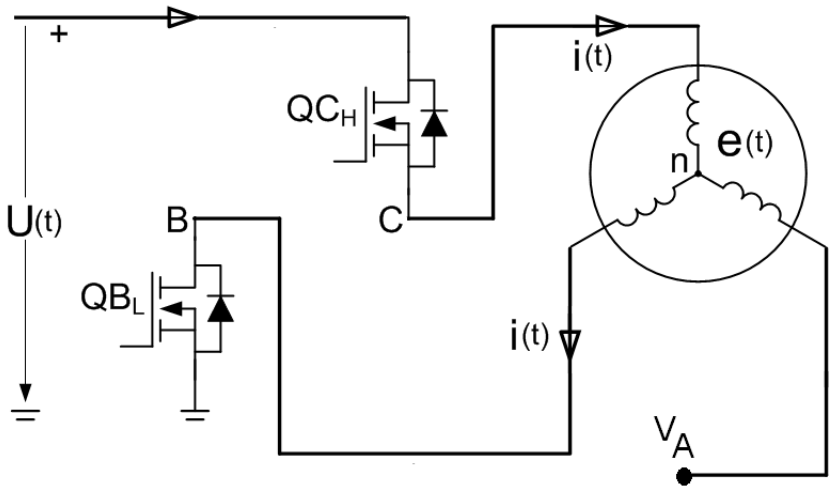

Figure 3.5 330º - 30º Silent phase interval motor drive schematic.

Thus, locating this ZCP or equivalently $e_a = 0$ would mean when the terminal voltage is equal to the neutral voltage or $v_{an} = 0$. While v_a can be measured from the terminals, v_n cannot be measured as the neutral terminal is not available. Different techniques have been developed to determine v_n. References [8-11] determine the neutral voltage to be seen at the terminal at these ZCP points while references [12-14] reconstruct a "virtual" neutral which provides equivalence to the actual neutral. The inception is rooted on the fundamentals of a balanced 3 phase network. For the spindle motor,

$$v_{bn} = v_{an}\left(\theta - \frac{2\pi}{3}\right), \tag{3-4}$$

and

$$v_{cn} = v_{an}\left(\theta - \frac{4\pi}{3}\right). \tag{3-5}$$

If the triplen harmonics can be neglected,

$$v_{an} + v_{bn} + v_{cn} = 0\,. \tag{3-6}$$

Expressing this equation in another form,

$$\begin{aligned} &v_{ao} - v_{no} + v_{bo} - v_{no} + v_{co} - v_{no} = 0, \\ &v_{no} = \frac{1}{3}\left(v_{ao} + v_{bo} + v_{co}\right). \end{aligned} \tag{3-7}$$

Hence, it can be seen that the neutral voltage can be obtained via a summation average of the three line voltages. This can be easily implemented by a star impedance network where

$$\begin{aligned} &v_{an'} + v_{bn'} + v_{cn'} = 0, \\ &v_{n'o} = \frac{1}{3}\left(v_{ao} + v_{bo} + v_{co}\right). \end{aligned} \tag{3-8}$$

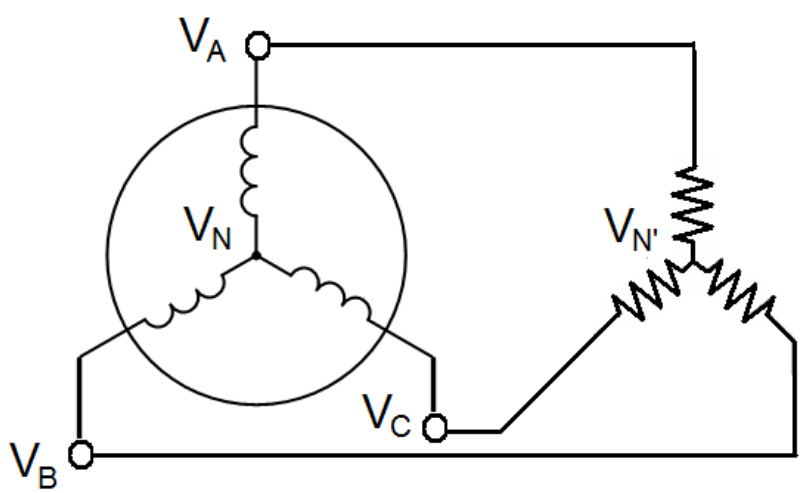

Figure 3.6 Star network for virtual neutral creation.

Consequently to generate the ZCPs, comparators are used to generate the polarities of v_{an}, v_{bn} and v_{cn}. However, this approach of terminal sensing suffers from the presence of false ZCPs due to phasor turned-off commutation. During a commutation, the switching off the transistor causes the current to freewheel through its corresponding paired transistor's diode, the result of which a voltage spike is seen in the terminal. As a result, false ZCPs are seen which, if not removed or not avoided, cause erratic positional sensing.

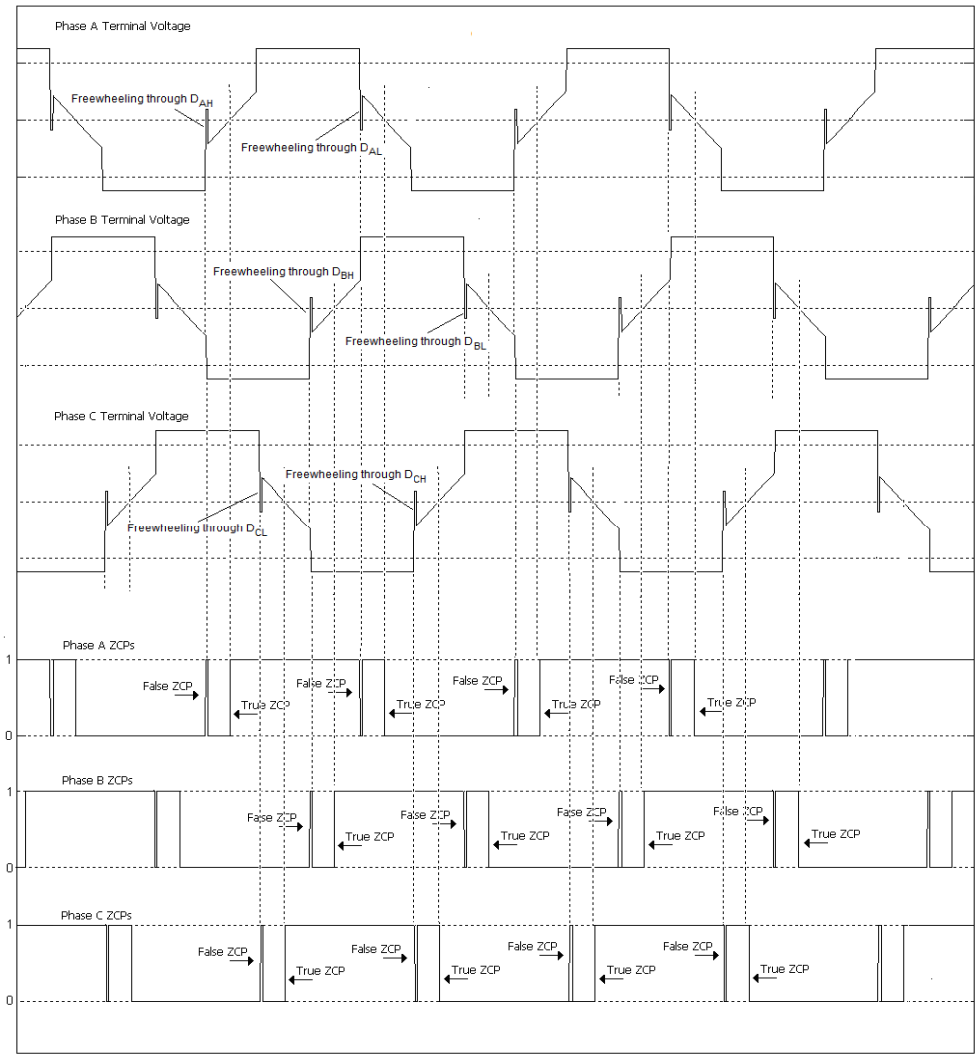

Figure 3.7 Terminal voltage and ZCP detection.

Conventionally, low-pass filters (LPF) [14-17] are used to remove these false ZCPs. In reference [12], digital masking, instead of LPF, is used. However, these methods invariably introduce delays resulting in sub-optimal performance. Figure 3.8 shows the deterioration in speed for a constant voltage drive due to phase shift.

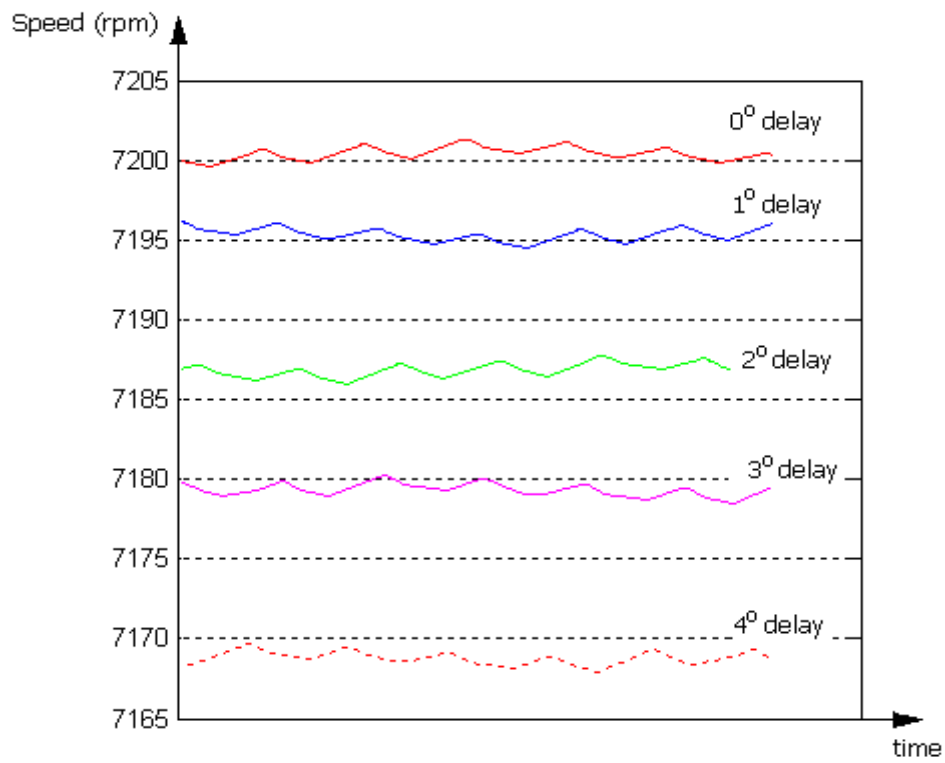

Figure 3.8 Simulated waveforms for constant voltage BLDC drive with ZCP delay.

3.3 Zero Delay Direct Back-EMF BLDC Drive

Most of the methods focus on the removal or exclusion of these false ZCPs when they occur. In this proposed method, an integrative zero delay direct back-EMF BLDC drive is utilized.

As highlighted earlier, in a BLDC drive, a commutation occurs 30 electrical degrees (30º) after every true ZCP is detected. And to achieve to zero delay, the true ZCP must be processed immediately when it is detected. The algorithm proposed below achieves the intended purpose.

a. A global free running counter is implemented in the design and latches are used to store the counter indices for all the ZCPs.

b. Positive edge transitions will be used to latch the 0°, 120° and 240° ZCPs counter indices whereas negative edge transitions will be used to latch the 60°, 180° and 300° ZCPs counter indices.

c. 30° time lag is to be estimated using the 60° time lapse from the last ZCP to latest ZCP detected. For example, to estimate the 30° time lag after the occurrence of 0° ZCP, the 30° time lag would be equivalent to the point whereby the counter has further increased by ½ × ($Latch_{0°}$ - $Latch_{300°}$). The factor of ½ is easily accomplished by a single bit right shift of ($Latch_{0°}$ - $Latch_{300°}$).

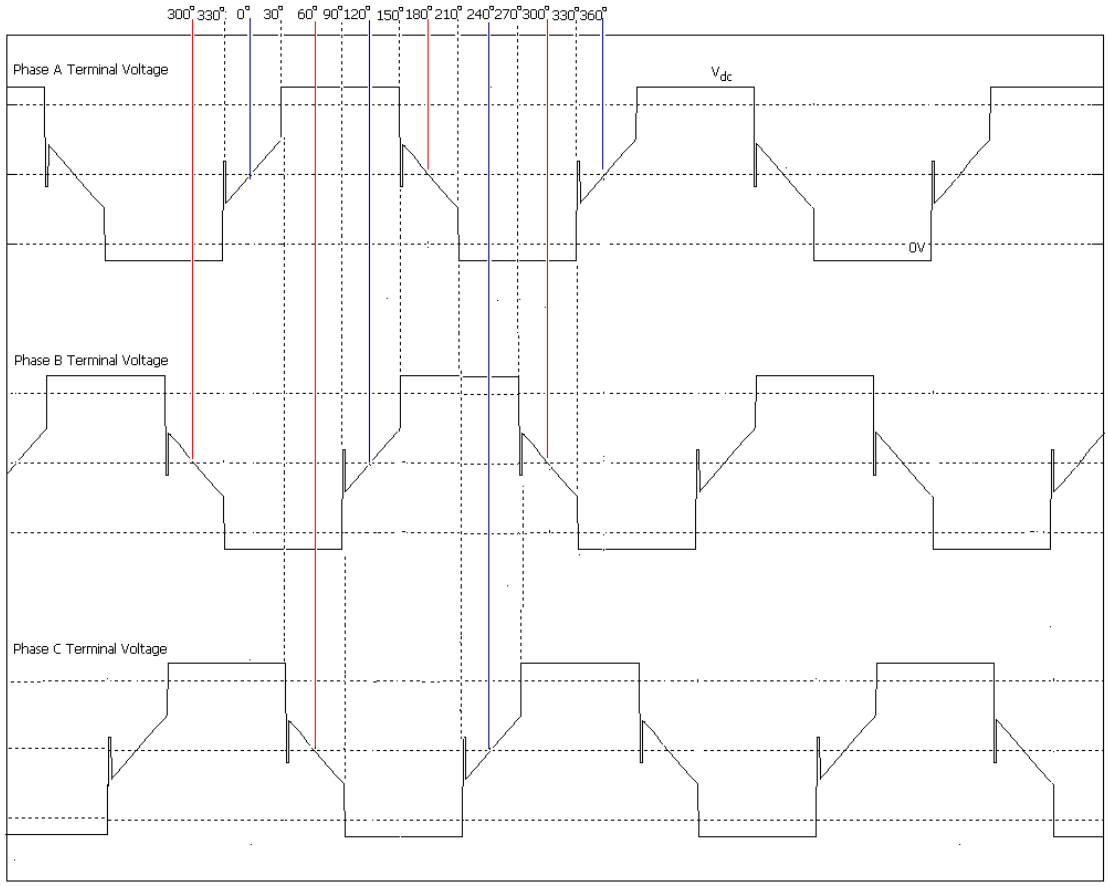

Figure 3.9 Terminal voltage for BLDC drive

The algorithm achieves zero delay BLDC drive at this juncture but it too suffers from the presence of false ZCPs, resulting in incorrect counter indices being latched. For example, in the scenario shown in Figure 3.10, owing to the presence of false ZCP, the counter value of x004 is latched resulting in a much earlier commutation count of x063.

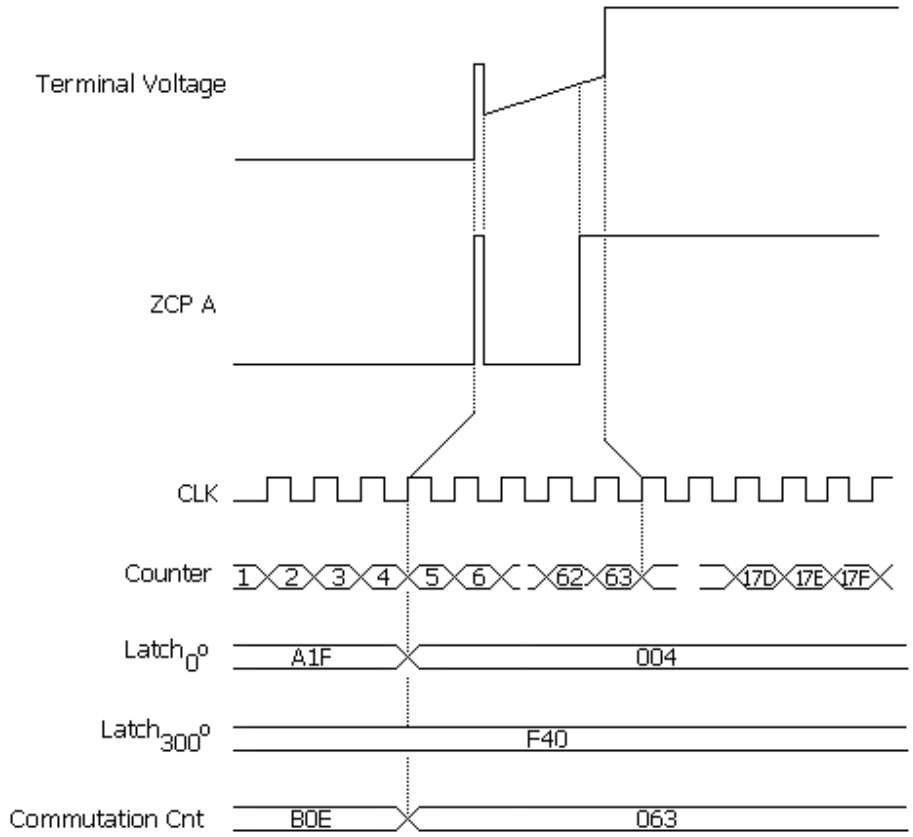

Figure 3.10 BLDC algorithm without false ZCP avoidance.

A quick or traditional fix would be to filter the ZCPs before processing. As mentioned earlier, this would bring about delay and sub-optimal commutation. To achieve zero delay ZCP detection, the rule that ZCPs (*true*) are to be processed immediately when it occurs must be respected. This constraint admits a pitfall, such that latching is done for all ZCPs, true or false.

This constraint can be elegantly respected by the inclusion of false ZCP avoidance within the BLDC drive algorithm. A unique property can be derived from the signals. After an active ZCP, during the 30° time lag for commutation, inactive ZCPs should

never occur during this period. For example, 0° ZCP counter count will be latched by positive or rising edge ZCP transitions. During the 30° time lag before commutation, inactive negative or falling edge ZCP will not occur if the preceding active ZCP is true. Hence, in the presence of an inactive ZCP during the 30° time lag interval, latch will be restored to its previous count and active edge ZCP transition is awaited. While this approach safeguards against positive 'glitches', additional measure is necessary to safeguard against negative 'glitches'. A solution would be to modify the proposed algorithm such that, in the presence of an inactive ZCP during the 30° time lag interval, the interval will be made inactive only if an active edge ZCP transition does not occur with certain time window. Such a modification allows commutations to be estimated from the true ZCPs without delay and at the same time, disregard the false ZCPs. Further additional level of heuristic control would be that apart from satisfying the 30° time lag, commutation should occur only at the active level. The integrated algorithm thus becomes,

a. A global free running counter is implemented in the design and latches are used to store the counter counts for all the ZCPs.

b. Positive edge transitions will be used to latch the 0°, 120° and 240° ZCPs counter counts whereas negative edge transitions will be used to latch the 60°, 180° and 300° ZCPs counter counts. 30° time lag is to be estimated using the 60° time lapse from the last ZCP to latest ZCP detected.

c. Occurrence of inactive edge transitions will reset ZCP counter counts to its previous counter values if a positive edge transition does not occur within a time window. Negative edge transitions will trigger a reset of the 0°, 120° and 240° ZCPs counter counts whereas positive edge transitions will trigger a reset of the 60°, 180° and 300° ZCPs counter counts.

d. If the current count minus the ZCP latched count equals to the estimated 30° time lag and current ZCP signal level remains active, commutation occurs.

e. A wait for the new ZCP in the adjacent phase commences.

Figure 3.11 gives a stateflow representation of the algorithm.

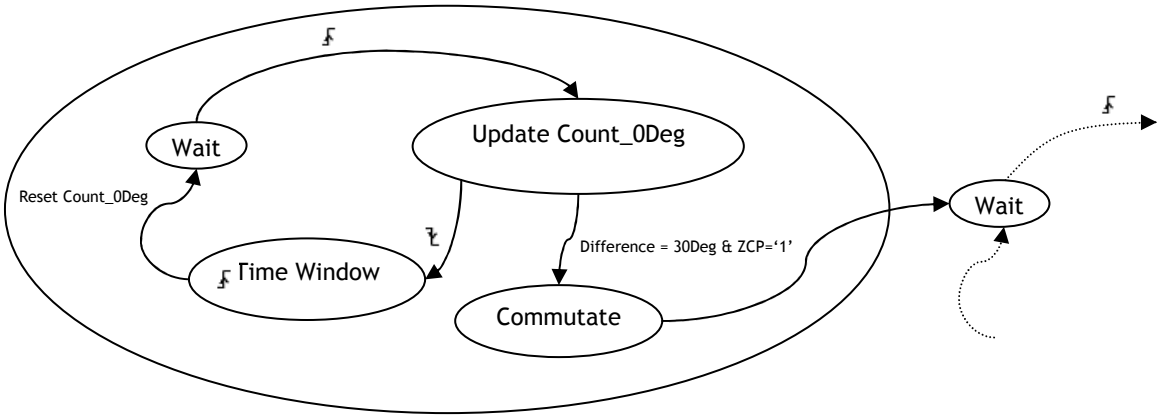

Figure 3.11 Stateflow representation of zero delay BLDC commutation

Commutation is accomplished via internal position updating. At the end of the 30° time lag, the internal position monitor is updated with an "advanced" position. Due to the position update, it will trigger the new set of gating signals.

Table 3.1 Updated Internal Positions for BLDC Commutation Signals Generation

Position, θ	Internal Position, θ_{int}	Commutation Signals
$30^\circ \leq \theta < 90^\circ$	60°	"Q_{AH}, Q_{BL}"
$90^\circ \leq \theta < 150^\circ$	120°	"Q_{AH}, Q_{CL}"
$150^\circ \leq \theta < 210^\circ$	180°	"Q_{BH}, Q_{CL}"
$210^\circ \leq \theta < 270^\circ$	240°	"Q_{BH}, Q_{AL}"
$270^\circ \leq \theta < 330^\circ$	300°	"Q_{CH}, Q_{AL}"
$330^\circ \leq \theta$; $\theta < 30^\circ$	0°	"Q_{CH}, Q_{BL}"

Applying this algorithm to the previous example in Figure 3.10, the result is shown in Figure 3.12. In the presence of false ZCP, similarly the counter value of x004 is latched with x063 being updated as the awaited commutation count. However presence of an inactive falling ZCP resets the latch to its previous value and waiting continues. Consequently, with the arrival of the real ZCP, correct ZCP counter value is latched.

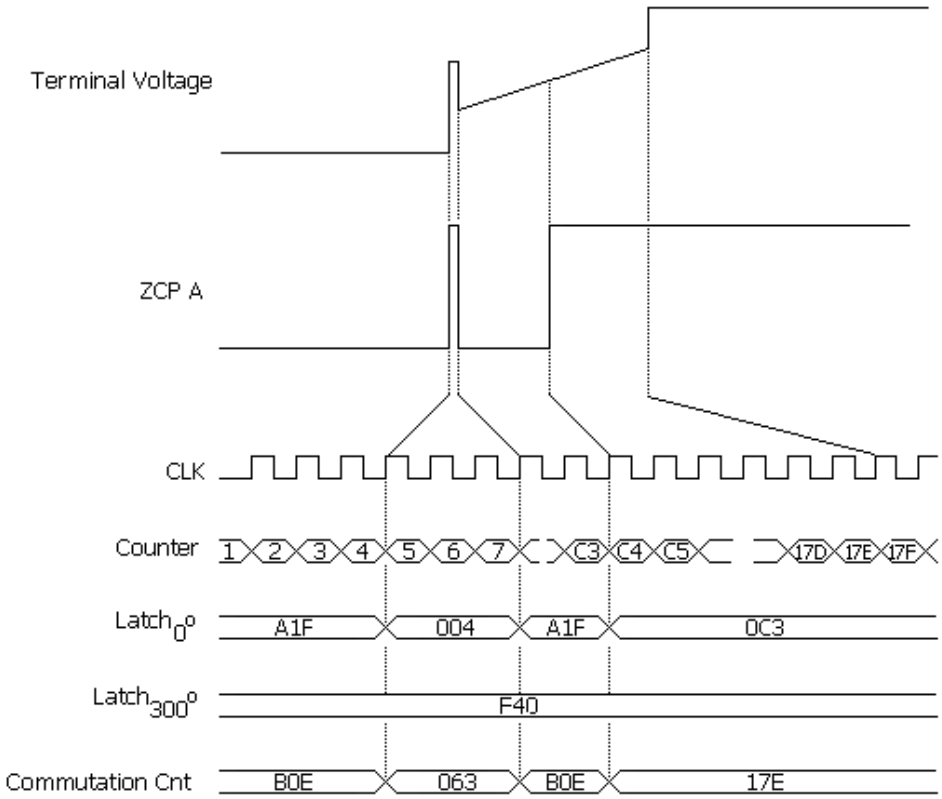

Figure 3.12 Proposed BLDC algorithm with false ZCP avoidance.

3.4 Simulation

In the investigation of the proposed algorithm, MATLAB®, a high performance language for technical computing, is used. For modeling, Simulink®, a software package which provides a graphical user interface for modeling, simulating, and analyzing dynamic systems, is used.

3.4.1 Overview

Figure 3.13 shows the Simulink top level block entry for the complete sensorless BLDC drive.

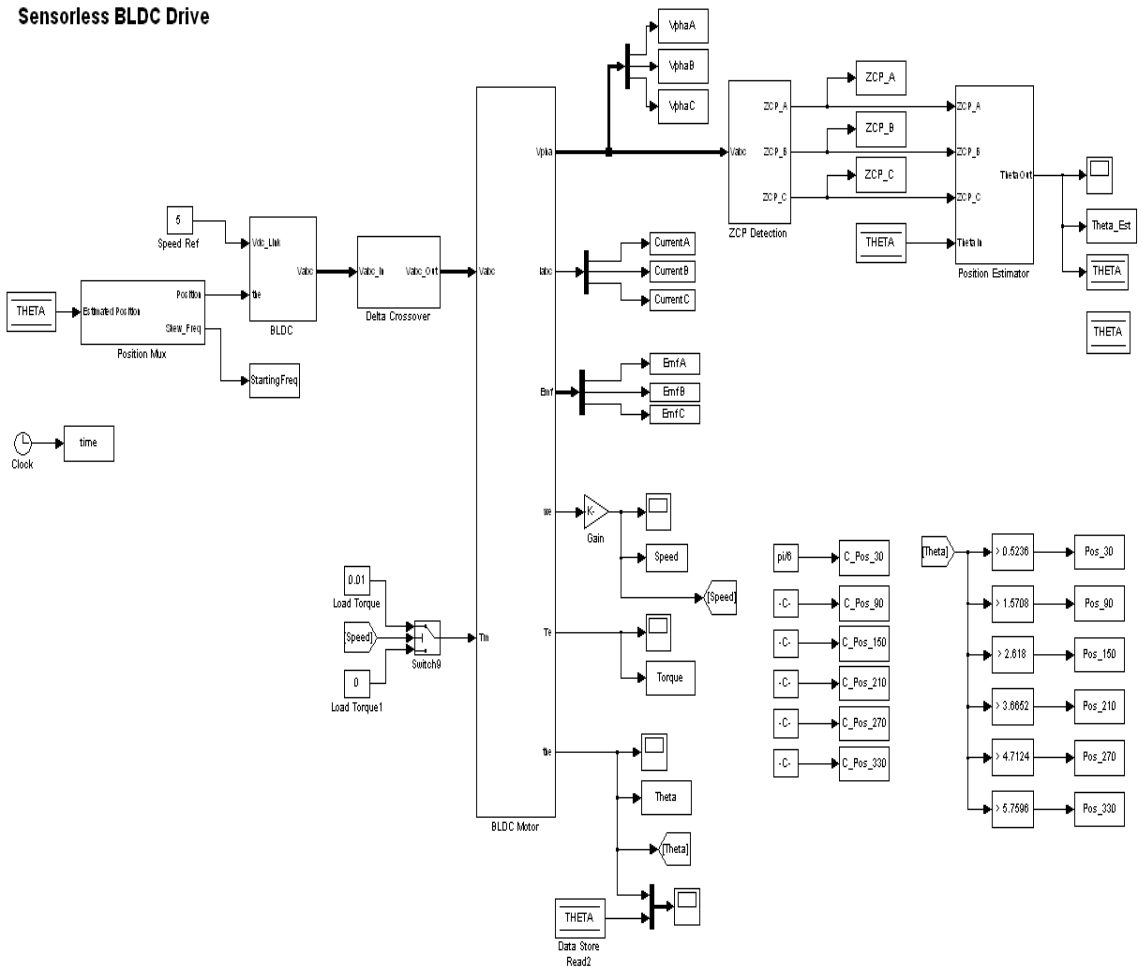

Figure 3.13 Simulink top level block entry for sensorless BLDC drive.

3.4.2 Spindle Motor Model

Figure 3.14 shows the Simulink block entry for the spindle motor and Figure 3.15 shows the electrical phase model. Figure 3.16 shows the dynamic mechanical model.

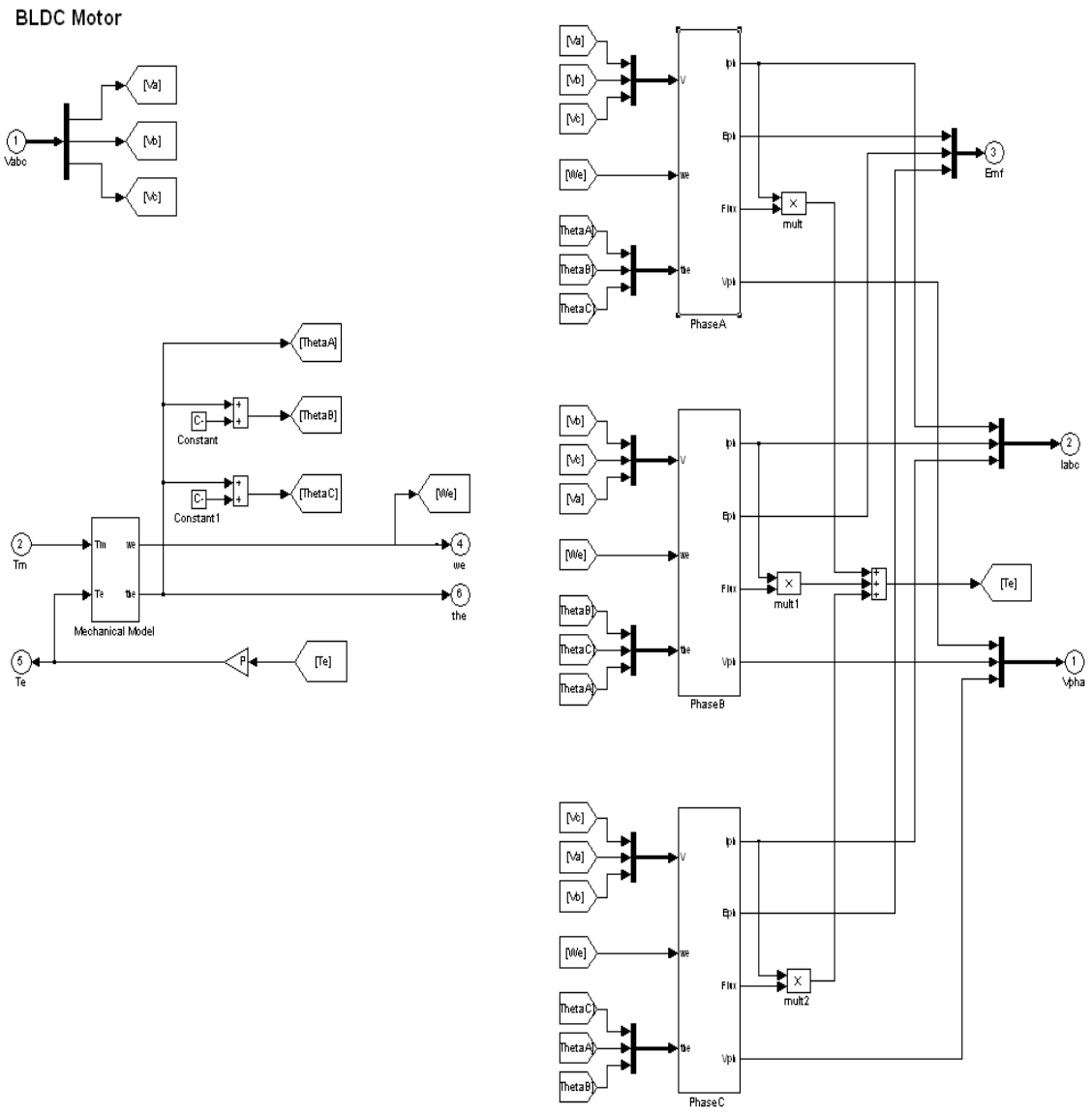

Figure 3.14 Simulink block entry for spindle motor.

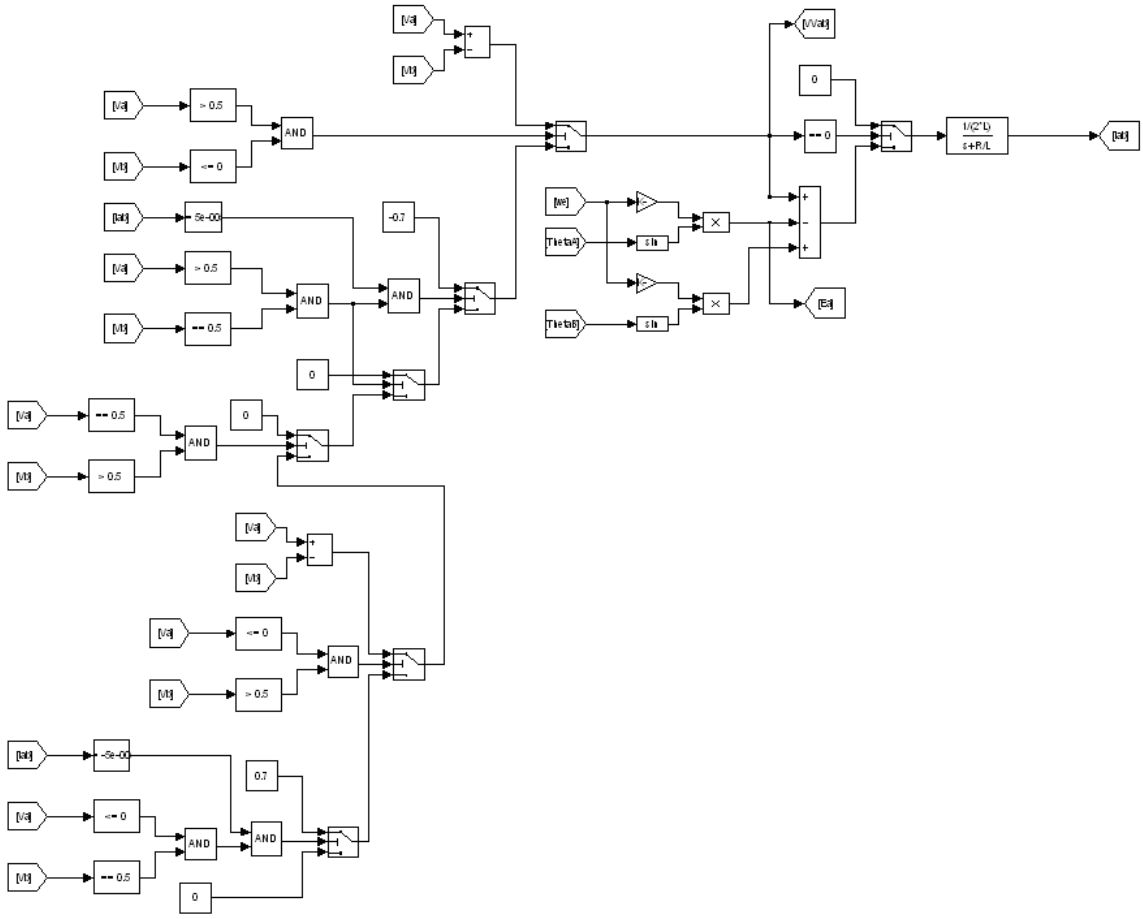

Figure 3.15 Simulink spindle motor phase AB current model.

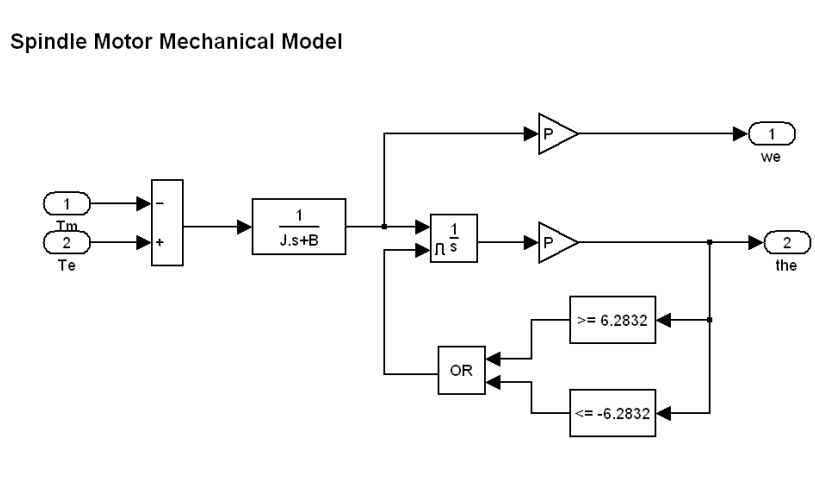

Figure 3.16 Simulink block entry for spindle motor mechanical model.

3.4.3 BLDC Voltage Signals Generation

Figure 3.17 shows the Simulink block entry for the bldc voltage signals generation. The voltage injection is generated via a look-up comparator method.

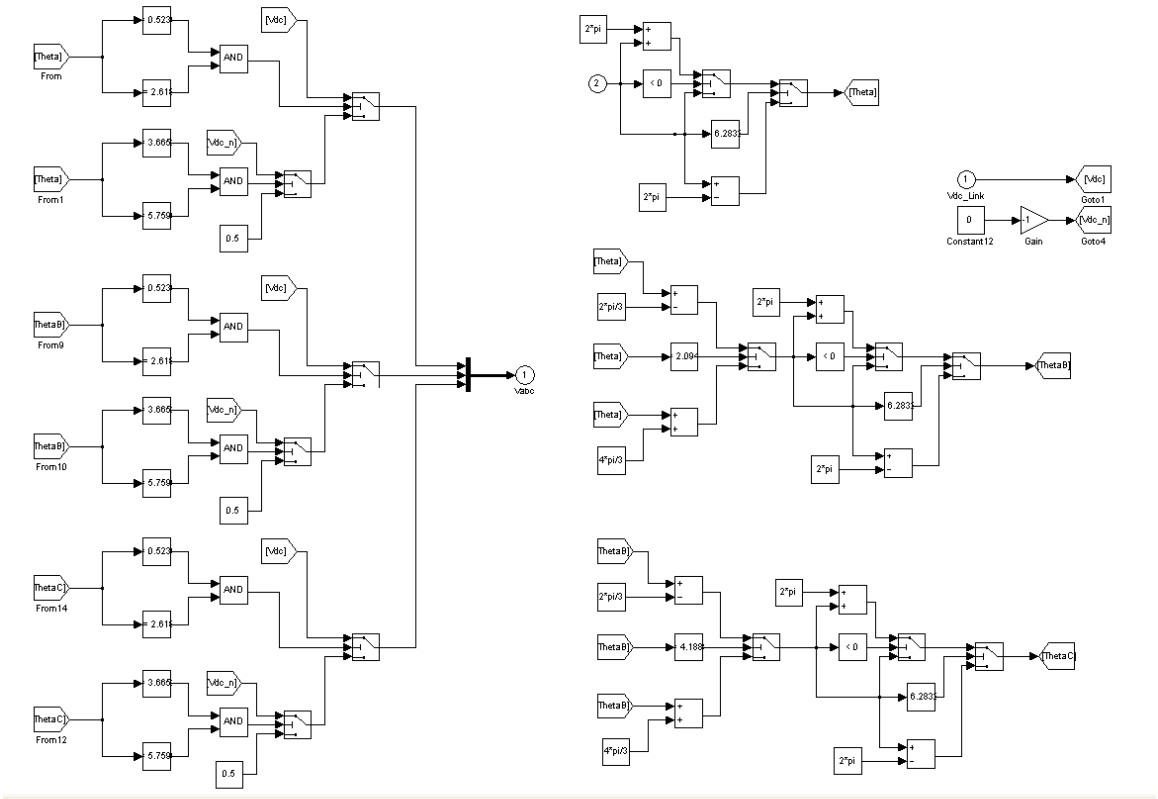

Figure 3.17 Simulink block entry for BLDC voltage signals generation.

3.4.4 Position Estimator

Figure 3.18 shows the Simulink block entry for ZCP generation where Figure 3.19 and Figure **3.20** show the position estimators based on the proposed algorithm.

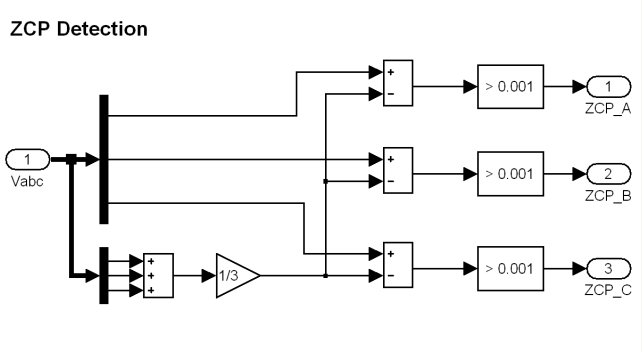

Figure 3.18 Simulink block entry for ZCP generation.

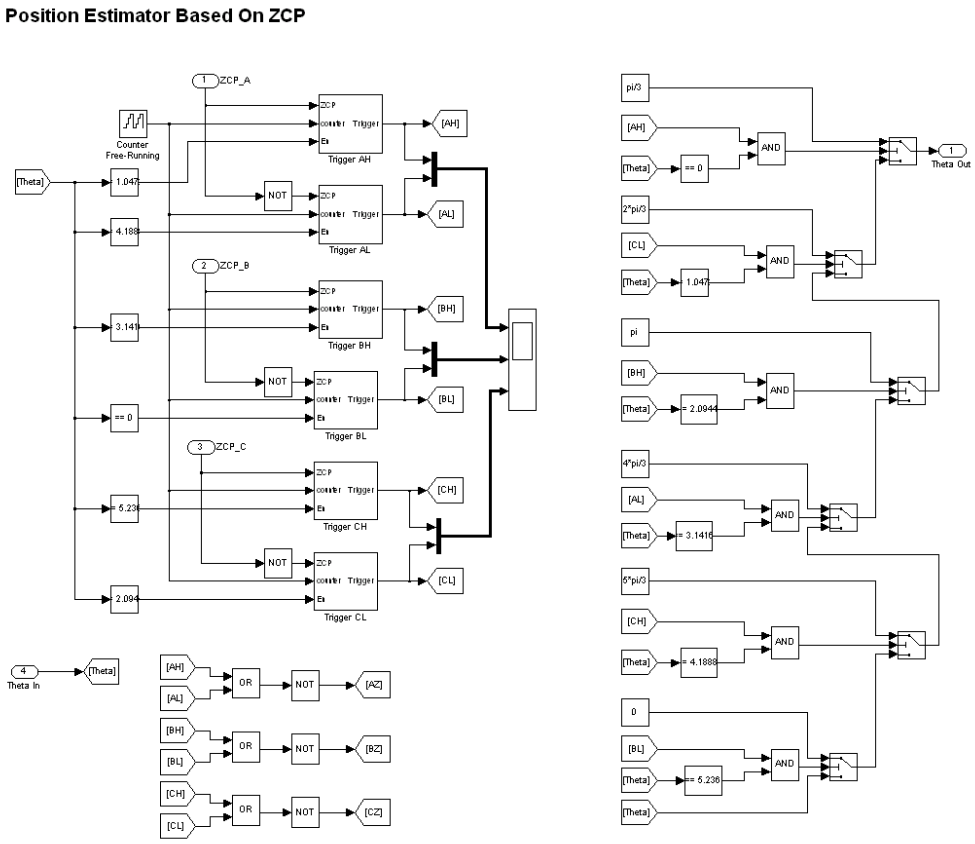

Figure 3.19 Simulink block entry for position estimator.

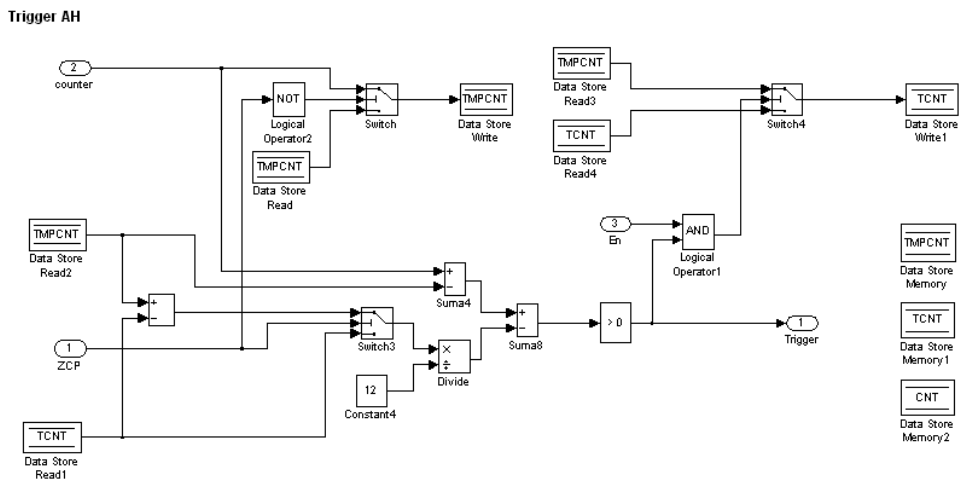

Figure 3.20 Simulink block entry for position update trigger signal.

3.4.5 Simulation Results

The design has been simulated and the waveforms are provided. Figure 3.21 shows plots of terminal voltages and neutral voltage. It can be observed that the three phases are spaced at 120˚ apart and with conduction angles of 120˚. Figure 3.22 shows the ZCP generation for Phase A. As mentioned, the terminal voltage is compared with the neutral voltage resulting in the ZCP waveform. It can be seen that true ZCPs occur when both the neutral and phase voltage are the same whereas false ZCPs occur during commutation. From Figure 3.23, it can be seen that the commutation for Phase A occurs exactly at the desired positional points, namely, 30°, 150°, 210° and 330°, thus proving the viability of the algorithm as well as its zero delay property.

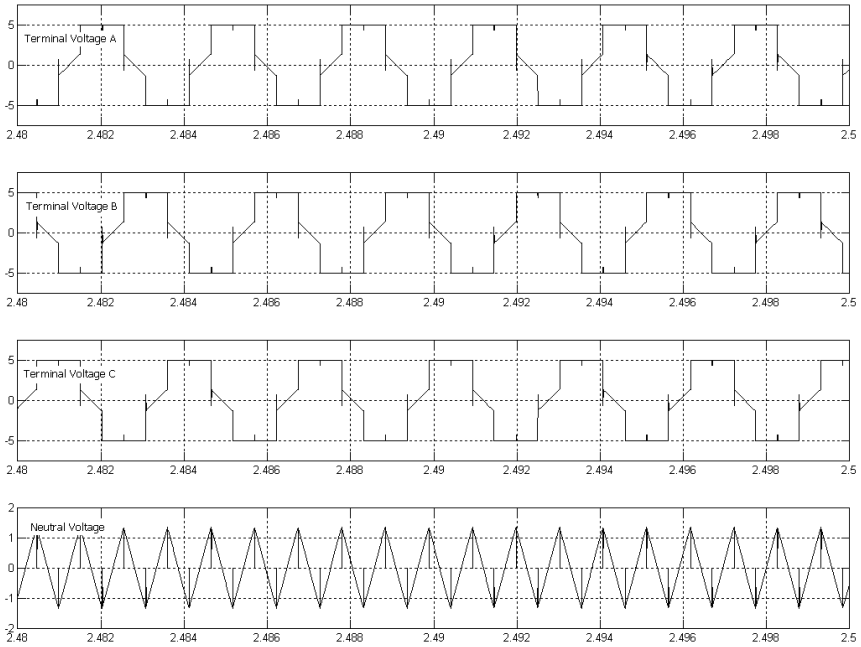

Figure 3.21 Plots of terminal voltages and neutral voltage.

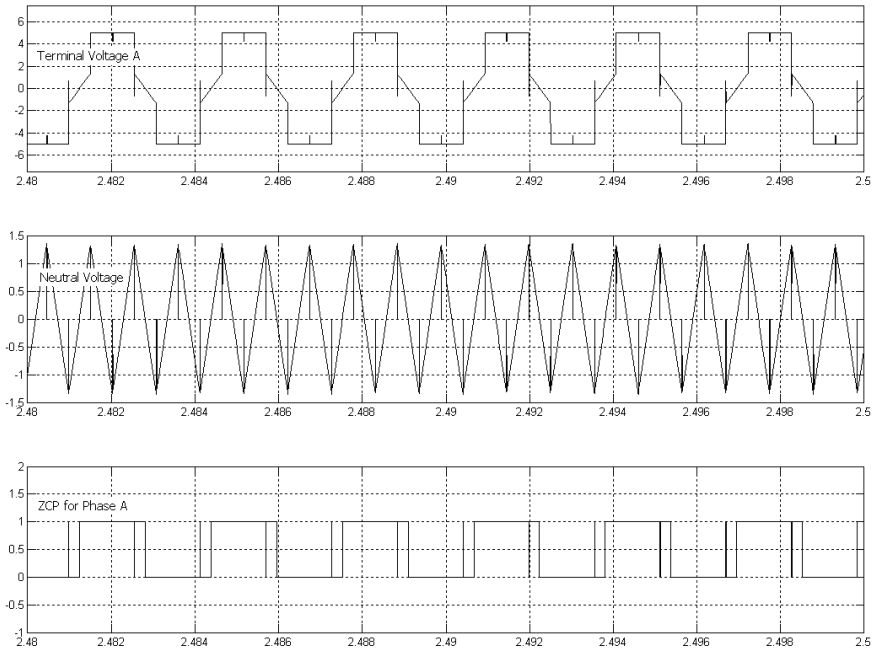

Figure 3.22 ZCP generation for phase A.

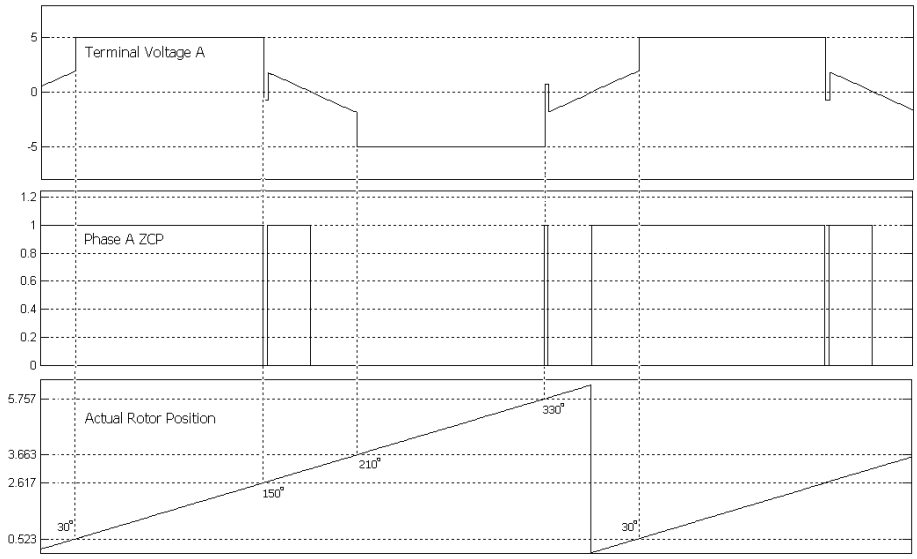

Figure 3.23 Simulated response for zero delay BLDC drive.

3.5 Hardware Implementation and Results

3.5.1 Hardware Implementation

To investigate the viability of the algorithm while at the same time taking interest with ease of adoption, the topology similar to that in a HDD drive as seen in Figure 3.24 is adopted.

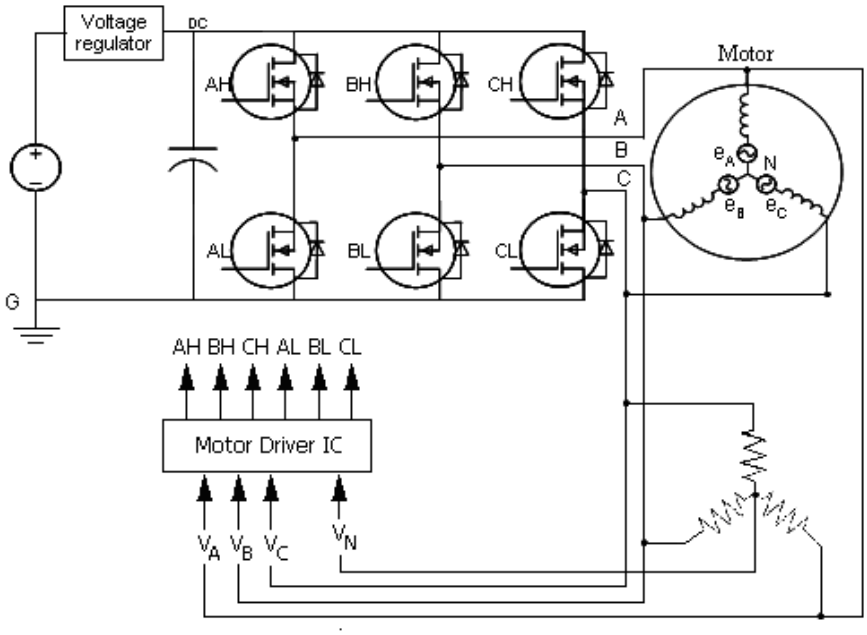

Figure 3.24 Typical topology of a HDD drive.

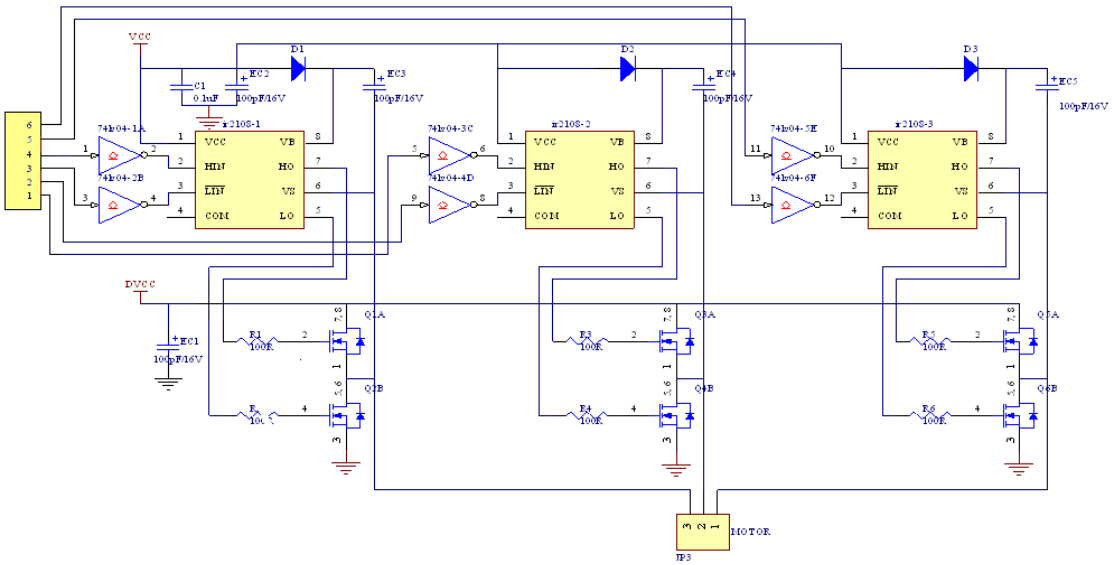

Figure 3.25 Schematic for motor drive circuit.

In the implementation, high and low side drivers (IR2101S) and dual N-channel MOSFETs (SI4920DY) are used. The IR2101S are high voltage; high speed power MOSFET and IGBT drivers with independent high and low side referenced output channels that are able to drive the N channel Mosfets. SI4920DY are N channel Mosfets interfaced directly for driving the spindle motor. As opposed to the utilization of a motor IC, a field programmable gate array (FPGA), Xilinx Virtex-4™ FX12 LC, is employed.

3.5.2 Experimental Results

The design has been implemented and the waveforms are captured. Figure 3.26 shows plots of terminal voltages and neutral voltage. It can be observed that the three phases are spaced at 120˚ apart and with conduction angles of 120˚. Figure 3.27 shows the ZCP generation for Phase A. As mentioned, the terminal voltage is compared with the neutral voltage resulting in the ZCP waveform. It can be seen that true ZCPs occur when both the neutral and phase voltage are the same whereas false ZCPs occur during commutation. Figure 3.28 shows the ZCP generation for all the three phases.

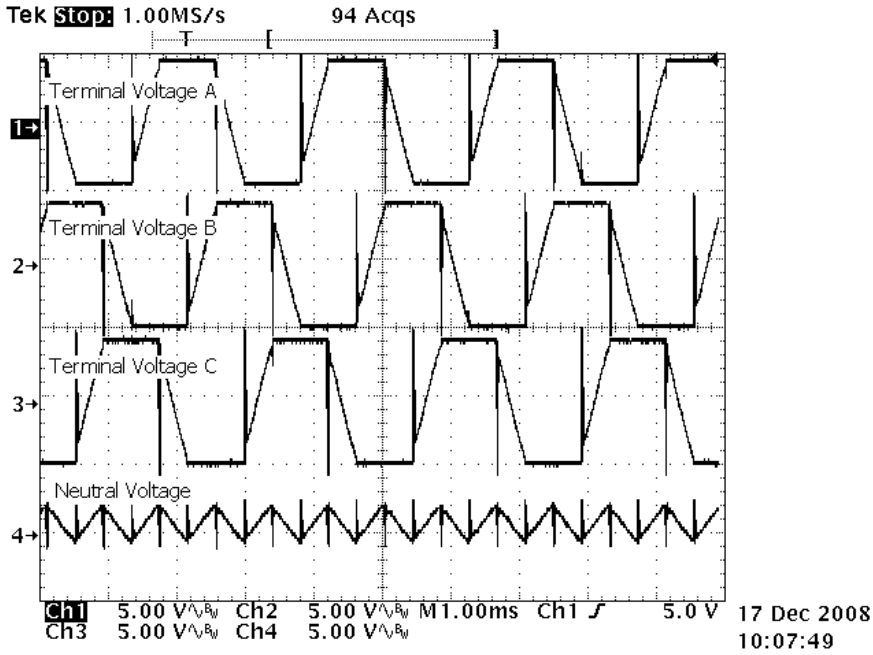

Figure 3.26 Plots of terminal voltages and neutral voltage.

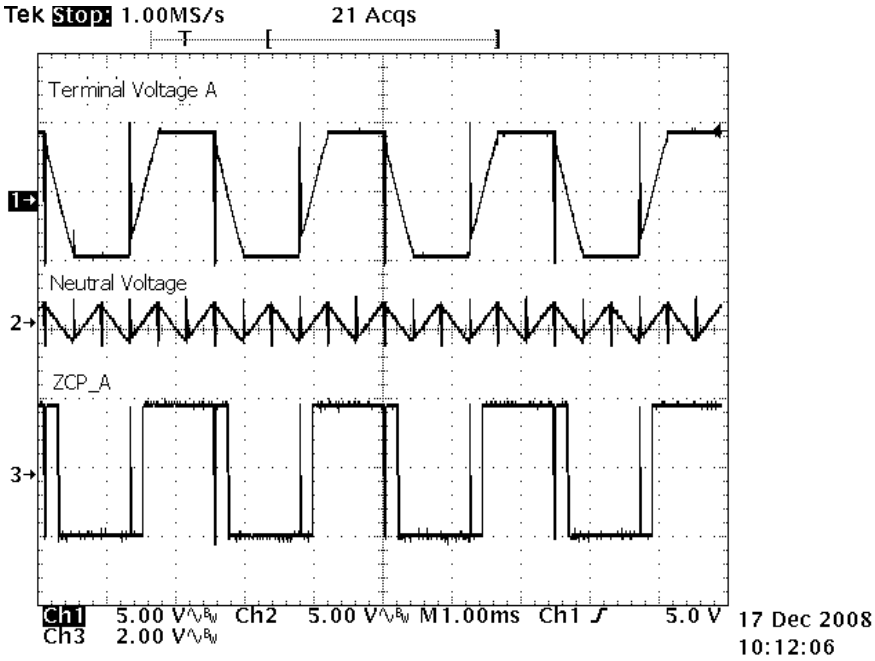

Figure 3.27 ZCP generation for phase A.

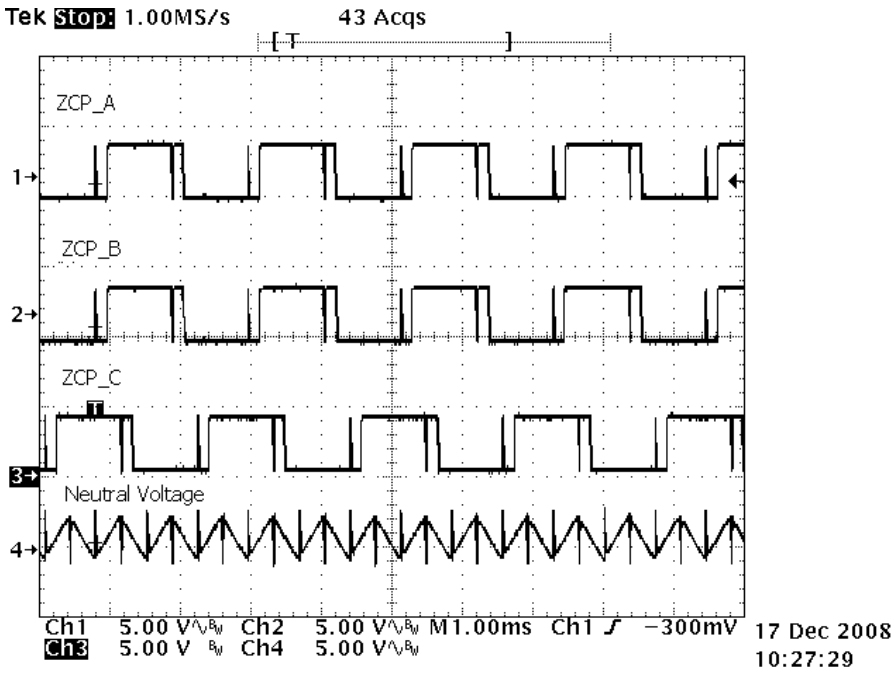

Figure 3.28 ZCP generation for phases A, B and C.

From Figure 3.29, it can be seen that the commutation for Phase A occurs at the desired positional points, namely, 330° and 30°, with the ZCP at the mid-point between the commutations, thereby demonstrating zero delay property of the algorithm. In order to demonstrate the robustness of the algorithm against noisy glitches, noise was introduced into the ZCP generation. Despite the presence of noise, Figure 3.30 shows that the algorithm was able to detect the false ZCPs and commutate with respect to the true ZCPs.

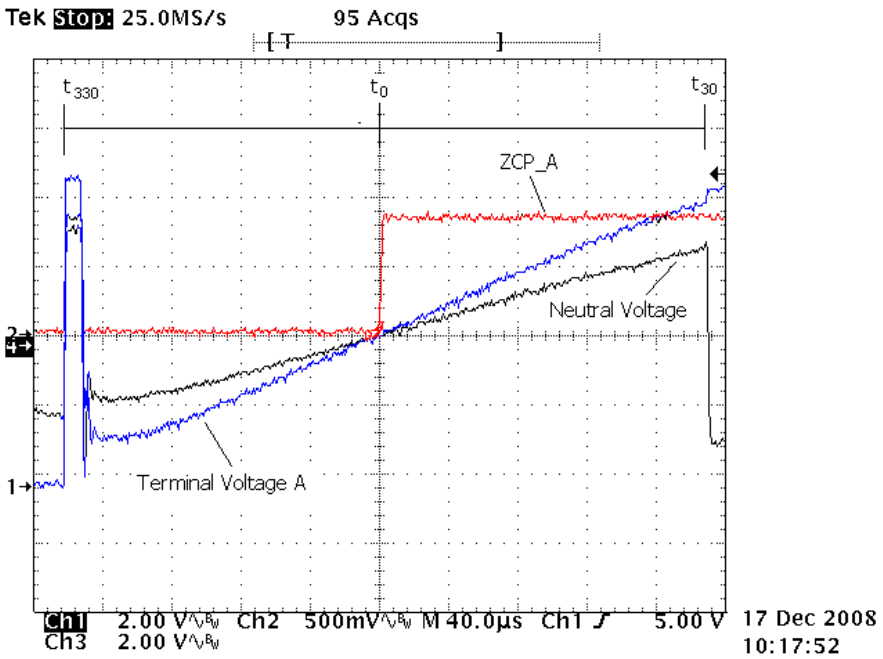

Figure 3.29 BLDC waveforms.

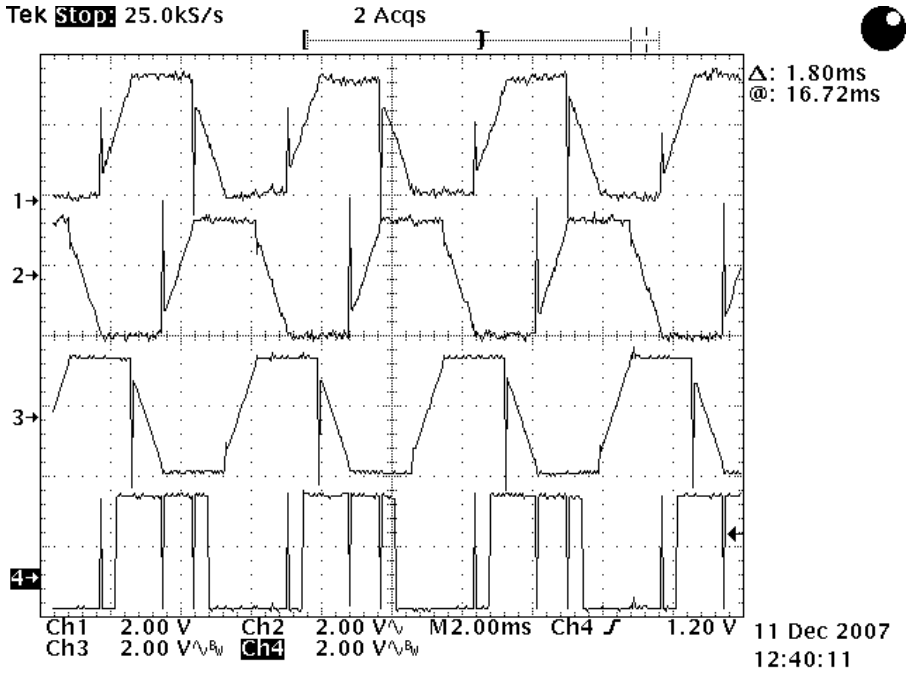

Figure 3.30 Illustration of algorithm's robustness under noisy ZCPs.

3.6 Conclusions

Terminal voltage sensing suffers from the presence of false ZCPs arising from freewheeling operation during commutations. These false ZCPs, if unremoved or unavoided, results in erratic sensorless BLDC operation. In this chapter, an innovative zero-delay back-EMF based BLDC drive was presented. It took an integrative approach in the design of the ZCP detection as well as the BLDC drive implementation. From both the simulation and experimental results, it was seen that the proposed algorithm while offering zero-delay, was able to avoid noise and false ZCPs. These are crucial issues to tackle, especially in high performance BLDC drives where wide speed range is expected. With the exception of comparators, this was achieved with pure digital implementation with the advantages of being reproducible as well as cost efficient.

CHAPTER 4. SENSORLESS QUASI-BLDC DRIVE

4.0 Introduction

Historically, BLDC drive is recommended and adopted for BLDC motor with trapezoidal back-EMF. At every commutation step, one winding terminal is connected to positive supply voltage with another connected to negative supply voltage. The third terminal is floated where it provides the back-EMF. In such a drive, the goal is to inject rectangular stator phasor currents for maximum and smooth torque production.

It is optimum to inject rectangular stator phase currents to a BLDC (with ideal trapezoidal back-EMF) for maximum torque and minimum torque ripple production. In many applications such as in HDDs, they have BLDC motors with sinusoidal back-EMFs. However, BLDC drive is nevertheless deployed due to its ease and simplicity of implementation. As a result, torque ripples are observed.

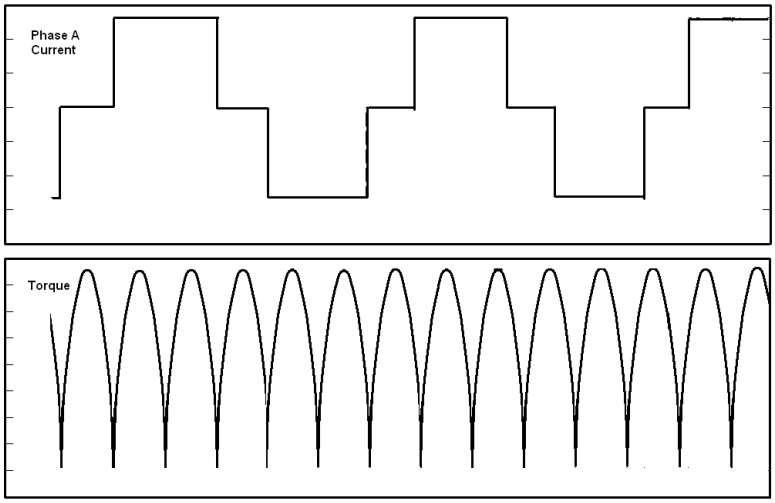

Figure 4.1 Torque profile with rectangular currents on sinusoidal back-EMF.

The situation is aggravated by the presence of inductance while using BLDC drive. Figure 4.2 shows the plot of current and torque. It can be seen that the resulting current and torque depart from those desired. The torque ripple is undesirable as it is a source of electrical and mechanical noise, and vibration.

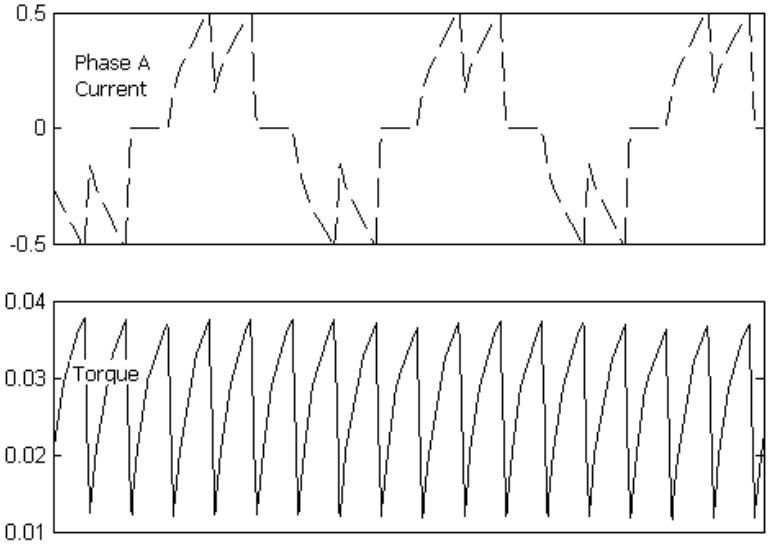

Figure 4.2 Current and torque response with inductive effects.

4.1 BLDC Current and Torque Analysis

It has been briefly mentioned that the presence of inductance has resulted in the deviation from the ideal case. However, in the goal of reducing the torque ripple, it would be informative to examine the current waveforms. An insightful step would be to examine the BLDC current for a motor sinusoidal back-EMF with zero inductance. For illustration, focusing on the 30˚ to 90˚ segment, during the $V_{AH}V_{BL}$ drive

$$v_{ab} = 2i_{ab}R + L\frac{di_{ab}}{dt} + e_{ab}. \tag{4-1}$$

Accordingly, if

$$\begin{aligned} e_{ab} &= E_m \sin(\theta) - E_m \sin\left(\theta - 2\pi/3\right) \\ &= \sqrt{3}E_m \cos\left(\theta - \pi/3\right) \end{aligned}, \tag{4-2}$$

and

$$L = 0, \tag{4-3}$$

$$v_{ab} = V_{DD}. \tag{4-4}$$

The current would be

$$i_{ab} = \left[V_{DD} - \sqrt{3}E_m \cos\left(\theta - \pi/3\right)\right] / (2R), \tag{4-5}$$

as provided in the simulated waveform.

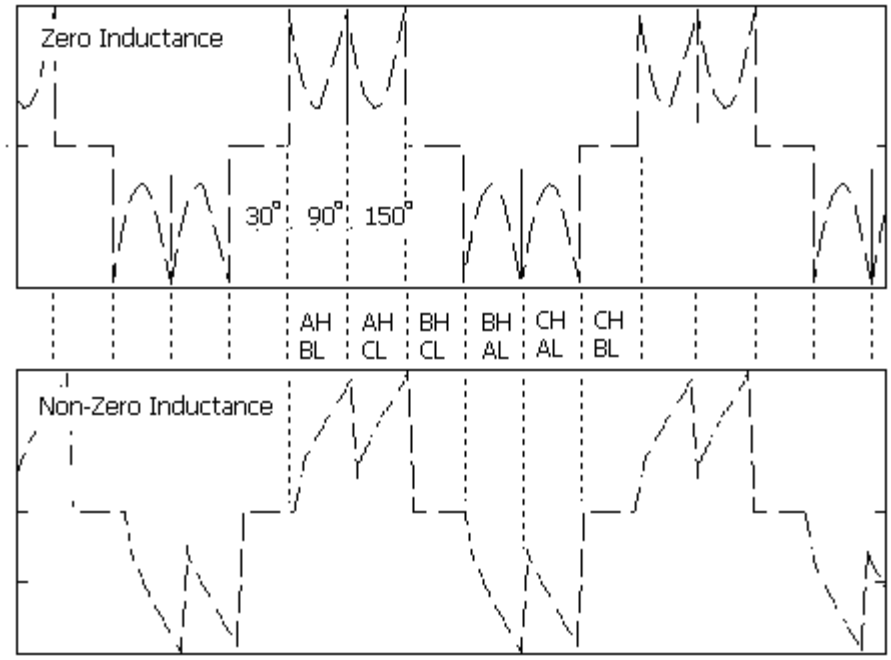

Figure 4.3 Phase A current with and without inductive effects.

Considering the effects of inductance, the current would be

$$i_{ab,(30^o,90^o)} = \frac{1}{2R}\left[V_{DD} - \sqrt{3}E_m \cos\left(\theta - \pi/3\right)\right]\left(1 - e^{-\frac{Rt}{L}}\right). \tag{4-6}$$

The corresponding rate of increase is given as

$$\frac{di_{ab,(30°-900°)}}{dt} = \frac{1}{2L}\left[V_{DD} - \sqrt{3}E_m \cos\left(\theta - \pi/3\right)\right]e^{-\frac{Rt}{L}}. \tag{4-7}$$

If the inductance is zero, the rate of increase is infinite. However, if it is not, the rate of increase is affected by both the inductance as well as the back-EMF term. During the commutation from (A_H, B_L) to (A_H, C_L), the current is profiled by

$$i_{ab,(90^o,150^o)} = \frac{1}{2R}\left[-\sqrt{3}E_m \cos\left(\theta - \pi/3\right)\right] + \frac{V_{DD}}{2R}e^{-\frac{Rt}{L}}, \tag{4-8}$$

and its rate of decay,

$$\frac{di_{ab,(90°-150°)}}{dt} = -\frac{V_{DD}}{2L} e^{-\frac{Rt}{L}}, \tag{4-9}$$

Similarly, if inductance is zero, the rate of decrease is infinite. The presence of inductance will slow down the rate of decrease.

It can also be observed from Figure 4.3 that a current "notch" occurs at the middle of the waveform due to commutation. The emergence of this notch can be explained based on the equations in the preceding paragraphs. It is effectively caused by the differences in the rate of decrease of $i_{ab,(90°-150°)}$ and the rate of increase of $i_{ac,(90°-150°)}$. By Kirchoff's current law, in the absence of neutral line,

$$i_a + i_b + i_c = 0. \tag{4-10}$$

Hence during commutation,

$$i_a = i_{ab,90^o-150^o} + i_{ac,90^o-150^o}, \tag{4-11}$$

where

$$i_{ab,(90^o,150^o)} = \frac{1}{2R}\left[-\sqrt{3}E_m \cos\left(\theta - \pi/3\right)\right] + \frac{V_{DD}}{2R} e^{-\frac{Rt}{L}}, \tag{4-12}$$

$$i_{ac,(90^o,150^o)} = \frac{1}{2R}\left[V_{DD} - \sqrt{3}E_m \cos\left(\theta - 2\pi/3\right)\right]\left(1 - e^{-\frac{Rt}{L}}\right). \tag{4-13}$$

In addition,

$$\frac{di_{ab,(90^o,150^o)}}{dt} = -\frac{V_{DD}}{2L} e^{-\frac{Rt}{L}}, \tag{4-14}$$

$$\frac{di_{ac,(90^o,150^o)}}{dt} = \frac{1}{2L}\left[V_{DD} - \sqrt{3}E_m \cos\left(\theta - \pi/3\right)\right] e^{-\frac{Rt}{L}}. \tag{4-15}$$

Established on the above, the slow rise of i_{ac} but rapid decay of i_{ab} gave rise to the notch. Referring to Figure 4.2, it can be seen that these "notches" are accountable for the ripples in the torque.

4.2 Quasi-BLDC Drive

Therefore, a direct method to improve the torque performance would be to reduce the current notches. As highlighted, these notches are the results of slow current rise and rapid current fall. To reduce the notches would be to match $di_{ab,(90^o,150^o)}/dt$ and $di_{ac,(90^o,150^o)}/dt$, where

$$\frac{di_{ab,(90^o,150^o)}}{dt} = -\frac{V_{DD}}{2L} e^{-\frac{Rt}{L}}, \tag{4-16}$$

$$\frac{di_{ac,(90^o,150^o)}}{dt} = \frac{1}{2L}\left[V_{DD} - \sqrt{3}E_m \cos\left(\theta - \pi/3\right)\right] e^{-\frac{Rt}{L}}. \tag{4-17}$$

It is impossible to reduce the inductance to zero or to reduce the back-EMF to zero. Nevertheless, whilst the rate of increase $di_{ac,(90^o,150^o)}/dt$ cannot be altered, the decay rate of $di_{ab,(90^o,150^o)}/dt$ can be changed. Instead of an abrupt gate removal or V_{DD} removal, an intermediate voltage V_{fDD} (< V_{DD}) is introduced. The current becomes

$$\begin{cases} i_{ab}\dfrac{R}{L} + \dfrac{di_{ab}}{dt} = \dfrac{1}{2L}\left[V_{fDD} - \sqrt{3}E_m \cos\left(\theta - \pi/3\right)\right] \\ i_{ab,(90^o,150^o)} = \dfrac{1}{2R}\left[V_{fDD} - \sqrt{3}E_m \cos\left(\theta - \pi/3\right)\right] + \dfrac{1}{2R}\left(V_{DD} - V_{fDD}\right) e^{-\frac{Rt}{L}} \end{cases}, \tag{4-18}$$

and

$$\frac{di_{ab,(90^o,150^o)}}{dt} = \frac{1}{2L}\left(V_{fDD} - V_{DD}\right)e^{-\frac{Rt}{L}}. \tag{4-19}$$

To match $di_{ab,(90^o,150^o)} / dt$ and $di_{ac,(90^o,150^o)} / dt$,

$$\begin{aligned} V_{fDD} &\approx \sqrt{3}E_m \cos\left(\theta - \pi/3\right)\Big|_{\theta=\frac{\pi}{2}} \\ &= 1.5E_m \end{aligned} \tag{4-20}$$

However, although notch is reduced, the drive becomes unbalanced (i.e. t1 ≠ t2).

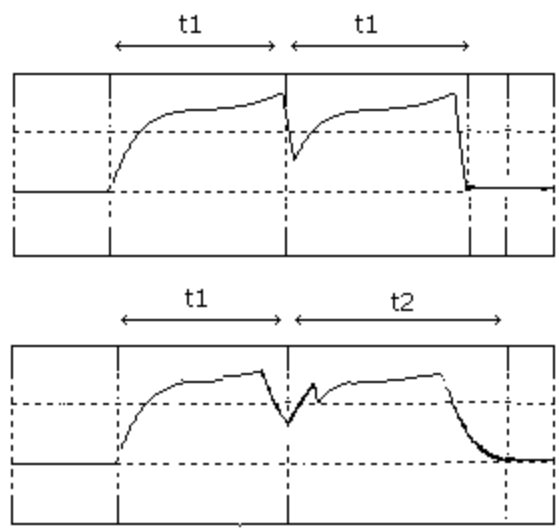

Figure 4.4 Illustration of unbalance caused by current change rate matching.

In order to resolve this unbalance, the gating must be correspondingly gate advanced. Instead of BLDC, QBLDC involves incorporating the matching of the current rise time and fall time as well as gate advancing into BLDC for the minimization of current notches. In the next section, different time constant windows of current rate matching and gate advance are investigated and optimized.

4.2.1 Simulation and Investigation

In the investigation of the proposed QBLDC, the top level Simulink block entry provided in Figure 4.5 is modified to replace the BLDC block with QBLDC.

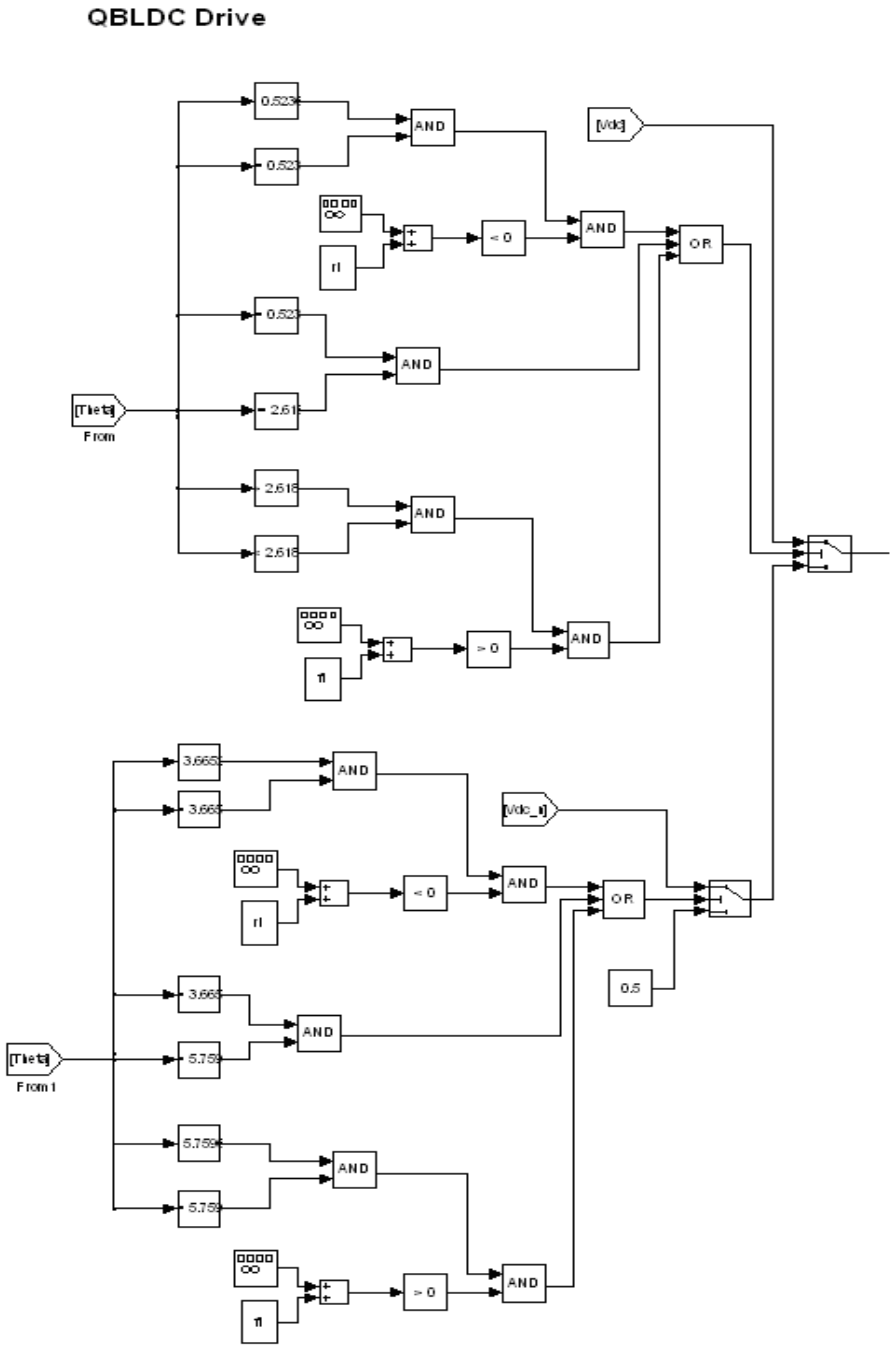

Figure 4.5 Simulink block entry for quasi-BLDC voltage signals generation.

4.2.2 Simulation Results

The design has been simulated and the voltage V_{fDD} is applied for various time constants, in steps of 0.5 × L/R. Figure 4.6 shows plots of phase voltages and the removal of gating injection or introduction of V_{fDD} accomplished by PWM.

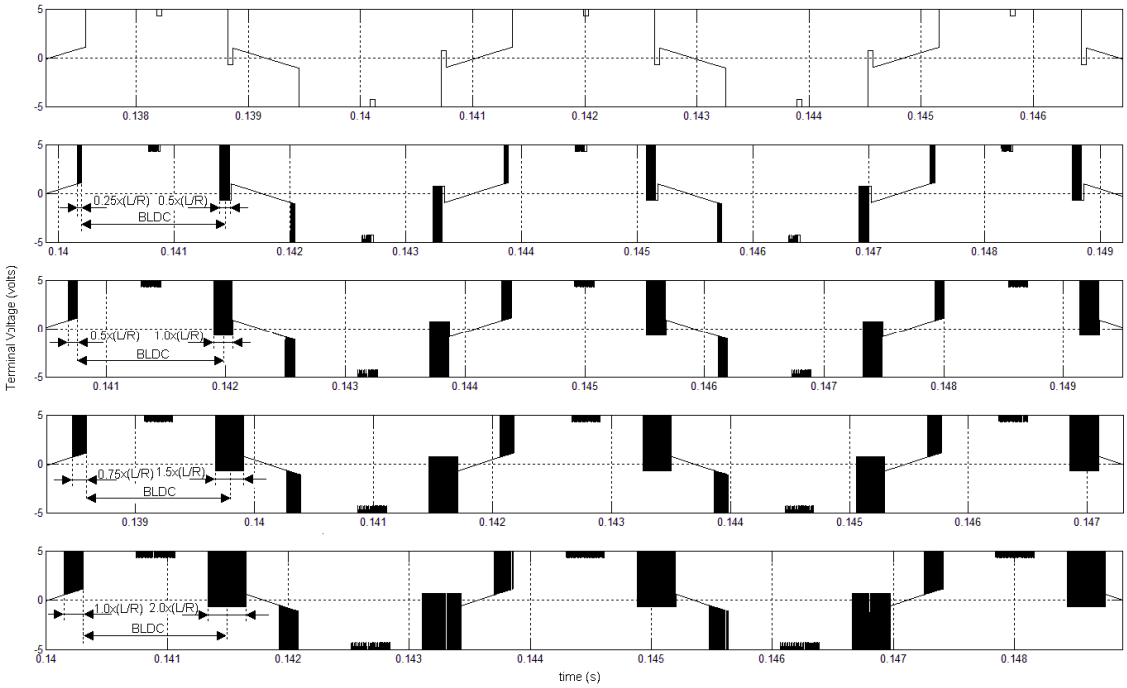

Figure 4.6 Plots of quasi-BLDC terminal voltages for time constants injection.

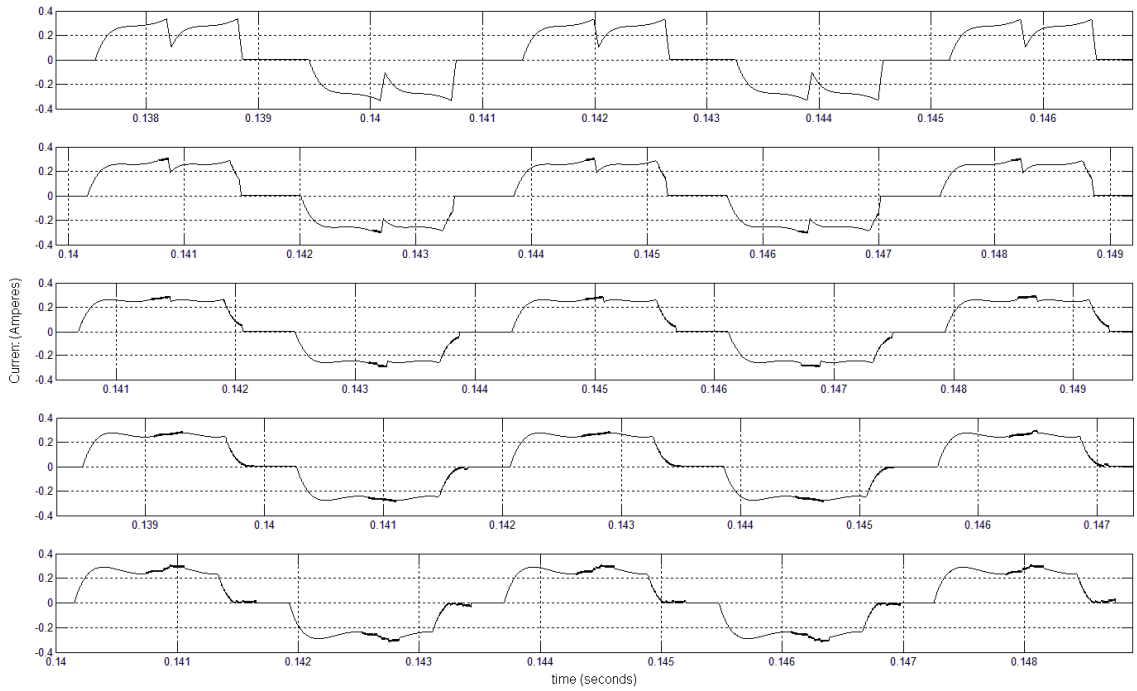

Figure 4.7 Plots of quasi-BLDC terminal current for time constants injection.

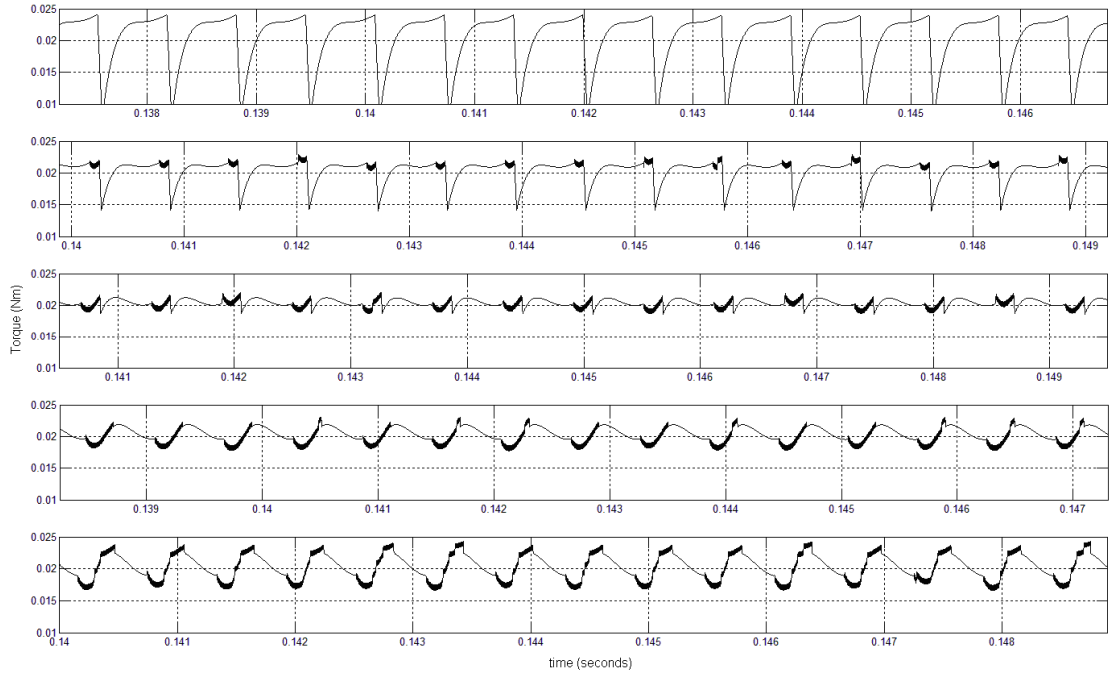

Figure 4.8 Plots of quasi-BLDC torque for various time constants injection.

It can be observed that for difference time constants of V_{fDD} injection, the notch at the commutation can be significantly improved. As seen in Figure 4.8, the best torque performance is provided by V_{fDD} injected at time constant of 1.0 × L/R advancement. Defining Torque Ripple Factor as

$$TRF = \frac{(T_{peak} - T_{av})}{T_{av}}, \tag{4-21}$$

and comparing the performance of BLDC drive against QBLDC drive, the TRF for BLDC is

$$TRF_{BLDC} \approx 65\%$$

while the TRF for QBLDC is

$$TRF_{QBLDC} \approx 12.5\%.$$

It can be seen that the torque ripple with consideration of inductance has been significantly improved by approximately 80% in QBLDC drive.

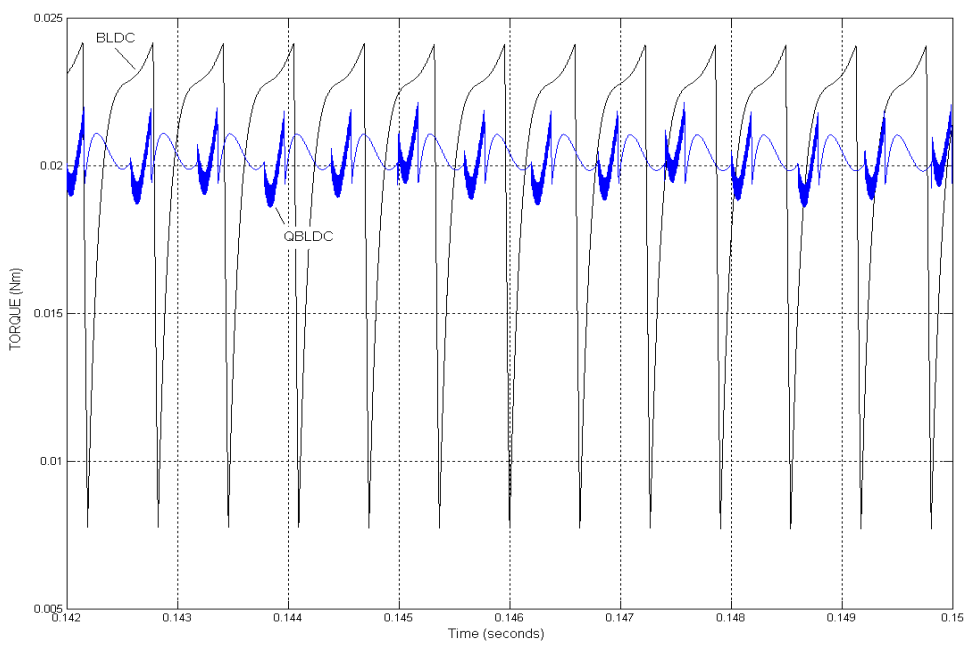

Figure 4.9 Comparison of BLDC and quasi-BLDC torques.

4.3 Hardware Implementation and Results

The same topology as described in 3.5.1 is adopted. The modification pertaining to Quasi-BLDC was isolated to the HDL codes within the FPGA.

The algorithm proposed for Zero-Delay BLDC incorporated with Quasi-BLDC has been designed and implemented. Figure 4.10 shows plots of terminal and neutral voltages. It can be observed that the three phases are spaced at 120˚ apart and with conduction angles of 120˚. Figure 4.11 shows the current comparison between BLDC and QBLDC. It can be seen that the spikes are reduced by 40%.

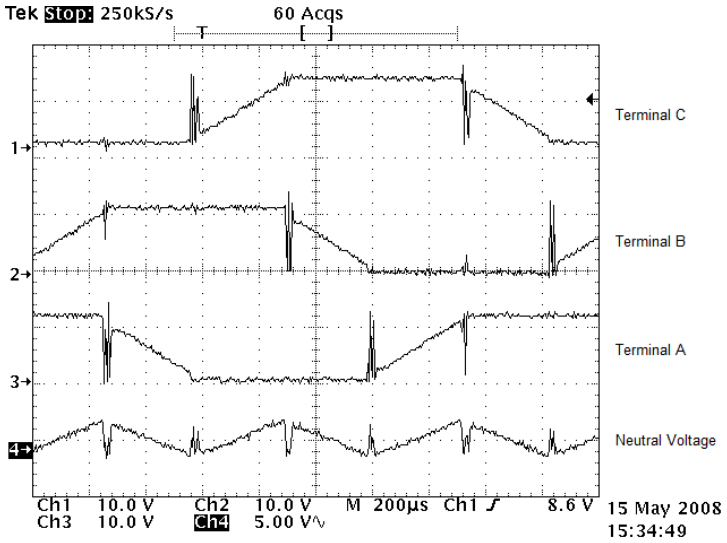

Figure 4.10 Plots of terminal and neutral voltages.

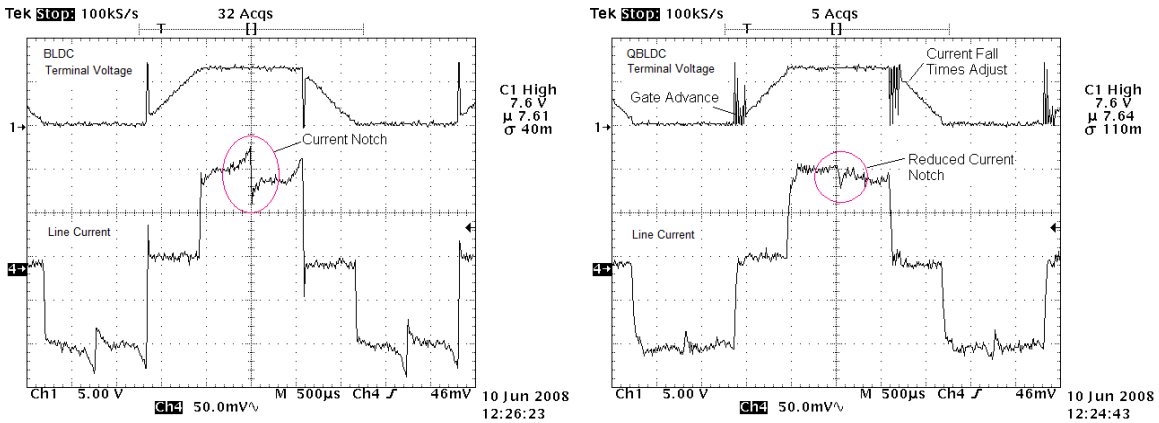

(a)

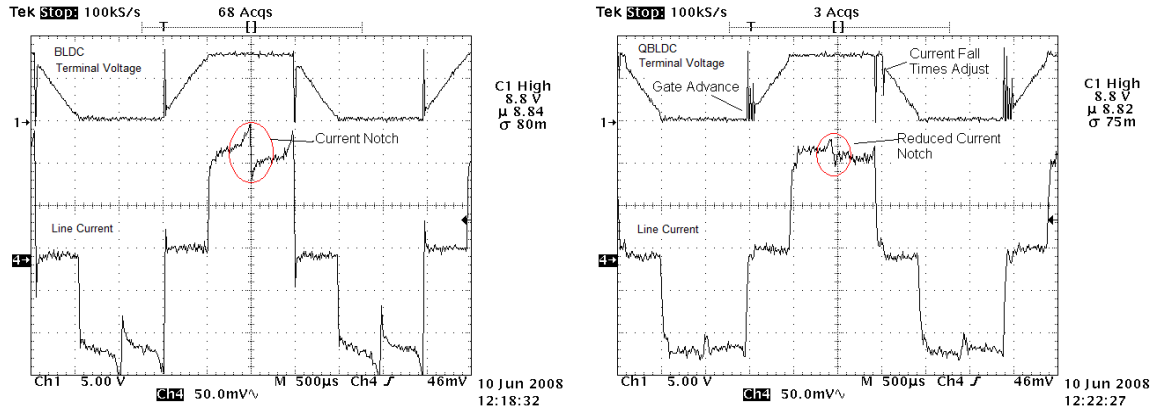

(b)

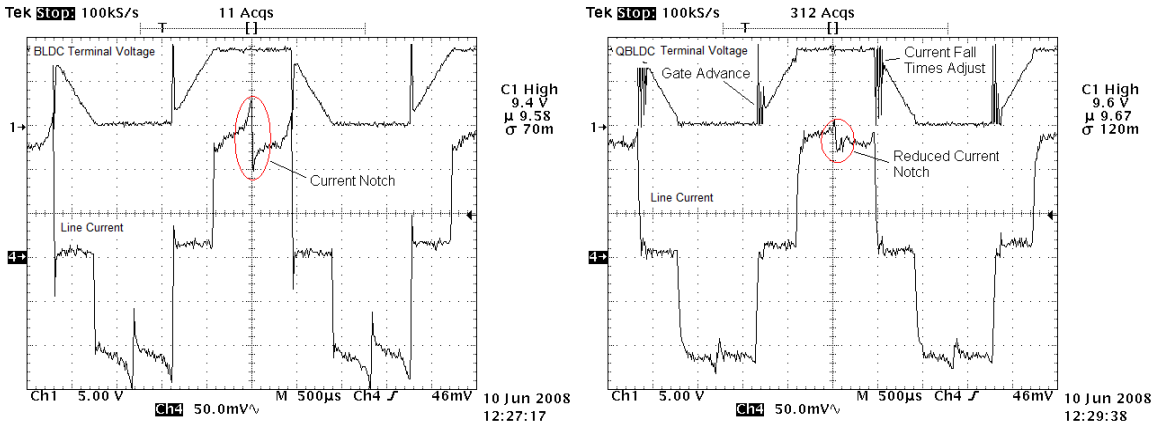

(c)

Figure 4.11 Current response for BLDC versus QBLDC under different voltages.

As an indicative measure of the torque, its effects on acoustics were measured. The sound levels emitted were measured and processed by a sound recording and analysis system shown as blocks in Figure 4.12. The acoustic noise measurements were made in an anechoic tank, with the microphone placed 40cm from the spindle motors that are installed in the hard disk bases.

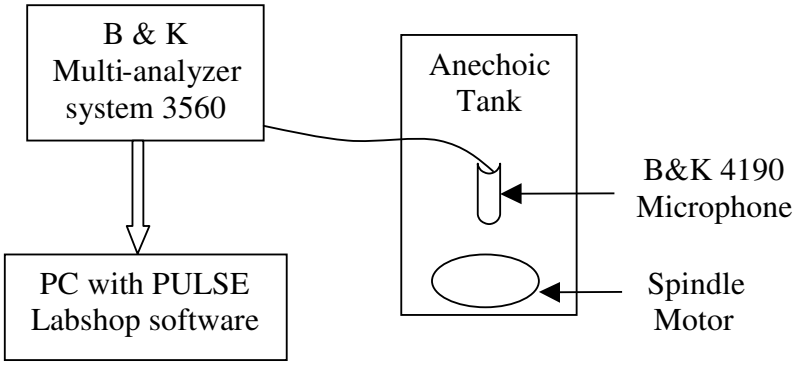

Figure 4.12 Acoustic noise measurement setup.

The acoustics noise was captured for HDD spindle at various speeds. Representative plots taken at speeds of 4800 rpm, 6000 rpm and 7200 rpm are provided in Figure 4.13. It can be seen that QBLDC reduces the acoustic peak amplitude by 0-15dB. This is intuitive as a spike is considered to be rich in frequencies and a reduction results in a reduction of noise frequency across a wide range. Acoustic noise was also measured for 2-platter and 4-platter HDDs. The plots are provided in Figure 4.14 and Figure 4.15 respectively. It can also be seen that for both cases, QBLDC has reduced the noise spikes observably, up to a maximum of 15dB.

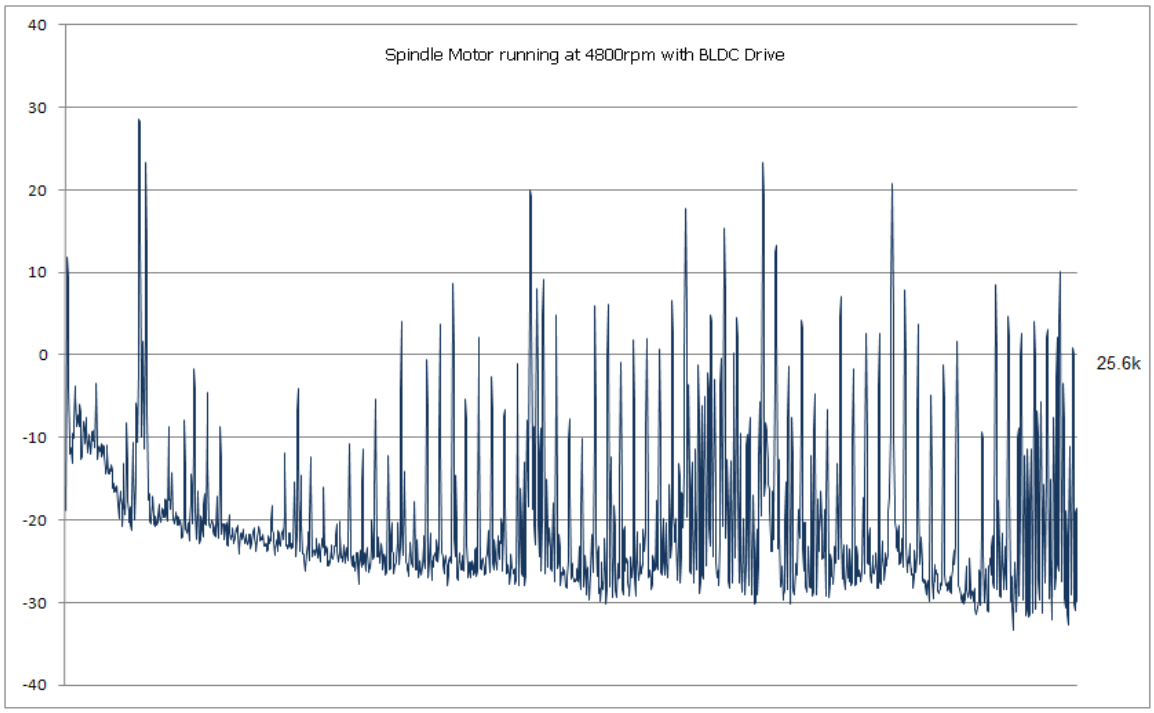
Spindle Motor running at 4800rpm with BLDC Drive
40
30
20
10
0
-10
-20
-30
-40
25.6k

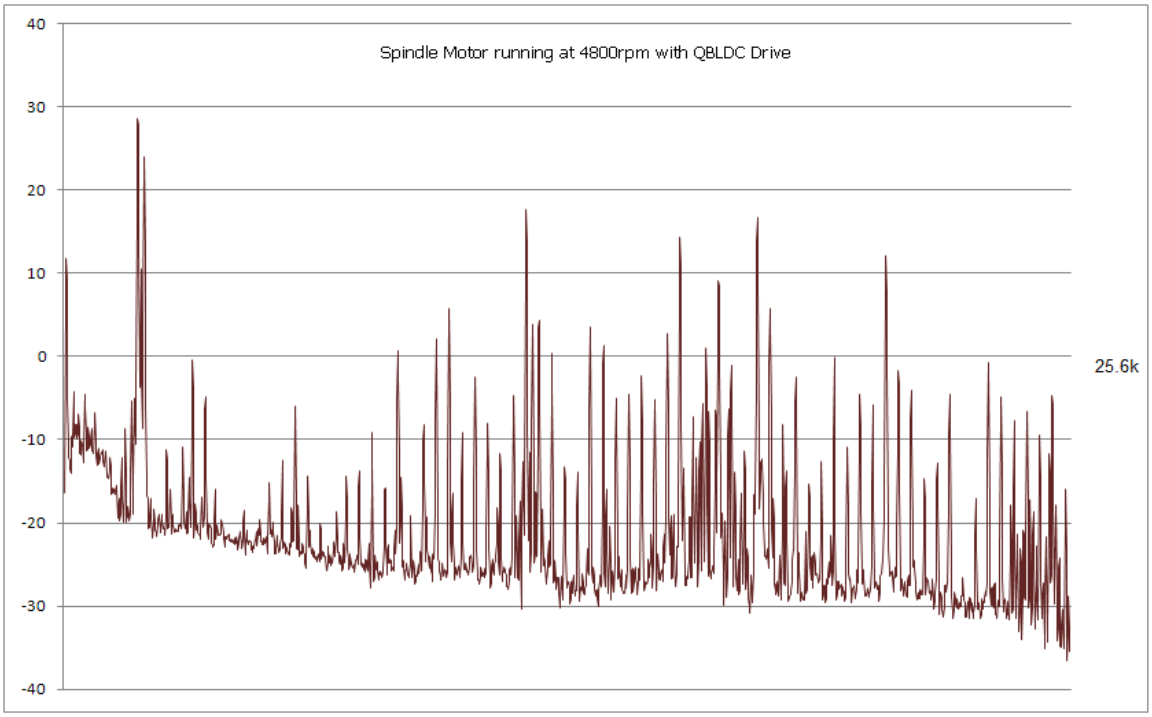
Spindle Motor running at 4800rpm with QBLDC Drive
40
30
20
10
0
-10
-20
-30
-40
25.6k

(a)

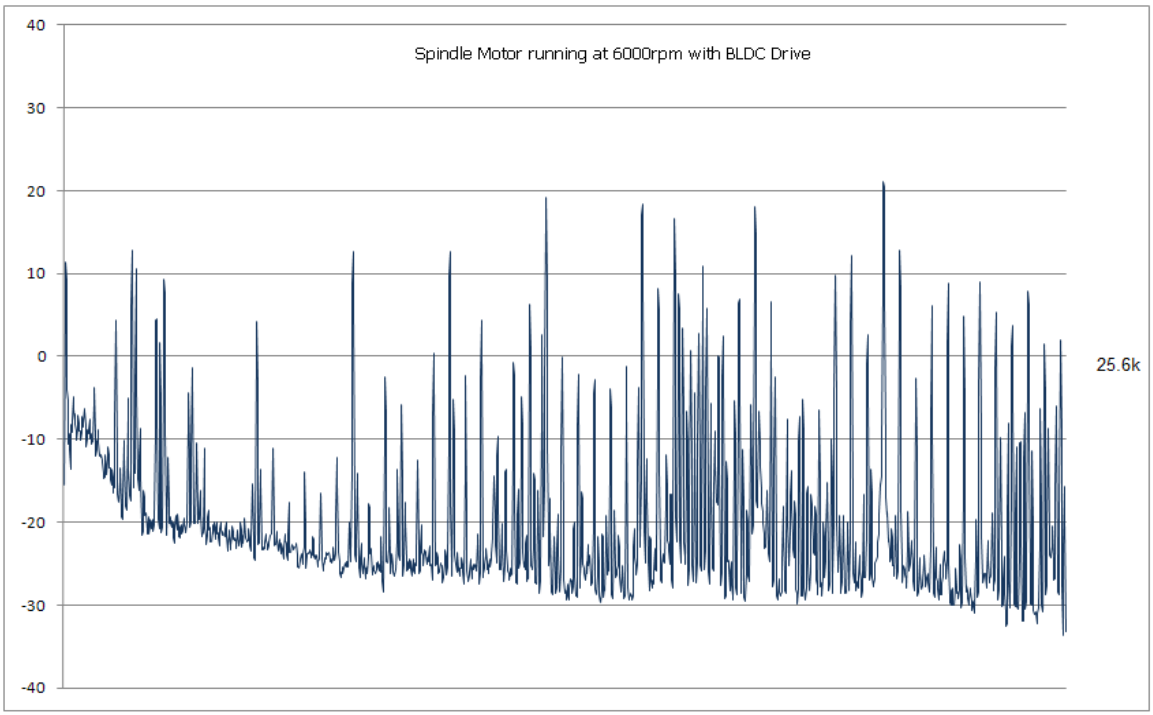
Spindle Motor running at 6000rpm with BLDC Drive
40
30
20
10
0
-10
-20
-30
-40
25.6k

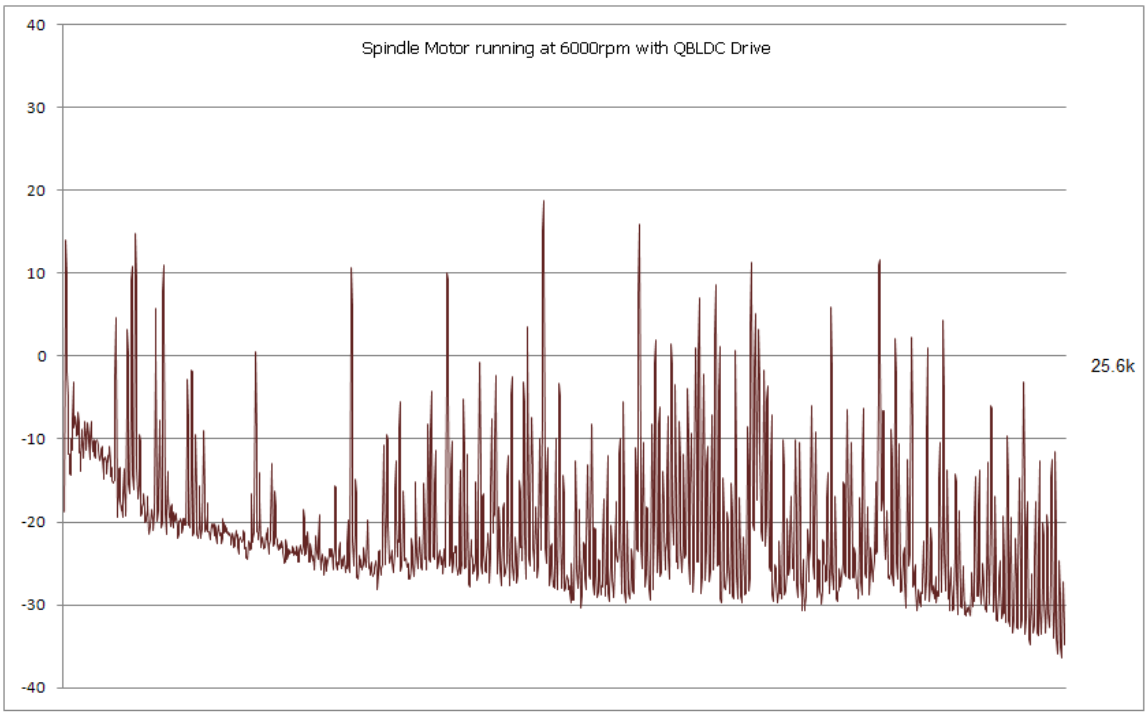
Spindle Motor running at 6000rpm with QBLDC Drive
40
30
20
10
0
-10
-20
-30
-40
25.6k

(b)

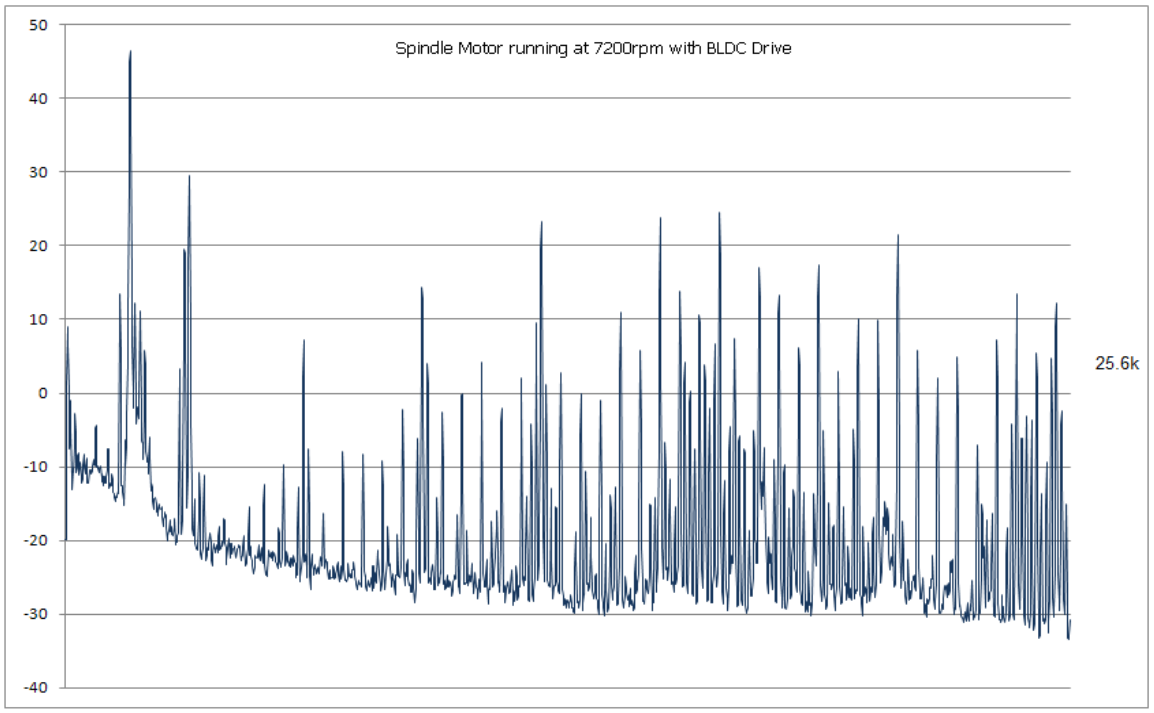

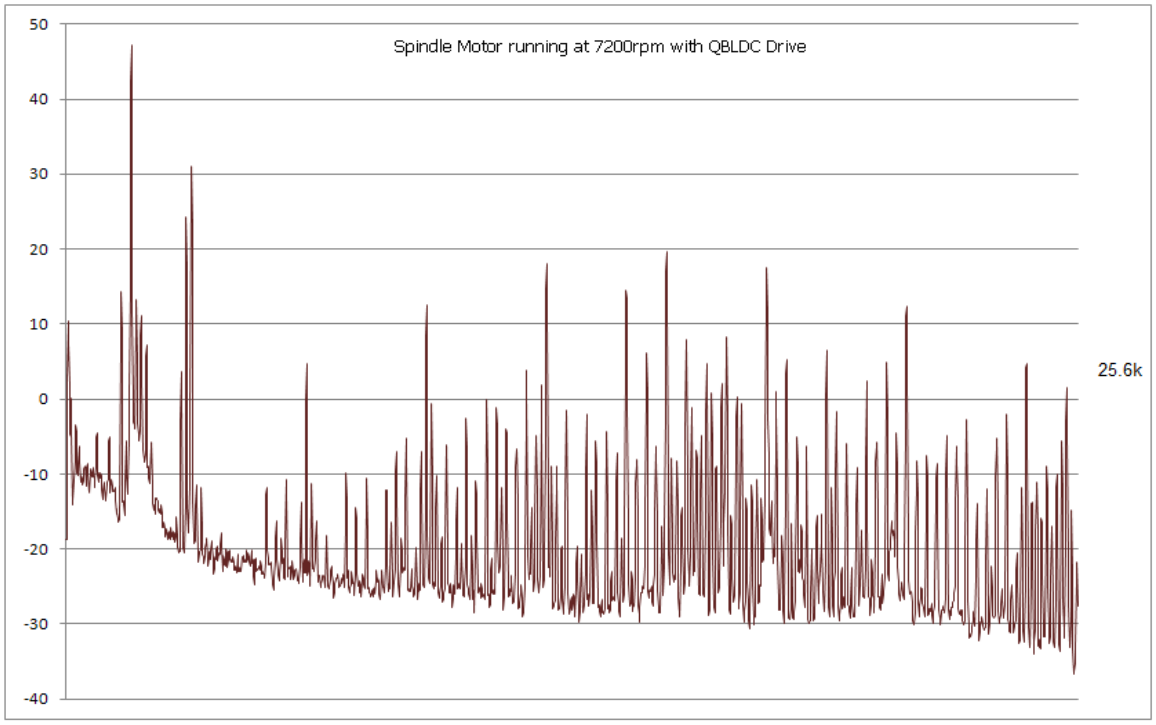

(c)

Figure 4.13 Acoustic plots for spindle motor running without load at (a) 4800 rpm (b) 6000 rpm (c) 7200 rpm.

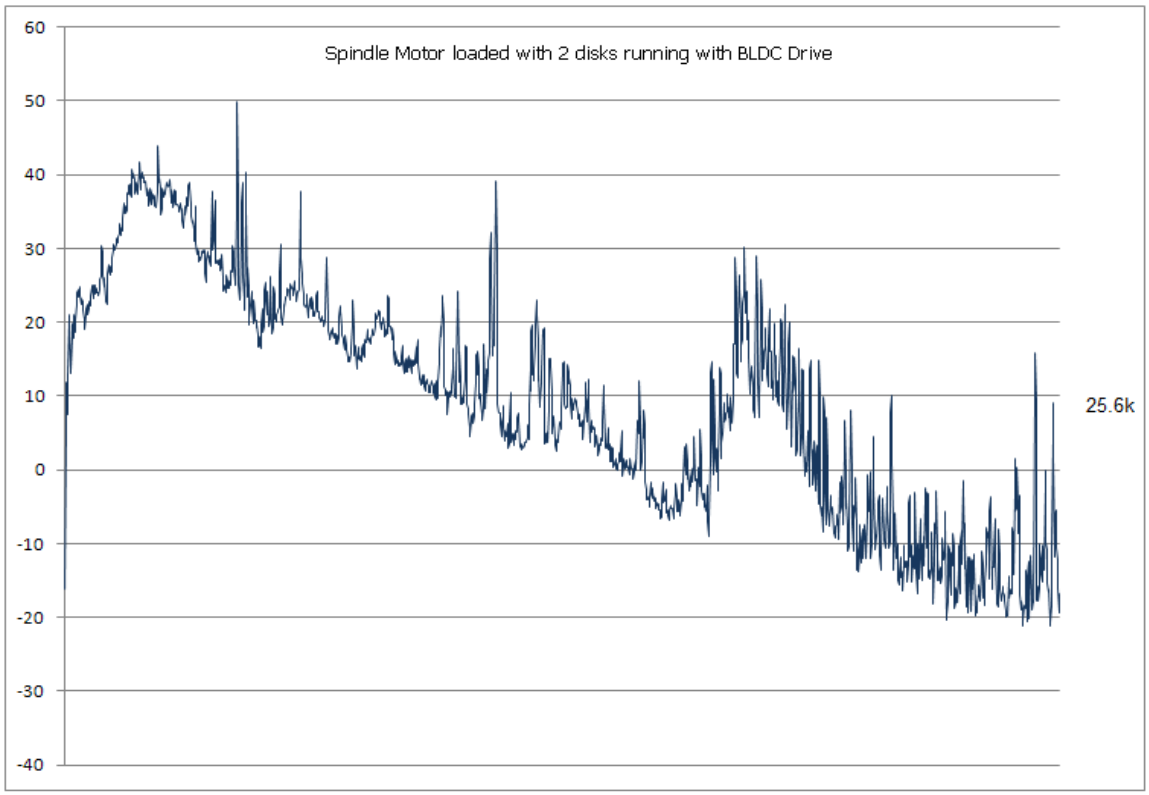

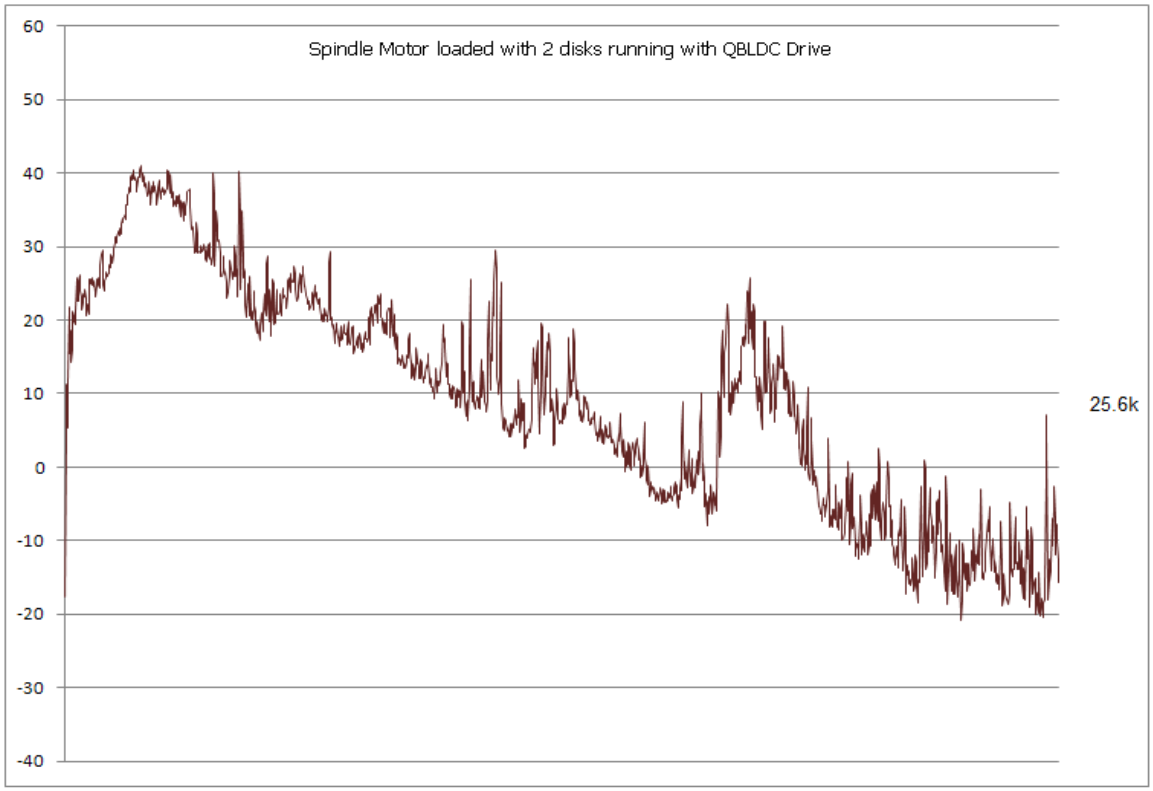

Figure 4.14 Acoustic comparison for spindle motor with 2 disks.

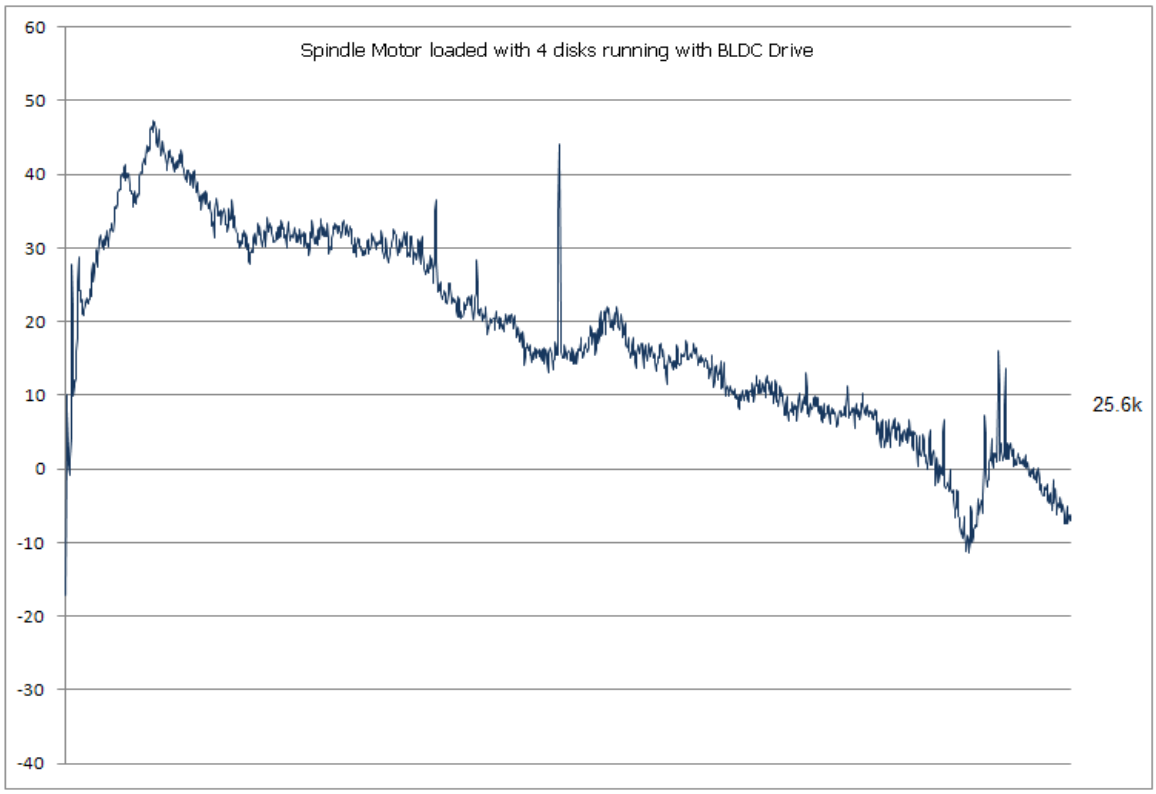

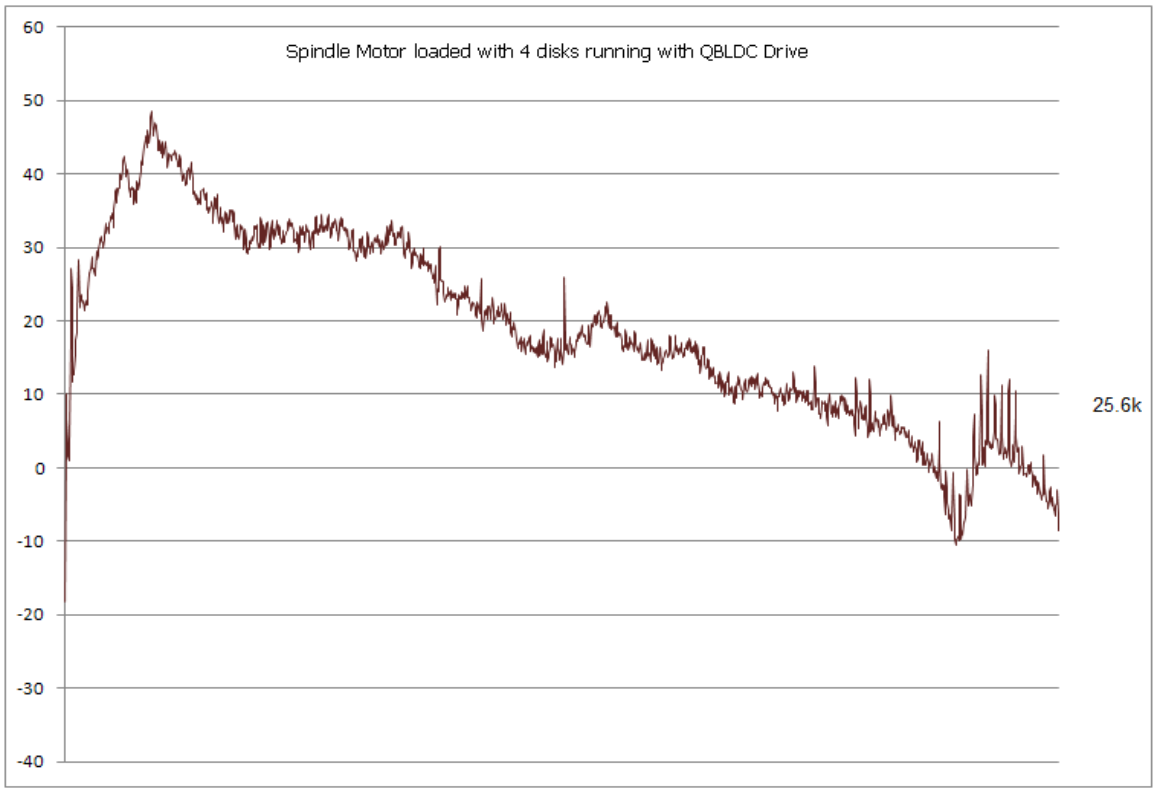

Figure 4.15 Acoustic comparison for spindle motor with 4 disks.

4.4 Conclusions

BLDC drive applied to PMSM brings about the advantages of robustness and simplicity, but unfortunately, suffered from severe torque pulsation, aggravated by commutation torque ripple. The root cause for this torque, namely presence of inductance and different back-EMF effects, has been derived and analyzed. In this chapter, a Quasi-BLDC drive utilizing current advance as well as varying voltage for rate of change of current matching was proposed. It was shown through simulation and confirmed by the experimental results that the commutation current spike was largely reduced. The torque ripple factor was significantly improved from 65% to 12.5% and the acoustic performance showed an overall improvement up to a maximum of 15dB.

CHAPTER 5. INITIAL ROTOR DETECTION THROUGH TERMINAL VOLTAGE

5.0 Introduction

Over the past two decades, significant efforts have been made in the research of PMSM drive without position sensors (sensorless drive) in view of reliability, robustness, compactness and cost. To implement a sensorless drive, a crucial aspect involves the starting of the motor from standstill. Schemes presented in published literature can be categorized into three types

1. Starting from open-loop,
2. Starting from aligned position, and
3. Starting from estimated position.

A brief introduction to these schemes has been presented in Section 1.2.4. Among these schemes, the last approach has drawn the greatest interest and attention [76-107]. Key to this approach is the utilization of inductance variation made distinct by armature reaction through pulse signal injection or sinusoidal carrier signal injection. However, this method relies heavily on acute armature reaction and is largely limited to interior PMSM. In this chapter, a unique pulse signal injection based method centering on

armature reaction phenomenon is presented. In particular, the dependency of current change rate in the stator winding on inductance, saturation of the iron, and the flux due to the position of the rotor's magnets are utilized. Several significant breakthroughs are achieved, namely,

1. Effects of armature reaction on motor inductance from positive and negative stator currents,
2. Unique amplification incremental motor inductance measurement method, and
3. Implementation through digitization simplification.

The method is effective as it does not rely on the absolute inductance value and does not require accurate current sensing. It can be used in many PMSM applications, even for surface mounted PMSM which has very weak salient effect.

The effects of armature reaction on the inductance due to both positive and negative currents are observed in this work. These effects, however, are difficult to be measured using indirect coarse current change rate approaches. This puts an application limitation on this phenomenon. In order to remove this limitation, a novel measurement method based on the third terminal voltage drop was conceived. The method makes intelligent use of the amplification of the current change rate in the measureable form of voltage drop. Highly accurate position precision of less than 15º can be achieved even on surface mounted PMSM. Further simplification is applied through digitalization for low cost implementation and position precision of less than 30º was obtained.

The proposed method is highly significant as it allows for a low cost, elegant and accurate initial rotor position detection method to be applied on surface mounted permanent magnet PMSM. In our analysis and experimentation, this method has been applied on a series of motors as well as 3-phase PMSM with surface mounted PM rotor. The inductance of this motor is small in the region of micro-henry and variation is weak. The successful application on this category of motor proved the effectiveness of the method.

5.1 Theory

In the detection of rotor position, a technique which makes use of the saturation effect of stator iron is proposed. In particular, the dependency of stator current change rate on inductance, saturation of the iron, and the flux due to the position of the rotor's magnets are utilized.

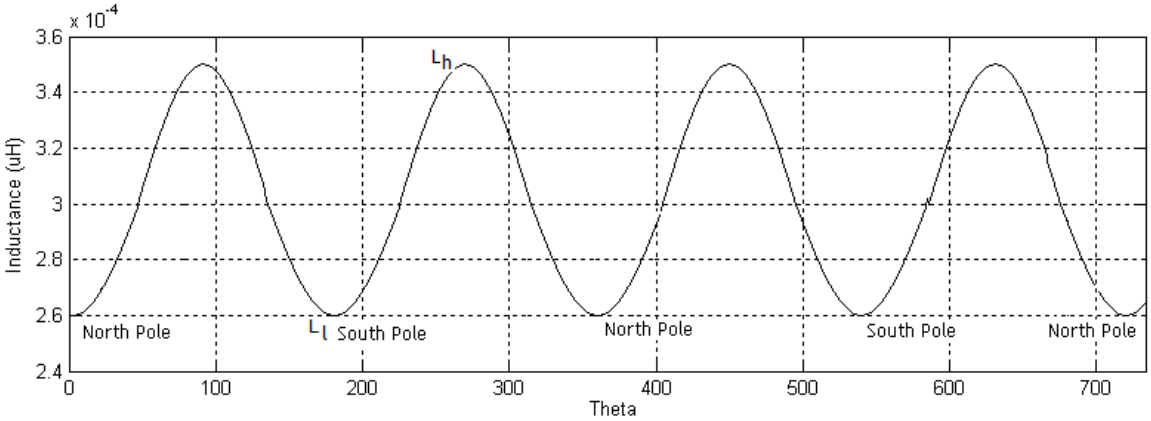

Figure 5.1 Motor positional inductance profile without saturation.

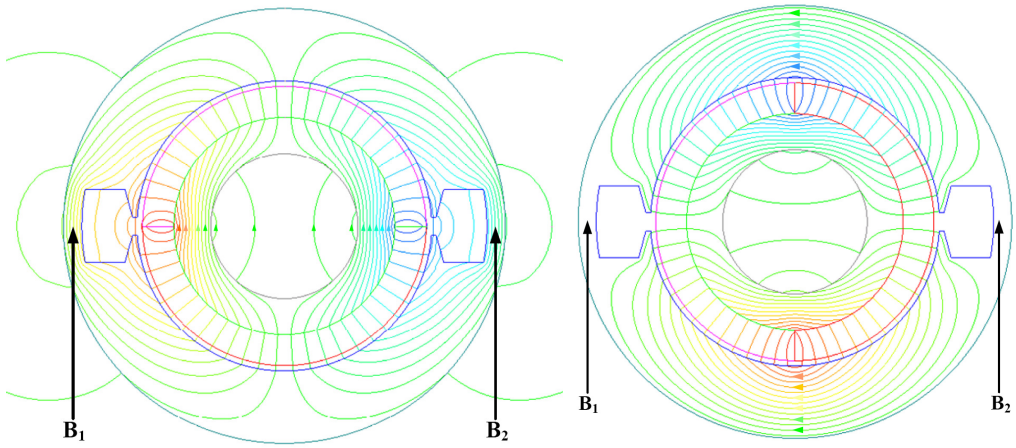

(a) Magnetic Field Distribution with Rotor at 0° position

(b) Magnetic Field Distribution with Rotor at 90° position

Figure 5.2 Magnetic field produced by permanent magnet on rotor.

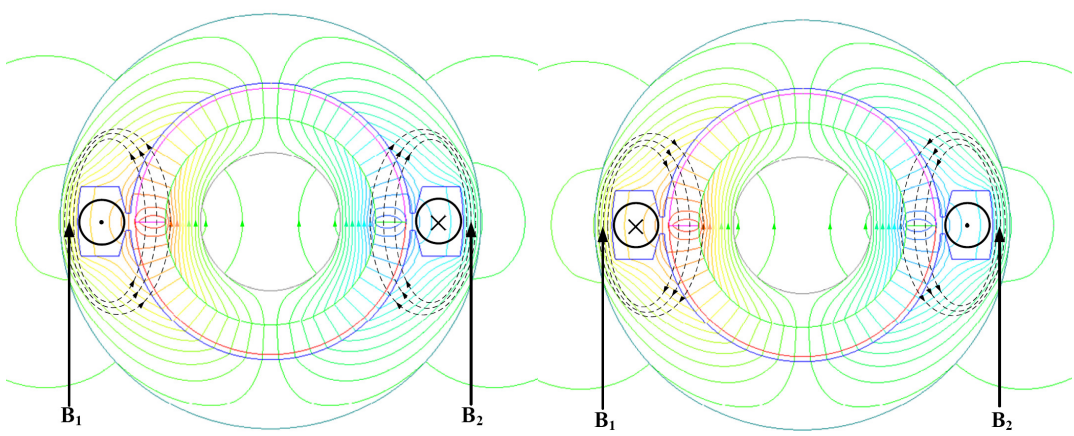

(a) Winding field is aligned with the rotor field at 0° position

(b) Winding field is opposite to the rotor field at 0° position

Figure 5.3 Influence of armature winding current to stator yoke at 0° position.

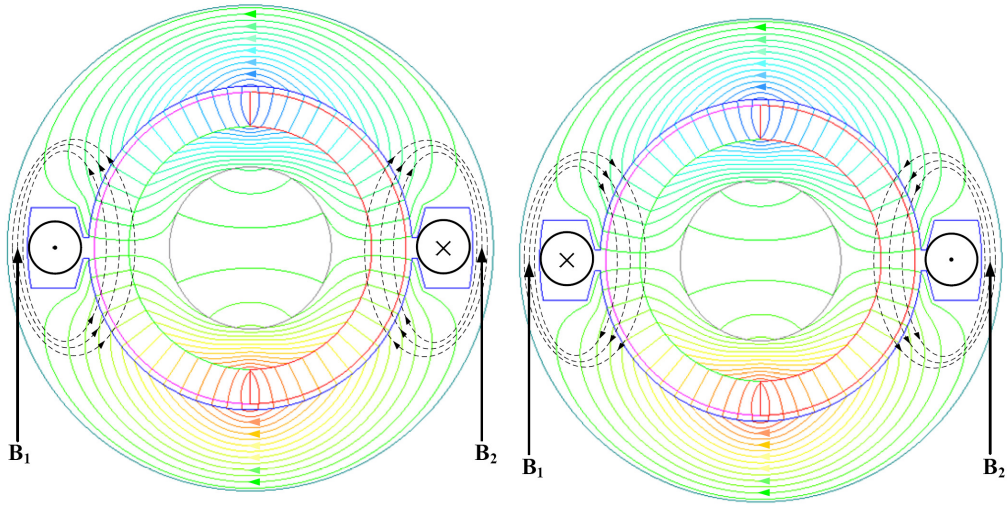

(a) Winding field is aligned with the rotor field at 90°

(b) Winding field is opposite with the rotor field at 90°

Figure 5.4 Influence of armature winding current to stator yoke at 90° position.

Figure 5.2 shows the magnetic field distributions of a motor when the rotor is located at 0° and 90° electrical degrees, respectively. For simplification, only one pair of slot is drawn. When the rotor is at 0° and 180°, the magnetic field generated by the permanent magnet of the rotor goes through the stator areas B_1 and B_2, and makes these areas saturated. On the other hand, when the rotor is at 90° and 270°, B_1 and B_2 are out of passage of the rotor field. Therefore, these areas are in linear state and their permeability is high. As a result, the inductance of the winding is not a constant and varies in the motor operation. The largest inductance value L_h, occurs at 90° and 270°, and lowest inductance value L_l occurs at 0° and 180°. When the rotor moves to other positions, the inductance changes smoothly, and the value is in the range of (L_l, L_h), and consists of two cycles in 360 electrical degrees, as illustrated in Figure 5.1. Therefore, through the variation of the inductance value, we can know whether the rotor is aligned or

perpendicular to the armature winding. However, it is not possible to perform meaningful position detection through the measurement of inductance or its associated effects as the relation between inductance and position is not unique due to the existence of two cycles within a 360º electrical degree.

In the presence of injected currents, the inductance profile is modified due to the effect of armature reaction. When the rotor is at 0°, if the current in the armature is positive, the field produced by the current also goes through B_1 and B_2, and the total field intensity in these areas will be further increased, and the saturation will be more pronounced as shown in Figure 5.3(a). Therefore, positive current further reduces the winding inductance. If the current is negative, as shown Figure 5.3(b), the total field going through B_1 and B_2 is reduced, and the saturation of these two areas will be slightly relaxed, and the winding inductance will be increased slightly. Thus, by differentiating the position where the inductance is the minimum with current injection, the position can be determined to be 0° or 180°. If the inductance under the positive current is smaller than the one under the negative current, the rotor is at 0°, and conversely, it is at 180°. These phenomenons are shown in Figure 5.5.

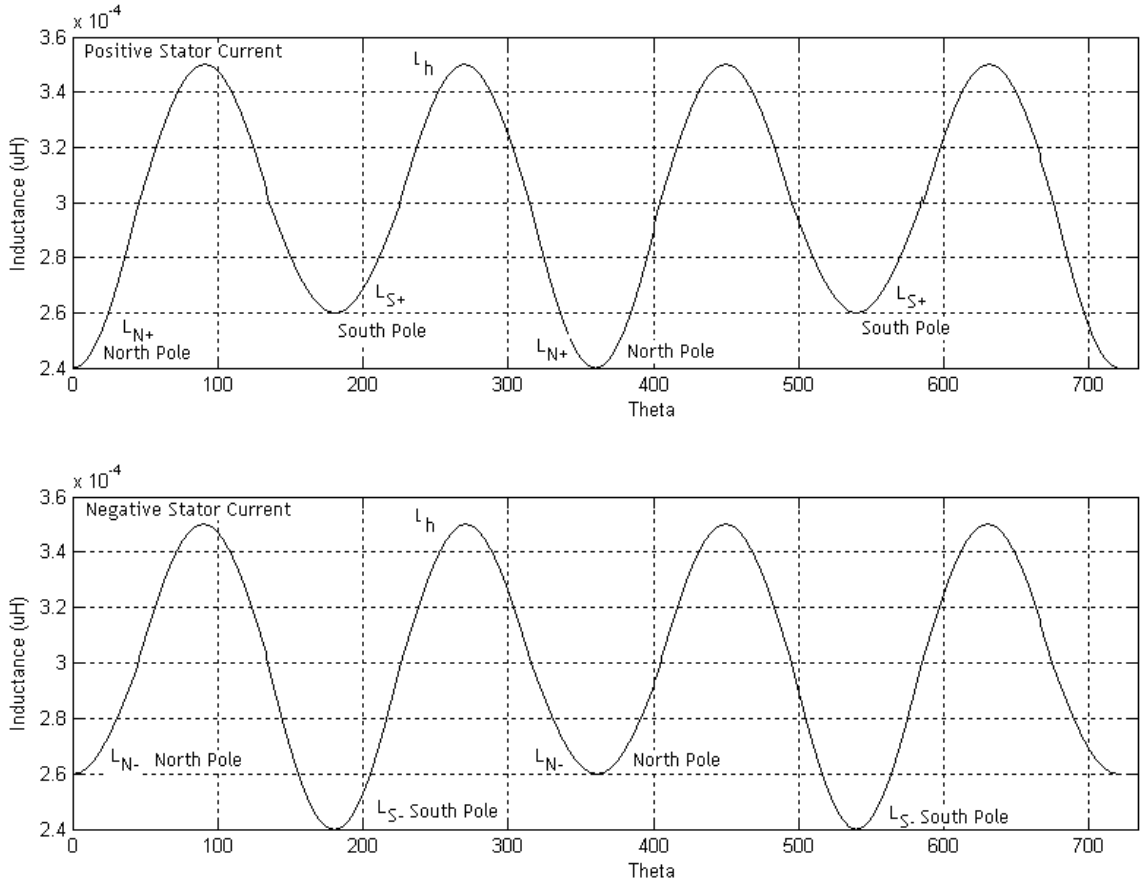

Figure 5.5 Motor positional inductance profile with saturation.

This strategy offers a new dimension. Instead of a direct measurement of inductance at north magnetic pole with positive injected current, L_{N+}, or inductance at south magnetic pole with positive injected current, L_{S+}, the differential inductance of L_{N+}-L_{N-} (inductance at north magnetic pole with negative injected current) can be utilized for north magnetic polarity detection. Similarly, for south magnetic polarity detection, the differential inductance of L_{S+}-L_{S-} can be utilized.

The current change rate in the stator is inversely proportional to the inductance. For instance, with magnetic north pole alignment, the rise time for a positive stator

current would be shorter than the rise time for a negative stator current. Conversely, with magnetic south pole alignment, the rise time for a negative stator current would be shorter than the rise time for a positive stator current. The absolute rise time pertaining to a north or south pole is no longer crucial but the relative rise time or polarity of the relative rise time would be sufficient for the determination of magnetic polarity. In conjunction with this strategy, taking a 3 phase inter-relationship, collating the inductance profiles under different phase currents as shown in Figure 5.6, by detection of the inductances or its corresponding rise time, a full 360° detection is possible.

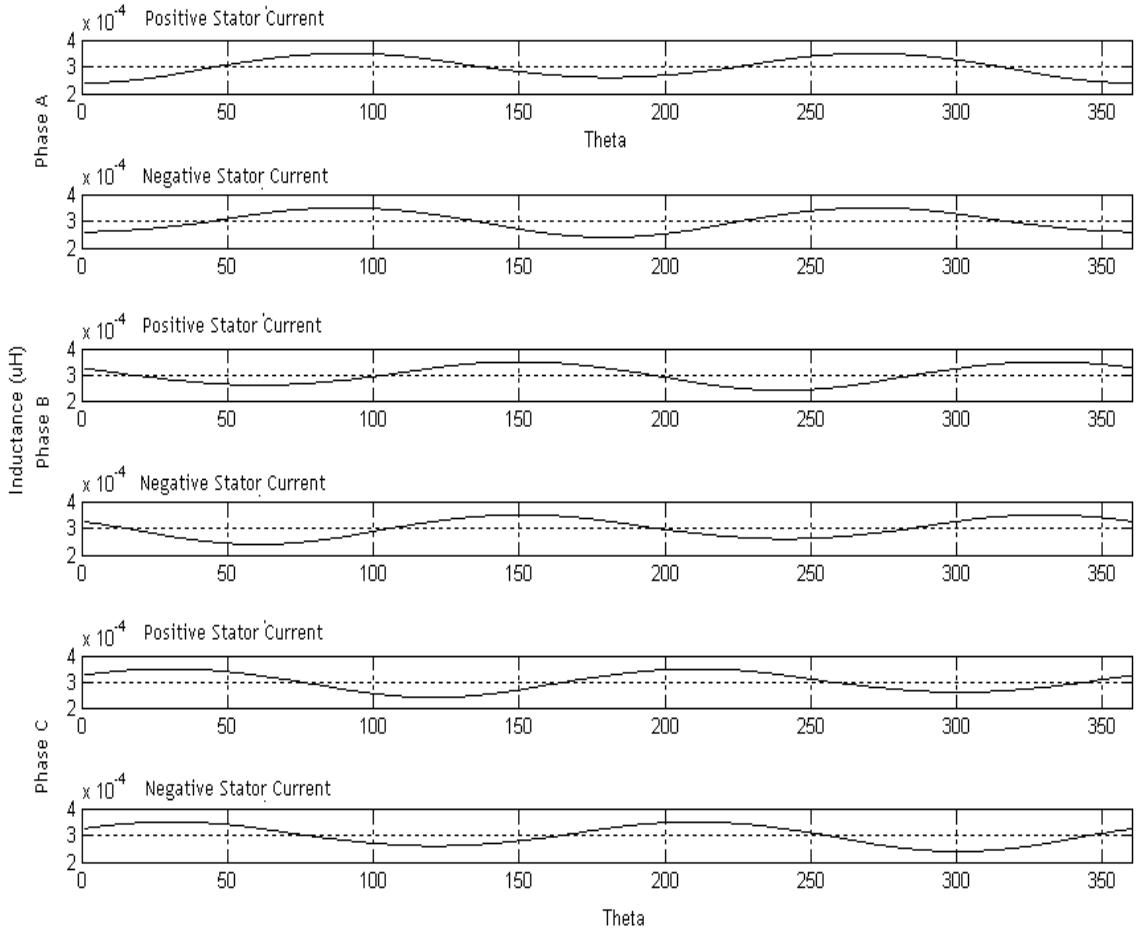

Figure 5.6 Motor positional phase inductance profile with saturation.

5.2 Methodology

5.2.1 Methodology I

Considering the theory described in 5.1, current change rate can be measured using sensing resistor at the DC link while injecting voltage through V_{AN}, V_{BN} or V_{CN}. However, this requires the neutral line to be available. An alternative solution would be to inject the voltage through V_{AB}, V_{BC} or V_{CA}. The current change rate would then be decided by the line to line inductance. For example, if the injection is through terminals A and B, the inductance would be $L_{A+}+L_{B-}$ (or L_{AB}) for positive V_{AB} and $L_{A-}+L_{B+}$ (or L_{BA}) for negative V_{AB} (or positive V_{BA}). The following figure shows the line to line inductance for all three line inductances.

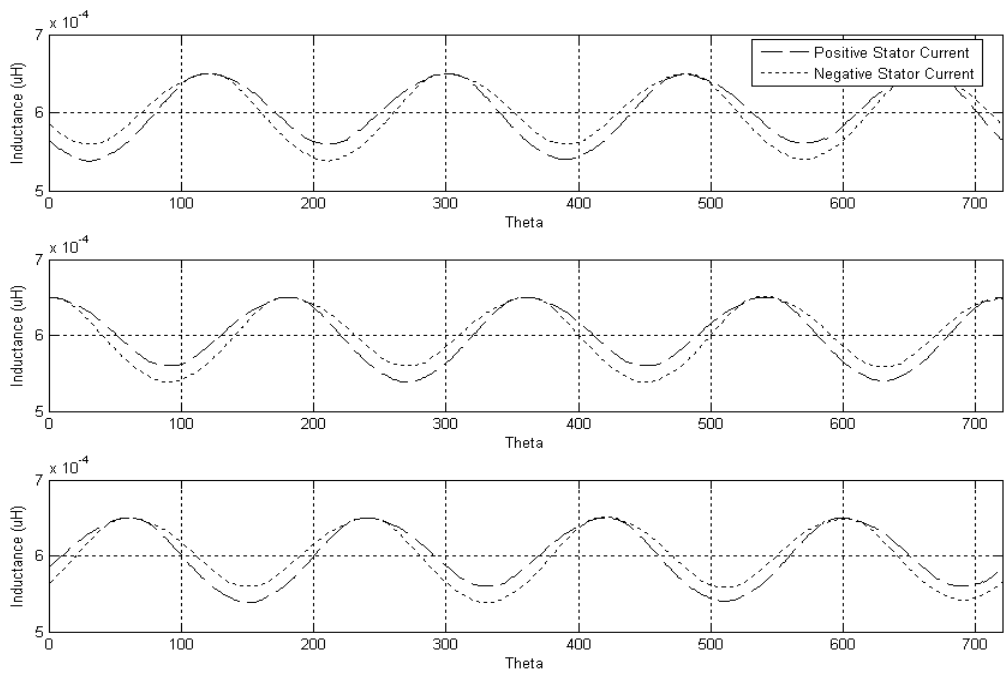

Figure 5.7 Line-line inductance.

Considering injected currents into phase A and out of phase B with phase C floating,

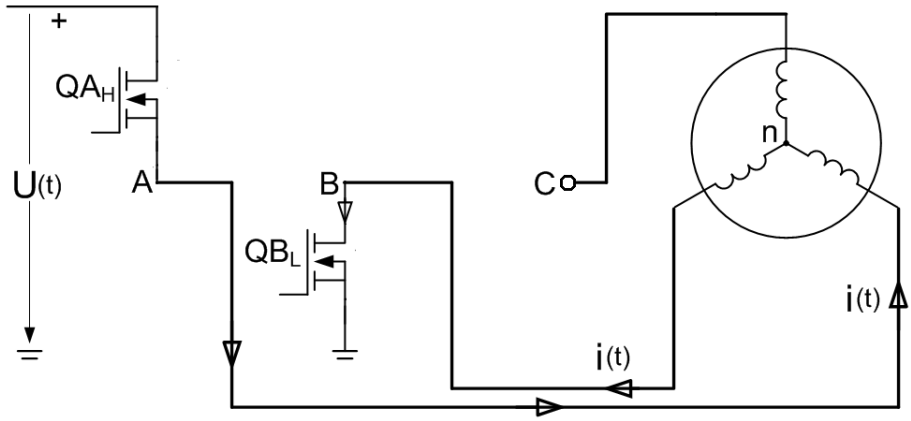

Figure 5.8 Motor drive schematic for positive line-line voltage.

$$v_{AB} = 2i_{ab}R + L_{AB}\frac{di_{ab}}{dt}, \tag{5-1}$$

where $L_{AB} = L_{A+} + L_{B-}$. Solving for the current,

$$i_{ab} = i_{dclink} = \frac{V_{dd}}{2R} - \frac{V_{dd}}{R}e^{-\frac{2R}{L_{AB}}t}. \tag{5-2}$$

Alternatively, considering injected currents out of phase A and into phase B,

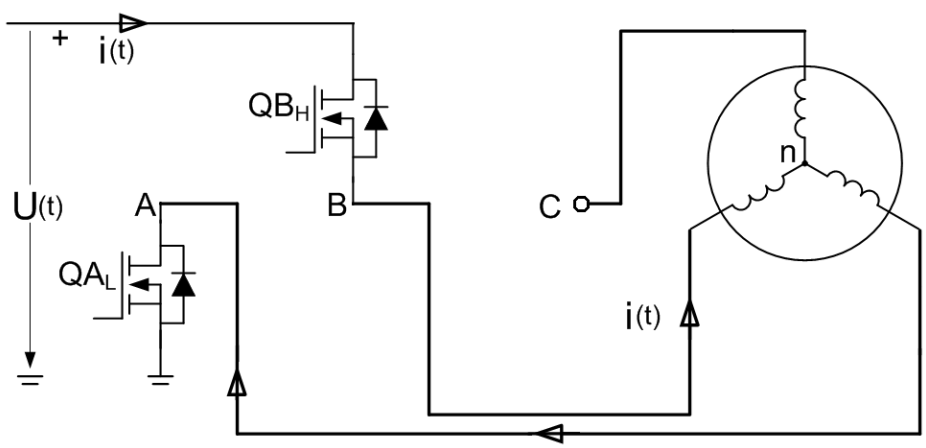

Figure 5.9 Motor drive schematic for negative line-line voltage.

$$v_{AB} = 2i_{ab}R + L_{BA}\frac{di_{ab}}{dt}, \tag{5-3}$$

where $v_{AB} < 0$, $i_{ab} < 0$ and $L_{BA} = L_{A-} + L_{B+}$.

$$i_{dclink} = \frac{V_{dd}}{2R} - \frac{V_{dd}}{R}e^{-\frac{2R}{L_{BA}}t}. \tag{5-4}$$

Thus, it can be seen that the dc link current would be profiled according to the line-line inductance. Figure 5.10 shows the AB line-line inductance.

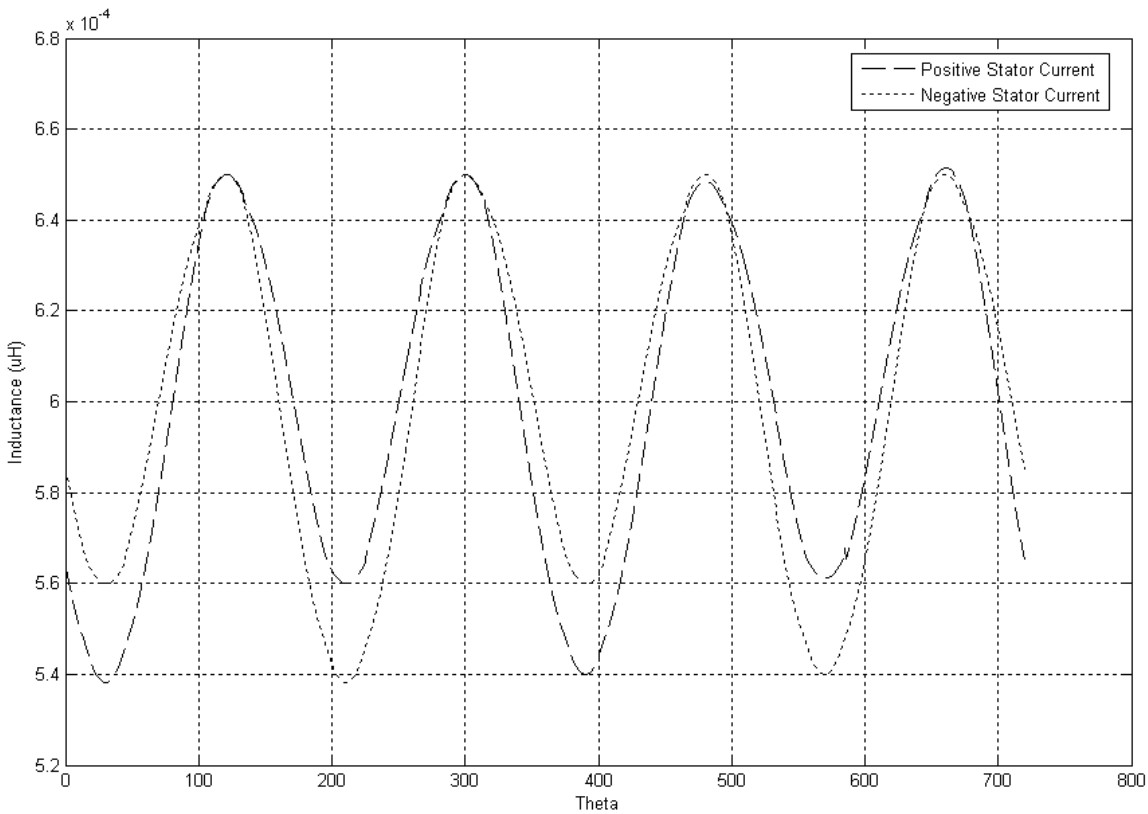

Figure 5.10 Line-line inductance

From Figure 5.10, this implies that it is possible to determine the position by collating the profile of all three phases. While this appears theoretically possible, practically it might be difficult to detect the differences in the dc link current. Assuming at the position of

36˚, where we have the largest inductance difference, we should obtain the largest difference in current change rate. The plot for a typical HDD spindle motor is simulated and shown in Figure 5.11.

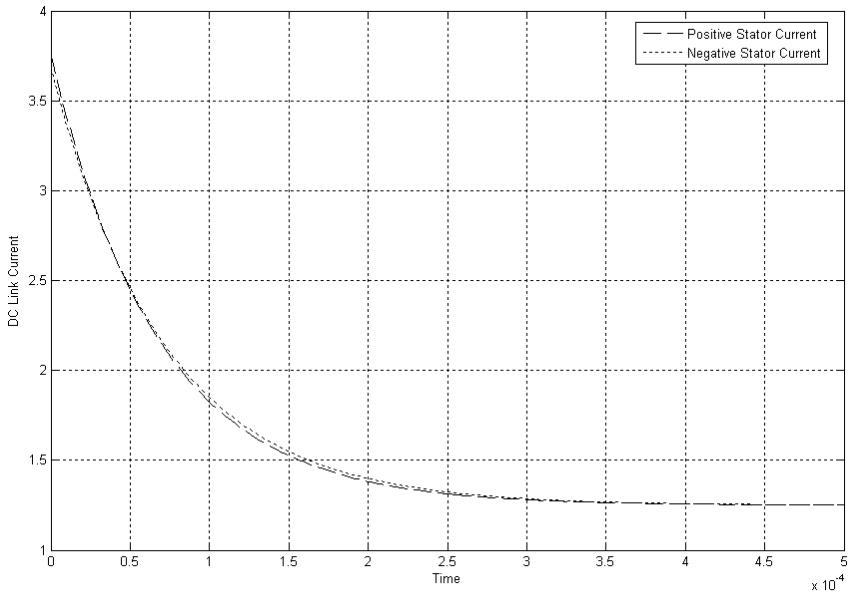

Figure 5.11 DC link current response for positive and negative stator current.

It can be seen that the difference might be difficult to be detected on the implementation level and largely dependent to the accuracy of the implemented system.

5.2.2 Methodology II

The previous proposed method, while shown to be effective in theory, lacks the practicality in HDD and requires the addition of a resistor across the dc link and thus reduces the efficiency and effectiveness of the BLDC drive. Apart from this, it is

necessary to measure the rise time and fall time of the currents accurately which is sensitive to noise and requires a relatively larger inductance difference. To counter these concerns, a novel design is applied into the theory. Observing the voltage equation,

$$v_{AB} = 2i_{ab}R + L_{AB}\frac{di_{ab}}{dt}, \tag{5-5}$$

It would be ideal if the voltage $L_{AB}\frac{di_{ab}}{dt}$ can be measured as the voltage level would provide a representative measure of the rise time. The equation can be expressed as

$$\begin{cases} v_{AB} = i_{ab}R + L_{A+}\frac{di_{ab}}{dt} + i_{ab}R + L_{B-}\frac{di_{ab}}{dt} \\ v_{AB} = v_{AN} + v_{NB} \end{cases}, \tag{5-6}$$

where

$$\begin{cases} v_{AN} = i_{ab}R + L_{A+}\frac{di_{ab}}{dt} \\ v_{NB} = i_{ab}R + L_{B-}\frac{di_{ab}}{dt} \end{cases}. \tag{5-7}$$

Since terminal B is grounded and terminal C is floated,

$$v_{NB} = v_{N0} = v_{C0}, \tag{5-8}$$

where v_{C0} is the voltage level measurable from terminal C. However, v_{C0} contains both the inductive and resistive voltage terms. Further insights can provide opportunities for exploitation,

$$\begin{cases} v_{C0,AB} = i_{ab}R + L_{B-}\frac{di_{ab}}{dt} \\ v_{C0,AB} = \frac{V_{dd}}{2} - V_{dd}e^{-\frac{2R}{L_{AB}}t} + L_{B-}\left(-\frac{V_{dd}}{R}\right)\left(-\frac{2R}{L_{AB}}\right)e^{-\frac{2R}{L_{AB}}t} \\ v_{C0,AB} = \frac{V_{dd}}{2} - V_{dd}\left(1 - \frac{2L_{B-}}{L_{AB}}\right)e^{-\frac{2R}{L_{AB}}t} \end{cases}. \tag{5-9}$$

Alternatively, considering injected currents out of phase A and into phase B,

$$\begin{cases} v_{C0,BA} = -i_{ab}R - L_{A-}\dfrac{di_{ab}}{dt} \\ v_{C0,BA} = \dfrac{V_{dd}}{2} - V_{dd}e^{-\frac{2R}{L_{BA}}t} - L_{A-}\left(\dfrac{V_{dd}}{R}\right)\left(-\dfrac{2R}{L_{BA}}\right)e^{-\frac{2R}{L_{BA}}t} \\ v_{C0,BA} = \dfrac{V_{dd}}{2} - V_{dd}\left(1 - \dfrac{2L_{A-}}{L_{BA}}\right)e^{-\frac{2R}{L_{BA}}t} \end{cases} \quad (5\text{-}10)$$

Comparing $v_{C0,AB}$ and $v_{C0,BA}$, it can be seen that apart from different time constants, it is modulated by a factor of $\frac{L_{B-}}{L_{AB}}$ and $\frac{L_{A-}}{L_{BA}}$, the result of $L\frac{di}{dt}$. From the plot, it can be seen that these factors exhibit a similar inter-relationship with the inductance profile. However, this inter-relationship is amplified thousands of times.

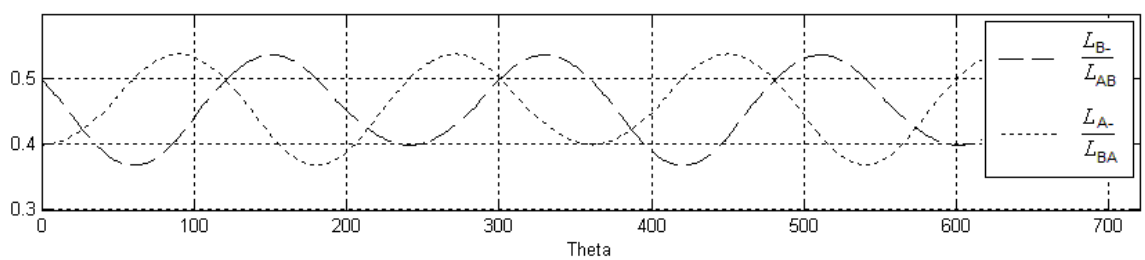

Figure 5.12 Modulating factor.

As an illustration, the voltage waveform seen at the floated terminal at position 75˚ is shown in Figure 5.13.

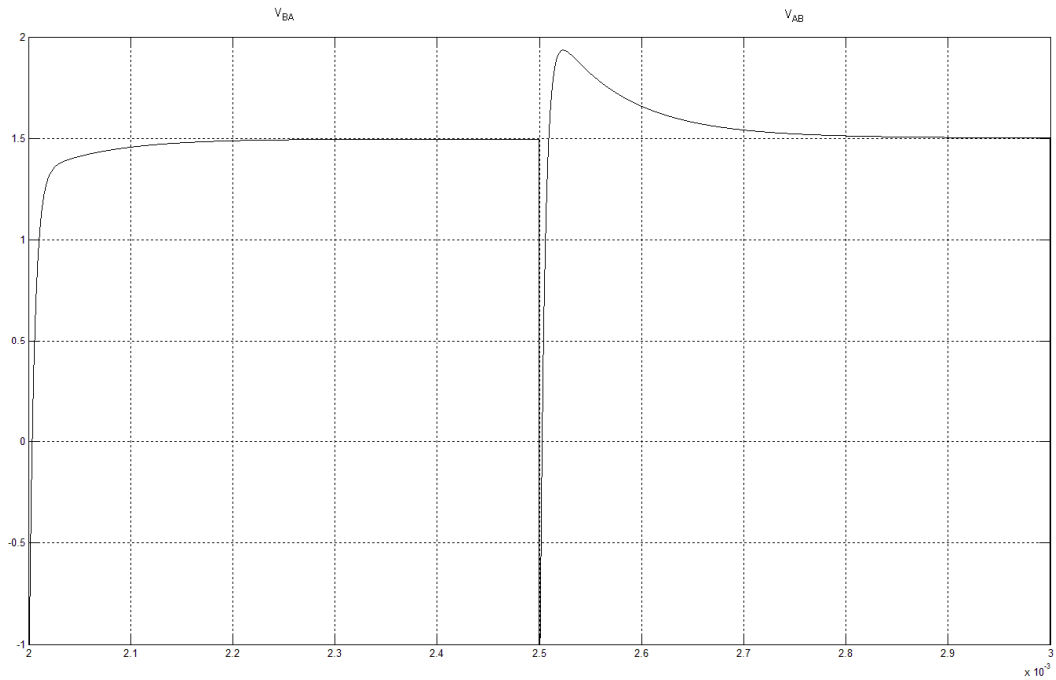

Figure 5.13 Terminal C voltage under phase AB pulses.

It can be seen that for this position, the signs of the waveform are different and the profile is significantly different due to the presence of $L\frac{di}{dt}$. The plots for various positions are shown. In the plots, V_{AB} means a positive current flowing into terminal A, and out of terminal B, and terminal C is floated. The same principle can be similarly applied for V_{AC}, V_{AB}, V_{BA}, V_{BC} and V_{CB}.

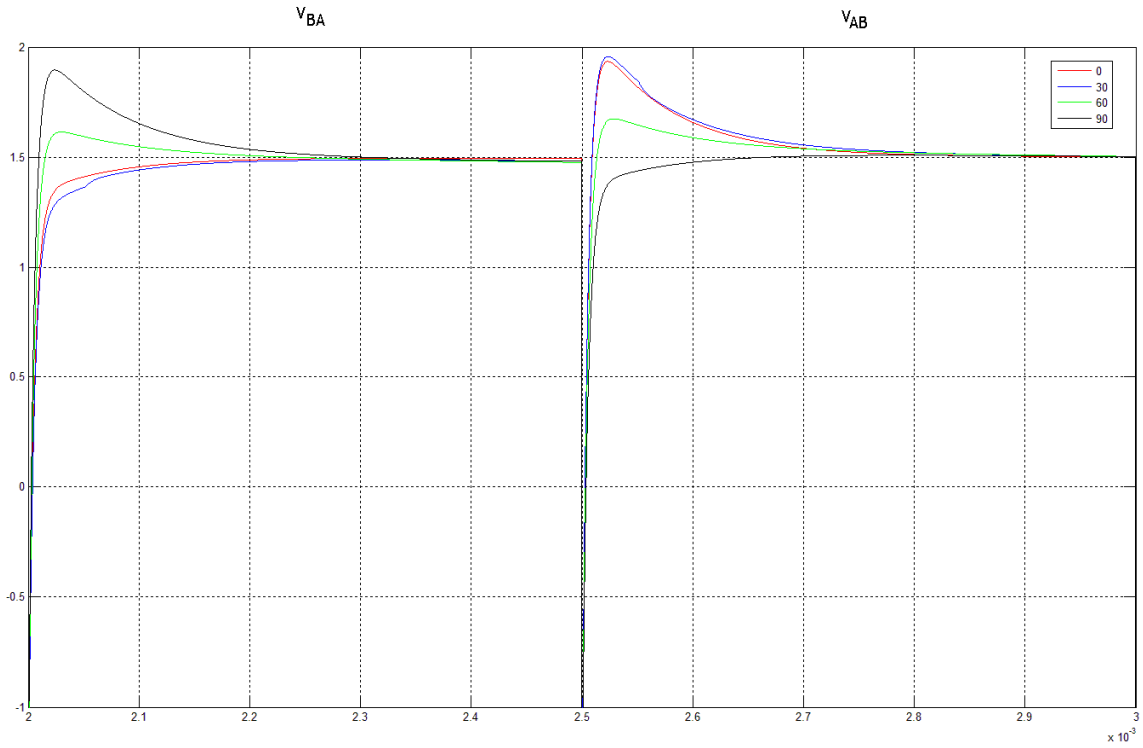
V_{BA}
V_{AB}
0
30
60
90
2
1.5
1
0.5
0
-0.5
-1
2
2.1
2.2
2.3
2.4
2.5
2.6
2.7
2.8
2.9
3
x 10^-3

(a)

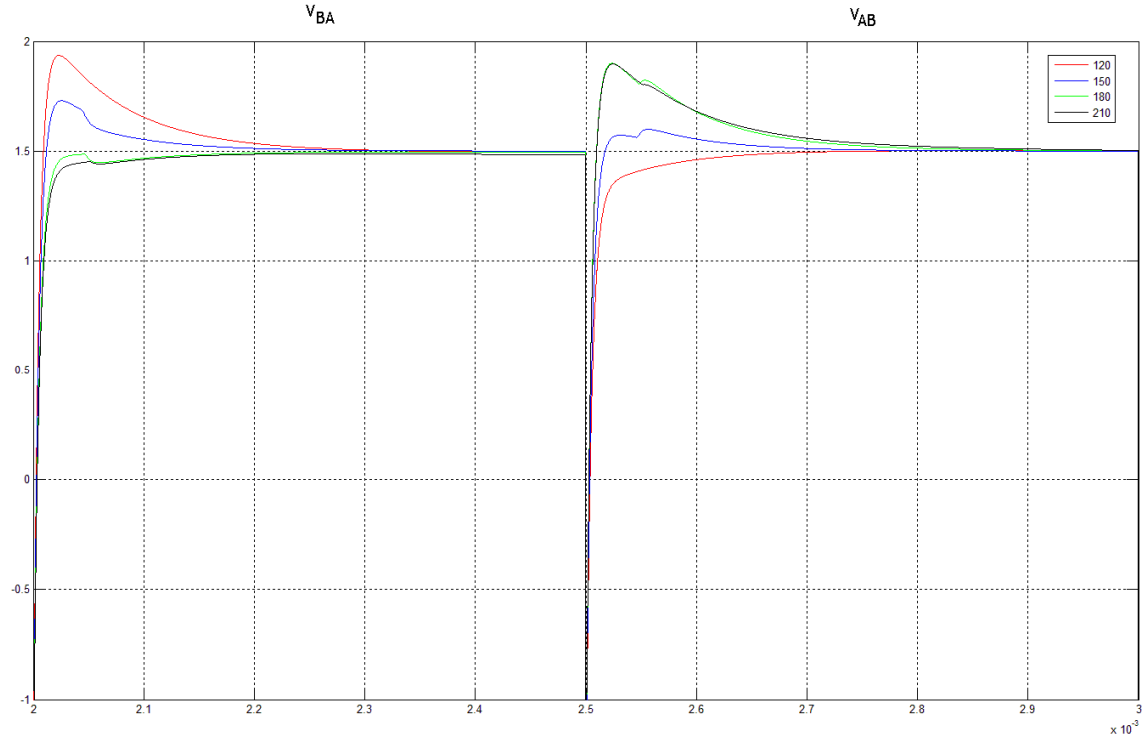
V_{BA}
V_{AB}
120
150
180
210
2
1.5
1
0.5
0
-0.5
-1
2
2.1
2.2
2.3
2.4
2.5
2.6
2.7
2.8
2.9
3
x 10^-3

(b)

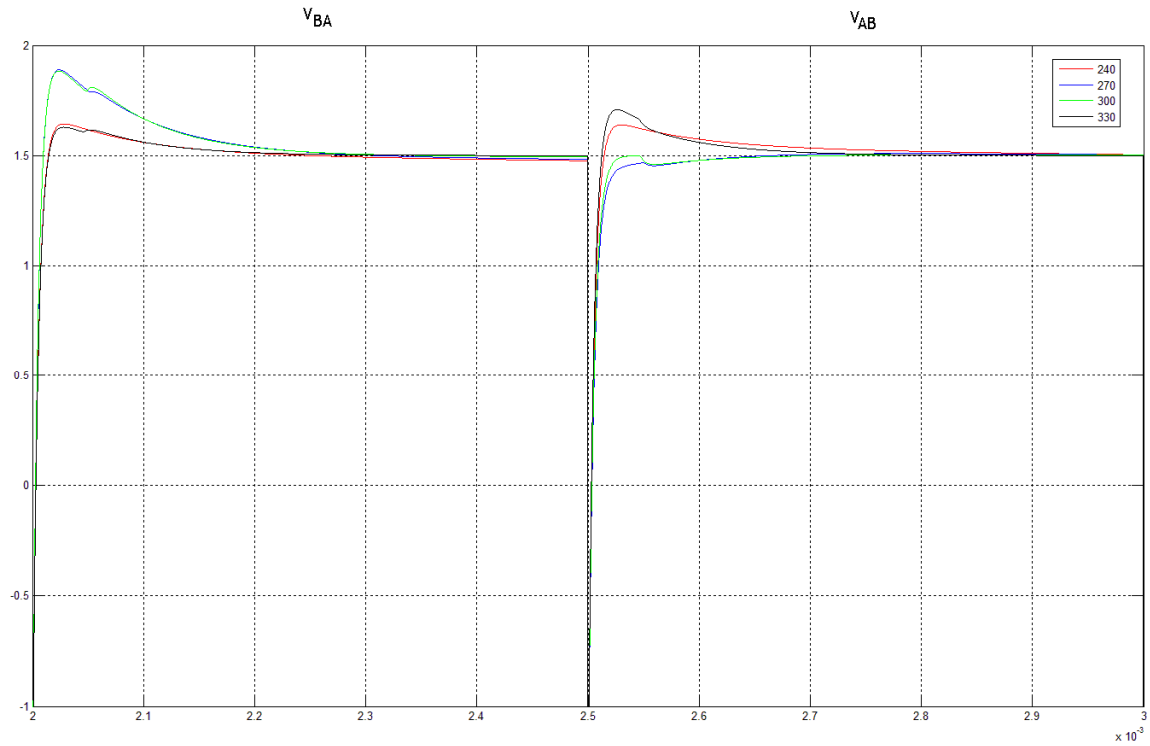

(c)

Figure 5.14 Terminal C voltage under phase AB pulses for various positions.

The plots seen are unique to its positions. Additional accuracy can be obtained if collectively pulses are injected into BC and CA phases. The responses are similarly shaped in accordance to the inductance ratios. The inductance ratio plots for $\frac{L_{B-}}{L_{AB}}$ and $\frac{L_{A-}}{L_{BA}}$, $\frac{L_{C-}}{L_{BC}}$ and $\frac{L_{B-}}{L_{BC}}$, $\frac{L_{C-}}{L_{CA}}$ and $\frac{L_{A-}}{L_{CA}}$ are shown respectively.

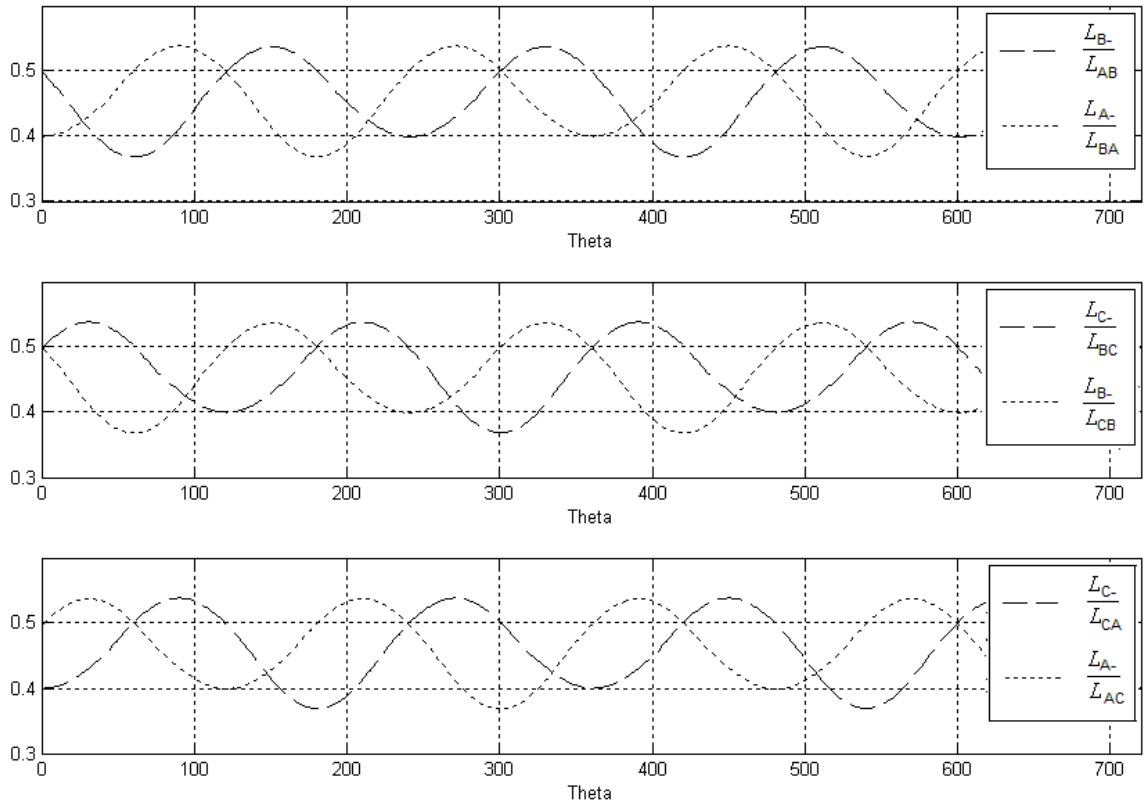

Figure 5.15 Modulating factors for all three phases

It can be seen that the ratios are interestingly unique which implies the corresponding voltages observed at the floating terminals would be unique. Figure 5.16 to Figure 5.18 show the different terminal voltages at various positions. Thus, through the detection of the floating terminal voltages, the rotor position can be detected.

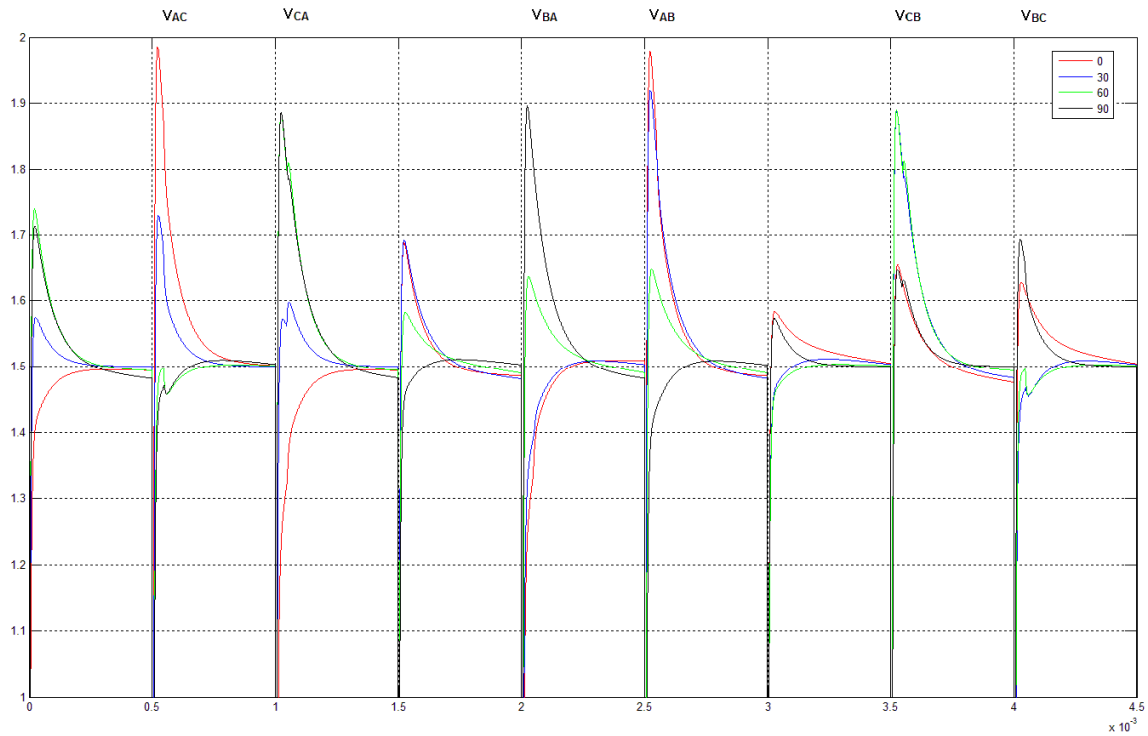

Figure 5.16 Plots of terminal voltages for 0° - 90°.

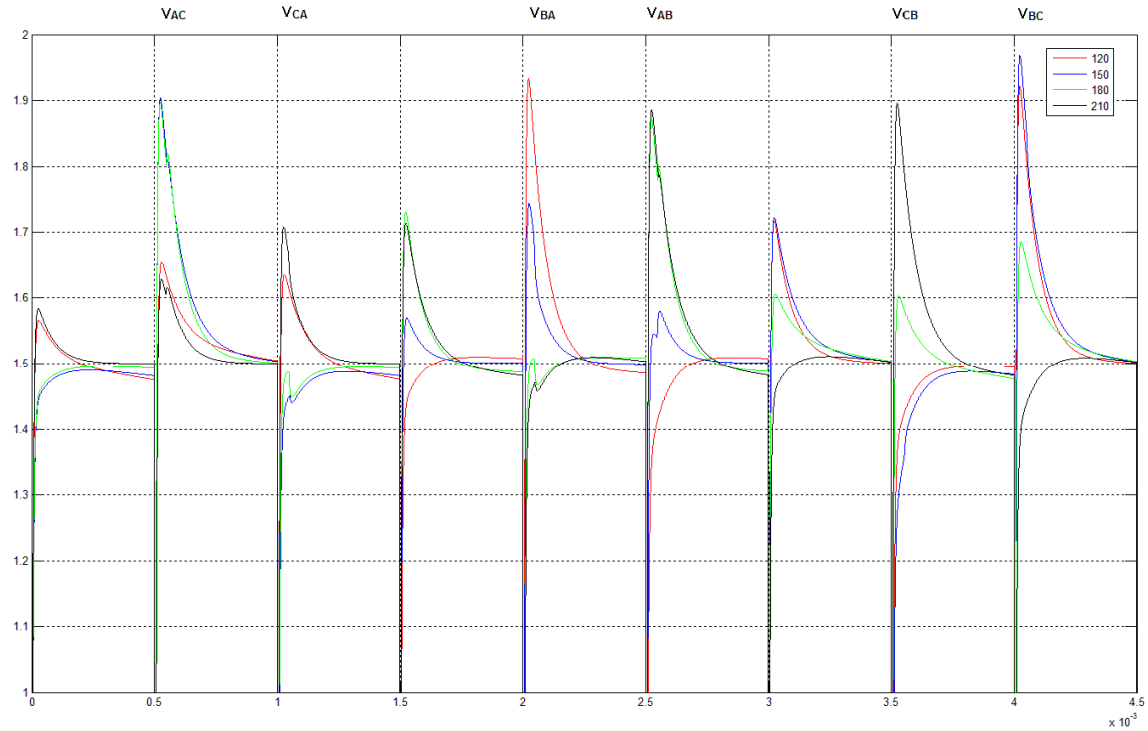

Figure 5.17 Plots of terminal voltages for 120° - 210°.

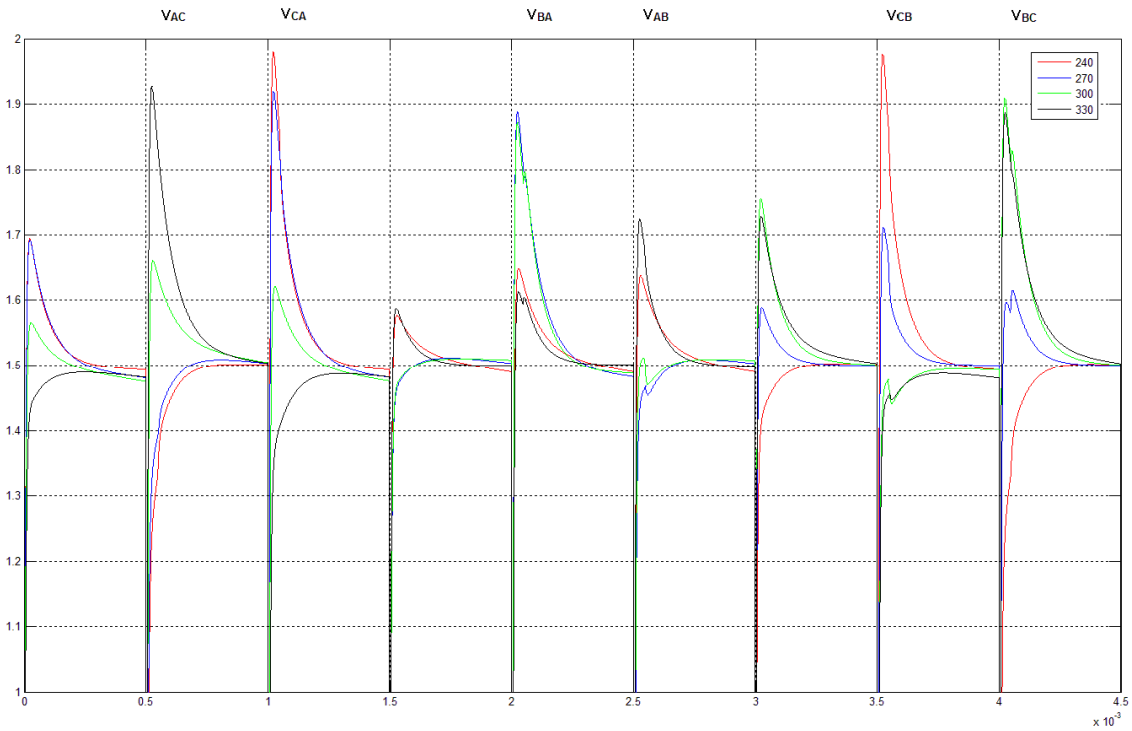

Figure 5.18 Plots of terminal voltages for 240° - 330°.

5.2.3 Methodology III

The above methodology can be further simplified by further scrutinizing the terminal equations. Focusing first on $v_{C0,AB}$ and $v_{C0,BA}$, it can be seen that

$$v_{C0,AB}(0) - \frac{V_{dd}}{2} = -V_{dd}\left(1 - \frac{2L_{B-}}{L_{AB}}\right), \tag{5-11}$$

$$v_{C0,BA}(0) - \frac{V_{dd}}{2} = -V_{dd}\left(1 - \frac{2L_{A-}}{L_{BA}}\right). \tag{5-12}$$

Developing it similarly for $v_{A0,BC}$ and $v_{A0,CB}$, $v_{B0,CA}$ and $v_{B0,AC}$,

$$v_{A0,BC}(0) - \frac{V_{dd}}{2} = -V_{dd}\left(1 - \frac{2L_{C-}}{L_{BC}}\right), \tag{5-13}$$

$$v_{A0,CB}(0)-\frac{V_{dd}}{2}=-V_{dd}\left(1-\frac{2L_{B-}}{L_{CB}}\right), \tag{5-14}$$

and

$$v_{B0,CA}(0)-\frac{V_{dd}}{2}=-V_{dd}\left(1-\frac{2L_{A-}}{L_{CA}}\right), \tag{5-15}$$

$$v_{B0,AC}(0)-\frac{V_{dd}}{2}=-V_{dd}\left(1-\frac{2L_{C-}}{L_{AC}}\right). \tag{5-16}$$

It can be seen that these initial values are modulated by the inductance ratios as well. These positional unique initial voltages are appropriate and elegant means for position detection as seen from Figure 5.16 to Figure 5.18. Based on these equations, the different maxima (peaks) or minima (troughs) initial values occur at different positions.

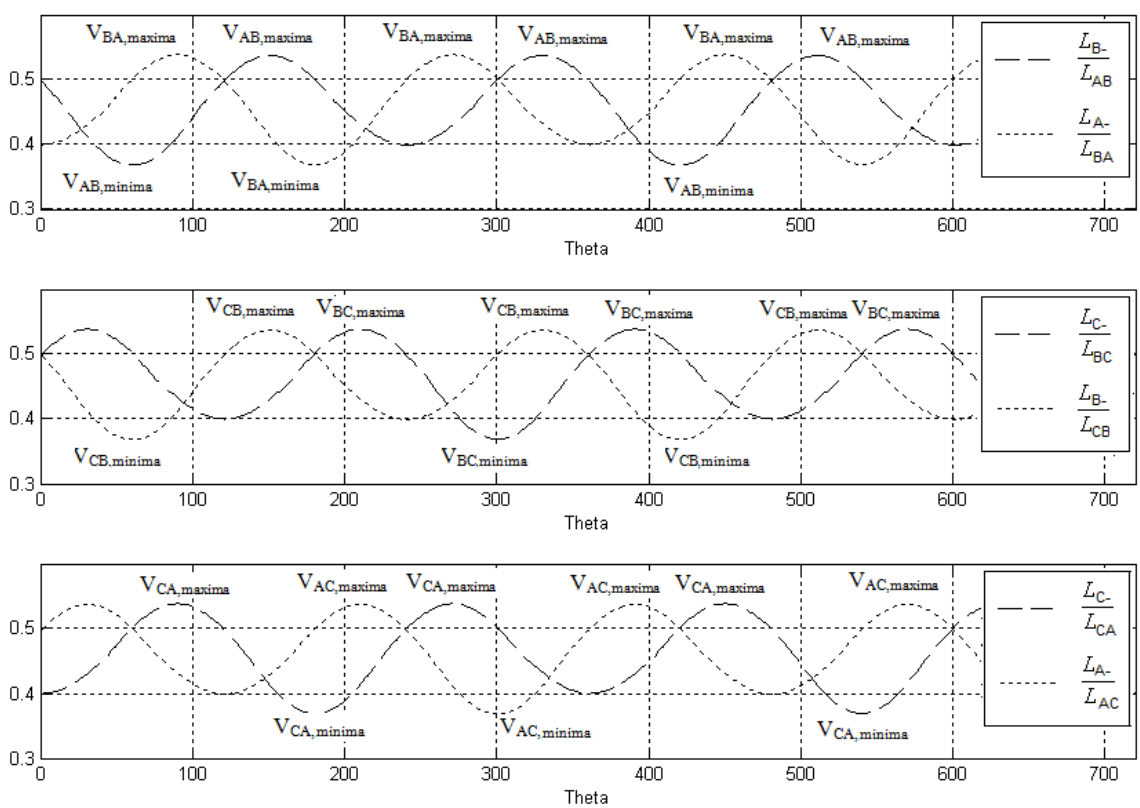

Figure 5.19 Inductance ratio against observed maxima/minima terminal voltages.

Figure 5.19 shows the correlation for the maxima and minima versus the inductance ratio at different positions. From this relationship, these maxima and minima can be used to derive a correlated equivalent set of commutation signals.

Table 5.1 Tabulated Terminal Voltages Comparator Output

Positional Codes	Equivalent Commutation Signals
$V_{CA,maxima}$, $V_{AB,maxima}$ and/or $V_{BC,minima}$, $V_{AC,minima}$	Q_{AH}, Q_{BL}
$V_{BC,maxima}$, $V_{AC,maxima}$ and/or $V_{BA,minima}$, $V_{CA,minima}$	Q_{AH}, Q_{CL}
$V_{BC,maxima}$, $V_{AC,maxima}$ and/or $V_{CB,minima}$, $V_{AB,minima}$	Q_{BH}, Q_{CL}
$V_{CB,maxima}$, $V_{BA,maxima}$ and/or $V_{BC,minima}$, $V_{AC,minima}$	Q_{BH}, Q_{AL}
$V_{CB,maxima}$, $V_{BA,maxima}$ and/or $V_{BA,minima}$, $V_{CA,minima}$	Q_{CH}, Q_{AL}
$V_{CA,maxima}$, $V_{AB,maxima}$ and/or $V_{CB,minima}$, $V_{AB,minima}$	Q_{CH}, Q_{BL}

In the determination of these maxima or minima, all measuring signals are fed into comparators and compared to tuned threshold voltages (approximately $0.5V_{dd}$ for the maxima and $0.2V_{dd}$ for the minima). By doing so, a digitized and simpler methodology can be realized.

5.3 Hardware Implementation and Results

The same topology as described in Section 3.5.1 is adopted. The modification pertaining to initial rotor detection is isolated to the HDL codes within the FPGA.

For the detection of rotor position, sequence of pulses was alternately injected and the plots were captured as in Figure 5.21 to Figure 5.26. V_{AB} means a positive current flowing into terminal A, and out of terminal B, and terminal C is floating measured terminal. The same principle can be similarly applied for V_{AC}, V_{AB}, V_{BA}, V_{BC} and V_{CB}. Hence, for rotor position detection, AB, BA, BC, CB, CA and AC were sequentially injected with the third floating terminal observed. Figure 5.20 shows a schematic illustration of the pulses injected. Comparison was made with reference to the simulation and it is observed that the terminal voltage plots agree well with the analytical and simulation results.

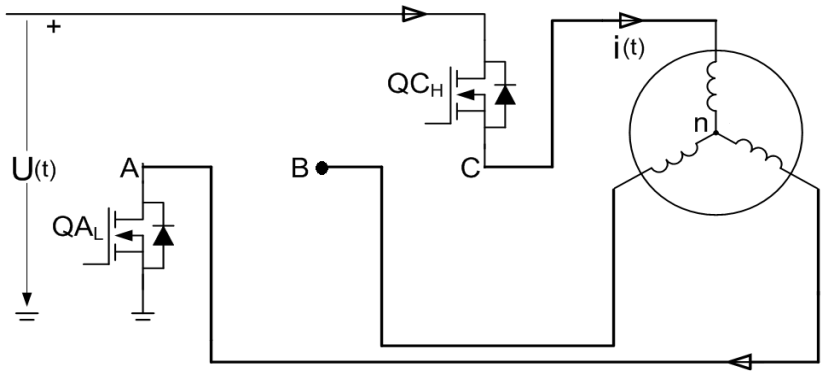

"V_{CA}" injection with Terminal C - Vdd, Terminal A - Gnd, Terminal B - Floating (Measured)

(a)

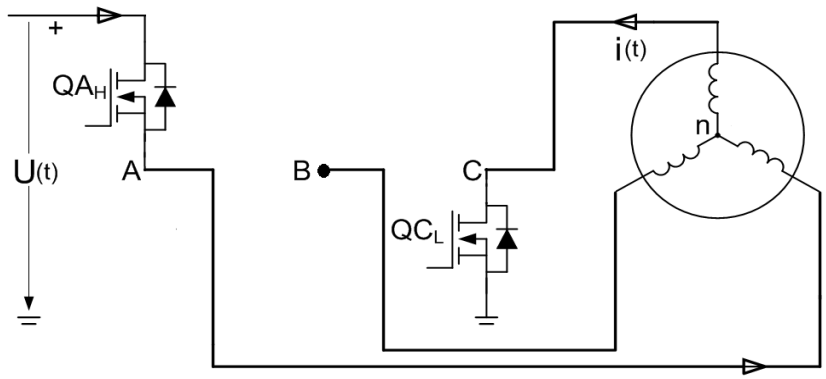

"V_{AC}" injection with Terminal A - Vdd, Terminal C - Gnd, Terminal B - Floating (Measured)

(b)

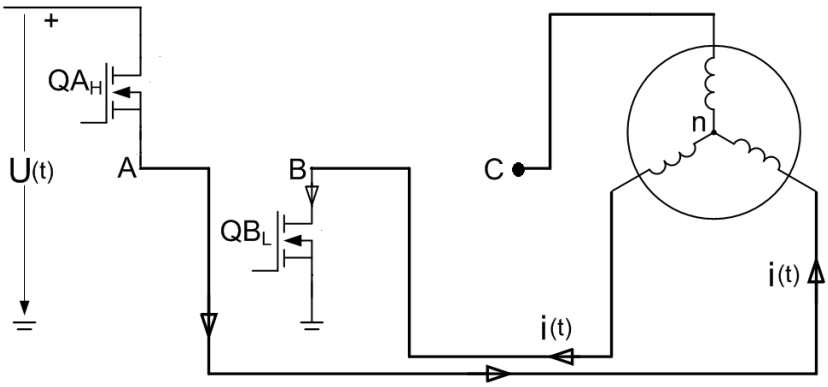

"V_{AB}" injection with Terminal A - Vdd, Terminal B - Gnd, Terminal C - Floating (Measured)

(c)

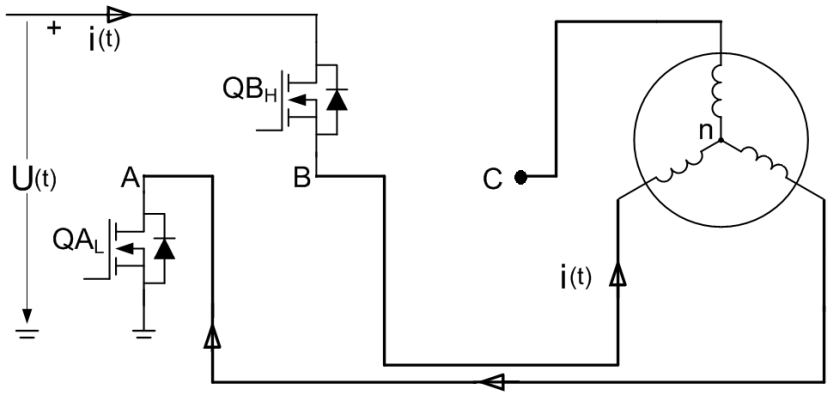

"V_{BA}" injection with Terminal B - Vdd, Terminal A - Gnd, Terminal C - Floating (Measured)

(d)

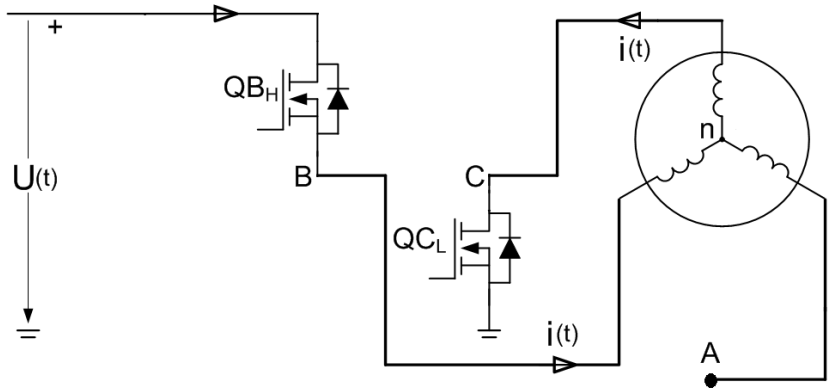

"V_{BC}" injection with Terminal B - Vdd, Terminal C - Gnd, Terminal A - Floating (Measured)

(e)

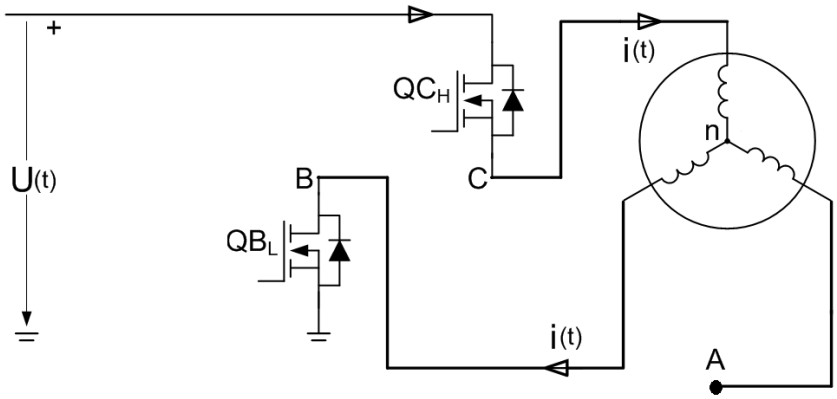

"V_{CB}" injection with Terminal C - Vdd, Terminal B - Gnd, Terminal A - Floating (Measured)

(f)

Figure 5.20 Schematic drawing for the various injections.

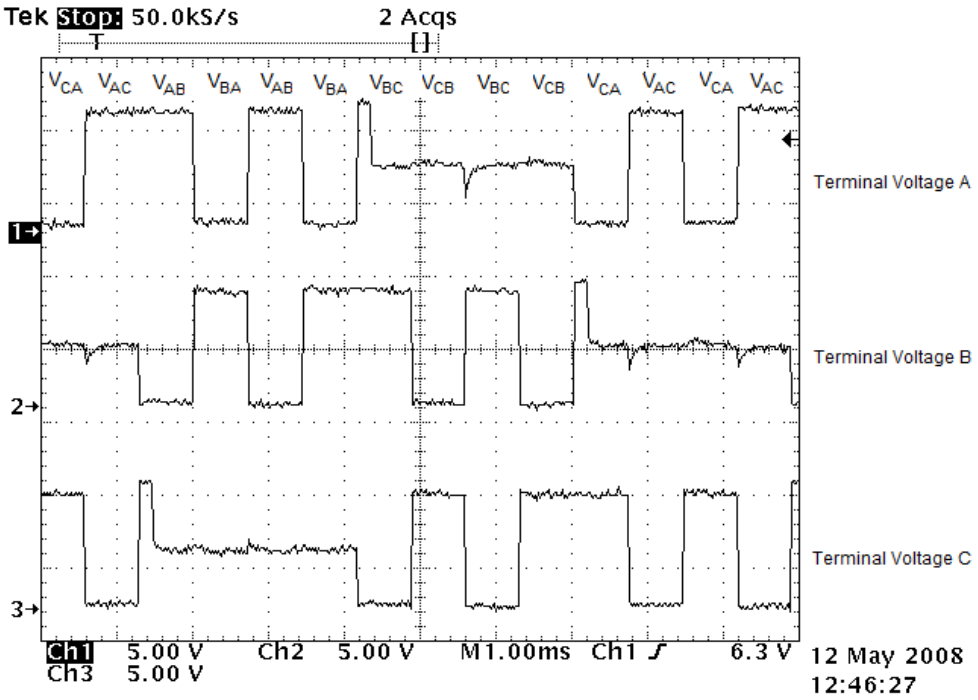

Figure 5.21 Plots of terminal voltages for θ = 300°.

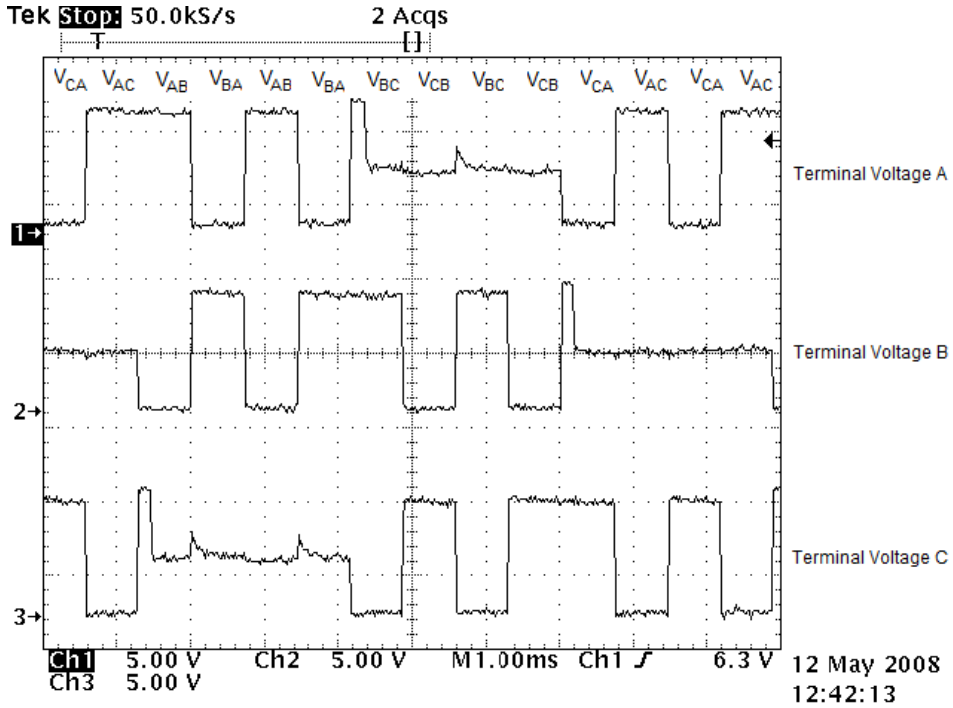

Figure 5.22 Plots of terminal voltages for θ = 240°.

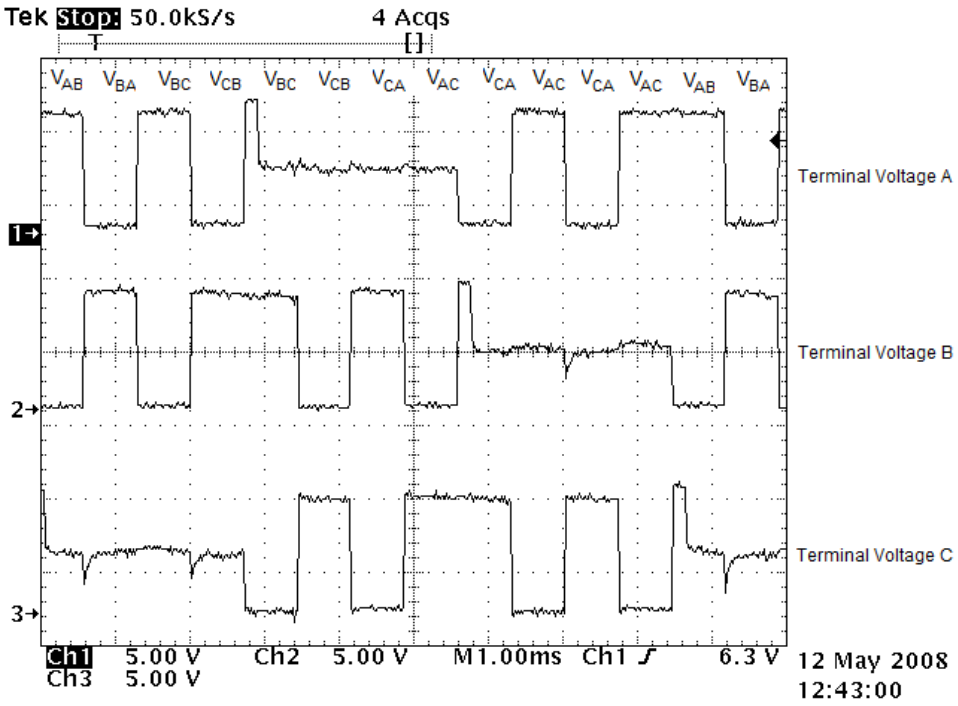

Figure 5.23 Plots of terminal voltages for θ = 180°.

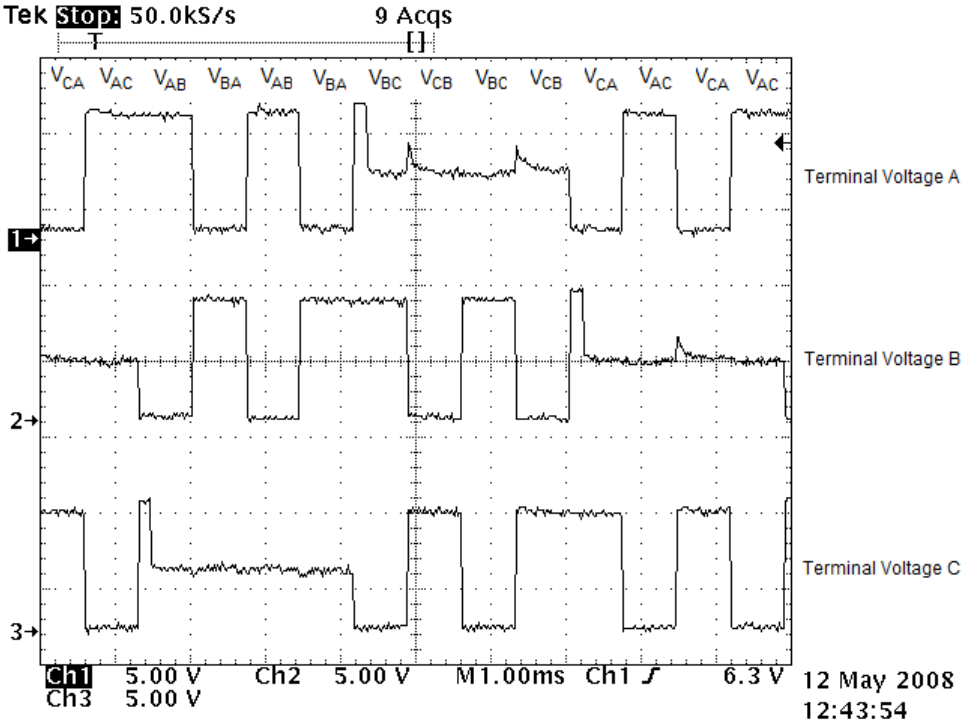

Figure 5.24 Plots of terminal voltages for θ = 120°.

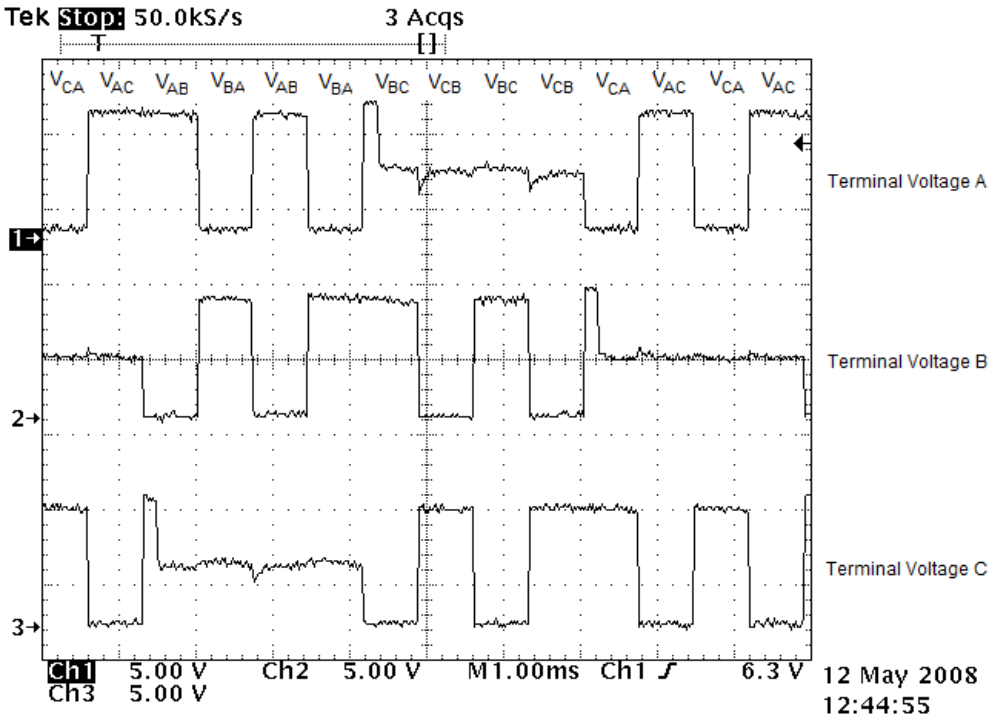

Figure 5.25 Plots of terminal voltages for θ = 60°.

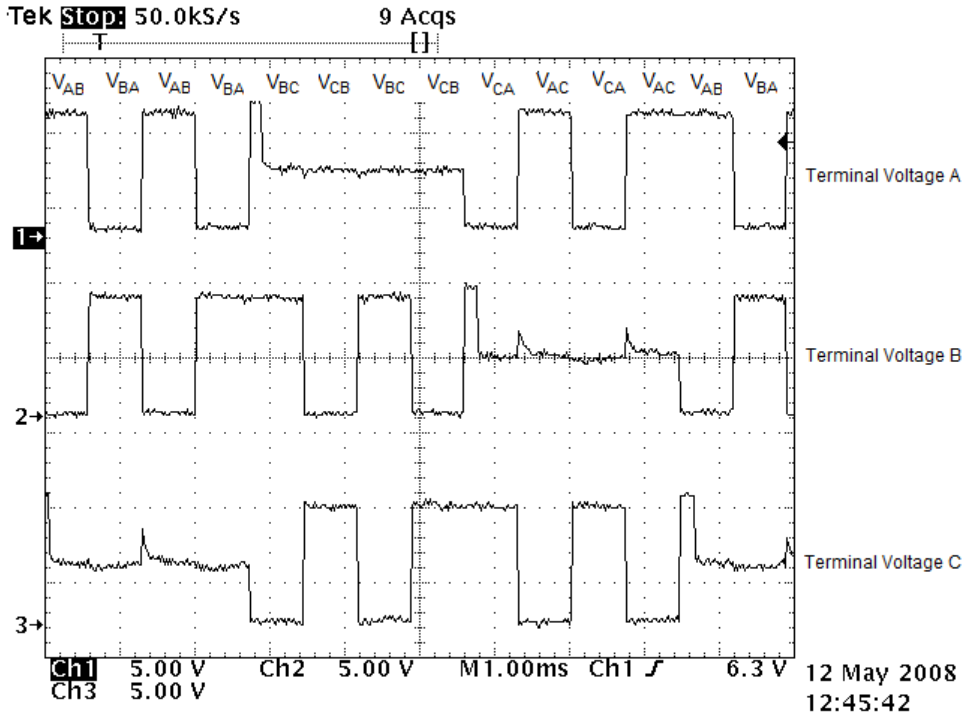

Figure 5.26 Plots of terminal voltages for θ = 0°.

The terminal voltages were individually fed into the comparators to locate the minima and maxima. Figure 5.27 and Figure 5.28 give the comparator output for the maxima and minima detection, respectively. The methodology agrees well with the simulated analysis provided in Table 5.1. The initial rotor detection has also been incorporated into the BLDC algorithm on FPGA implementation and its starting performance is significantly improved.

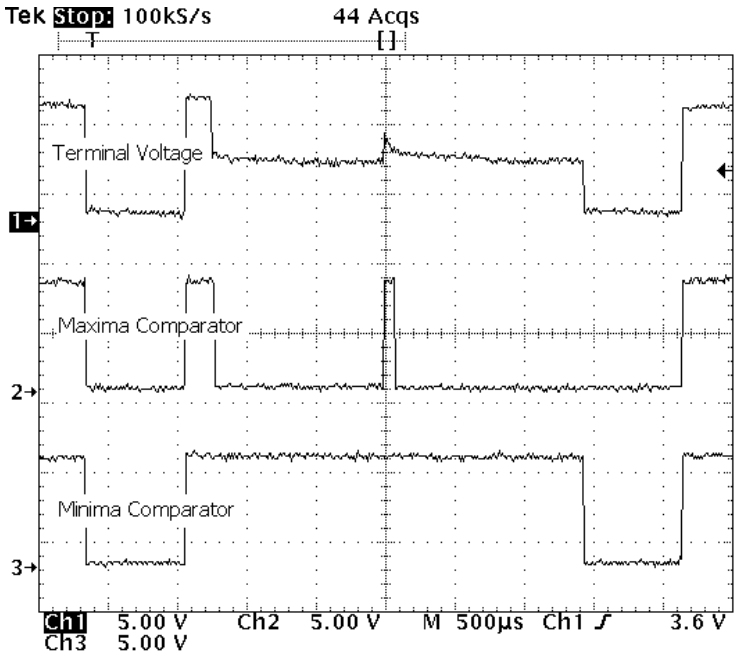

Figure 5.27 Comparator output for illustrating maxima detection.

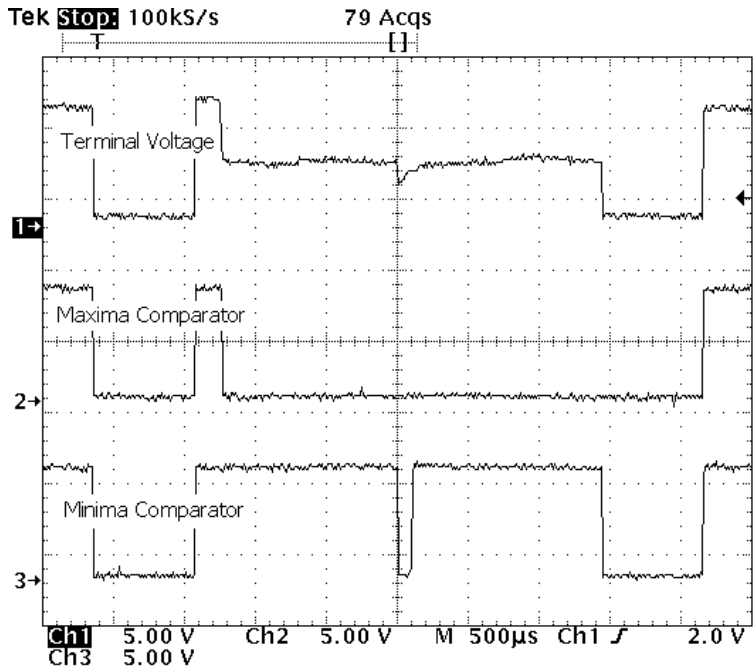

Figure 5.28 Comparator output for illustrating maxima detection.

5.3.1 Application of Algorithm on BLDC Drive

To validate and establish the effectiveness of this method, it is integrated into the BLDC and QBLDC drives presented earlier. It is compared to a typical open loop skew startup with gate turn-off crossover and the results are overwhelming. The plots for starting are shown in Figure 5.29 and Figure 5.30. The open loop starting yields an initial startup time (best case) of 4.6s to BLDC while the proposed algorithm only requires an initial startup time of 0.5s, shaving 90% off the time required. The integrated drive is also applied to several motors, such as spindle motors with 0-11 discs, 80W Shinano PMSM, 300W Yaskawa Electric PMSM, Maxon 6mm Micromotor etc. The drive has demonstrated to be effective for all cases. The snapshots of the motors as well as its startup plots are provided in Figure 5.32 to Figure 5.35.

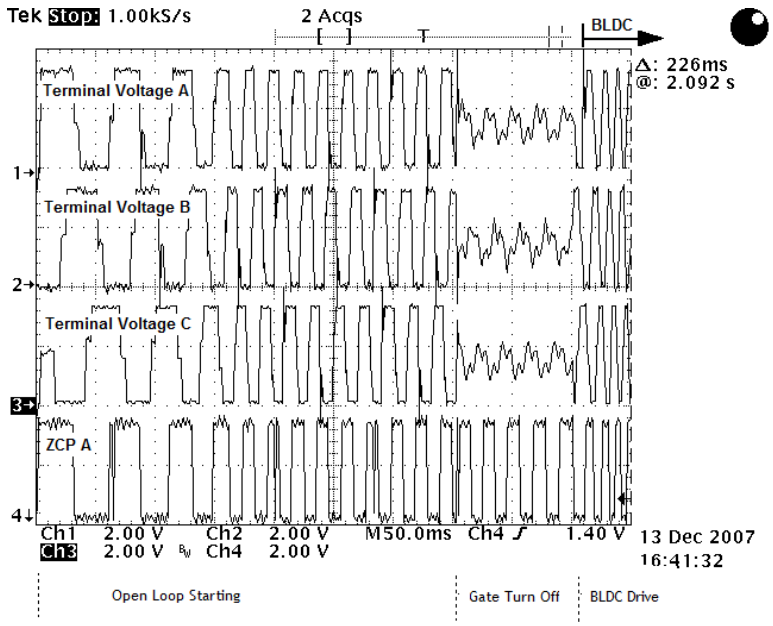

Figure 5.29 Starting with open loop skew and gate turn off crossover.

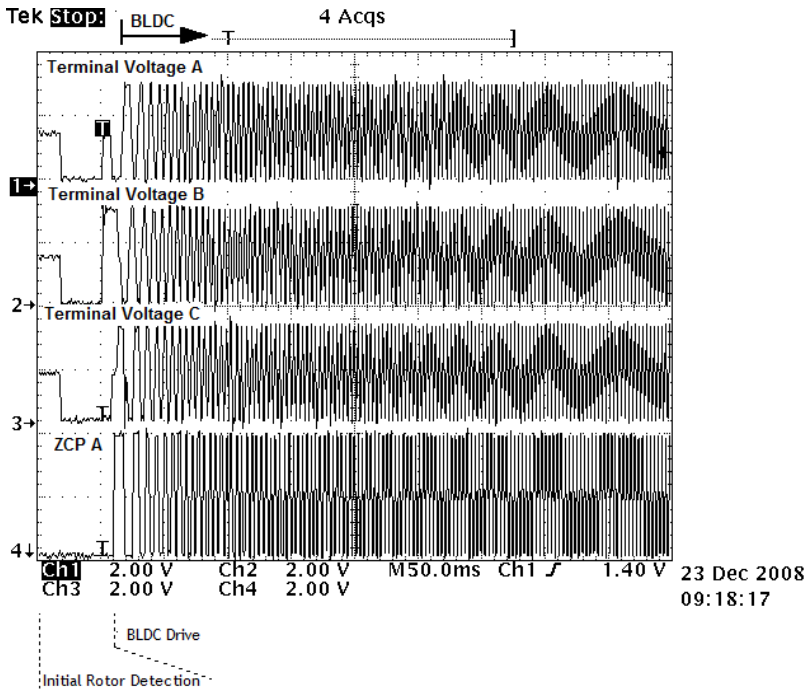

Figure 5.30 Starting with initial rotor position detection.

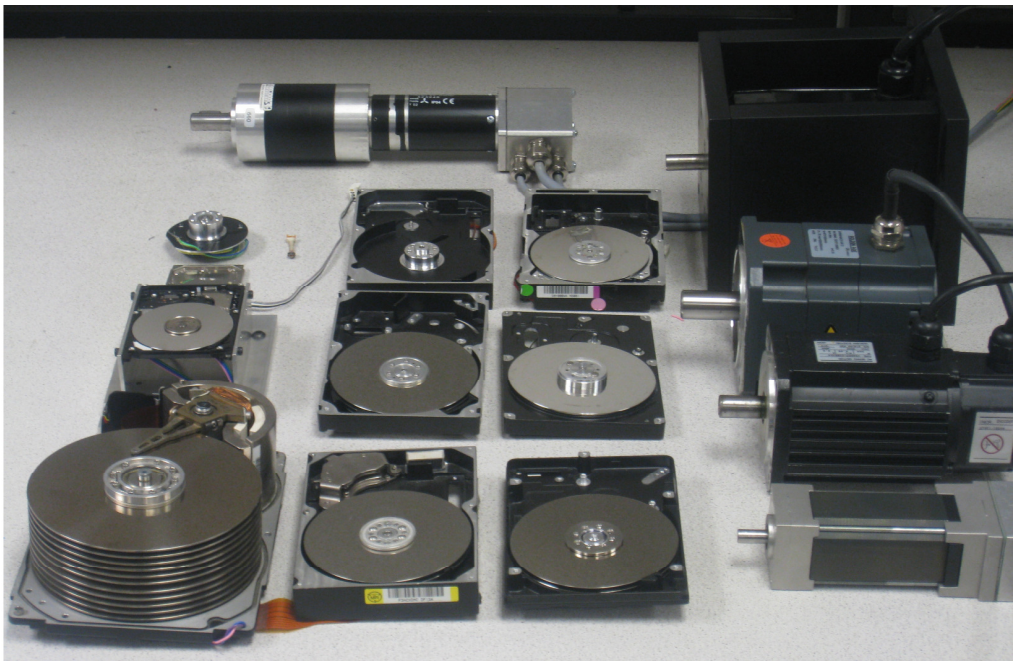

Figure 5.31 Photo of PMSMs tested with integrated drive.

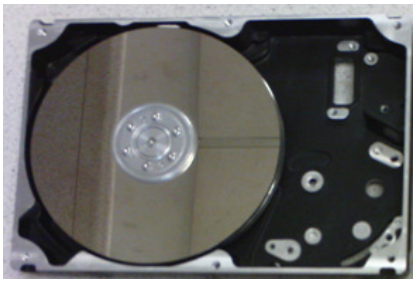

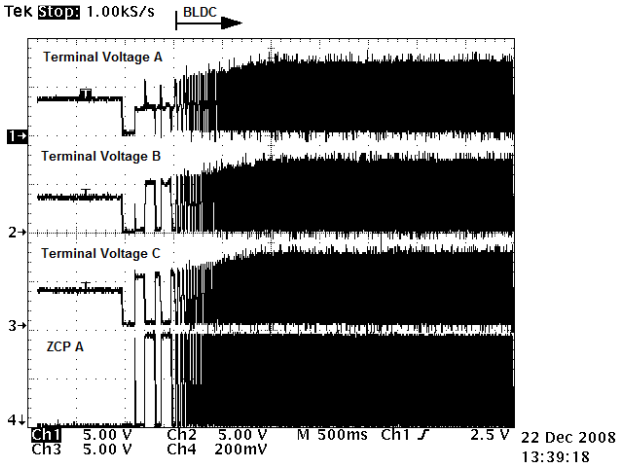

Figure 5.32 Starting with initial rotor position detection for 4 disks HDD.

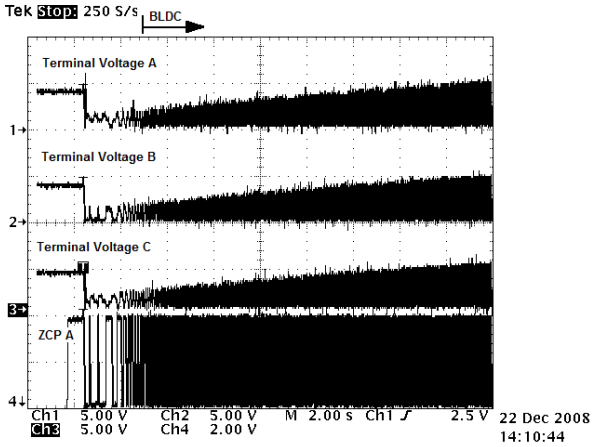

Figure 5.33 Starting with initial rotor position detection for 11 disks HDD.

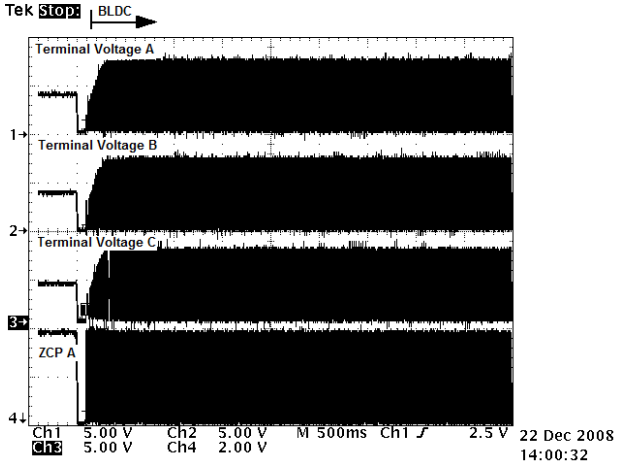

Figure 5.34 Starting with initial rotor position detection for enterprise HDD.

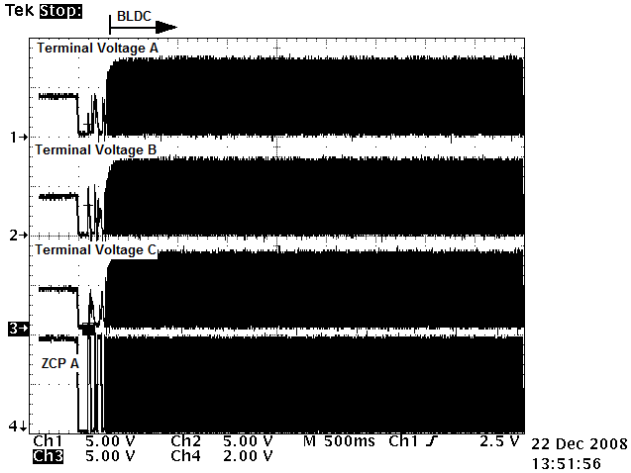

Figure 5.35 Starting with initial rotor position detection for 80W Hurst PMSM.

5.4 Conclusions

Self-starting has been, and still is, a key concern in sensorless drives and particularly crucial for surface mounted PMSM. To address this challenging class of motor, a novel initial rotor detection method has been conceptualized and successfully applied. The proposed method is presented together with detailed analysis including numerical simulations. A digital variant of the method is implemented on hardware and has been successfully deployed for sensorless BLDC self-starting on various HDDs. This method shaves off a 90% of the starting times, an enticing figure for the industry. It has also proved to be robust towards a series of motors. In addition, using this method, no additional power loss is induced in the initial rotor position detection as only terminal voltages are sensed and measured. Coupled with the ill-presence of existing solution towards initial rotor position detection for surface mounted PMSM, successful application of the proposed method to this challenging class of motor has drawn both academic and industry interests.

CHAPTER 6. BUMPLESS δ CROSSOVER & STARTING

6.0 Introduction

As highlighted in the earlier section, the three common classifications of starting the motor from standstill include:

1. Starting from open-loop,
2. Starting from aligned position, and
3. Starting from estimated position.

Under schemes (2) and (3) where the motor is started from known positions, it is possible that the back-EMF might be too small and starting might be continued with open loop starting.

During open loop starting, specific gate patterns providing a rotating stator field are injected. These signals are voltage skewed and/or frequency skewed providing a rotating torque increasing in magnitude and/or frequency. The voltage and/or frequency skew profile has to be carefully established, failure of which will result in starting failure. Once the motor reaches a particular threshold speed, $\omega_{crossover}$, open loop operation is switched to closed loop sensorless operation. At the $\omega_{crossover}$, two conditions must be met; (i) back-EMF is sufficiently large to be detected and (ii) ZCPs occur during the unexcited phase of gating. Figure 6.1 gives the gating signals with respect to the ZCP signals in an ideal crossover.

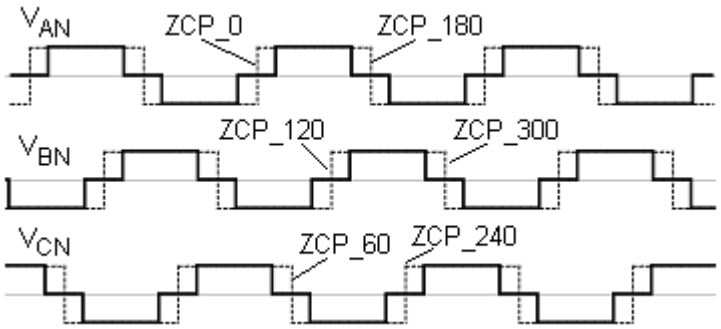

Figure 6.1 Gating & back-EMF waveforms.

However, practically, it is necessary to tune the drive in order to achieve the gating and ZCP phasor relationship. Such an approach, apart from requiring time and effort, is system dependent. Another approach is to switch off all the gates and detect the ZCPs as soon as the phase currents decrease to zero. This method, though simple, causes the motor to decelerate and its corresponding back-EMF to diminish which inevitably requires a higher $\omega_{crossover}$. Furthermore, the deceleration of the motor causes a speed blip/bump in the crossover. In addition, in the event of a failure, restarting is difficult as it has to be restarted only when the motor reaches a standstill.

6.1 Bumpless δ Crossover & Starting

In this proposed methodology, a novel gate signal masking technique is utilized, making back-EMF detection possible without a complete removal of gating signals. The proposed method, not only ensures a smooth and robust crossover to BLDC mode, but also shortens the starting time. To provide insights into this, it would be appropriate to understand the operation of six stepping better. During open loop six stepping, generally,

the waveform do not allow for ZCP detection. Typically, the drive is over-driven to provide a higher starting torque for acceleration as well as overcoming frictional, viscous torque. The phasor relationship between the gating and back-EMF will differ by a larger angle than that observed in Figure 6.1. Generally, the phasor relation is similar to that illustrated in Figure 6.2. In this case, the ZCPs no longer occur during the silent phase and are wholly masked by the terminal injection.

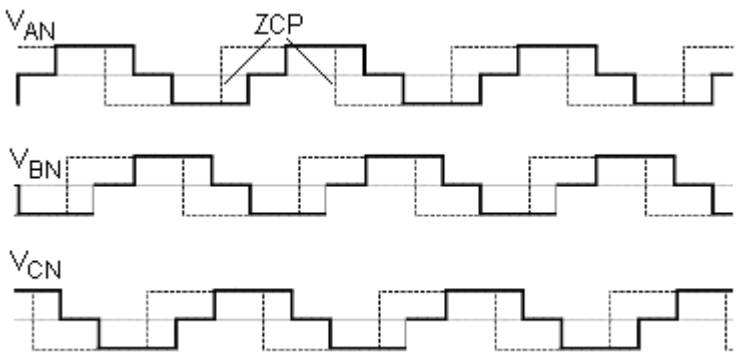

Figure 6.2 Gating & back-EMF waveforms during open-loop starting

As mentioned, to extract the ZCPs, the system can be tuned or all the gates are turned off. This matter, however, can be elegantly rectified by performing gate masking.

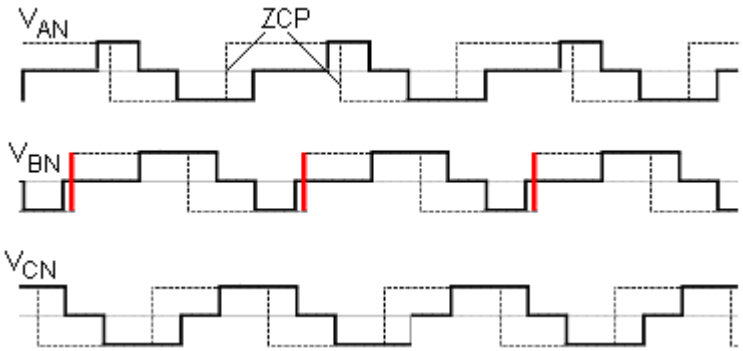

Figure 6.3 Gating & back-EMF waveforms with δ masking, δ = 60°.

The motor is similarly started on a six-stepping mode. However, the gating signals are masked out an arbitrary angle, δ, as soon as the motor rotates. This increases the silent phase window and for any $\delta \geq 60°$, guarantees at least one ZCP detection. Figure 6.3 illustrates the possible detection of a ZCP with gate signal masking.

In doing so, as only 60º of the gating signals are masked out, together with the inertia of the motor, motor rotation will be maintained in contrast with the complete removal of gating signals. Thus, as the motor is not made to decelerate, a smoother transfer is possible. Robustness is also improved since even if the window/back-EMF is missed, the same back-EMF amplitude is available for detection after a 300º angle rotation. In addition, the assumption that the back-EMF is large enough for detection is no longer necessary as such strategy allows the skewing of frequency to be continued till back-EMF is large enough for ZCP to be detected.

An extension of the method is to mask the gating signals by δ=120º. In doing so, an additional 60º window will make two ZCPs available for detection. This will greatly reduce the possibility of erroneous detection since dual detection is provided. However, it must be noted that, by setting up gate masking, starting torque will be reduced. Nevertheless, it should not be a concern as the motor is commonly overdriven at starting.

6.2 Simulation

In the investigation of the proposed δ Crossover, the top level Simulink block entry provided in Figure 3.13 is modified to insert a Delta Crossover Block as shown in Figure 6.4.

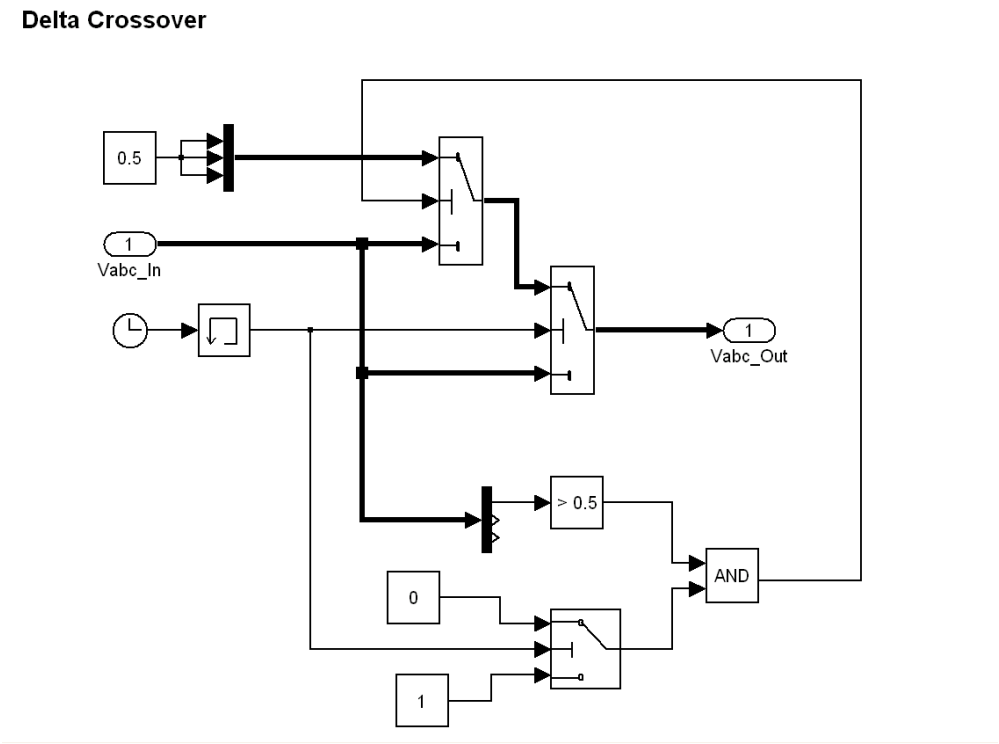

Figure 6.4 Simulink block entry for δ crossover.

Prior to the presentation of the algorithm simulated results, the operation of open loop spin up with gate turn-off is simulated and results are shown in Figure 6.5. It can be seen from the plots that during open loop operation, the back-EMF ZCPs for all three phases occur during active phase instead of during the silent phase. A direct impact of this

approach is that the ZCPs are no longer equal to the ZCPs of the comparator output. In an attempt to extract the ZCPs, a typical method is to turn off the gating and extract the ZCPs. The plots for such a scheme are provided in Figure 6.6 and Figure 6.7. It can be seen that in this instance, five ZCPs can be detected under ideal conditions before the speed (and back-EMF) drops to zero. Another observation is that only during gate turn-off period, the ZCPs are equivalent to the comparator ZCP outputs.

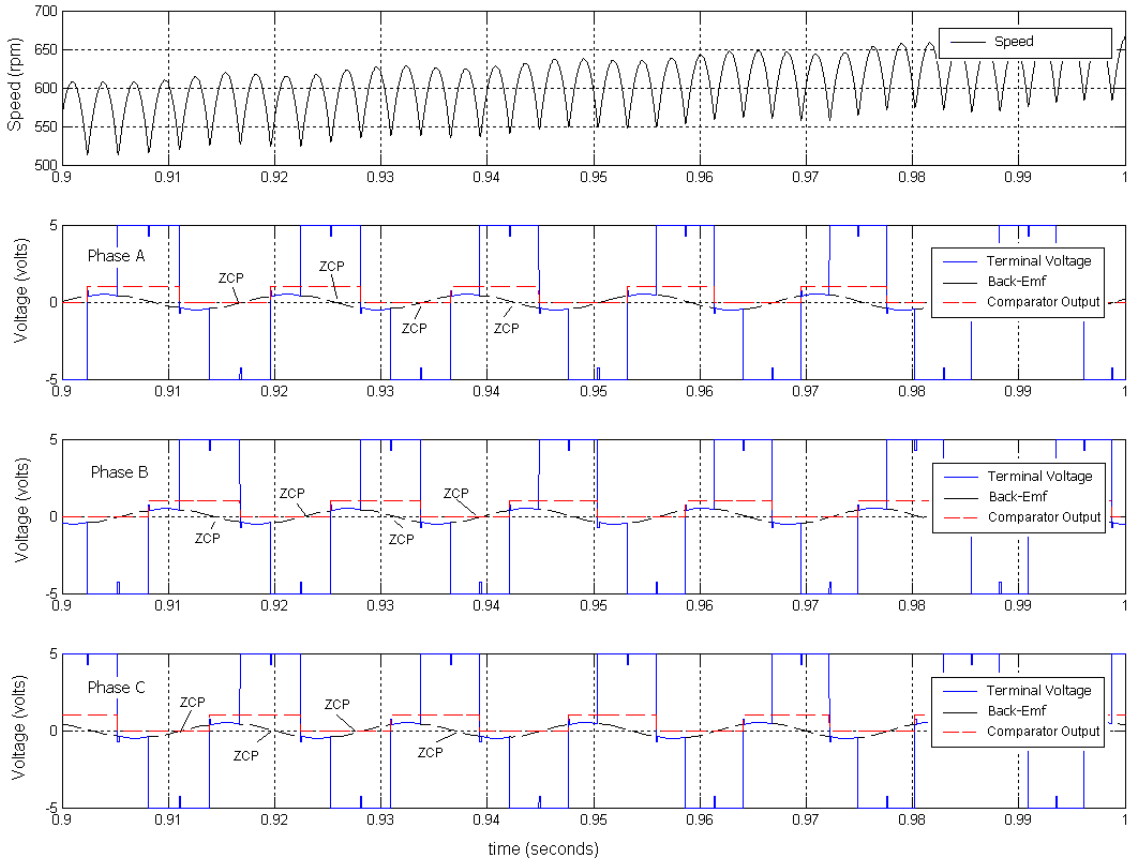

Figure 6.5 Simulation plots during open loop operation.

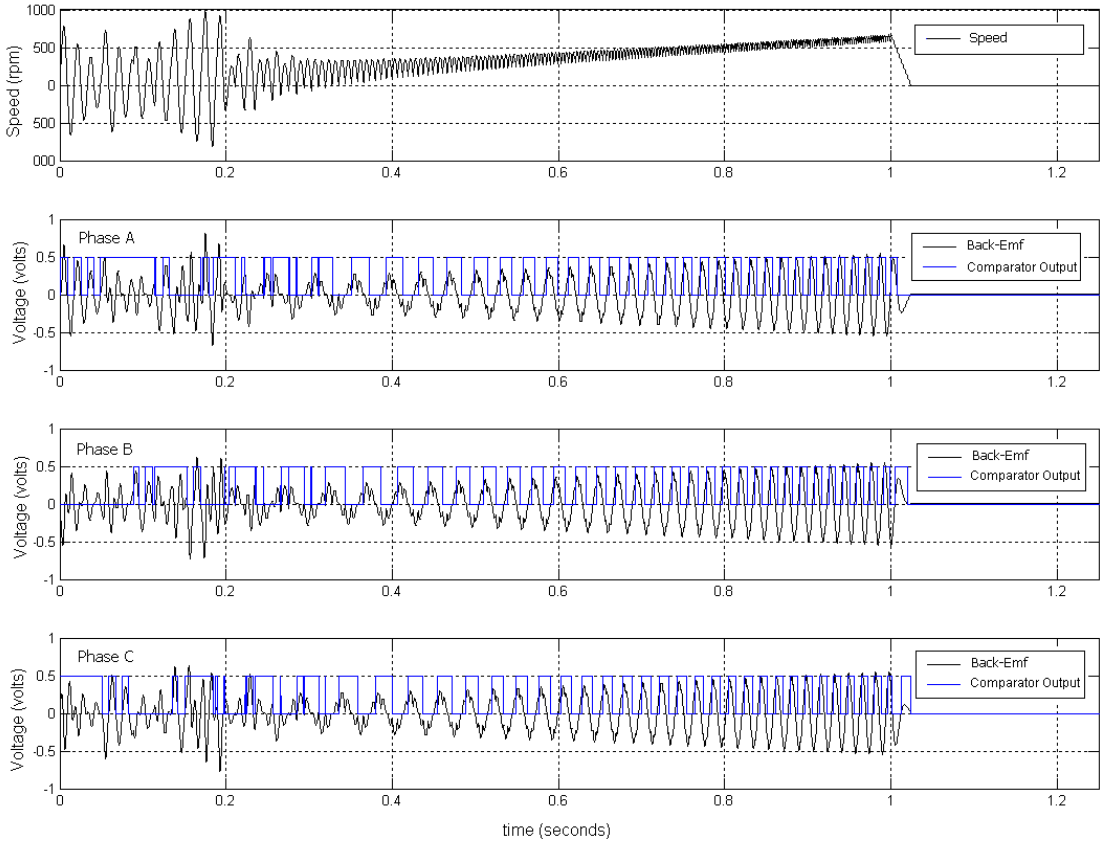

Figure 6.6 Simulation plots using gate turn off crossover.

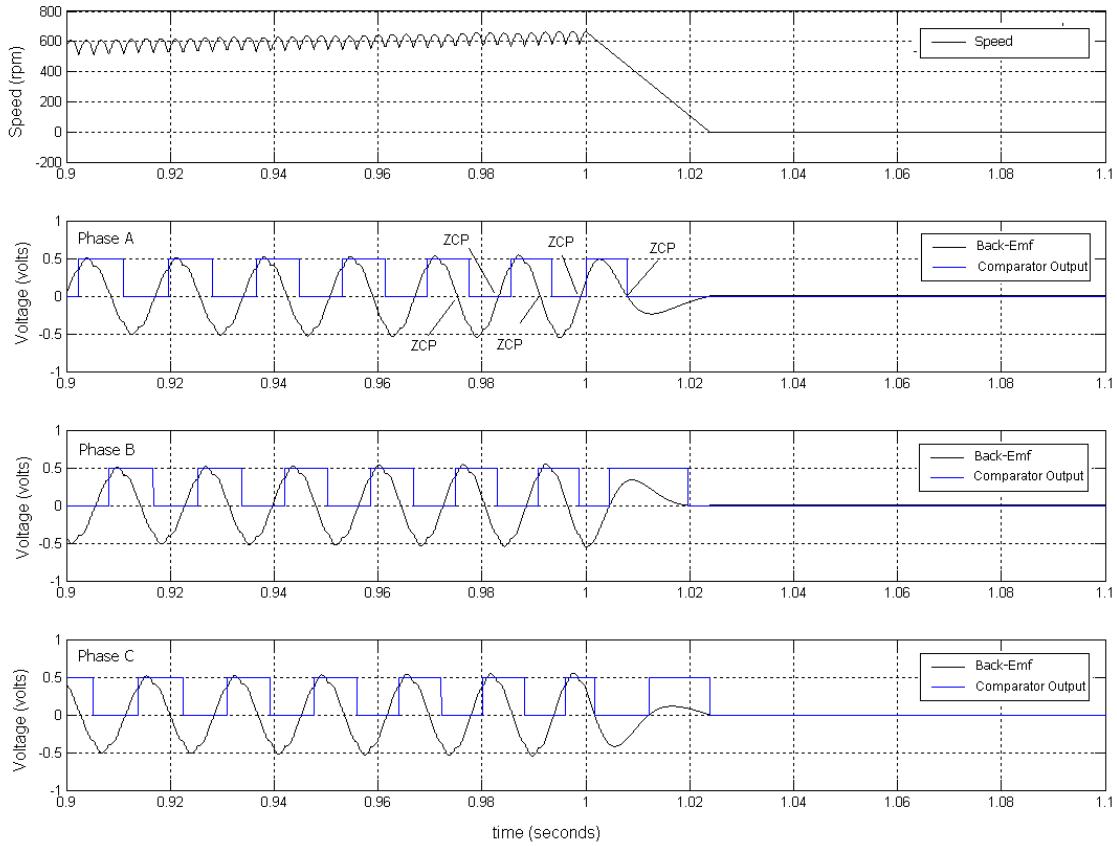

Figure 6.7 Zoom-in simulation plots using gate turn off crossover.

In the adoption of the proposed methodology, the motor is similarly driven using open loop but as opposed to gate turn off, δ crossover is employed. Figure 6.8 shows the δ crossover simulation plots. It can be seen that ZCP120 and ZCP180 can be detected consistently. During the δ crossover period, both these ZCPs are revealed and are also matched by the ZCPs of the comparators outputs. In addition, skew of the frequency was continued to further increase the speed in the presence of low back-EMF. Figure 6.9 shows the simulated spin up operation with δ crossover. It can be seen with the ZCPs detected, crossover to BLDC is smooth and successful.

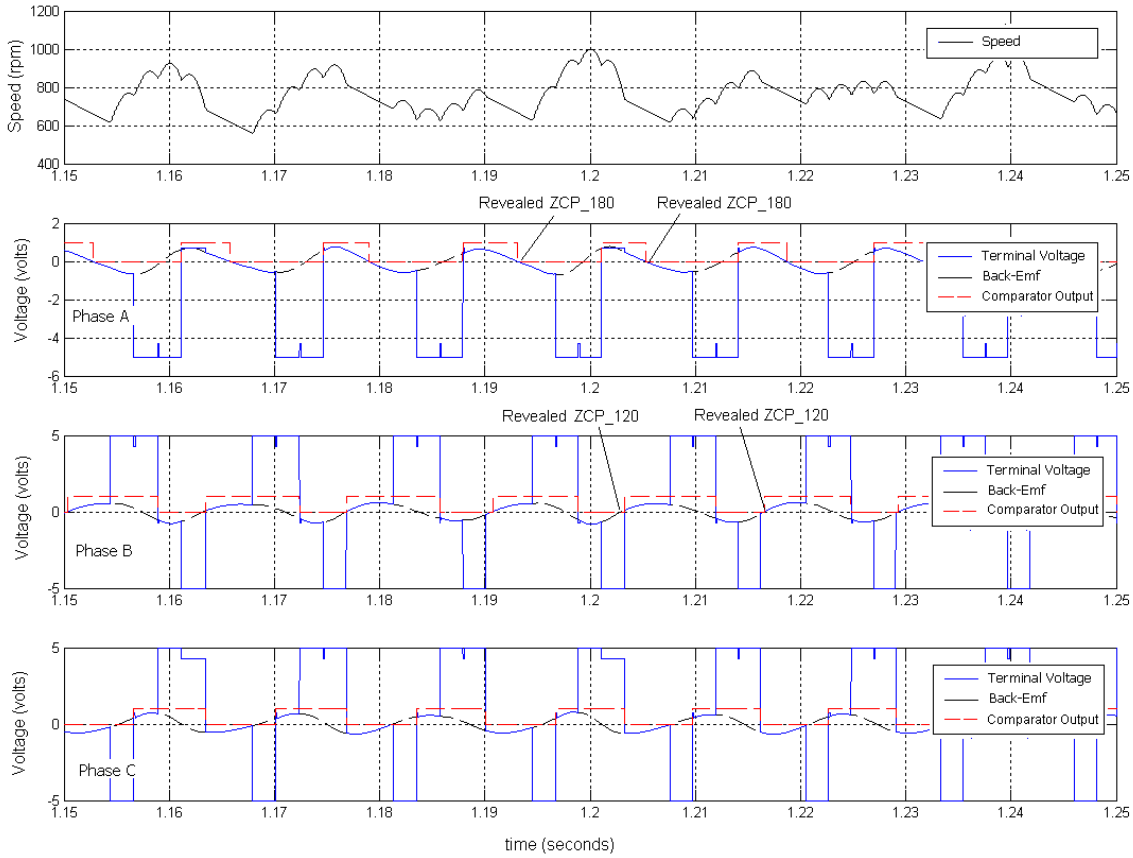

Figure 6.8 Simulation plots using δ crossover.

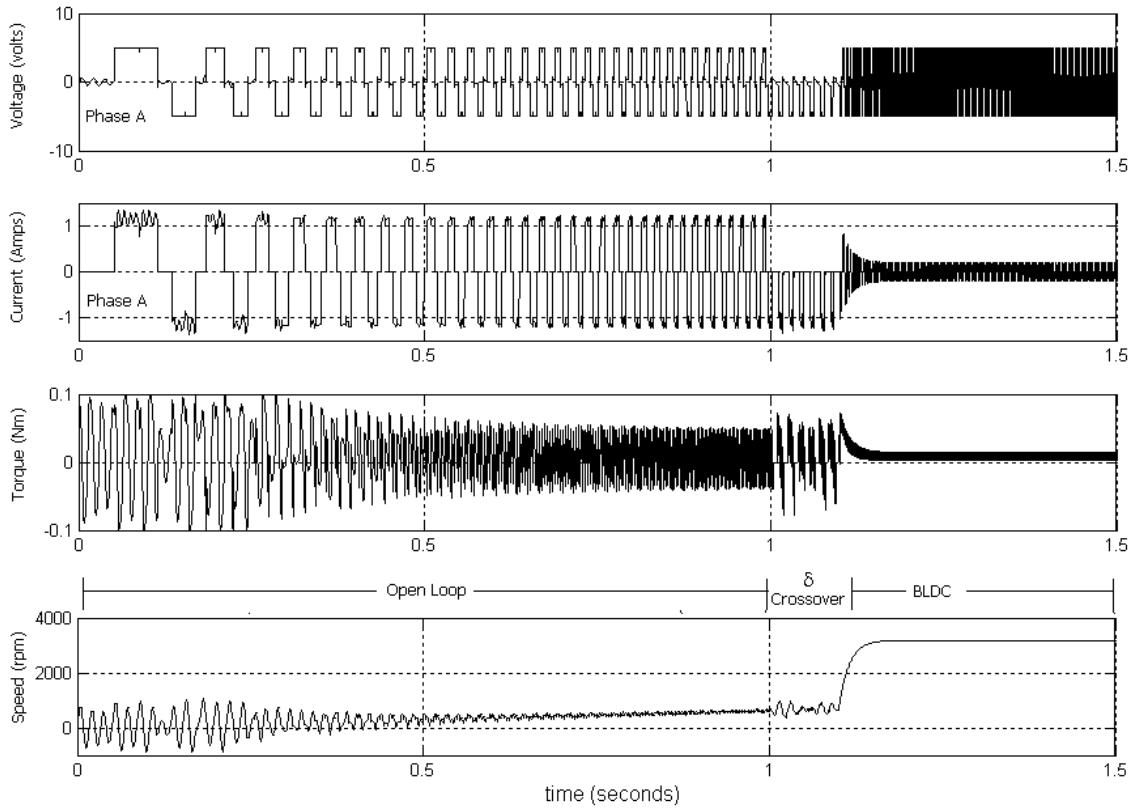

Figure 6.9 Simulation spin-up plot using δ crossover.

6.3 Hardware Implementation and Results

Topology described in section 3.5.1 is used. The modification pertaining to δ crossover is isolated to the HDL codes within the FPGA.

6.3.1 Open Loop and δ Crossover Operation

The open loop operation has been implemented and the terminal voltage is provided in Figure 6.10. It can be seen that the active phases completely engulf the back-EMF ZCPs, rendering detection impossible. δ Crossover implemented opens up window for ZCP detection as seen in Figure 6.11 and the ZCP generation for phase A is provided in Figure 6.12. It can be observed that detection is possible with the adopted scheme.

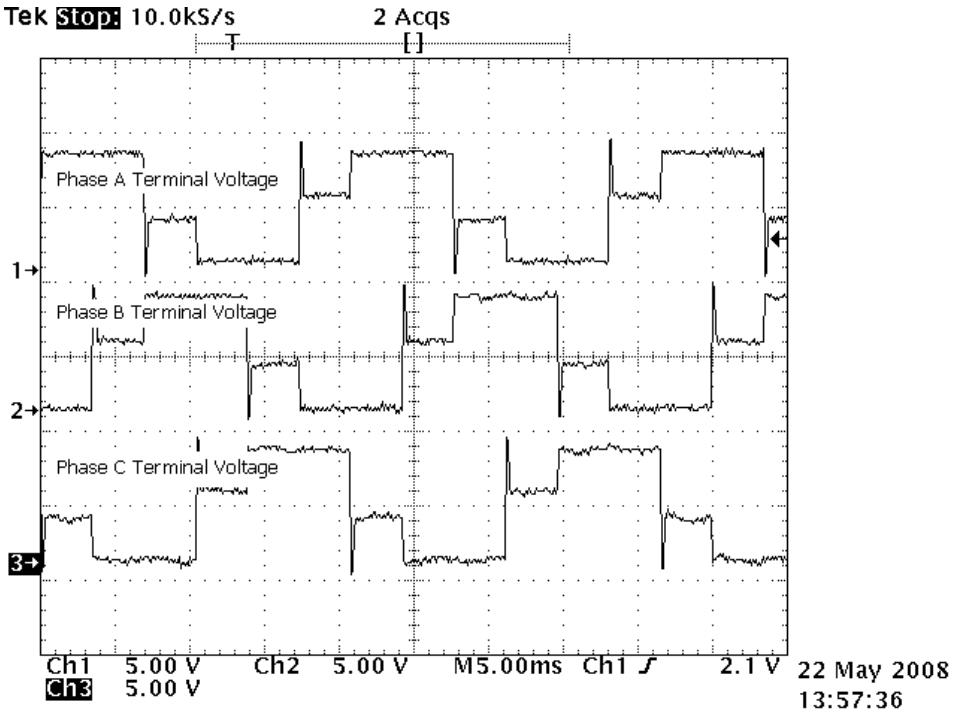

Figure 6.10 Terminal voltages during open loop operation.

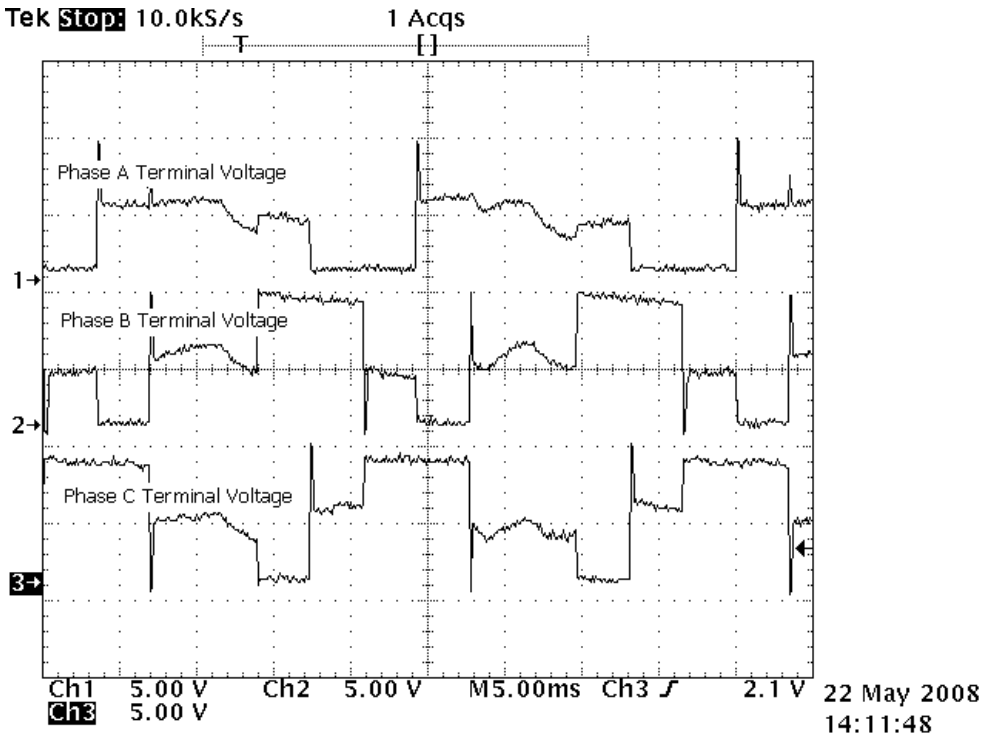

Figure 6.11 Terminal voltages during δ crossover operation.

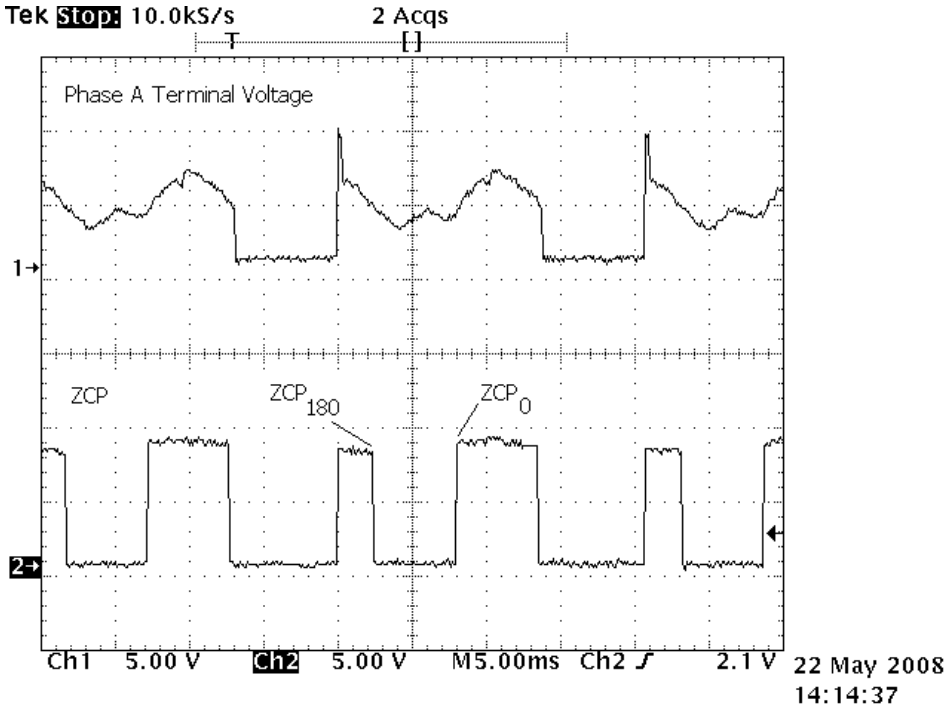

Figure 6.12 Phase A ZCP generation during δ crossover operation.

6.3.2 Open Loop and δ Crossover Spin Up

Figure 6.13 shows the implementation for 120º, 150º and 180º open loop starting. All three schemes are possible since δ crossover can be applied such that ZCP detection is possible. It can be observed that regardless of which scheme, crossover is achieved.

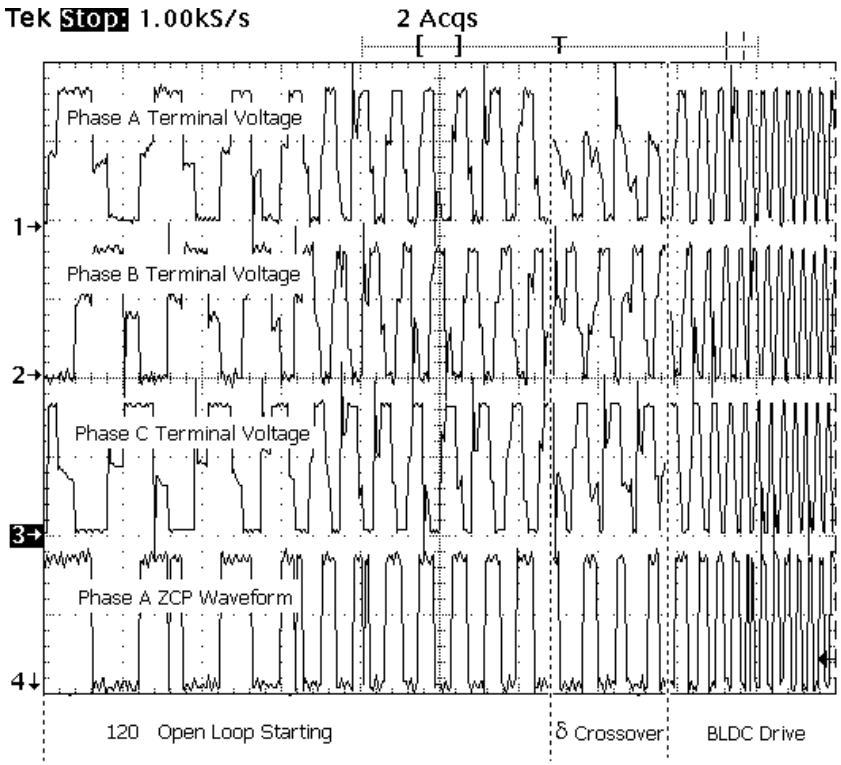

(a)

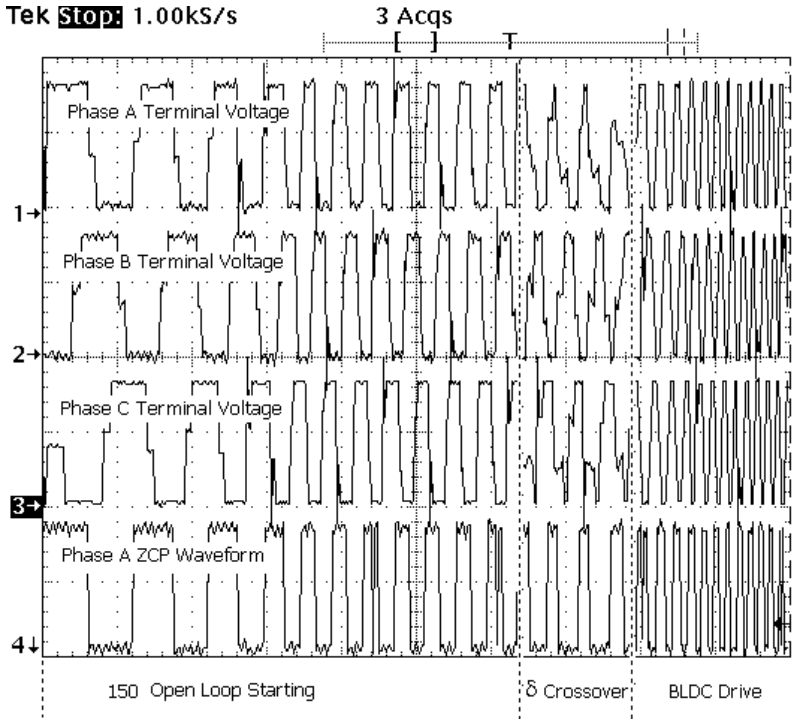

(b)

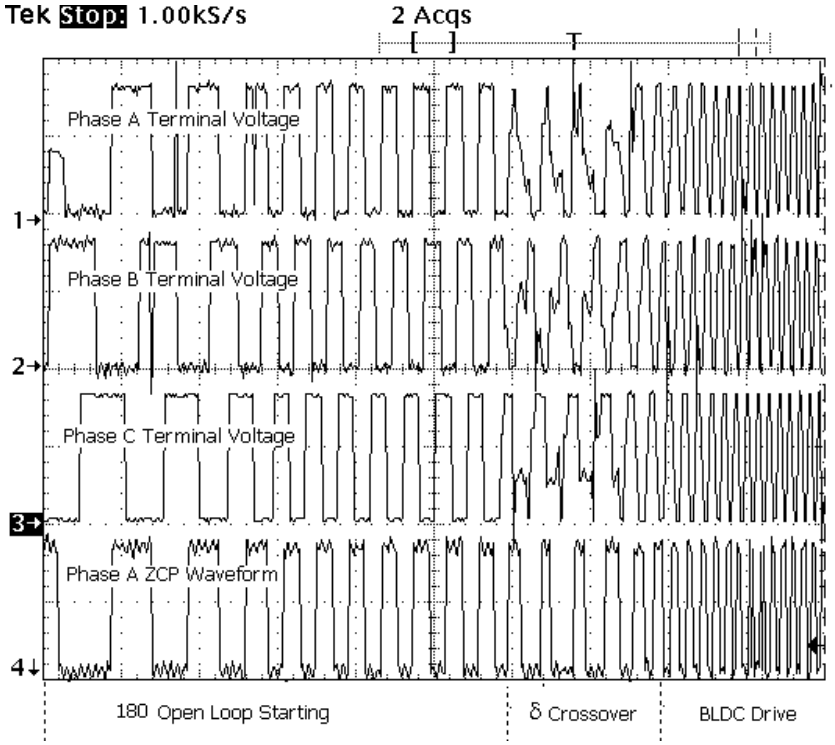

(c)

Figure 6.13 Waveforms for (a) 120˚, (b) 150˚ and (c) 180˚ open loop starting.

Since both 150˚ and 180˚ open loop starting schemes are possible, an improved starting strategy can be designed. The advantage of the 150˚ open loop starting is that it provides a smaller "rotational" step and as such it reduces the open loop deadzone or alternatively, allows for a higher starting frequency [143]. The advantage of the 180˚ open loop starting is that it provides a higher torque and hence a faster skew. Therefore, it would be beneficial to incorporate the 150˚ open loop together with δ crossover applied into the 180˚ open loop starting. Such a scheme would bring about the advantage of the 150˚ open loop starting while at the same time; provide the higher torque of the 180˚ open loop starting during δ crossover. Figure 6.14 shows the scheme for illustration.

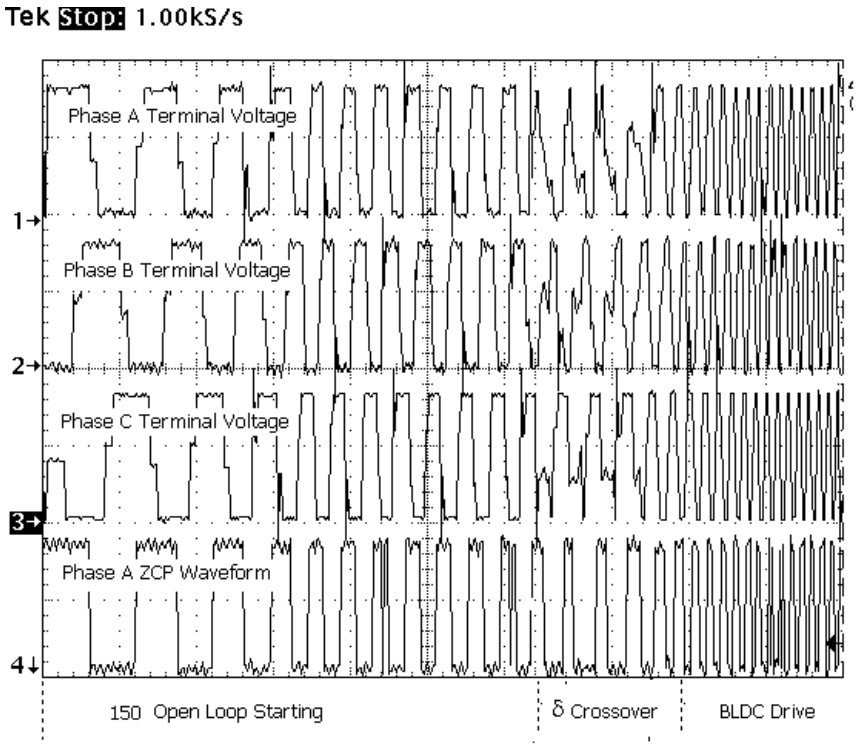

Figure 6.14 Hybrid startup with δ crossover.

As a comparison between δ crossover and gate turn-off crossover, the skew frequency has been optimized and their respective performances are evaluated. The following shows the plot for starting from known positions (from estimation or alignment), and the most optimal gate injection is introduced. The δ crossover versus gate turn-off crossover shows a marginal improvement of 0.425s from 0.46s

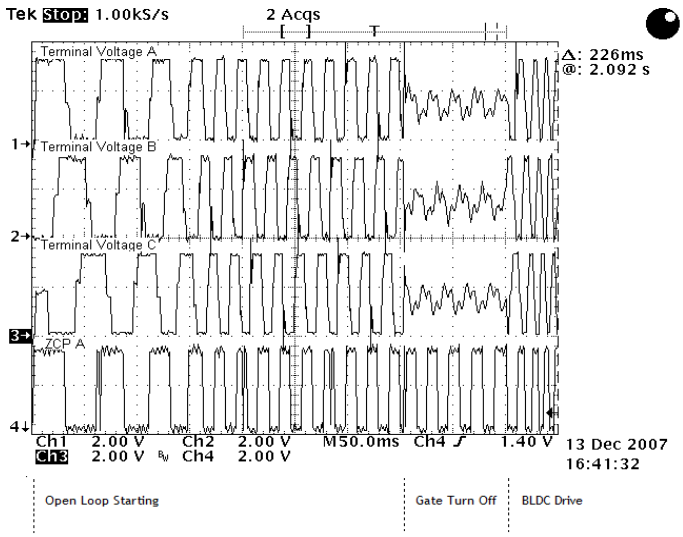

(a)

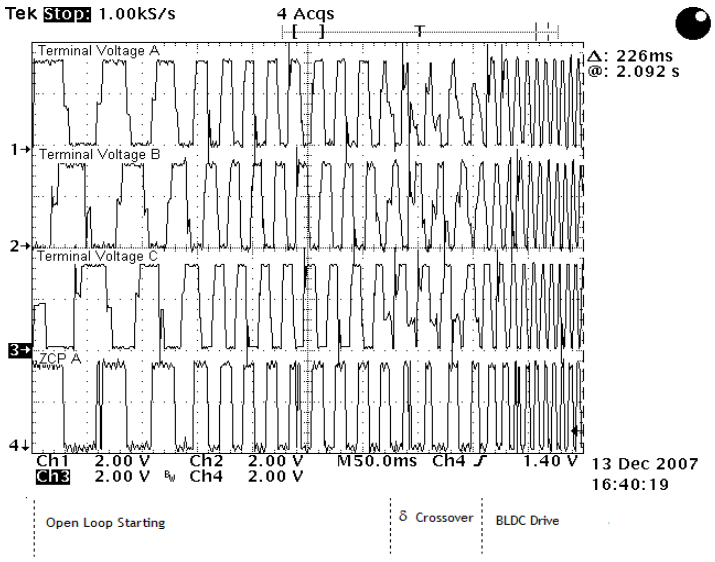

(b)

Figure 6.15 Comparison between (a) gate turn off and (b) δ crossover.

Alternatively, if the starting is from an unknown position, at the worst case, δ crossover versus gate turn-off crossover shows a great improvement of 0.425s from 0.7s.

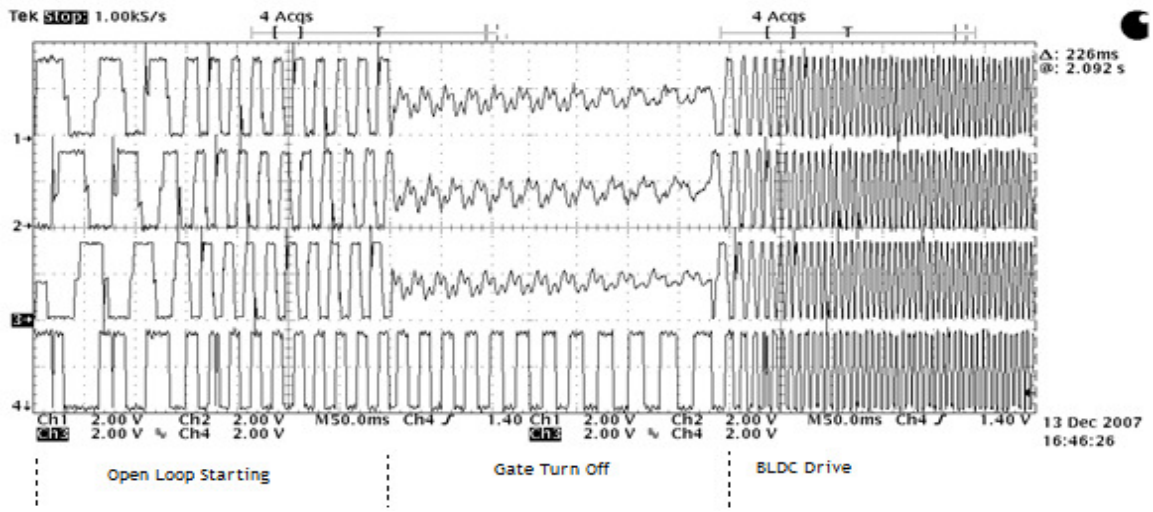

Figure 6.16 Gate turn off waveform starting at dead zone.

Based on the results in this chapter and chapters 3 to 5, the following starting methodology is proposed and applied.

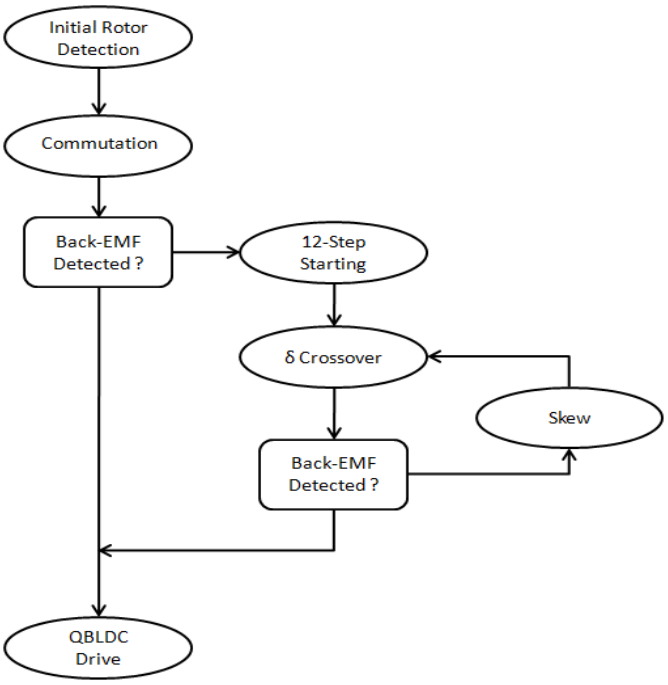

Figure 6.17 Proposed starting methodology.

6.4 Conclusions

In this chapter, the operation of open loop spin up has been studied and investigated. The drawback of ZCP immersed within the voltage injection is addressed. In contrast to the prevailing solution of gate turn-off, δ crossover is proposed. In the proposed scheme, it takes the advantage of (1) ZCP availability and (2) continuance of skew. It has been seen from both the numerical simulation and hardware implementation that the scheme is effective and integrated into BLDC drive. Significant improvements are achieved with a 40% improvement in spin up time.

CHAPTER 7. SENSORLESS SINUSOIDAL-BLDC DRIVE

7.0 Introduction

It is well known that, for the PMSMs with sinusoidal back-EMF, its drive current should be sinusoidal in order to eliminate the ripples of the electromagnetic torque. However, in many applications, such as in HDDs, BLDC drive is nevertheless deployed despite having BLDC motors with sinusoidal back-EMFs due to its simple implementation. Sensorless BLDC gains its popularity as it allows for straightforward and direct position sensing off the actual back-EMF. Typically, these methods are based on the detection of back-EMF Zero Crossing which is largely acute. On the other hand, sensorless sinusoidal methods rely on indirect position sensing off a calculated back-EMF through mathematical modeling or observer measurements. These computational intensive methods, apart from being susceptible to current distortions and parameter variations, require DSP and current sensors. Therefore, BLDC drive is applied on PMSMs at the expense of increased harmonics and power loss, as well as increased torque pulsation.

Application of such a drive on sinusoidal back-EMF motors results in torque ripple. Torque ripple is undesirable as it is a source of electrical and mechanical noise and vibration. Figure 7.1 shows the plots of the current and torque. It can be seen that resulting current and torque depart from those desired.

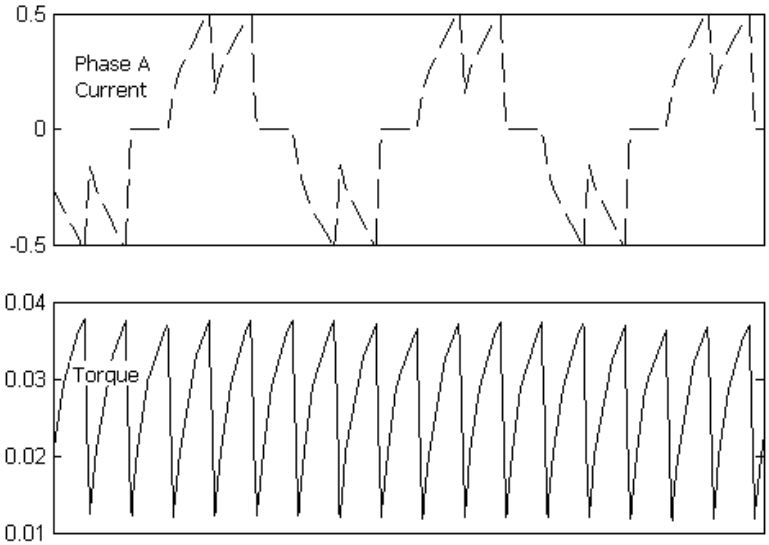

Figure 7.1 BLDC current and torque response.

In this chapter, a sensorless optimal sinusoidal BLDC drive is presented [146-148]. The drive inverter topology as shown in Figure 3.1 with PWM sinusoidal is deployed. The proposed derived scheme is simple and straightforward which brings about the benefits of sensorless sinusoidal drive and negates the need for current sensors by utilizing the freewheeling diodes.

In Section 7.2, the derivation for optimal sinusoidal drive is presented. In the derivation, to achieve power efficiency, the equations for current and back-EMF alignment are setup. Built upon these optimal sinusoidal equations, Section 7.3 proposes a power angle control scheme to accomplish an optimal sinusoidal BLDC where the linear relations between the current and torque, voltage and speed are maintained. In an attempt to execute the scheme sensorlessly, an innovative power angle measurement scheme is devised in Section 7.5. Sections 7.4 and 7.6 present the proposed scheme validated with simulation and experimental results, respectively.

7.1 Sinusoidal Current Drive Operation

For BLDC motors with sinusoidal back-EMFs, it is optimum to inject sinusoidal currents for maximum torque and zero torque ripple production. The torque of a motor is given as

$$T_m = T_a(\theta, i_a) + T_b(\theta, i_b) + T_c(\theta, i_c)\,. \tag{7-1}$$

From (2-35), it is known that

$$T_a = \frac{p}{2}\left[i_a i_f \frac{dM_{af}}{d\theta}\right],\ \ T_b = \frac{p}{2}\left[i_b i_f \frac{dM_{bf}}{d\theta}\right],\ \ T_c = \frac{p}{2}\left[i_c i_f \frac{dM_{cf}}{d\theta}\right], \tag{7-2}$$

and

$$i_f \frac{dM_{af}}{d\theta} = K_e \sin\theta,\ \ i_f \frac{dM_{bf}}{d\theta} = K_e \sin\left(\theta - \frac{2\pi}{3}\right),\ \ i_f \frac{dM_{cf}}{d\theta} = K_e \sin\left(\theta - \frac{4\pi}{3}\right). \tag{7-3}$$

Assuming sinusoidal currents,

$$i_a = I_m \sin(\theta - \phi),\ \ i_b = I_m \sin\left(\theta - \frac{2\pi}{3} - \phi\right),\ \ i_c = I_m \sin\left(\theta - \frac{4\pi}{3} - \phi\right), \tag{7-4}$$

the generated torque would be

$$T_m = \frac{3p}{4} I_m K_e \cos\phi\,. \tag{7-5}$$

From (7-5), it can be seen that with sinusoidal drive, the torque is constant and for maximum torque production, the angle $\phi = 0$. Equivalently, this means the phase currents are in phase with their respective back-EMFs since

$$\begin{cases} Emf_a = K_e \omega \sin\theta \\ Emf_b = K_e \omega \sin\left(\theta - \frac{2\pi}{3}\right) \\ Emf_c = K_e \omega \sin\left(\theta - \frac{4\pi}{3}\right) \end{cases} . \tag{7-6}$$

7.2 Optimal Sinusoidal Drive Equations

The former optimal drive is possible only in the presence of position encoders. In this section, the equations of optimal sensorless sinusoidal drive are derived. Taking the phase current as reference,

$$I_a = I_m \sin\theta . \tag{7-7}$$

Accordingly, the phase voltage V_a and back-EMF E_a can be defined as

$$V_a = V_m \sin(\theta + \alpha) , \tag{7-8}$$

$$E_a = E_m \sin(\theta + \phi) = K_e \omega \sin(\theta + \phi) , \tag{7-9}$$

where V_m is the peak value of the phase voltage,

α denotes the power angle,

E_m is the peak value of the phase back-EMF and

ϕ is the angular phase difference between I_a and E_a.

To simplify the analysis, the impedance of the phase is represented as

$$R_a = Z_a \cos\delta, \tag{7-10}$$

$$\omega L_a = Z_a \sin\delta, \tag{7-11}$$

where $\delta = \tan^{-1}\left(\frac{\omega L_a}{R_a}\right)$,

$$Z_a = \sqrt{R_a^2 + (\omega L_a)^2}. \tag{7-12}$$

With these definitions, the equation representing equivalent electrical circuit is

$$V_m(\cos\alpha + j\sin\alpha) = I_m Z_a(\cos\delta + j\sin\delta) + E_m(\cos\phi + j\sin\phi). \tag{7-13}$$

Equating the real part of equation,

$$I_m Z_a \cos\delta = V_m \cos\alpha - E_m \cos\phi. \tag{7-14}$$

Similarly, equating the imaginary part of equation,

$$I_m Z_a \sin\delta = V_m \sin\alpha - E_m \sin\phi. \tag{7-15}$$

In addition, from the electromagnetic power equation, the load torque, T_L, at speed ω is determined by

$$T_L = \frac{1.5 E_m I_m \cos\phi}{\omega}. \tag{7-16}$$

For optimal drive, it is desirable to have $\phi = 0$. Hence, the optimal current would be defined as

$$I_{opt} = \frac{T_L \omega}{1.5 E_m}. \tag{7-17}$$

From phasor diagram,

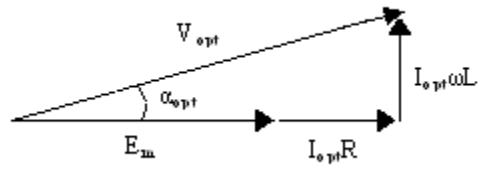

it can be shown that,

$$V_{opt} = \sqrt{\left(I_{opt}\omega_{opt}L\right)^2 + \left(E_m + I_{opt}R\right)^2}\ , \tag{7-18}$$

where $\alpha_{opt} = \tan^{-1}\left(\dfrac{I_{opt}\omega_{opt}L}{E_m + I_{opt}R}\right)$ or (7-19)

$$\alpha_{opt} = \delta - \sin^{-1}\left(\frac{K_e\omega_{opt}}{V_{opt}}\sin\delta\right). \tag{7-20}$$

In reference [143], the equations of optimal sinusoidal drive have been derived based on power equations. The presented approach in this section is different but simpler.

Based on the equations, the following control was proposed as in reference [139]. The methodology, however, was applied under steady state conditions. The fundamental approach is to adjust the applied voltage to its optimal level based on power angle, α, deviation from its optimal value, α_{opt}.

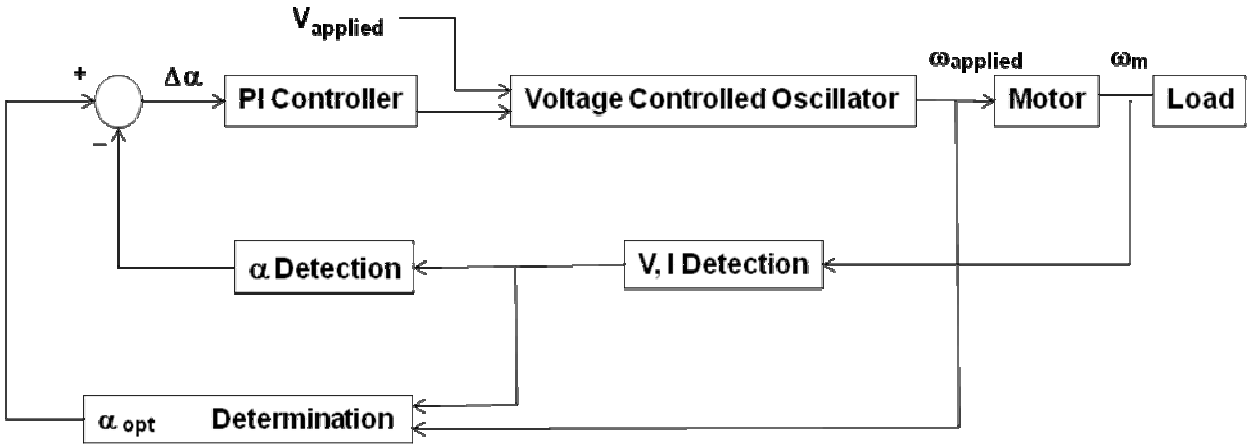

Figure 7.2 Steady state sinusoidal control.

However, in this methodology, the determination of α_{opt} is necessary which requires the knowledge of ω_{opt} or I_{opt}, and indirectly, T_L. Extending from (7-14) and (7-15),

$$\tan\delta = \frac{V_m \sin\alpha - E_m \sin\phi}{V_m \cos\alpha - E_m \cos\phi}. \tag{7-21}$$

It can be shown that

$$\phi = \delta - \sin^{-1}\left\{\left(\frac{V_m}{E_m}\right)\sin(\delta - \alpha)\right\}. \tag{7-22}$$

If α, the angular difference between the zero crossings of V_a and I_a is measurable, ϕ, the delay of E_a with respect to I_a, can be determined. And peak current value, I_m, can be obtained from (7-23)

$$I_m = \frac{V_m \cos\alpha - E_m \cos\phi}{Z_a \cos\delta}. \tag{7-23}$$

With I_m and ϕ available, T_L can be obtained from (7-16). Consequently, I_{opt} can be obtained and alternatively, with the usage of current sensors, I_a can be measured and α_{opt}

can be determined accordingly. The voltage can then be adjusted accordingly to obtain optimality.

In contrast to what has been proposed in this section, where for a given load and rotational speed, the voltage is adjusted to its optimality, the next section introduces a new concept whereby for a given load and voltage, the speed will run up to an appropriate speed to match the applied voltage.

7.3 Optimal Sinusoidal BLDC Drive

In this section, the concept of sensorless sinusoidal BLDC is described. The aim is to conceive a drive scheme such that, as with BLDC drive, the speed varies with voltage injected but with sinusoidal current. For a BLDC motor under BLDC drive [142,145],

$$V_{m,applied} \approx \left(\frac{3\sqrt{3}}{\pi}\right) K_e \omega \,, \tag{7-24}$$

$$T_L \approx \left(\frac{3\sqrt{3}}{\pi}\right) K_e I_m \,. \tag{7-25}$$

Alternatively, under optimal sinusoidal drive,

$$V_{m,applied} \approx K_e \omega_{opt} + I_{m,opt} R \,, \tag{7-26}$$

$$T_L = 1.5 K_e I_{m,opt} \,. \tag{7-27}$$

In other words, under optimal sinusoidal drive, the optimal state is similar to BLDC operation whereby the voltage and speed, torque and current are linearly related. What is different is, in BLDC operation, the voltage is applied together with the position feedback

in a coordinated fashion and brings the speed of the motor to an equilibrium speed. In what has been proposed in Section 7.2, on the contrary, the voltage is controlled at an equilibrium level with the speed held at constant. What is to be achieved is under an applied voltage, the speed of the motor is controlled at equilibrium but yet with sinusoidal currents. It is coined as sinusoidal BLDC, and together with maximum efficiency, it is termed as optimal sinusoidal BLDC.

Recall from (7-19), α_{opt} is given by.

$$\alpha_{opt} = \tan^{-1}\left(\frac{I_{opt}\omega_{opt}L}{E_m + I_{opt}R}\right) \tag{7-28}$$

One strategy would be to pre-determine the optimal angle, α_{opt}, for the applied voltage and load. The injected frequency is skewed until the power angle, α_{meas} reaches α_{opt}. Such a scheme, even if the determination of I_{opt} is possible (as in Section 7.2), would not be able to drive it to optimal operation. The reason lies in the non-uniqueness of the optimal power angle value. For illustration purposes, the power angle waveform during a speed ramp-up waveform is provided in Figure 7.3.

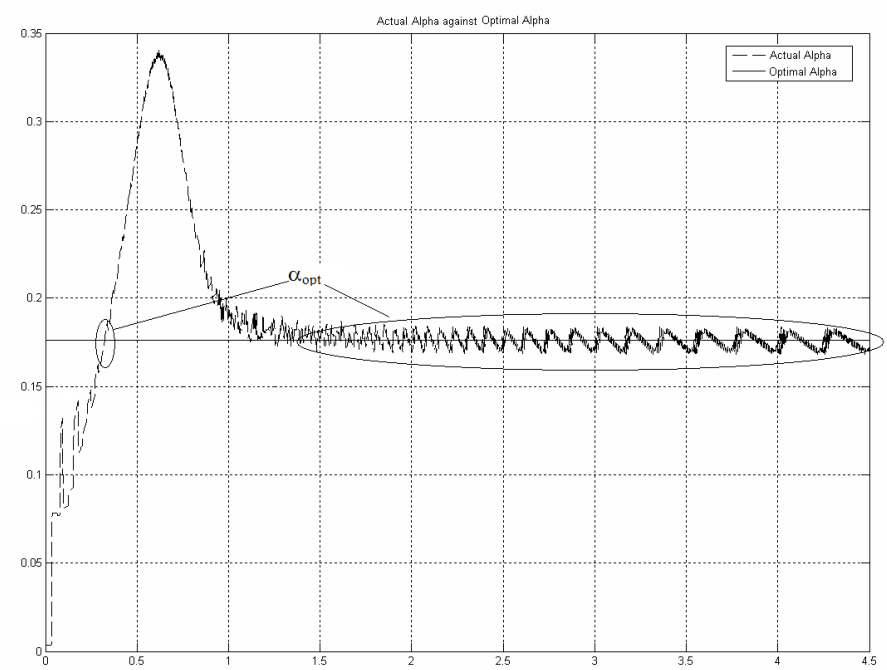

Figure 7.3 Plot of actual angle, α_{meas}.

It can be seen that in the steady state power angle stays at α_{opt}. However, there lies another point in the initial ramp up which can give the same power angle value. In essence, if $\omega = \omega_{opt} \Rightarrow \alpha = \alpha_{opt}$ but if $\alpha = \alpha_{opt} \not\Rightarrow \omega = \omega_{opt}$. Therefore, if the injected frequency is skewed until the power angle reaches α_{opt}, it would not reach ω_{opt}.

At this juncture, two issues need to be considered, the determination of α_{opt} and the skewing technique. We propose to tackle this issue concurrently by introducing a modification to (7-20). From (7-22), it can be shown that

$$\alpha = \delta - \sin^{-1}\left(\frac{K_e \omega}{V_{applied}} \sin(\delta - \phi)\right). \tag{7-29}$$

In optimality, $V_{applied} = V_{opt}$, $\omega = \omega_{opt}$ and $\phi = 0$ and (7-20) are met. Accordingly, an elegant modification can be made to (7-20) .

$$\alpha_{opt,applied} = \delta - \sin^{-1}\left(\frac{K_e \omega_{applied}}{V_{applied}} \sin\delta\right). \tag{7-30}$$

(7-30) is equivalent to (7-29) only at optimality and interestingly, $\alpha = \alpha_{opt,applied}$ only when $\phi = 0$, ie. optimality. In other words, by controlling α to $\alpha_{opt,applied}$ would be to make $\phi = 0$. The plot of the simulation result for the optimal power angle versus the measured power angle is provided in Figure 7.4. It can be observed that in this case, $\omega = \omega_{opt} \Leftrightarrow \alpha = \alpha_{opt,applied}$.

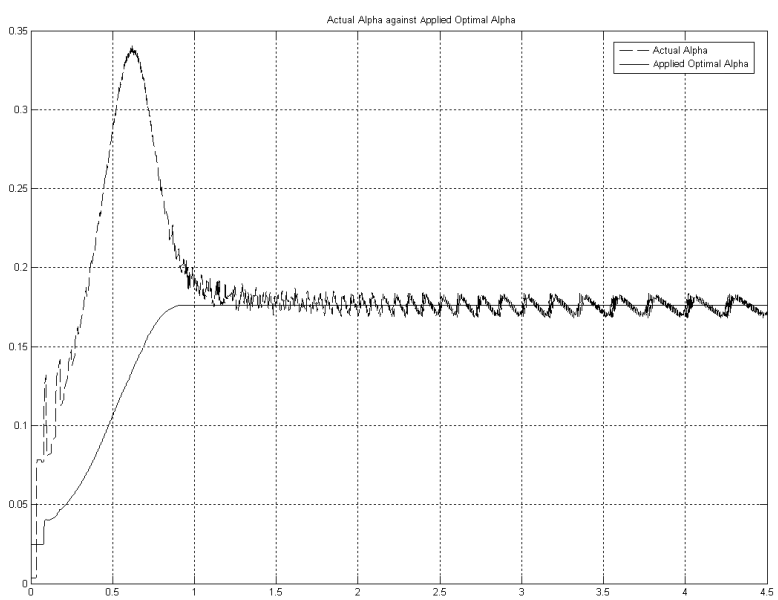

Figure 7.4 Plot of actual angle, α_{meas} versus applied optimal angle, $\alpha_{applied}$.

Another significant contribution to this strategy is that it allows for the determination of α_{opt} without the need for I_{opt} determination as the system can be controlled to its optimal state. With this, the following control methodology is proposed.

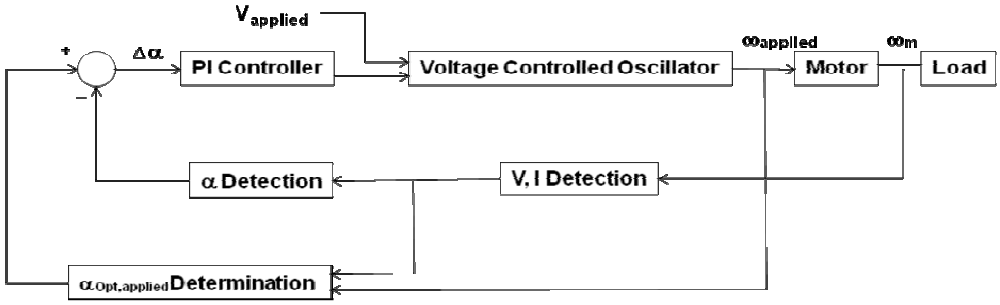

Figure 7.5 Sinusoidal BLDC control.

7.4 Simulation

7.4.1 Overview

Figure 7.6 shows the Simulink top level block entry for the complete sensorless sinusoidal BLDC drive.

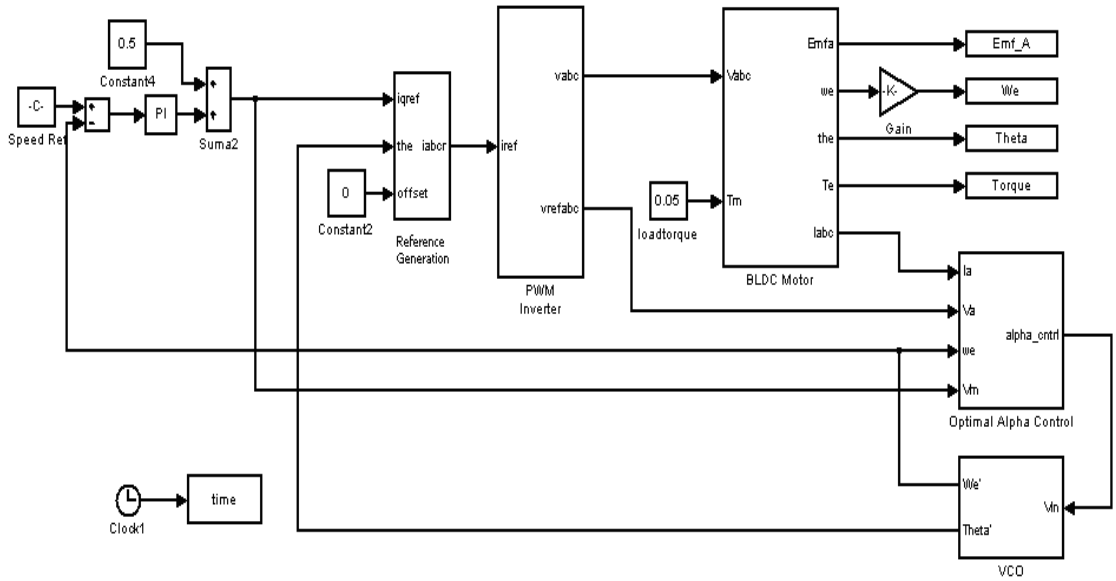

Figure 7.6 Simulink top level block entry for sensorless sinusoidal BLDC drive.

7.4.2 Best Efficiency Angle Controller

Figure 7.7 shows the Simulink block entry for the best efficiency angle controller. The signals α_{opt} and $\alpha_{opt,meas}$ are both fed to a PI controller for VCO control.

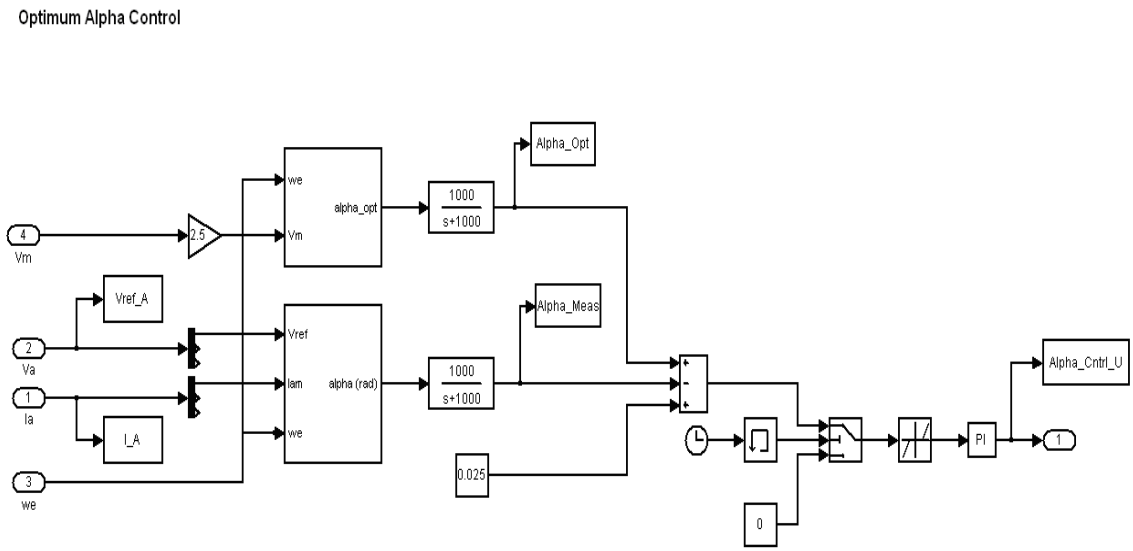

Figure 7.7 Simulink block entry best efficiency angle controller.

7.4.3 Voltage Controlled Oscillator

Figure 7.8 shows the Simulink block entry for voltage controlled oscillator (VCO). A PI controller based on the power angle difference controls the VCO. The VCO, in turn, generates the virtual position for sinusoidal reference generation.

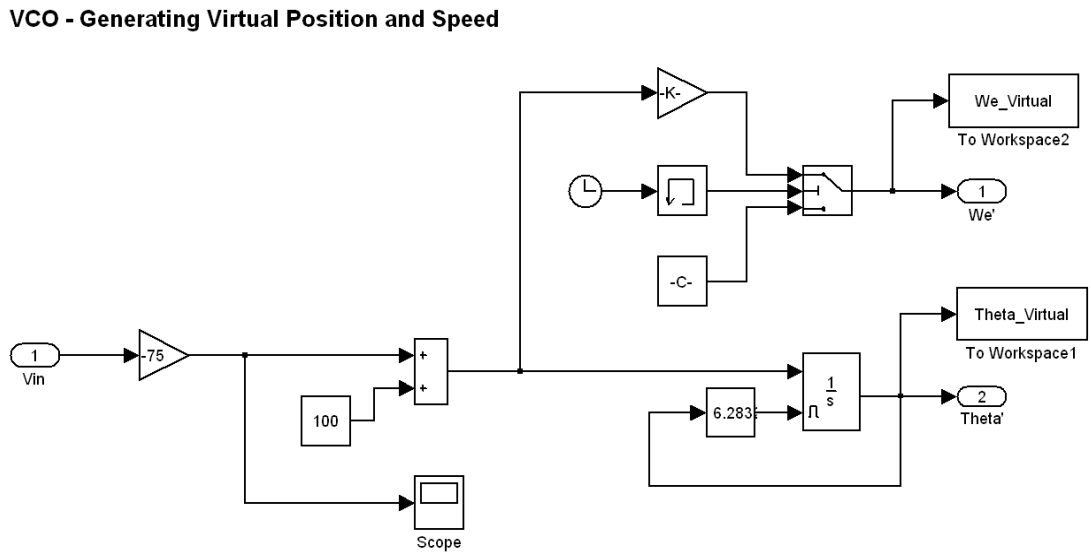

Figure 7.8 Simulink block entry for voltage controlled oscillator.

7.4.4 Simulation Results

The motor was started from standstill and various plots were captured for analysis. Figure 7.9 shows the plots of phase current versus phase voltage as well as phase current versus back-EMF during starting. It can be seen that the angle between phase current and back-EMF is not optimal. Nevertheless, in the steady state as seen in Figure 7.10, the phase current and back-EMF are in phase, illustrating the optimality convergence of the design.

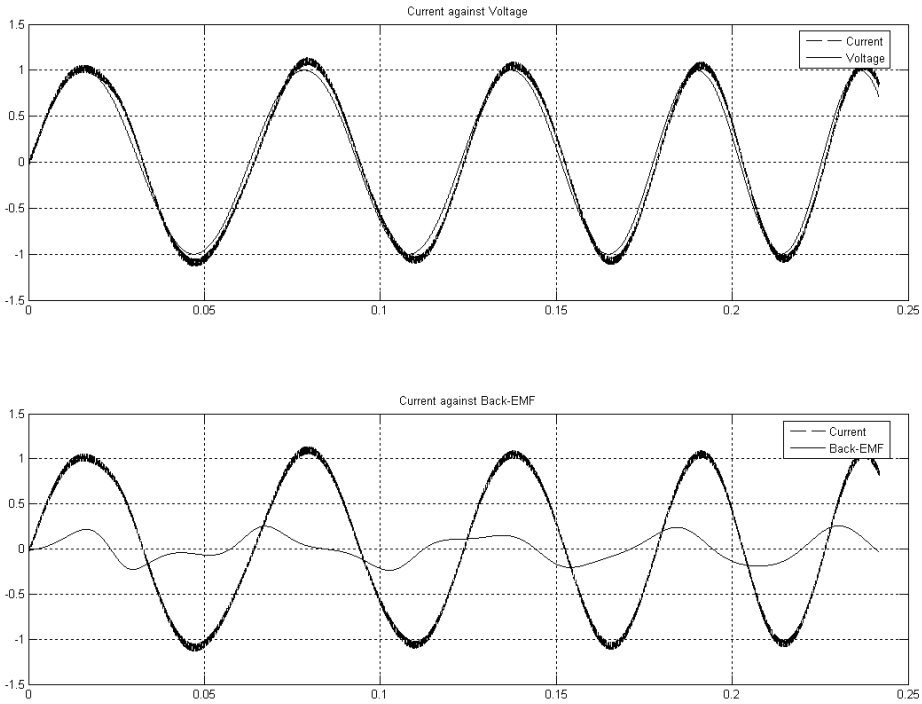

Figure 7.9 Simulated plots for motor during starting.

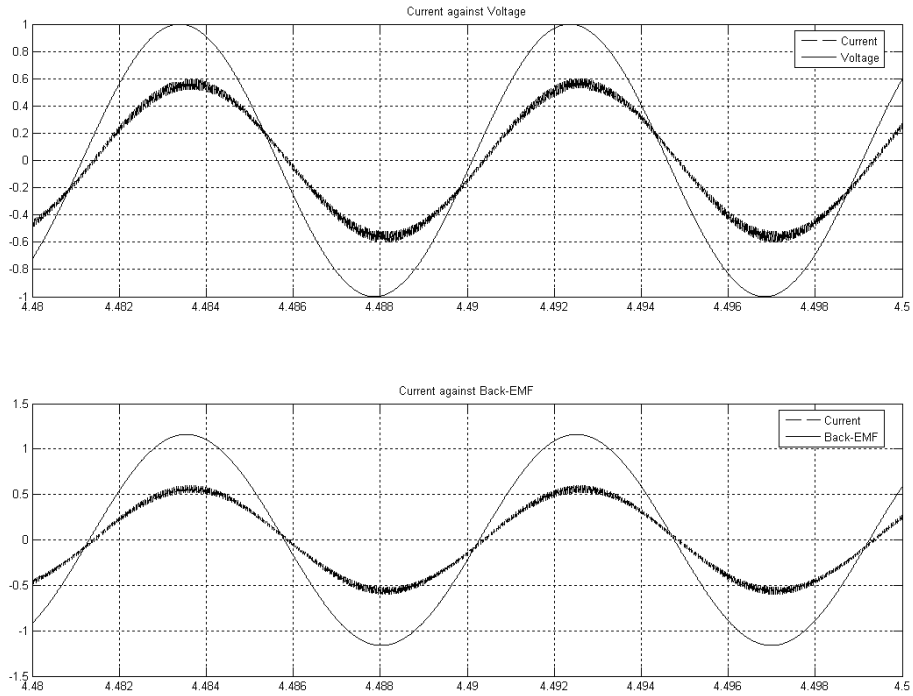

Figure 7.10 Simulated plots for motor in steady state.

Figure 7.11 shows the plot of the measured power angle, $\alpha_{opt,meas}$, versus the optimal power angle, α_{opt}. From the plot, it can be seen that, the angle converges to the optimum value, offset by a safety margin. Figure 7.12 shows the speed plot for the controller. As a comparison of the torque performance, Figure 7.13 shows the torque plot for BLDC versus the proposed drive. The torque ripple factor is improved from 65.0% to 12.5%.

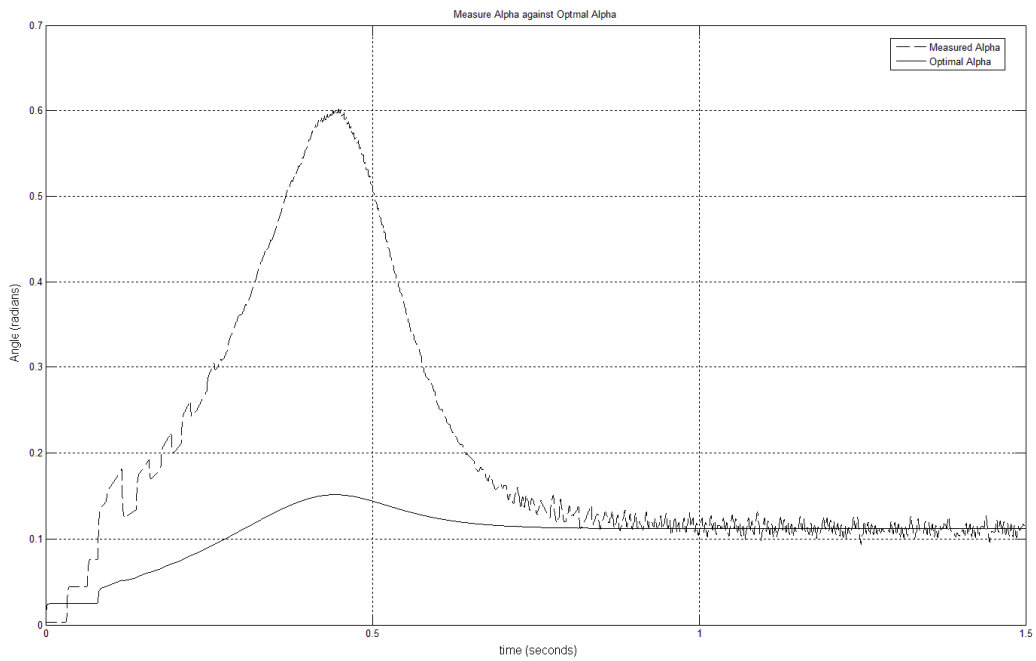

Figure 7.11 Simulated plots for α_{opt} versus α_{meas}.

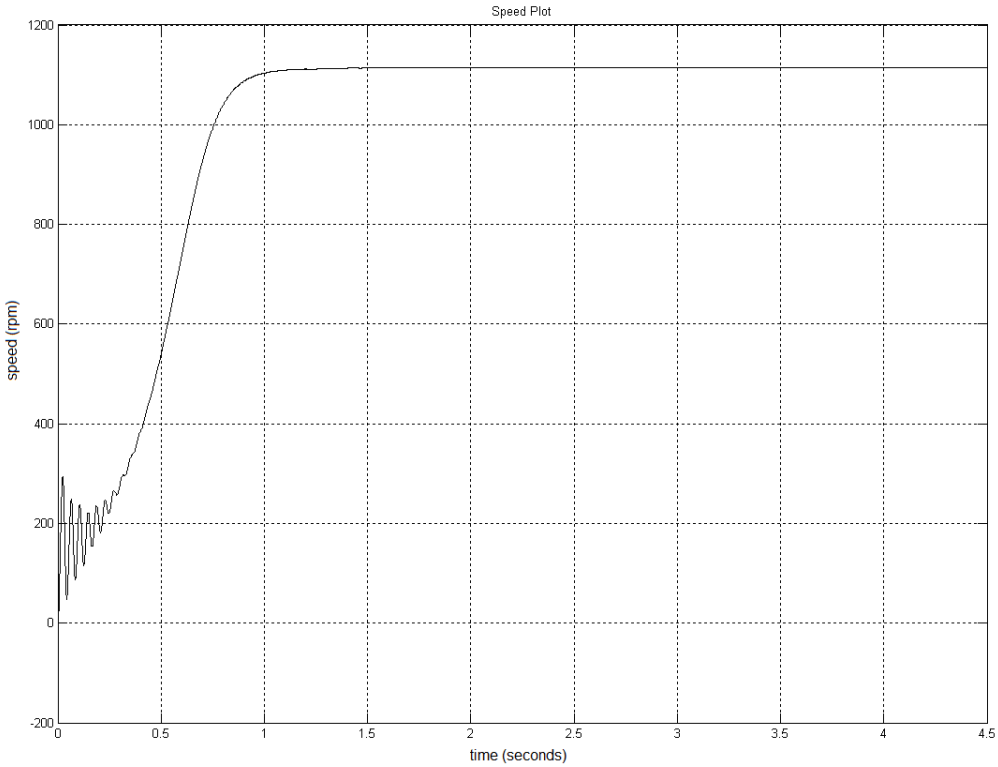

Figure 7.12 Simulated plots for motor speed from standstill.

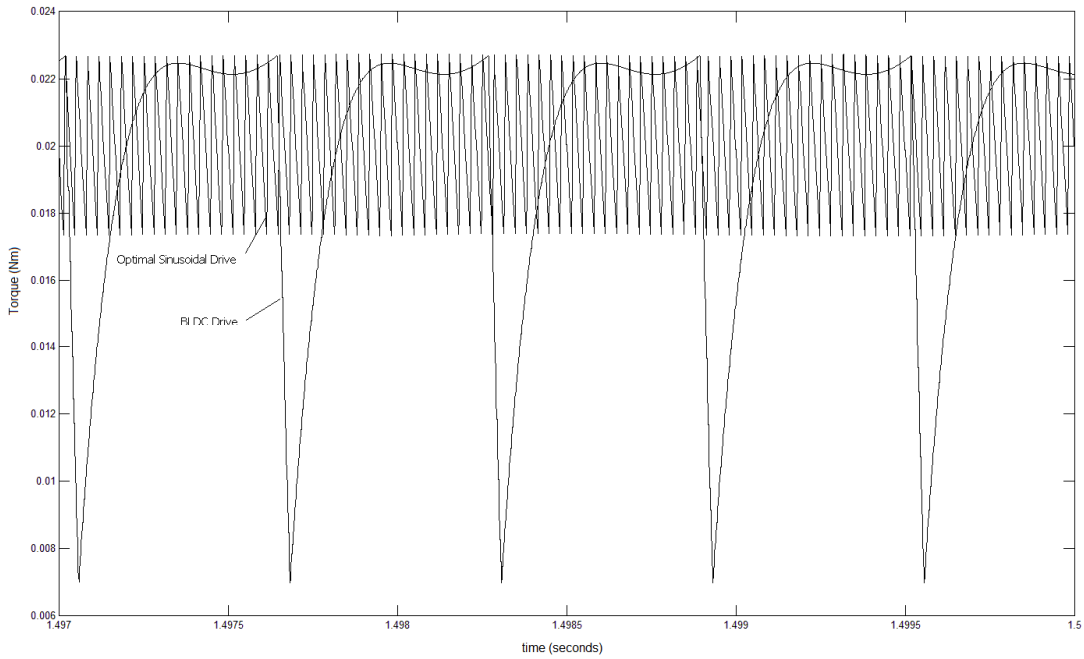

Figure 7.13 Simulated plot for BLDC driven and sinusoidal driven torques.

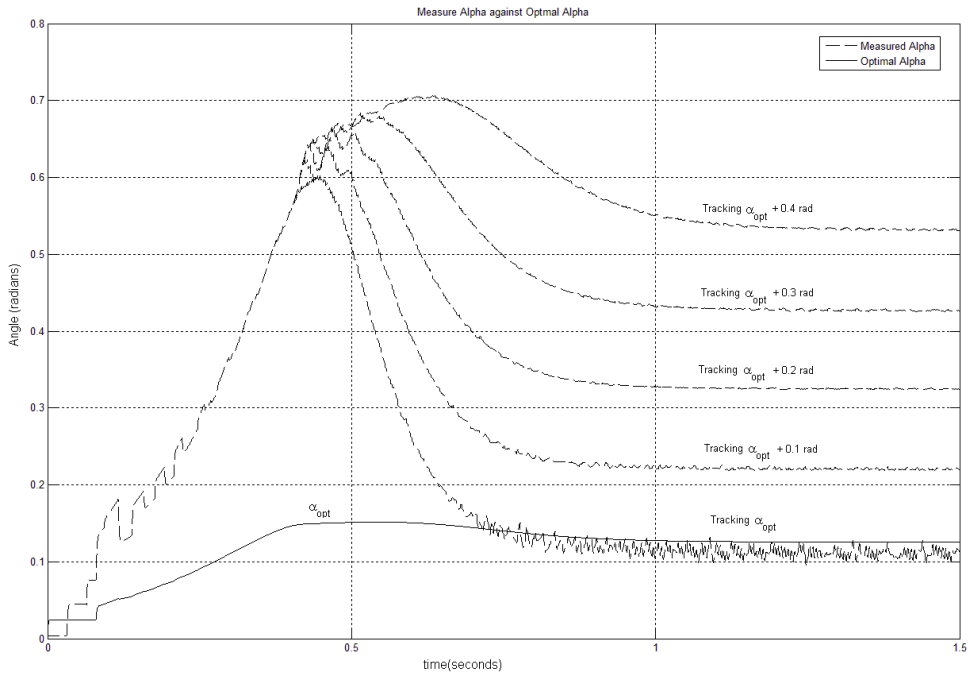

Figure 7.14 Simulated plot for drive tracking sub-optimal angles.

As an illustration, the system has been simulated to track at various power angles, α_{opt}+0.1n rad where n=0-4. The plots for the various angles are provided in Figure 7.14. The copper loss is tabulated in Table 7.1. It can be seen that at the optimum angle, the power loss is the lowest for the system.

Table 7.1 Tabulated Copper Loss for Various Power Angles

$\alpha_{meas=}$	α_{opt}	α_{opt}+0.1rad	α_{opt}+0.2rad	α_{opt}+0.3rad	α_{opt}+0.4rad
Copper loss	0.5	0.51	0.55	0.6	0.72

As highlighted earlier, the objective is to achieve sinusoidal BLDC and the input voltage is varied at several steps. The subsequent speed waveform is provided in Figure 7.15. From the plot, it can be seen that with increased voltage, increased speed is reached at steady state.

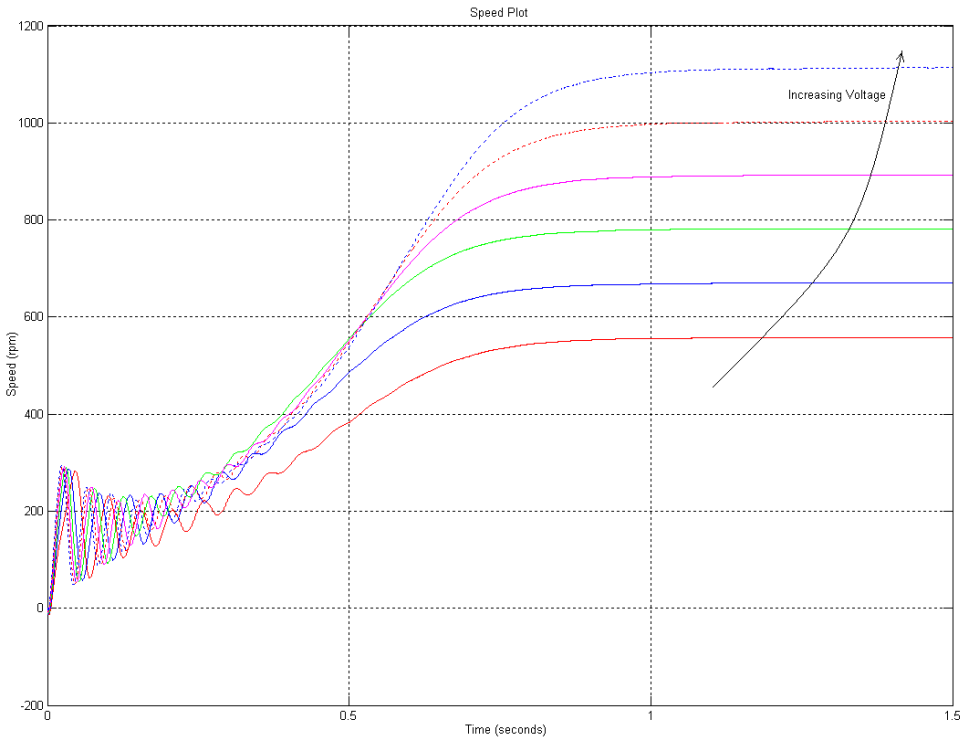

Figure 7.15 Simulated plots for motor speed for various input voltages.

7.5 Optimal Sensorless Sinusoidal BLDC Drive

In the adoption of the proposed control methodology, the measurement of the power angle, α_{meas}, is crucial. In the measurement of α_{meas}, the relative positions of voltage and current are to be determined. A counter can be triggered at voltage zero crossing points and it is latched at instants of current zero crossing points. The latched counter values would provide the clock counts for the time lapse between the two zero crossing points. To obtain α_{meas},

$$\alpha_{meas} = \frac{\Delta t}{T} \times 2\pi \tag{7-31}$$

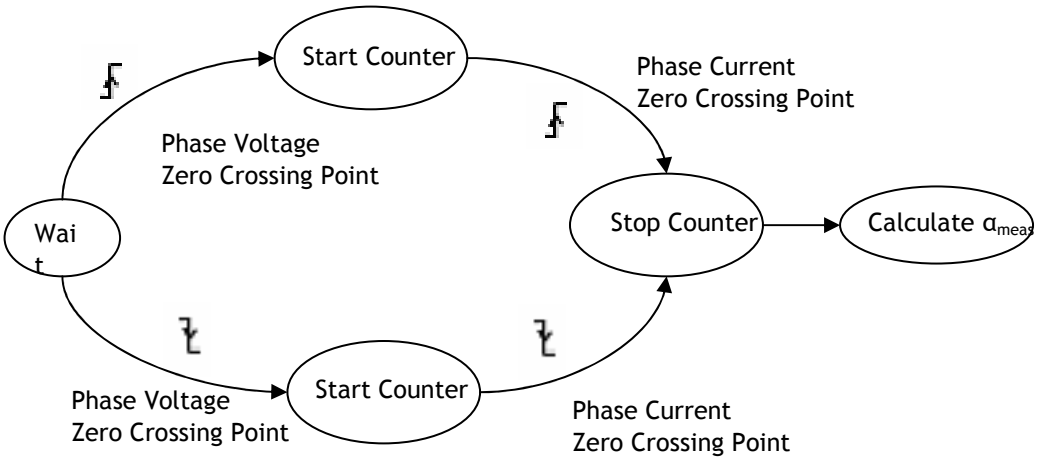

Figure 7.16 Flow chart for α measurement.

The voltage zero crossing points can be estimated using the applied voltage zero crossing points instead of a direct measurement.

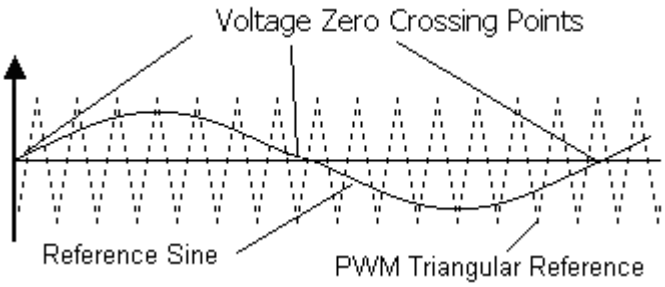

Figure 7.17 Voltage zero crossing points estimation.

As for the current zero crossing points (IZCPs) detection, traditional method accomplishes this task using sensing resistors connected in series to the motor windings. The polarity of the resistive voltage will provide the current direction and the zero current crossing is given by the instant of voltage polarity change. The drawbacks of this method are (1) it incurs additional resistive loss and (2) it requires the use of additional resistors.

A method which avoids the shortcomings of the resistors by making use of the freewheeling diodes for detection is proposed.

The PMSM is driven by a three-phase inverter circuit as shown in Figure 1.2. It consists of six power semiconductor transistors with a protection diode connected in parallel to each of these transistors. In a PWM drive, the upper and lower switches are gated simultaneously. For example, prior to the gating of the lower switch Q_{AL}, if the output current is negative, it will be freewheeling through the diode D_{AH}. This freewheeling gives rise to a diode voltage across D_{AH}.

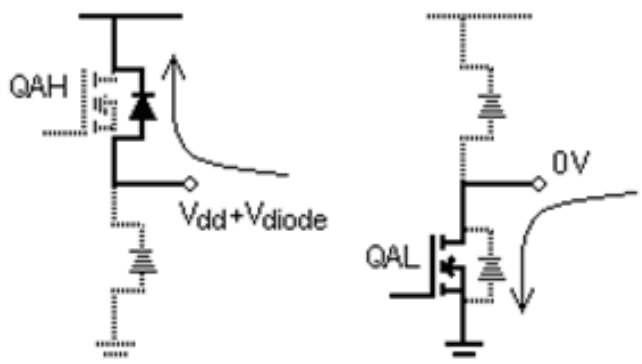

Figure 7.18 Negative current freewheeling.

Conversely, if the output current is positive, prior to turning on the upper switch Q_{AH}, the current will be freewheeling through the diode D_{AL}. This freewheeling similarly gives rise to a diode voltage drop across D_{AL}.

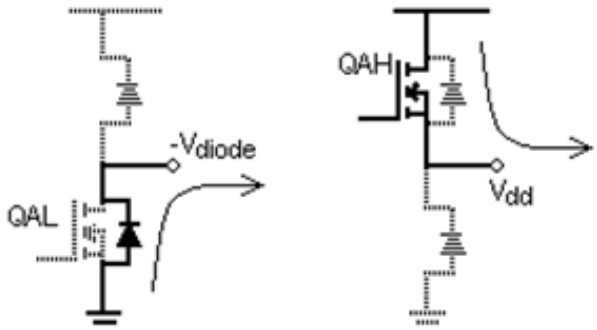

Figure 7.19 Positive current freewheeling.

The polarity of the current can thus be determined from the occurrence of voltage drop across D_{AH} or D_{AL}. A negative current will give voltage drop across D_{AH} and a positive current will give voltage drop across D_{AL}. Consequently, current zero crossing can be given by the polarity change crossing points. The rising edge of voltage drop across D_{AH} will give the zero crossing of positive to negative current and, conversely, the falling edge of voltage drop across D_{AL} will give the zero crossing of negative to positive current.

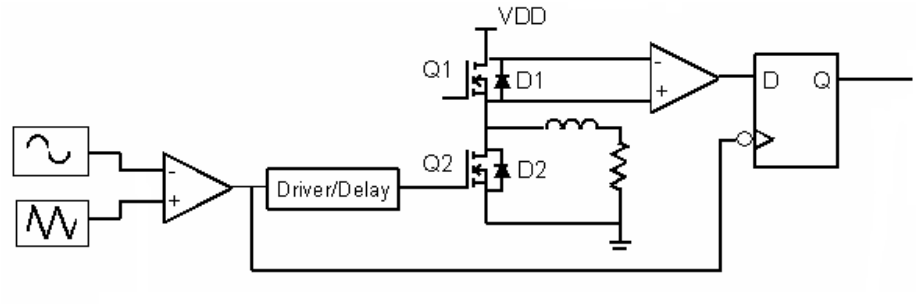

Figure 7.20 Schematic for current zero crossing detection.

Similarly, the rising edge of the voltage drop across D_{AL} will give the zero crossing of negative to positive current and, conversely, the falling edge of voltage drop across D_{AL} will give the zero crossing of positive to negative current.

In the initial investigation of this proposed method, due to the narrowing pulse width of the gating signal as the current magnitude increases as seen in Figure 7.21, the voltage drop across the diode is difficult to be detected as the notch goes narrower.

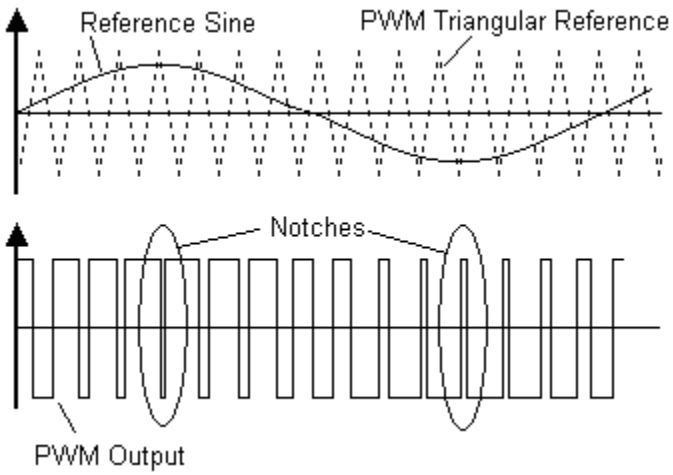

Figure 7.21 PWM plots.

The resultant current zero crossing waveform is distorted. Figure 7.22 shows the distorted current ZCP waveform for the upper diode.

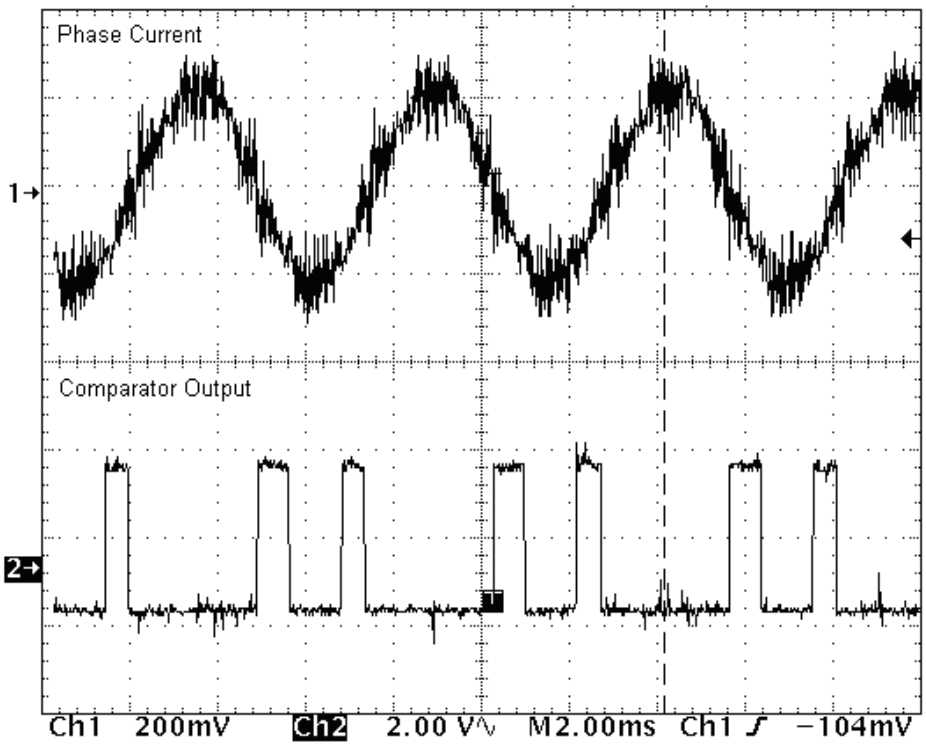

Figure 7.22 Current and IZCP Waveforms

To rectify this problem, it would be useful to retrieve the information that can be available from the waveform generated. Taking a sinusoidal reference, it is reasonable to assume that the current transitions will not occur from 210° - 330° as well as the current would be negative in that interval. Hence, by doing a logic OR, the gap will be set to high. Conversely, in the detection of positive currents, it is reasonable to assume that current transitions would not occur 30° - 150°. Figure 7.23 shows the schematic diagram of the algorithm and Figure 7.24 gives the experimental waveform of the modified algorithm.

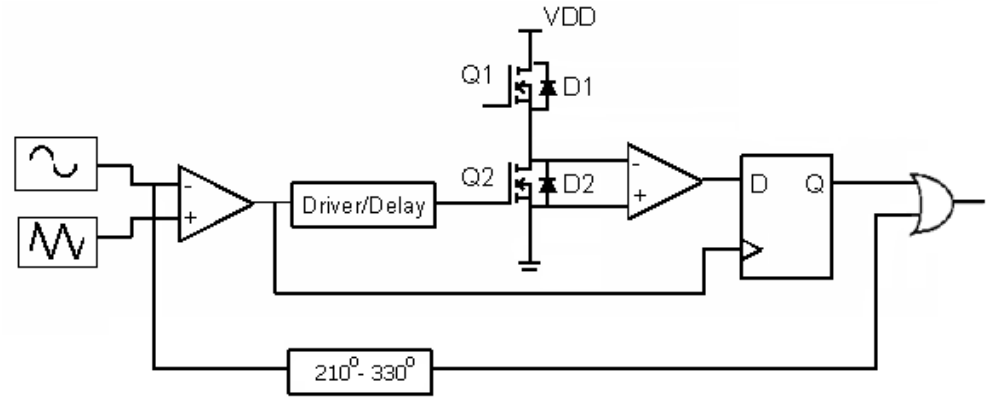

Figure 7.23 Modified schematic current ZCP detection.

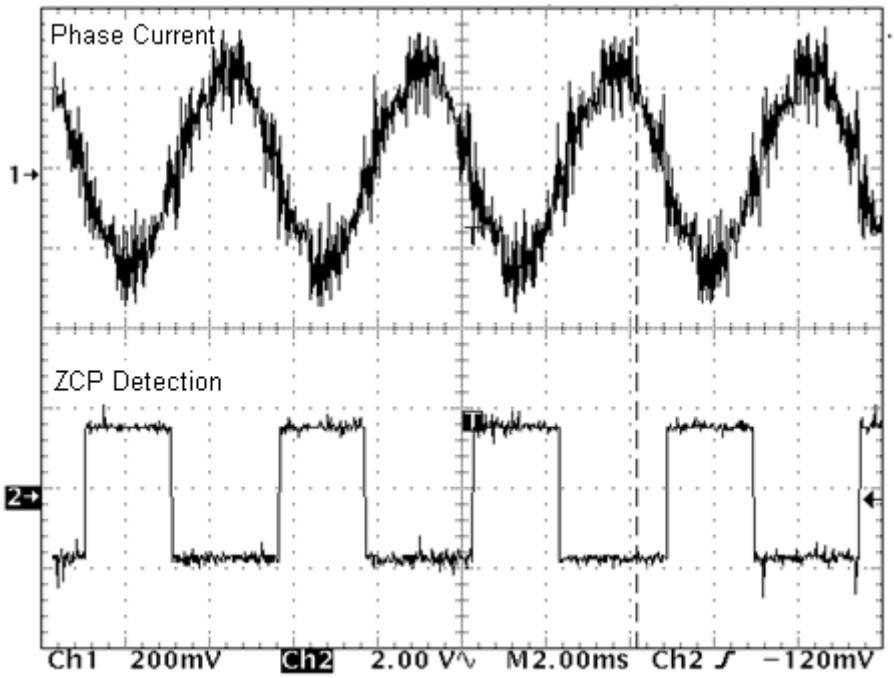

Figure 7.24 Current and its ZCP waveforms based on modified algorithm.

Thus, lossless current zero crossing can be detected with the freewheeling diodes without introducing additional elements.

7.6 Hardware Implementation and Results

The resulting controller is implemented to get the voltage and current waveforms at two different voltages, V_{DC} = 5V and 8.48V, shown in Figure 7.25 to Figure 7.27. It can be seen that for a higher voltage, a higher speed is achieved. This is consistent with the objective of sensorless sinusoidal BLDC. In addition, additional load was introduced and sinusoidal currents were maintained but at a lower speed. The plot is shown in Figure 7.27.

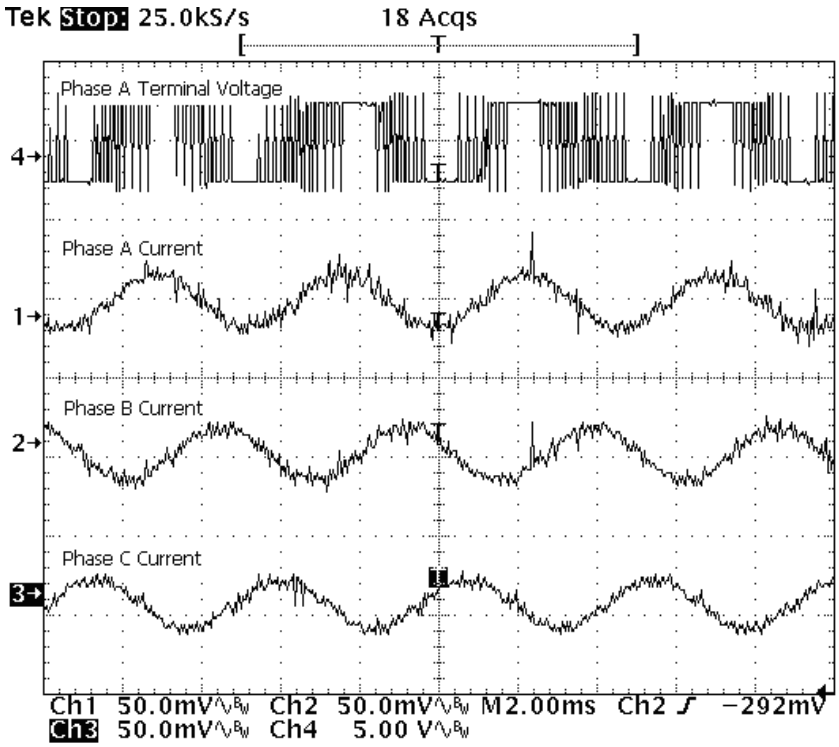

Figure 7.25 Captured voltage and current waveforms for V_{DC} = 5V.

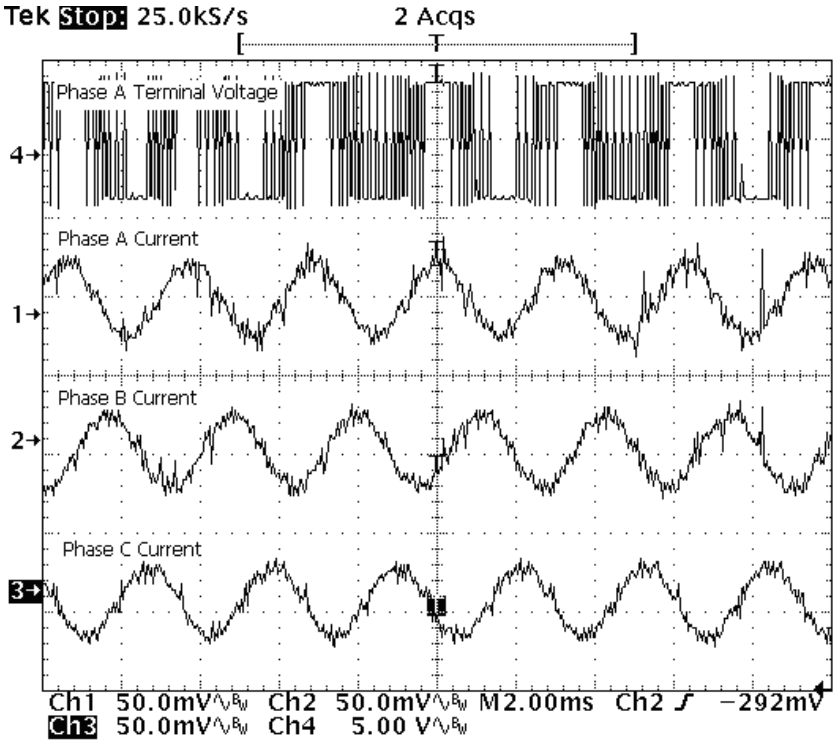

Figure 7.26 Captured voltage and current waveforms for V_{DC} = 8.48V.

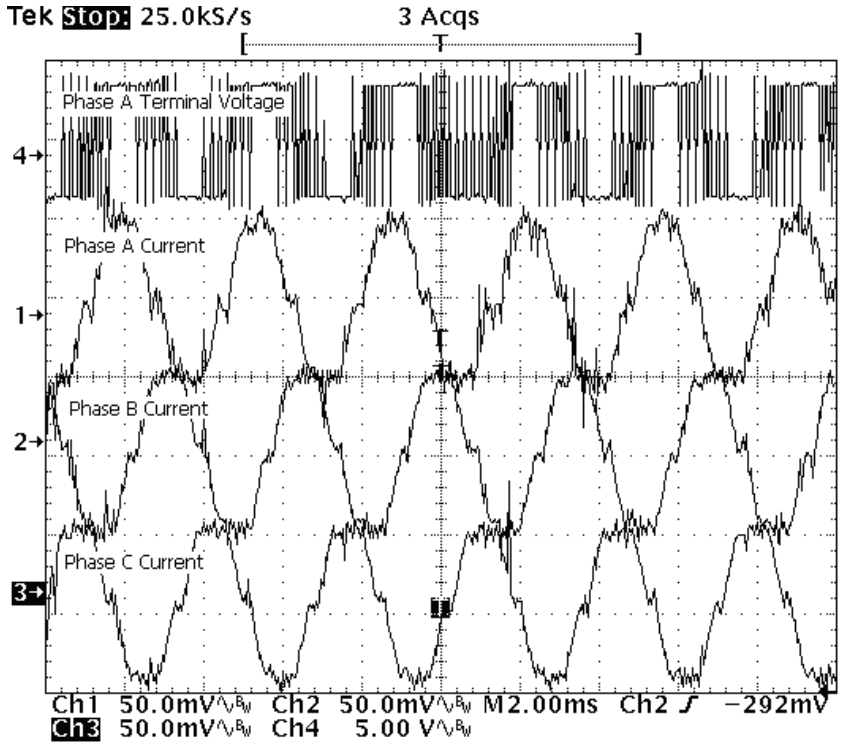

Figure 7.27 Captured waveforms for V_{DC} = 8.48V with increased load.

For the investigation of optimality, an encoder (Gurley Instruments) was mounted onto the spindle motor and aligned with its back-EMF. The bit changes for the MSB are mechanically aligned with the back-EMF ZCPs. During the operation, it can be seen from the bit changes are aligned with the current ZCPs. This implies that the current is in phase with the back-EMF and thus operation is kept at optimality for the maximum power and minimum copper loss.

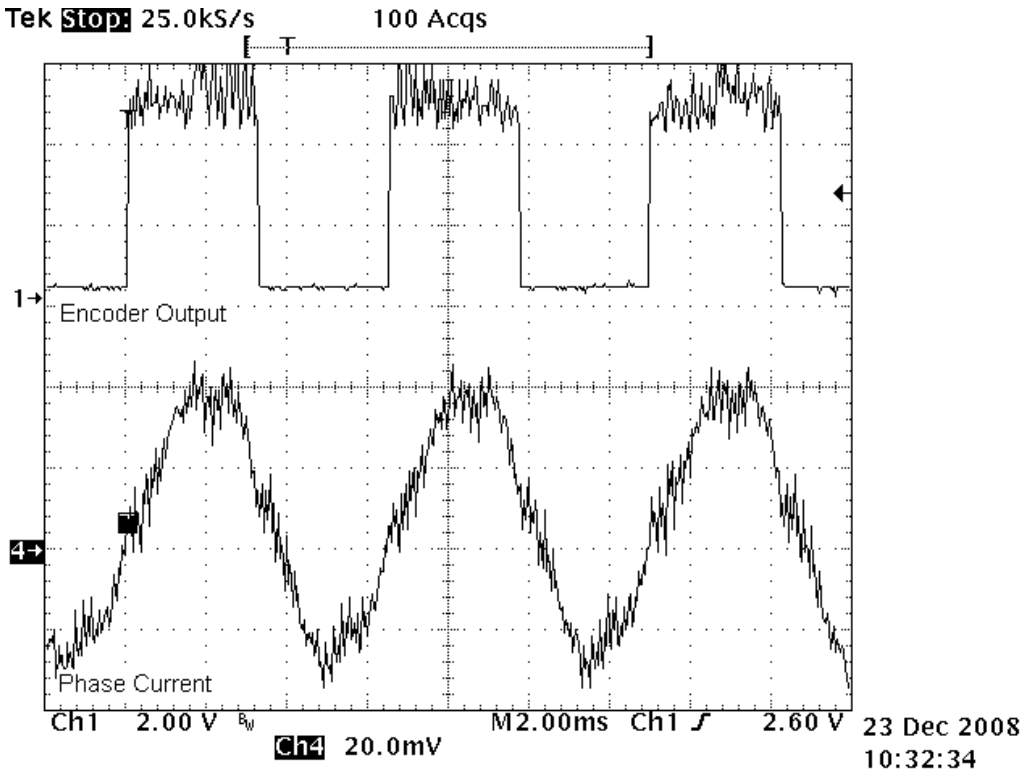

Figure 7.28 Encoder MSB (back-EMF ZCPs) versus phase current.

As an indicative measure of the torque, its effects on acoustics were measured. The same setup provided in section 4.5.1 was used. It can be seen that a significant improvement of up to 30dB can be observed.

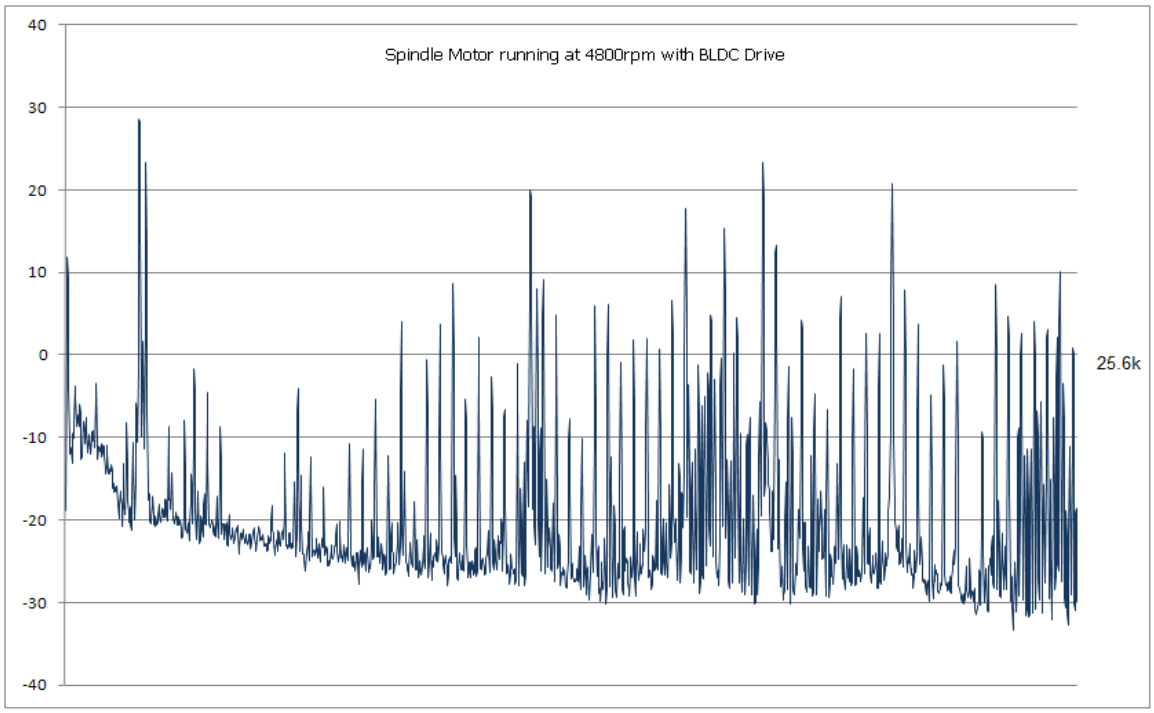
Spindle Motor running at 4800rpm with BLDC Drive
40
30
20
10
0
-10
-20
-30
-40
25.6k

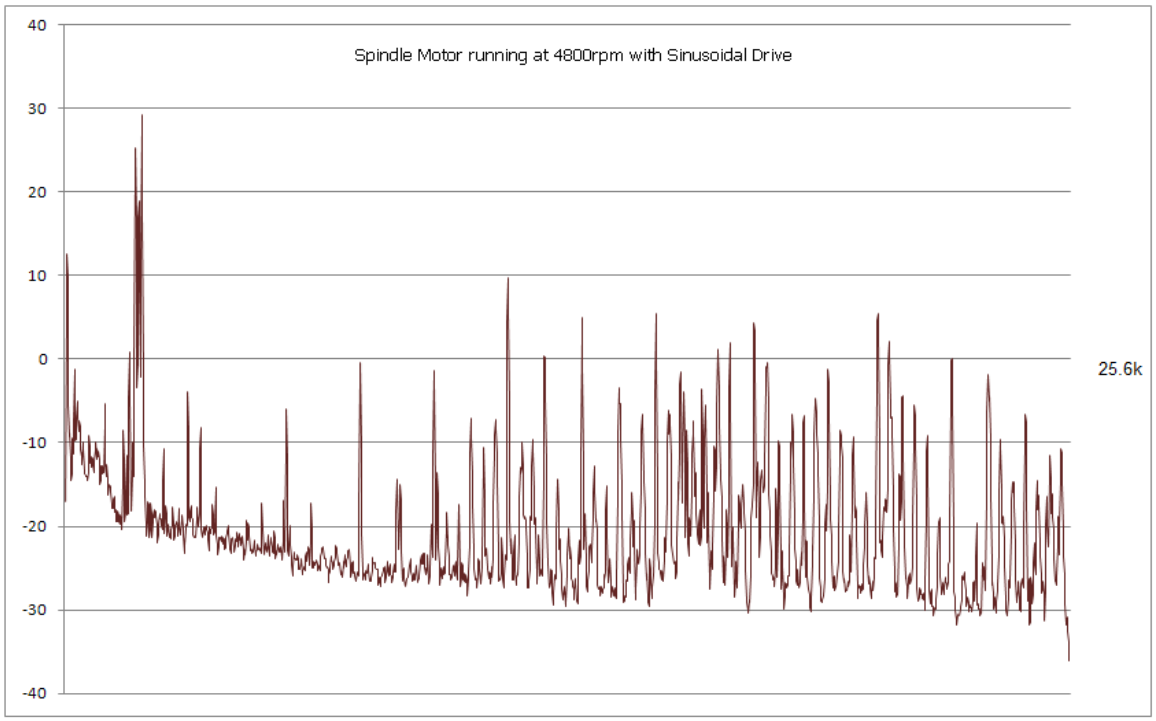
Spindle Motor running at 4800rpm with Sinusoidal Drive
40
30
20
10
0
-10
-20
-30
-40
25.6k

(a)

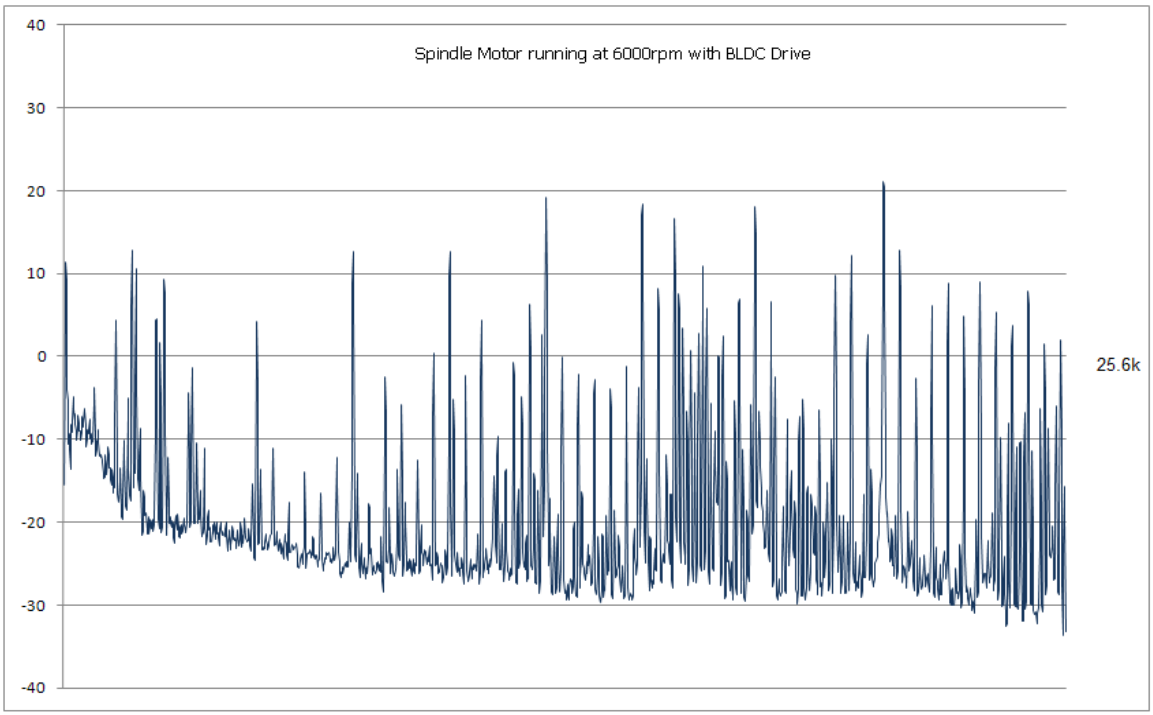
Spindle Motor running at 6000rpm with BLDC Drive
40
30
20
10
0
-10
-20
-30
-40
25.6k

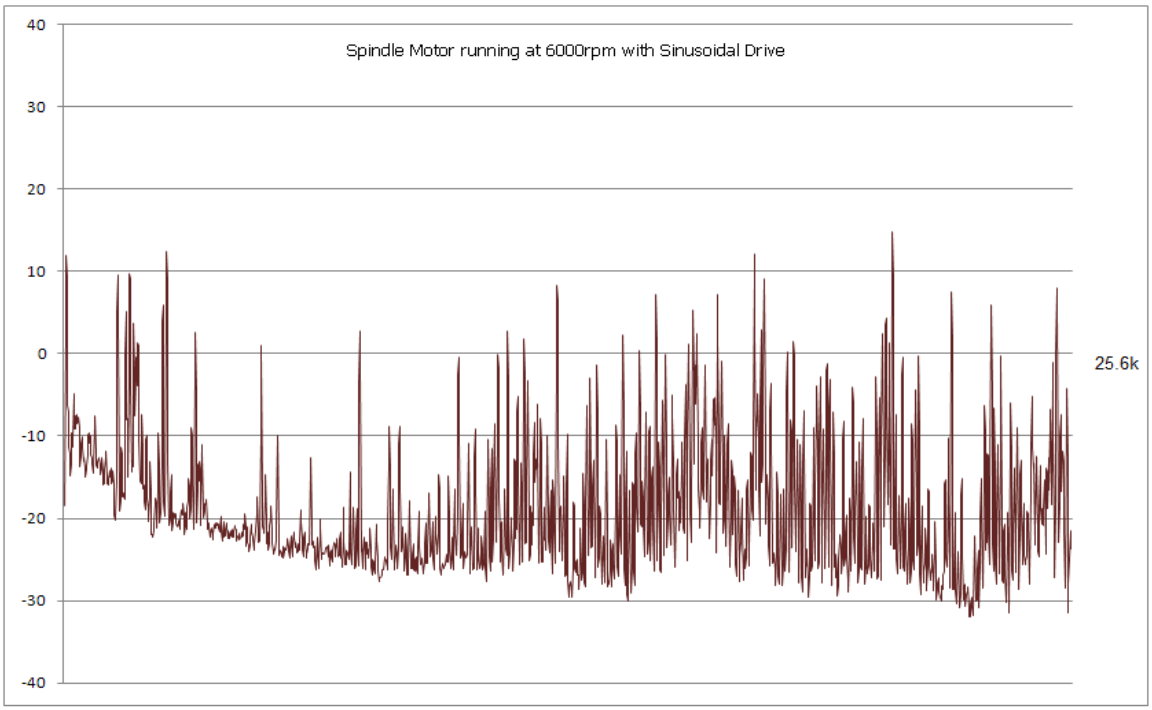
Spindle Motor running at 6000rpm with Sinusoidal Drive
40
30
20
10
0
-10
-20
-30
-40
25.6k

(b)

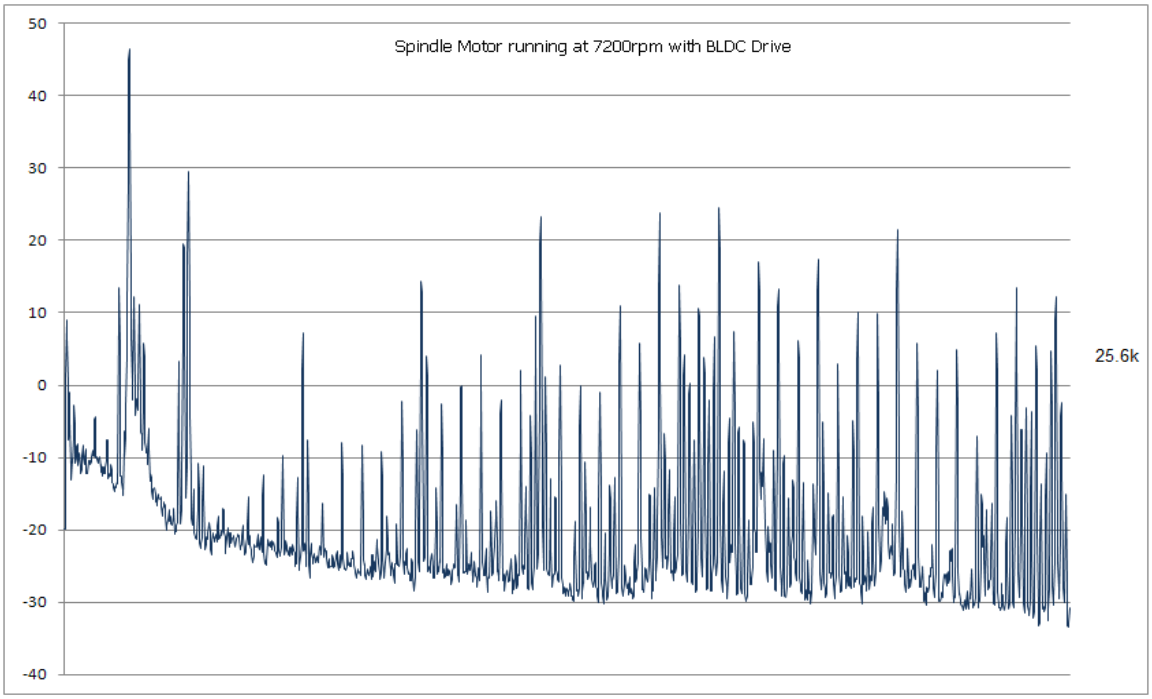

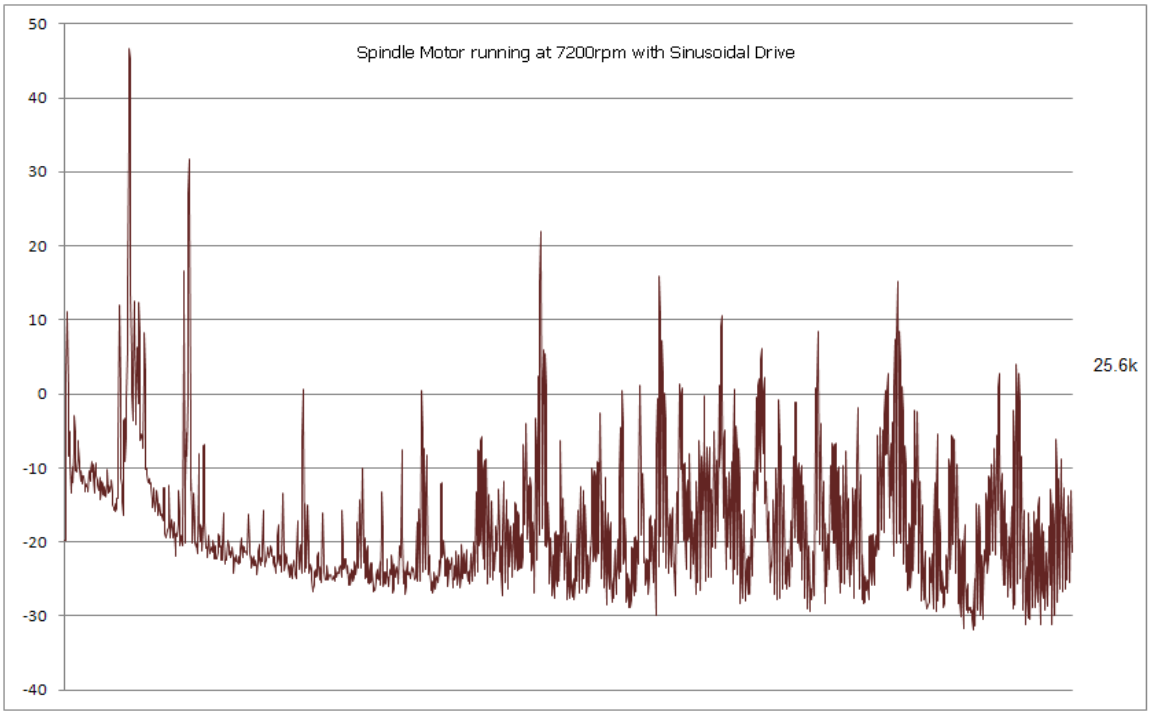

(c)

Figure 7.29 Acoustic performance for BLDC versus sinusoidal BLDC running at (a) 4800 rpm (b) 6000 rpm (c) 7200 rpm

7.7 Conclusions

In this chapter, a sensorless optimal sinusoidal BLDC drive for PMSM was proposed. In the proposed drive, the torque performance was improved, the power was optimal as the motor current and its respective back-EMF were aligned, sensorless control was achieved as no position or current sensors were used and the drive made BLDC as the proportional relationship between dc link voltage and speed was maintained. The novel strategy encompasses a power angle control to provide an optimal sinusoidal BLDC and an innovative power angle measurement based on freewheel currents to construct a sensorless drive. It has been shown both on simulation and hardware that the control drive accomplished the intended objectives, and the results proved the effectiveness of the proposed method.

CHAPTER 8. CONCLUSIONS

Initiated by the advent high performance processors and energy concerns, Permanent Magnet Synchronous Motors (PMSM) are widely adopted in numerous consumer products. PMSM with sensors are traditionally driven sinusoidally. However, in many applications, Brushless DC (BLDC) drive despite existing drawbacks is applied onto PMSM because of its low cost, reliability and robustness. The research work in this thesis aims to address these outstanding issues in BLDC drive deployment. In an attempt to introduce and integrate the work to the industry, the architectural design, algorithm codes and on-board testing are performed on Field Programmable Gate Array (FPGA).

The most commonly used sensorless control scheme for BLDC drive is the Terminal Voltage Sensing. This method relies on the detection of back-EMF zero crossing points (ZCPs), which suffers from inductive spikes brought about by commutation. The tainted ZCPs waveform is traditionally filtered prior to usage for BLDC commutation. Such a strategy limits its performance, especially at high speed. In this thesis, a sensorless BLDC drive derived from ZCP centering was conceived and heuristic logic was incorporated for zero delay ZCP detection. The implemented design, as intended, operated with zero delay yet was robust against spikes and made the drive well-suited for a wide speed range.

BLDC drive applied on PMSM while brought about the advantages of robustness and simplicity, unfortunately, suffered from severe torque pulsation, aggravated by commutation torque ripple. The root causes for this torque, namely the presence of inductance and back-EMF, have been derived and analyzed. A quasi-BLDC drive utilizing current advance as well as varying voltage for current change rate matching was proposed. It was shown through numerical simulation and confirmed by the experimental results that the commutation current spike was largely improved. The torque ripple factor gave a significant improvement from 65% to 12.5%.

Self-Starting has been, and still is, a key concern in sensorless drives and particularly crucial for surface mounted PMSM. To address this challenging class of motor, a novel initial rotor detection method has been conceptualized and successfully applied. The proposed method, simple yet accurate, was presented together with detailed analysis including numerical simulations. A digital variant of the method was implemented on hardware and has been successfully deployed for sensorless BLDC self-starting on various HDDs. This method shaved off a 90% of the starting time, an enticing figure for the industry. In the absence of established solution towards initial rotor position detection for surface mounted PMSM, the successful application of the proposed method on this challenging class of motor has drawn both academic and industry interests.

In applications where motors with large inertia or low back-EMFs are used, knowledge of initial rotor position will be insufficient to launch a successful start-up.

Existing methods of open loop start-up coupled with gate turn-off prove deficient. A novel gate signal masking six step open loop strategy was proposed and investigated. It has been shown through numerical simulation and hardware implementation that the method was able to achieve: (i) an earliest possible crossover while making no assumption on the crossover frequency, (ii) smooth crossover as the motor rotation was continued, and (iii) continuance of frequency skewing during the detection. Apart from improved operation and robustness, the hardware implementation indicated an improvement of 40% in starting time over the conventional method of gate turn-off.

From the perspective of torque performance, a PMSM should be driven sinusoidally. BLDC drive is employed due to its simplicity and robustness. In this thesis, a sensorless optimal sinusoidal BLDC was proposed. In the proposed drive, the torque performance was improved due to sinusoidal drive, the power was optimal as the motor currents and its respective back-EMFs were aligned, sensorless control was achieved with no position or current sensors and the drive made BLDC as proportional relationship between dc link voltage and speed was maintained. The novel strategy encompasses a power angle control with derivation conducted to provide an optimal sinusoidal BLDC and an innovative power angle measurement based on freewheel current to construct a sensorless drive. The proposed sensorless optimal sinusoidal method does not use current sensor or current sampling resistors, therefore it can be realized with low cost and high efficiency. It has been shown from numerical simulation and hardware implementation that the control drive accomplished the intended objectives.

CHAPTER 9. FUTURE WORK

The algorithms have been tested extensively and proven to be robust against a wide variety of motors in terms of inertia, load and power. However, several issues remain that can give rise to scope for future work. They are

(1) Motor Runout Performance

Performance indices such as copper loss, acoustics have been compared in this study. Another key index in HDD industry is the motor runout. It would be beneficial to investigate the impact or the improvement of the proposed drives on the motor runout.

(2) Megapower Motor Applications

The initial rotor detection algorithm requires an application of pulses at rated voltage which will draw large currents for high-power applications. In order for it to be adapted for megawatts motor, further investigation and adaption will be required.

(3) Parameter Sensitivity

The proposed sinusoidal BLDC drive works well for a known parameterized motor. Future work is necessary if robustness against motor parameters variation is required.

PAPERS ARISING FROM DISSERTATION

1 Soh C.S., Bi C., Chua K.C., "Direct PID Tuning for Spindle Motor Systems", Asia-Pacific Magnetic Recording Conf, 2006. APMRC 2006, pp. 1-2, 29 Nov – 1 Dec 2006.

2 Phyu H.N., Bi C., Soh C.S., "Study of a Spindle Motor Starting using Circuit-Field Coupled System", Int Conf on Elect Mech and Syst, 2007. ICEMS 2007, pp. 456-461, 8-11 Oct 2007.

3 Soh C.S., Bi C., "Self-Sensing Sinusoidal Drive for Spindle Motor Systems", 33rd Annual Conf of the IEEE Ind Elect Soc, 2007. IECON 2007, pp. 998-1002, 5-8 Nov 2007.

4 Soh C. S., Bi C., Teo K.K., "FPGA Implementation of Quasi-BLDC Drive", 7th Int Conf on Power Elect and Drive Syst, 2007. PEDS 2007, pp. 883-888, 27-30 Nov 2007.

5 Bi C., Soh C.S., "Copper Loss of PM-BLDC Motor in High Speed Operation", Int Conf on Elect Mach and Syst, 2008. ICEMS 2008, 17-20 Oct 2008.

6 Soh C.S., Bi C., "Sensorless Optimal Sinusoidal BLDC for Hard Disk Drives", 53rd Annual Conference on Magnetism and Magnetic Materials, 10-14 Nov 2008.

7 Soh C.S., Bi C., Yong Z.H., Lim C.P., "Contactless Measurement Method for HDD Spindle Motor Parameters", Asia-Pacific Magnetic Recording Conf, 2009, 14-16 Jan 2009

8 Soh C.S., Bi C., "Sensorless Optimal Sinusoidal BLDC for Hard Disk Drives", Journal of Applied Physics, vol. 105, issue 7, pp. 07F118 - 07F118-3, Apr 2009.

9 Soh C.S., Bi C., Yong Z.H., Lim C.P., "Contactless Measurement Method for Hard Disk Drive Spindle Motor Impedance", IEEE Trans on Magnetics, vol. 45, issue 11, pp. 5168 - 5171, Nov 2009

REFERENCES

1 Lorenz, R.D., "Practical issues and research opportunities when implementing zero speed sensorless control", in Proceedings of the Fifth International Conference on Electrical Machines and Systems, 2001. ICEMS 2001. Volume 1, Issue , 2001 Page(s):1 – 10

2 Johnson, J.P. Ehsani, M. Guzelgunler, Y., "Review of sensorless methods for brushless DC", Thirty-Fourth IAS Annual Meeting. Conference Record of IEEE Industry Applications Conference, 1999. Volume: 1, Page(s): 143-150

3 Tae-Hyung Kim; Hyung-Woo Lee; Mehrdad Ehsani, "State of the art and future trends in position sensorless brushless DC motor/generator drives", 31st Annual Conference of IEEE Industrial Electronics Society, 2005. IECON 2005. Issue , 6-10 Nov. 2005 Page(s): 1718-1725

4 Kim, T. Lee, H-W. Ehsani, M., "Position sensorless brushless DC motor/generator drives: review and future trends", Electric Power Applications, IET. July 2007, Volume: 1, Issue: 4 Page(s): 557-564

5 Acarnley, P.P.; Watson, J.F., "Review of position-sensorless operation of brushless permanent-magnet machines", IEEE Transactions on Industrial Electronics, April 2006, Volume 53, Issue 2, Page(s): 352 - 362

6 Montesinos, D.; Galceran, S.; Blaabjerg, F.; Sudria, A.; Gomis, O., "Sensorless control of PM synchronous motors and brushless DC motors - an overview and evaluation", European Conference on Power Electronics and Applications, 2005, 11-14 Sept. 2005, Page(s): 1-10

7 Montesinos, D. Galceran, S. Sudria, A. Gomis, O. Blaabjerg, F., "Low cost sensorless control of permanent magnet motors - an overview and evaluation", IEEE International Conference on Electric Machines and Drives, 2005, 15-18 May 2005, Page(s): 1681- 1688

8 Jianwen Shao; Nolan, D.; Hopkins, T., "A novel direct back EMF detection for sensorless brushless DC(BLDC) motor drives", Seventeenth Annual IEEE Applied Power Electronics Conference and Exposition, 2002. APEC 2002. Volume 1, 2002 Page(s): 33 – 37

9 Jianwen Shao; Nolan, D.; Hopkins, T., "Improved direct back EMF detection for sensorless brushless DC (BLDC) motor drives", Eighteenth Annual IEEE Applied Power Electronics Conference and Exposition, 2003. APEC 2003. Volume 1, 9-13 Feb. 2003 Page(s): 300 – 305

10 Shao, J. Nolan, D., "Further improvement of direct back EMF detection for sensorless brushless DC (BLDC) motor drives", Twentieth Annual IEEE Applied Power Electronics Conference and Exposition, 2005. APEC 2005. 6-10 March 2005 Volume: 2, Page(s): 933-937

11 Yen-Shin Lai Fu-Shan Shyu Wei-Hwa Rao, "Novel back-EMF detection technique of brushless DC motor drives for whole duty-ratio range control", 30th Annual Conference of IEEE Industrial Electronics Society, 2004. IECON 2004. 2-6 Nov. 2004 Volume: 3, On page(s): 2729- 2732

12 Jiang, Q.; Bi, C.; Huang, R., "A new phase-delay free method to detect back EMF zero crossing points for sensorless control of spindle motors", Asia-Pacific Magnetic Recording Conference, 2004. APMRC 2004. 16-19 Aug. 2004 Page(s): 2

13 Jiang, Q. Bi, C. Lin, S., "Sensorless control of permanent magnet spindle motors used in hard disk drives", Proceedings of the Eighth International Conference on Electrical Machines and Systems, 2005. ICEMS 2005. 27-29 Sept. 2005 Volume: 1, Page(s): 177- 182

14 Iizuka, Kenichi et al, "Microcomputer Control for Sensorless Brushless Motor", IEEE Transactions on Industry Applications, May 1985, Volume: IA-21, Issue: 3 Page(s): 595-601

15 Doo-Hee Jung; In-Joong Ha, "Low-cost sensorless control of brushless DC motors using a frequency-independent phase shifter", IEEE Transactions on Power Electronics, Volume 15, Issue 4, Jul 2000 Page(s):744 – 752

16 Gui-Jia Su; McKeever, J.W., "Low cost sensorless control of brushless DC motors with improved speed range", Seventeenth Annual IEEE Applied Power Electronics Conference and Exposition, 2002. APEC 2002. Volume 1, Page(s):286 – 292

17 Zhigan Wu; Jin Wang; Jianping Ying; Jianhong Zeng, "Sensorless brushless DC motor drive for air-conditioner compressor", Proceedings of the Fifth International Conference on Electrical Machines and Systems, 2001. ICEMS 2001. Volume 2, Aug 2001 Page(s):968 – 971

18 M. Jufer and R. Osseni, "Back-EMF indirect detection for self-commutation of synchronous motors," in *Proc. 1987 Eur. Conf. Power Electronics and Applications, EPE'87*, 1987, pp. 1125–1129.

19 J. C. Moreira, "Indirect sensing for rotor flux position of permanent magnet AC motors operating over a wide speed range," *IEEE Trans. Ind. App.*, vol. 32, pp. 1394–1401, Nov./Dec. 1996.

20 F. Profumo, G. Griva, M. Pastorelli, J. C. Moreira, and R. D. Donker, "Universal field oriented controller based on airgap flux sensing via third-harmonic stator voltage," *IEEE Trans. Ind. Appl.*, vol. 30, pp.448–455, Mar./Apr. 1994.

21 A. Testa, A. Consoli, M. Coco, and L. Kreindler, "A new stator voltage third-harmonic based direct field oriented control scheme," in *Conf. Rec. IEEE-IAS Annu. Meeting*, 1994, pp. 608–615.

22 Shen, J.X., Zhu, Z.Q. and Howe, D., "Sensorless flux-weakening control of permanent-magnet brushless machines using third harmonic back EMF" *IEEE Trans. Ind. Appl.*, vol. 40, pp. 1629-1636, Nov-Dec 2004

23 Shen, J.X., Zhu, Z.Q. and Howe, D**., "**Sensorless flux-weakening control of permanent magnet brushless machines using third-harmonic back-EMF IEEE International Electric Machines and Drives Conference, 2003. IEMDC'03., vol.2, 1-4 June 2003, pp.1229 - 1235

24 Shen, J.X., Zhu, Z.Q. and Howe, D., "Practical Issues in Sensorless Control of PM Brushless Machines Using Third-Harmonic Back-EMF**",** CES/IEEE 5th International Power Electronics and Motion Control Conference, 2006. IPEMC '06. vol.2, 14-16 Aug. 2006, pp. 1 – 5

25 Shen, J.X.; Iwasaki, S., "Improvement of ASIC-based sensorless control for ultrahigh-speed brushless DC motor drive", IEEE Intl. Elec. Mach. and Drives Conf., 2003. IEMDCapos;03, vol. 2, 1-4 June 2003, pp. 1049 -1054

26 Shen, J.X.; Iwasaki, S., "Sensorless control of ultrahigh-speed PM brushless motor using PLL and third harmonic back EMF", IEEE Transactions on Ind. Elec., vol. 3, Apr 2006, pp. 421-428

27 S. Ogasawara and H. Akagi, "An approach to position sensorless drive for brushless DC motors", *IEEE Trans. Ind. App.*, vol. 27, Sept./Oct. 1991, pp. 928-933.

28 M.D. Erdman, H.B. Harms, and J.L. Oldenkamp, "Electronically Commutated DC Motors for the Appliance Industry", *IEEE IAS Conf Rec*, 1984, pp.1339-1345

29 R. C. Becerra, T. M. Jahns, and M. Ehsani,,"Four-quadrant sensorless brushless ECM drive," in *Proc. IEEE APEC'91 Conf.*, 1991, pp.202-209.

30 T. M. Jahns, R. C. Becerra, and M. Ehsani, "Integrated current regulation for a brushless ECM drive", *IEEE Trans. Power Elec.*, vol. 6, Jan. 1991, pp.118-126.

31 D. Regnier, C. Oudet, and D. Prudham, "Starting brushless DC motors utilizing velocity sensors", in *Proc. 14th Annual Symposium on Incremental Motion Control Systems and Devices*, 1985, 1985, pp. 99-107.

32 D. Peters and J. Harth, "ICs provide control for sensorless DC motors", in *Proc. EDN*, 1993, pp.85-94.

33 R. Wu and T. Noguchi, “A permanent magnet motor drive without shaft sensors”, IEEE Trans. Ind. Appl., vol. 27, pp.1005-1011, 1991.

34 H. Tajima and Y. Hori, “Speed sensorless field oriented control of the induction machine”, IEEE IAS Conf. Rec., pp.385-391, 1991.

35 T. Liu and C. Cheng, “Controller design for a sensorless permanent magnet synchronous motor drive”, IEEE Proc-B, pp.369-378, Nov 1993.

36 A. Consli et al, “Sensorless vector and speed control of brushless motor drives”, IEEE Trans Ind Elec, pp.91-95, 1994.

37 T. Liu and C. Cheng, “Adaptive control for a sensorless permanent magnet synchronous motor drive”, IEEE Trans on Aerospace and Elec Syst, pp.900-909, Jul 1994.

38 Jun Hu and Bin Wu, “New integration algorithms for estimating motor flux over a widespeed range”, IEEE Trans. Pwr. Elec., vol. 13, pp.969-977, Feb 1998.

39 L. Harnefors and H.P. Nee, “A general algorithm for speed and position estimation of AC motors”, IEEE Trans. Ind. Elec., vol. 47, pp.77-83, Feb 2000.

40 B. Terzic and M. Jadric, “Design and implementation of the extended kalman filter for the speed and rotor position estimation of brushless DC motor”, IEEE Trans. Ind. Elec, vol. 48, pp.1065-1073, Dec 2001.

41 L. A. Jones and J. H. Lang, “A state observer for the permanent magnet synchronous motor,” IEEE Trans. Ind. Electron., vol. 36, no. 3, pp. 346–354, Aug. 1989.

42 M. Schroedl, “Operation of the Permanent Magnet Synchronous Machine Without a Mechanical Sensor”, IEE Proc. Int’l. Conf. on Power electronics and Variable Speed Drives, pp. 51-56, July 1990.

43 M. Schroedl, “Digital Implementation of a Sensorless Control Algorithm for Permanent Magnet Synchronous Motors”, Proc. Int’l. Conf. “SM 100”, ETH Zurich (Switzerland), pp. 430-435, 1991.

44 N. Matsui and M. Shigyo, “Brushless DC motor control without position and speed sensors,” IEEE Trans. Ind. Appl., vol. 28, no. 1, pp. 120–127, Jan./Feb. 1992.

45 T. Furuhashi, S. Sangwongwanich, and S. Okuma, “A Position-and-Velocity Sensorless Control for Brushless DC Motors using an Adaptive Sliding Mode Observer”, IEEE Trans. on Industrial Electronics, vol. 39, pp. 89-95, April 1992.

46 R. B. Sepe, and J. H. Lang, “Real-Time Observer-Based (Adaptive) Control of a Permanent-Magnet Synchronous Motor without Mechanical Sensors”, IEEE Trans. on Industry Applications, vol. 28, pp. 1345-1352, November/December 1992.

47 Shouse, K.R. and Taylor, D.G., “Observer-based control of permanent-magnet synchronous motors”, Ind Elec, Control, Instr and Automatn, 1992. Proc 1992 Int Conf 'Power Elect and Motion Control, 9-13 Nov. 1992, pp. 482 - 1487.

48 B. J. Brunsbach, G. Henneberger, and T. Klepsch,“Position Controlled Permanent Magnet Excited Synchronous Motor without Mechanical Sensors”, IEE Conf. on Power Electronics and Applications, vol. 6, pp. 38-43,1993.

49 G. Yang, R. Tomioka, M. Nakano, and T. H. Chin, “Position and speed sensorless control of brushless DC motor based on an adaptive observer,” IEEE Trans. Ind. Appl., vol. 113, no. 5, pp. 579–586, May 1993.

50 J. Hu, D. Zhu, Y. Li, and J. Gao, “Application of Sliding Observer to Sensorless Permanent Magnet Synchronous Motor Drive System”, IEEE Power Electronics Specialist Conf., vol. 1, pp. 532-536, 1994.

51 A. Consoli, S. Musumeci, A. Raciti, and A. Testa, “Sensorless Vector and Speed Control of Brushless Motor Drives”, IEEE Trans. on Industrial Electronics, vol. 41, pp.91-96, February 1994.

52 Z. Peixoto and P. Seixas, “Application of Sliding Mode Observer for Induced e.m.f., Position and Speed Estimation of Permanent Magnet Motors”, IEEE Conf. Proc. of IECON, pp. 599-604, 1995.

53 T. Senjyu and K. Uezato, “Adjustable Speed Control of Brushless DC Motors without Position and Speed Sensors”, Int’l. IEEE/IAS Conf. Proc. on Industrial Automation and Control: Emerging Technologies, pp. 160-164, 1995.

54 T. Senjyu, M. Tomita, S. Doki, and S. Okuma, “Sensorless Vector Control of Brushless DC Motors using Disturbance Observer”, PESC ’95 Record, 26th Annual IEEE Power Electronics Specialists Conf., vol. 2, pp. 772-777, 1995.

55 N. Matsui, “Sensorless pm brushless DC motor drives,” IEEE Trans. Ind. Electron., vol. 43, no. 2, pp. 300–308, Apr. 1996.

56 J. Kim and S. Sul, “High Performance PMSM Drives without Rotational Position Sensors using Reduced Order Observer”, Record of the 1995 IEEE Industry Applications Conf., vol. 1, pp. 75-82, 1995.

57 J. Solsona, M. I. Valla, and C. Muravchik, “A nonlinear reduced order observer for permanent magnet synchronous motors,” IEEE Trans. Ind.Electron., vol. 43, no. 4, pp. 492–497, Aug. 1996.

58 Y. Kim, J. Ahn, W. You, and K. Cho, "A Speed Sensorless Vector Control for Brushless DC Motor using Binary Observer", Proc. of the 1996 IEEE IECON 22nd Int'l. Conf. on Industrial Electronics, Control, and Instrumentation, vol. 3, pp. 1746-1751, 1996.

59 Schmidt, P.B.and Wijenayake, A.H, "Sensorless control of a permanent magnet synchronous machine down to near zero speed applied to position motion control", 31st IAS Annual Meetg, Ind Appl Conf, 1996. IAS '96., vol 1, 6-10 Oct. 1996, pp. 21 - 28.

60 Parasiliti, F., Petrella, R.and Tursini, M, "Sensorless speed control of a PM synchronous motor by sliding mode observer", Proc IEEE Intl Symp on Ind Elec, 1997. ISIE '97., 7-11 July 1997, pp. 1106-1111

61 K. Tatematsu, D. Hamada, K. Uchida, S. Wakao, and T. Onuki, "Sensorless control for permanent magnet synchronous motor with reduced order observer," in Proc. IEEE PESC, Jun. 1998, pp. 125–131.

62 Shouse, K.R. and Taylor, D.G., "Sensorless velocity control of permanent-magnet synchronous motors", IEEE Trans on Control Syst Tech, vol 6, May 1998, pp. 313 – 324

63 Z. Chen, M. Tomita, S. Doki and S. Okuma "New Adaptive Sliding Observers for Position- and Velocity-Sensorless Controls of Brushless DC Motors", IEEE Trans. on Industrial Electronics, Vol.47, No.3, June, pp.582-591, 2000.

64 J. Solsona, M.I. Valla, and C. Muravchik, "On speed and rotor position estimation in permanent-magnet AC drives," IEEE Trans. Industrial Electronics, vol. IE-47, pp. 1176-1180, Sept. 2000.

65 Y.S.Han, J.S. Choi and Y.S. Kim, "Sensorless PMSM drive with a sliding mode control based adaptive speed and stator resistance estimator", IEEE Trans Mag, vol.36, pp.3588-3591, Sept 2000

66 Pek, W.K., Lim, K.W. and Panda, S.K, "Evaluating the robustness of a sensorless controller for permanent magnet synchronous motor drives", 26th Annual Conf IEEE Indl Elec Society, 2000. IECON 2000, vol 2, 22-28 Oct. 2000, pp. 1389-1394

67 Parasiliti, F, Petrella, R and Tursini, M., "Sensorless speed control of a PM synchronous motor based on sliding mode observer and extended Kalman filter", Conf Rec Ind Appl Conf, 2001. Thirty-Sixth IAS Annual Meeting, vol 1, 30 Sept.-4 Oct. 2001, pp. 533-540

68 T. Takeshita, A. Usui, and N. Matsui, "Sensorless salient-pole PM synchronous motor drive in all speed ranges," Electr. Eng. Jpn., vol. 135, no. 3, pp. 64–73, 2001.

69 G. D. Andreescu, “Adaptive observer for sensorless control of permanent magnet synchronous motor drives,” Electr. Power Compon. Syst., vol. 30, no. 2, pp. 107–119, Feb. 2002.

70 M.Elbuluk and C. Li, “Sliding mode observer for wide-speed sensorless control of PMSM drives”, Conf Rec IEEE-IAS Annual Meeting, vol. 1, 2003, pp.480-485

71 B. Nahid-Mobarakeh, F. Meibody-Tabar, and F.-M. Sargos, “Mechanical sensorless control of PMSM with online estimation of stator resistance,” IEEE Trans. Ind. Appl., vol. 40, no. 2, pp. 457–471, Mar./Apr. 2004.

72 K. Y. Cho, S. B. Yang, and C. H. Hong, “Sensorless control of a PM synchronous motor for direct drive washer without rotor position sensors,” Proc. Inst. Elect. Eng.—Electr. Power Appl., vol. 151, no. 1, pp. 61–69,Jan. 2004.

73 K.-W. Lee, D.-H. Jung, and I.-J. Ha, “An online identification method for both stator resistance and back-EMF coefficients of PMSMs without rotational transducers,” IEEE Trans. Industrial Electronics, vol. 51, pp. 507-510, Apr. 2004.

74 K. Kang et al, “Sensorless control of PMSM in high speed range with iterative sliding mode observer”, Conf. Rec IEEE- APEC'04, vol. 2, pp. 1111-1116, 2004

75 Phyu H.N., Bi C., Soh C.S., “Study of a Spindle Motor Starting using Circuit-Field Coupled System”, Int Conf on Elect Mech and Syst, 2007. ICEMS 2007, pp. 456-461, 8-11 Oct 2007.

76 N. Matsui and T. Takeshita, “A Novel Starting Method of Sensorless Salient-Pole Brushless Motor”, vol. 1, pp. 386-392, Oct 1994.

77 T. Takeshita and N. Matsui, “Sensorless Control and Initial Position Estimation of Salient-Pole Brushless DC Motor”, Proc. 4th Int Workshop on Advanced Motion Control, vol. 1, pp. 18-23, Mar 1996.

78 N. Matsui, “Sensorless PM Brushless DC Motor Drives”, IEEE Trans. on Industry Applications, vol. 43, pp. 300-308, Apr 1996.

79 S. Ostlund and M. Brokemper, “Sensorless Rotor-Position Detection from Zero to Rated Speed for an Integrated PM Synchronous Motor Drive”, IEEE Trans. on Industry Applications, vol. 32, Sep/Oct 1996.

80 M. Schroedl, “Sensorless Control of AC Machines at Low Speed and Standstill based on the INFORM Method”, Conf Rec 31st IAS Annual Meeting, vol. 1, pp. 270-277, Oct 1996.

81 P.B. Schmidt et al, "Initial Rotor Angle Detection of a Non-Salient Pole Permanenet Magnet Synchronous Machine", Conf Rec 32nd IAS Annual Meeting, vol. 1, pp. 459-463, Oct 1997.

82 F. Parasiliti and R. Petrella, "Initial Rotor Position Estimation Method for PM Motors", Industry Applications Conference 2000, vol. 2, pp. 1190-1197, 2000.

83 S. Nakashima, Y. Inagaki and I. Miki, "Sensorless Initial Rotor Position Estimation of Surface Permanent-Magnet Synchronous Motor", IEEE Trans. on Industry Applications, vol. 36, pp. 1598-1603, Nov/Dec 2000.

84 K. Matsuse et al, "Position-Sensorless Starting Method and Driving Characteristics of Closed-Slot Small Permanent-Magnet Motor", IEEE Trans. on Industry Applications, vol. 39, pp. 451-456, Mar/Apr 2003.

85 M. Tursini, R. Petrella and F. Parasiliti, "Initial rotor position estimation method for PM motors**",** IEEE Trans. on Industry Applications, vol. 39, pp. 1630-1640, Nov/Dec 2003

86 D.F. Chen, T.H. Liu and C.K Hung, "Design and Implementation of a Sensorless PMSM Drive Including Standstill Starting", 30th Annual Conference of IEEE, IECON 2004, vol. 1, pp. 987-992, Nov 2004.

87 M. Boussak, "Implementation and Experiemental Investigation of Sensorless Speed Control with Initial Rotor Position Estimation for Interior Permanent Magnet Synchronous Motor Drive", IEEE Trans. on Power Electronics, vol. 20, no. 6, Nov 2005.

88 W.J. Lee, S.K. Sul, "A New Starting Method of BLDC Motors Without Position Sensor", IEEE Trans Ind Appl, vol. 42, pp. 1532-1538, Nov-Dec. 2006.

89 P. L. Jansen and R. D. Lorenz, "Transducerless position and velocity estimation in induction and salient AC machines," IEEE Trans. on Industry Applications, vol. 31, pp. 240–247, Mar./Apr. 1995.

90 J. Cilia, G. M. Asher, and K. G. Bradley, "Sensorless position detection for vector controlled induction motor drives using an asymmetric outersection cage," in Conf. Rec. IEEE-IAS Annual Meeting, San Diego, CA, Oct. 1996, pp. 286–292.

91 S. Ogasawara and H. Akagi, "Implementation and Position Control Performance of a Position-Sensorless IPM Motor Drive System Based on Magnetic Saliency", IEEE Transactions on Industry Applications, vol. 34, pp. 806-812, Jul/Aug 1998.

92 M.J. Corley and R.D. Lorenz, "Rotor Position and Velocity Estimation for a Salient-Pole Permanent Magnet Synchronous Machine at Standstill and High

Speeds", IEEE Trans. on Industry Applications, vol. 34, no. 4, pp. 784–789, Jul/Aug 1998.

93 L. A. S. Ribeiro, M. W. Degner, F. Briz, and R. D. Lorenz, "Comparing carrier frequency voltage and current injection for the estimation of flux, position and velocity in sensorless AC drives," in Conf. Rec. IEEE-IAS Annual Meeting, St. Louis, MO, Oct. 1998, pp. 452–459.

94 A. Consoli and A. Testa, "Sensorless Control of AC Motors at Zero Speed", Proc IEEE Int Symposium on Industrial Electronics, vol. 1, pp. 373-379, 1999.

95 T. Aihara et al, "Sensorless torque control of salient-pole synchronous motor at zero-speed operation", IEEE Trans Power Elec, vol. 14, pp.202-208, Jan 1999

96 J. Ha and S. Sul, "Sensorless field-orientation control of an induction machine by high-frequency signal injection," IEEE Trans. on Industry Applications, vol. 35, pp. 45–51, Jan./Feb. 1999.

97 M. W. Degner and R. D. Lorenz, "Position estimation in induction machines utilizing rotor bar slot harmonics and carrier frequency signal injection," IEEE Trans. on Industry Applications, vol. 36, pp. 736–742, May/June 2000.

98 A. Consoli, G. Scarcella, and A. Testa, "A new zero-frequency flux-position detection approach for direct-field-oriented-control drives," IEEE Trans on Industry Applications, vol. 36, pp. 797–804, May/June 2000.

99 A. Consoli, G. Scarcella and A. Testa, "Industry Application of Zero-Speed Sensorless Control Techniques for PM Synchronous Motors", IEEE Trans on Industry Applications, vol. 37, pp. 513-521, Mar/Apr 2001.

100 N. Teske, G. M. Asher, M. Sumner, and K. J. Bradley, "Encoderless position estimation for symmetric cage induction machines under loaded conditions," IEEE Trans. on Industry Applications, vol. 37, pp. 1793–1800, Nov./Dec. 2001.

101 F. Briz, M. W. Degner, A. Diez, and R. D. Lorenz, "Static and dynamic behavior of saturation-induced saliencies and their effect on carrier signal based sensorless AC drives," IEEE Trans. on Industry Applications, vol. 38, pp. 670–678, May/June 2002.

102 J.L. Ha et al, "Sensorless Rotor Position Estimation of an Interior Permanent Magnet Motor from Initial States", IEEE Trans. on Industry Applications, vol. 39, pp. 761-767, May/Jun 2003.

103 J.H.Jang et al, "Sensorless drive of surface-mounted permanent-magnet motor by high-frequency signal injection based on magnet saliency", IEE Trans Ind Appl, vol. 39, pp. 1031-1039, Jul-Aug 2003

104 H. Kim, KK. Huh and RD Lorenz, “A novel method for initial rotor position etimation for IPM synchronous machine drives”, IEEE Trans Ind Appl, vol. 40, pp. 1379-1378, Sep/Oct 2004.

105 R. Chandru and J.G. Zhu, “Sensorless Rotor Position Detection using Differential High Frequency Phase Current Method”, Int Conf on Power Electronics and Drives Systems, 2005, vol. 1, pp. 355-359, Jan 2006.

106 F. Zhao et al, “Sensorless Control of Interior Permanent Magnet Machine at Standstill and Low Speed”, 12th Int Power Elect and Motion Control Conf, 2006. EPE-PEMC 2006. pp. 1289-1294 Aug. 2006

107 Q.J. Guo et al, “A Novel Sensorless Control Method for IPM Synchronous Machine Drives by Carrier Signal Injection based on Magnetic Saliency”, 32nd Annual Conf IEEE Ind Elect, IECON 2006, pp. 1023 – 1028, Nov. 2006.

108 S. Ogarawara and H. Akagi, "An Approach to Position Sensorless Drive for Brushless DC Motors", IEEE Trans. on Industry Applications; vol. 27, pp 928-933, Sep-Oct 1991

109 K. R. Shouse and D. G. Taylor, “Sensorless Velocity Control of Permanent-Magnet Synchronous Motors”, Proc. of the 33rd Conf. on Decision and Control, pp. 1844-1849, Dec 1994.

110 J. C. Moreira, “Indirect sensing for rotor flux position of permanent magnet AC motors operating over a wide speed range”, ", IEEE Trans. on Industry Applications, vol. 32, pp 1394-1401, Nov-Dec 1996

111 F. Parasiliti, R. Petrella and M. Tursini, ”Sensorless speed control of a PM synchronous motor based on sliding mode observer and Kalman filter”, Proc. ISIE ’97, vol.3, pp. 1106-1111, Guimarães, 1997.

112 K. R. Shouse and D. G. Taylor, “Sensorless Velocity Control of Permanent-Magnet Synchronous Motors”, IEEE Trans. on Control Systems Technology, pp. 313-324, May 1998.

113 F. Parasiliti, R. Petrella and M. Tursini, ”Sensorless speed control of a PM synchronous motor based on sliding mode observer and extended Kalman filter”, IEEE Industry Applications, 36th IAS Annual Meething, vol. 1, pp. 533-540, Sep-Oct 2001.

114 T. Senjyu and K. Uezato, “Adjustable Speed Control of Brushless DC Motors without Position and Speed Sensors”, Int’l. IEEE/IAS Conf. Proc. on Industrial Automation and Control: Emerging Technologies, pp. 160-164, 1995.

115 J. Hu, D. Zhu, Y. Li, and J. Gao, "Application of Sliding Observer to Sensorless Permanent Magnet Synchronous Motor Drive System". IEEE Power Electronics Specialist Conf., vol. 1, pp.532.536 1994.

116 N. Ertugrul and P. Acarnley, "A New Algorithm for Sensorless Operation of Permanent Magnet Motors", IEEE Trans. on Industry Applications, vol. 30, pp. 126-133, Jan-Feb 1994

117 M. Park and H Lee, "Sensorless Vector Control of Permanent Magnet Synchronous Motor Using Adaptive Identification", IEEE Conf. on Industrial Electronics Society, vol. 1, pp. 209-214, 1989.

118 N. Matsui, "Sensorless Operation of Brushless DC Motor Drives", Proc. IECON '93, vol. 2, pp. 739-744, Nov 1993.

119 N. Matsui, T. Takeshita and K. Yasuda, "A New Sensorless Drive of Brushless DC Motor", Proc. IECON '92, vol. 1, pp. 430-435, Nov 1992.

120 Bi C., Soh C.S., "Copper Loss of PM-BLDC Motor in High Speed Operation", Int Conf on Elect Mach and Syst, 2008. ICEMS 2008, 17-20 Oct 2008.

121 T. M. Jahns, "Torque production in permanent-magnet synchronous motor drives with rectangular current excitation," IEEE Trans. Ind. Appl, vol. 20, pp. 803-813, July/Aug. 1984.

122 H. R. Bolton and R.A. Ashen, "Influence of motor design and feedcurrent waveform on torque ripple in brushless DC drives," IEE Proc, vol. 131, pp. 82-90, May 1984.

123 H. Le-Huy, R. Perret, and R. Feuillet, "Minimization of torque ripple in brushless dc motor drives," IEEE Trans. Ind. Appl, vol. 22, no. 4, pp. 748-755, July/Aug. 1986.

124 Y. Murai, Y. Kawase, K. Ohashi, K. Nagatake, and K. Okuyama, "Torque ripple improvements for brnshless DC miniature motors," IEEE Trans. Ind. Appl, vol. 25, pp. 441-450, May/June 1989.

125 E. Favre and M. Jufer, "Cogging torque suppression by a current control," Proc. Ind. Conf Elec. Mach, pp. 601-606, Aug. 1990.

126 R. Carlson, M. Lajoie-Mazenc, and J. dos S. Fagundes, "Analysis of torque ripple due to phase commutation in brushless DC machines," Rec. IEEE Ind. Appl. Soc. Annu. Meet., Oct. 1990, pp.287-292.

127 L. Schlting and H-C Skudelny, “A control method for permanent magnet synchronous motors with trapezoidal electromotive force,” in Proc. Eur. Conf Power Elec. Appl, vol. 4, pp.117-122, 1991.

128 D. Hanselman, J. Y. Hung, and M. Keshura, “Torque ripple analysis in brushless permanent magnet motor drives,” Proc. Int. Conf Elec.Mach, pp. 823-827, Sept.1992.

129 J.Y. Hung and 2. Ding, “Minimization of torque ripple in permanent magnet motors: A closed-form solution,” Proc. 18th IEEE Ind.Elect. Conf, pp. 459-463, Nov. 1992.

130 T.M. Jahns, and W.L. Soong, “Pulsating torque minimization techniques for permanent magnet AC motor drives-a review” IEEE Trans Ind Elec, vol. 43, Apr 1996, pp. 321-330

131 S.J. Park et al, “A new approach for pulsating torque minimization of brushless PM motor”, 26th Annual Conf IEEE Ind Elec Soc, 2000, vol 1, 22-28 Oct. 2000, pp.76-82

132 K.W. Lee et al, “Commutation torque ripple reduction in a position sensorless brushless DC motor drive”, IEEE 35th Annual Power Elec Spec Conf, 2004, vol 2, 20-25 June 2004, pp. 1419-1423

133 K.Y. Nam et al, “Reducing torque ripple of brushless DC motor by varying input voltage”, IEEE Trans Magnetics, vol 42, Apr 2006 pp.1307-1310

134 Dae-Kyong Kim et al, “Commutation Torque Ripple Reduction in a Position Sensorless Brushless DC Motor Drive”, IEEE Trans Power Elec, vol. 21, Nov 2006, pp.1762-1768

135 J.C.G. Pimentel and L.H. Hoang, “A VHDL-based methodology to develop high performance servo drivers”, Conf Rec IEEE Ind Appl Conf 2000, vol. 3, 2000, pp.1505-1512

136 M. Cirstea et al, "Vector control system design and analysis using VHDL", IEEE 32nd Annual Power Elec Spec Conf, vol.1 , 2001, pp. 81-84

137 Soh C. S., Bi C., Teo K.K., “FPGA Implementation of Quasi-BLDC Drive”, 7th Int Conf on Power Elect and Drive Syst, 2007. PEDS 2007, pp. 883-888, 27-30 Nov 2007.

138 Z.Y. Zhou et al, "FPGA realization of a high-performance servo controller for PMSM”, 19th Annual IEEE Applied Power Elec Conf and Expos, vol. 3, pp. 1604-1609, 2004.

139 T. Takahashi and J. Goetz, "Implementation of complete AC servo control in a low cost FPGA and subsequent ASSP conversion", 19th Annual IEEE Applied Power Elec Conf and Expos, vol. 1, pp. 565-570, 2004.

140 Y.S. Rung, P.G. Huang and C.W. Chen, "Development of a SOPC for PMSM drives", 47th Midwest Symp on Circuits and Systems, vol.2, 25-28 July 2004, pp. 329-332

141 Y.C. Chang and Y.Y. Tzou, "Single-chip FPGA Implementation of a Sensorless Speed Control IC for Permanent Magnet Synchronous Motors", IEEE Pwr Elec Spec Conf 2007, pp. 593-598, 17-21 June 2007.

142 Soh C.S., Bi C., Chua K.C., "Direct PID Tuning for Spindle Motor Systems", Asia-Pacific Magnetic Recording Conf, 2006. APMRC 2006, pp. 1-2, 29 Nov – 1 Dec 2006.

143 Lin Song, "Advanced Sensorless Control of Micro PMSM and its Application in Hard Disk Drives", Thesis (PHD)--Dept. of Electrical and Computer Engineering, Faculty of Engineering, National University of Singapore, 2005.

144 Jacek F. Gieras, Mitchell Wing, "Permanent Magnet Motor Technology", Marcel Dekker Inc, 2nd Edition, pp. 109.

145 Takashi Kenjo and Shigenobu Nagamori, "Brushless Motors Advanced Theory and Modern Applications", Sogo Electronics Press 2003, pp221-281

146 Soh C.S., Bi C., "Self-Sensing Sinusoidal Drive for Spindle Motor Systems", 33rd Annual Conf of the IEEE Ind Elect Soc, 2007. IECON 2007, pp. 998-1002, 5-8 Nov 2007

147 Soh C.S., Bi C., "Sensorless Optimal Sinusoidal BLDC for Hard Disk Drives", 53rd Annual Conference on Magnetism and Magnetic Materials, 10-14 Nov 2008.

148 Soh C.S., Bi C., "Sensorless Optimal Sinusoidal BLDC for Hard Disk Drives", Journal of Applied Physics, May 2009

149 Abdullah Al Mamun, Bi Chao, Guoxiao Guo, "Hard Disk Drive Mechatronics and Control", CRC Press, 2006